SIEMENS

MAGNETOM Flash

The Magazine of MRI

Issue Number 3/2015 | RSNA Edition

Not for distribution in the US

Point-of-Care MR Imaging. Thoughts on a Potential New Strategy
Gustav Andreisek
Page 4

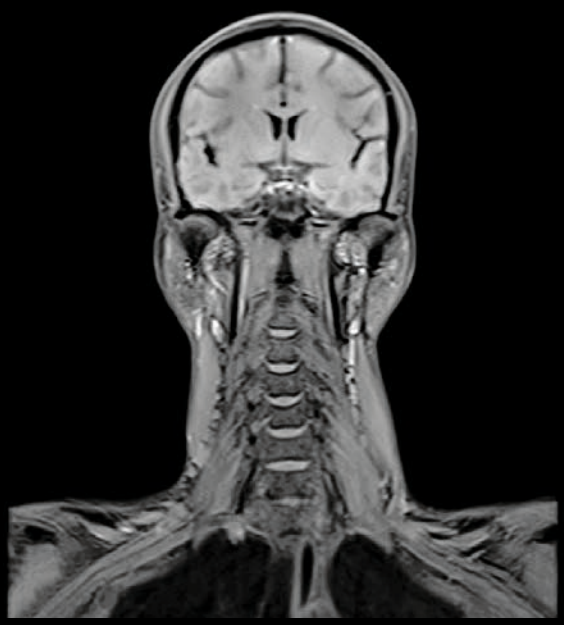
RESOLVE in Breast MRI
Sung Hun Kim
Page 29

MRI for Parathyroid Imaging
Kambiz Nael
Page 31

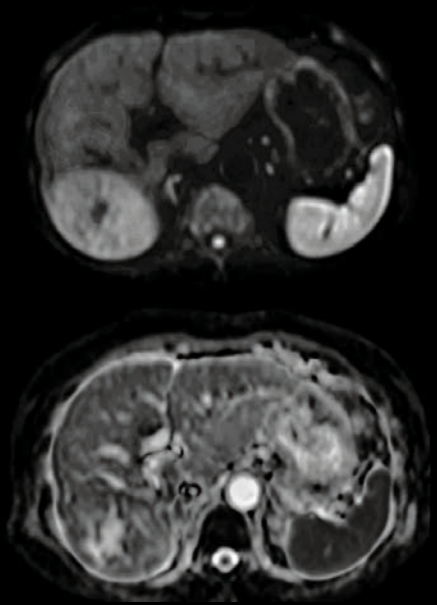
Neurovasculature imaging with Dot and T1 SPACE
Michel Paret
Page 36

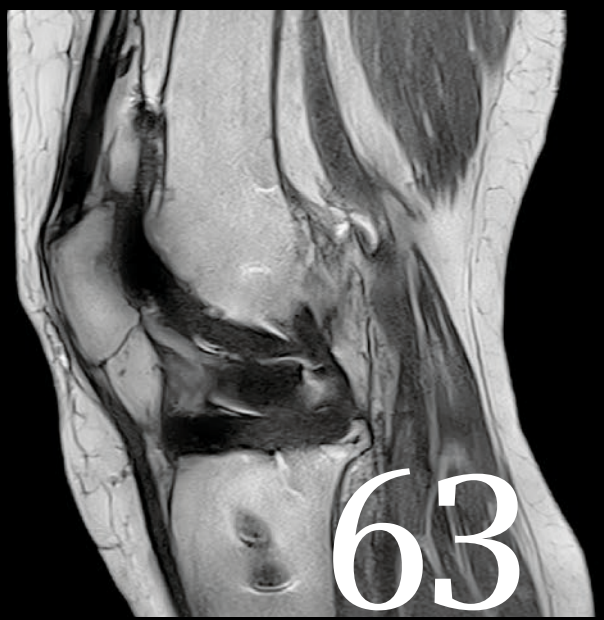


Cover images
MAGNETOM Amira



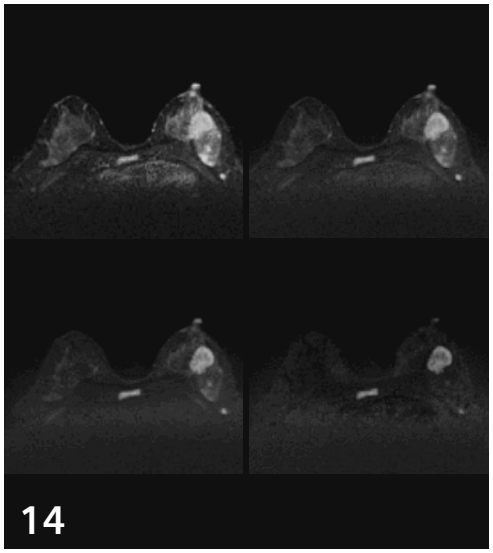




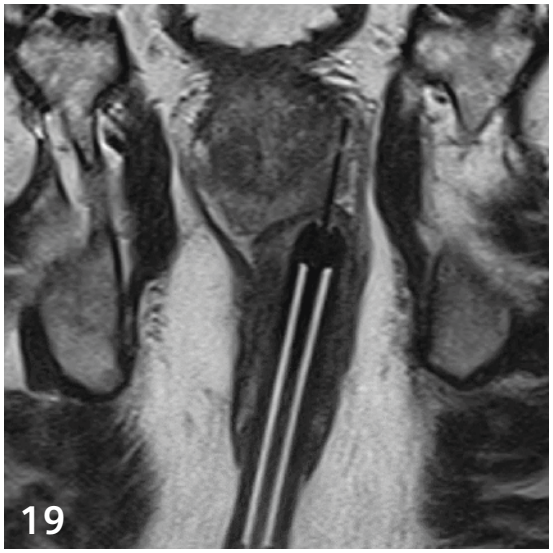


63

Content



Computed b-values with *syngo*.via



MR-guided biopsy of the prostate in supine patient position

Spotlight

4 Point-of-Care MR Imaging and How We can Learn from Other Imaging Modalities. Thoughts on a Potential New Strategy
Gustav Andreisek, University Hospital Zurich, Switzerland

Oncological Imaging

8 ^{18}F-FDG PET/MR: Its Incremental Value in Assessing the Multiple Myeloma Patient
Shetal N. Shah, et al., Imaging Institute, Cleveland Clinic, Cleveland, OH, USA

11 **How-I-do-it:** New 'ADC & b-value' Tool in *syngo*.via
Anja Fernandez, et al., Siemens Healthcare, Erlangen, Germany

Men's Health

16 Hybrid PET/MR Imaging with PSMA-Ligands: the Future Standard in the Diagnosis of Prostate Cancer?
Ali Afshar-Oromieh, et al., Heidelberg University Hospital, Heidelberg, Germany

19 MR-Guided Biopsies of the Prostate in Supine Patient Position
Florian Schneider, et al., Martha-Maria Hospital, Nürnberg, Germany

Technology

22 A Novel Model-Based MR Attenuation Correction Method for PET/MR Hybrid Imaging Considering Bone
Daniel H. Paulus, et al., Friedrich-Alexander-University Erlangen-Nürnberg, Erlangen, Germany

Women's Health

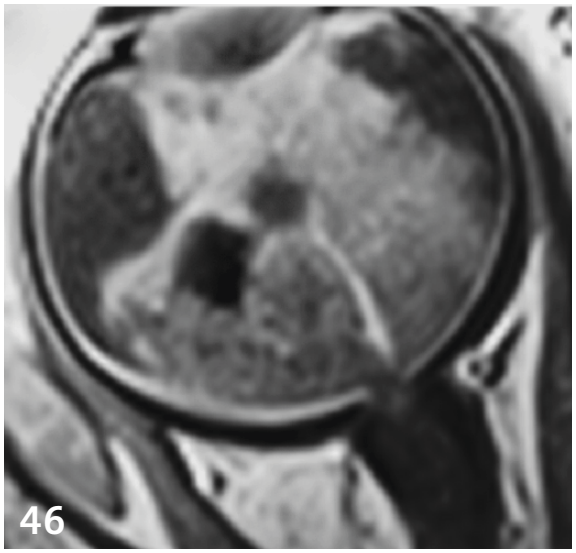
29 Breast MRI: Improved Image Quality with RESOLVE
Sung Hun Kim, The Catholic University of Korea, Seoul, Korea

Head and Neck Imaging

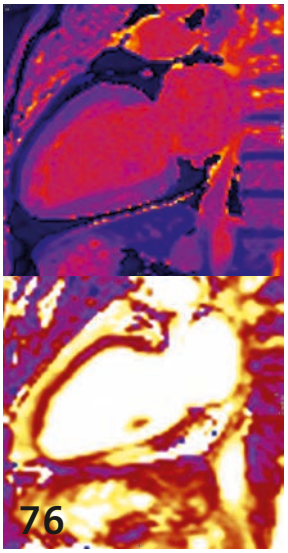
31 **How-I-do-it:** MRI for Parathyroid Imaging
Kambiz Nael, Mount Sinai Hospital, New York, NY, USA



Cover images
1.5T MAGNETOM Amira
Courtesy of Radiologische Gemeinschaftspraxis, Halle, Germany and Munakata Shukokai Sogo Hospital, Fukuoka, Japan.



Pediatric pathologies that have leukocoria as presenting sign



Non-contrast tissue characterization with T1 and T2 mapping



QISS lower extremity MRA

Neurology

36 Reliable Imaging of Neurovasculature with Dot and T1 SPACE
Michel Paret, et al., GIE IRMAS, Saint-Priest-en-Jarez, France

41 How to get Inline Reconstructed Rotating MIPs with a 3D SPACE Measurement
Thomas Illigen, Siemens Healthcare, Mannheim, Germany

Pediatrics

46 Pediatric Pathologies that have Leukocoria as Presenting Sign
Paolo Galluzzi, et al., Azienda Ospedaliera e Universitaria Senese, Siena, Italy

Image Gallery

59 Image Gallery MAGNETOM Amira

Cardiovascular Imaging

64 Self-Navigated Free-Breathing High-Resolution 3D Cardiac Imaging: A New Sequence for Assessing Cardiovascular Congenital Malformations
Juerg Schwitter, et al., University Hospital of Lausanne (CHUV), Lausanne, Switzerland

72 Utility of Delayed Enhanced Cardiac MRI in the Assessment of Cardiomyopathies
Dipan J. Shah, et al., Houston Methodist Hospital, Houston, TX, USA

76 Case Report: Acute Myocardial Syndrome in a 37-Year-Old Patient with Severe Renal Impairment
Anna S. Herrey, et al., The Barts Heart Centre, London, UK

78 Case Report: Detection of Myocardial Changes in a Patient Undergoing Chemotherapy
Steve W. Leung, et al., University of Kentucky Medical Center, Lexington, KY, USA

80 Case Report: QISS MRA at 3T
Anna-Maria Lydon, et al., University of Auckland, New Zealand

82 Quiescent Interval Single-Shot (QISS) Lower Extremity MRA for the Diagnosis of Peripheral Artery Disease: Case Presentations
Akos Varga-Szemes, et al., Medical University of South Carolina, Charleston, SC, USA

87 **How-I-do-it:** Using Remote Assist to Expand Your Expertise
Gary Smith, Siemens Healthcare, Great Britain and Ireland

The information presented in MAGNETOM Flash is for illustration only and is not intended to be relied upon by the reader for instruction as to the practice of medicine. Any health care practitioner reading this information is reminded that they must use their own learning, training and expertise in dealing with their individual patients. This material does not substitute for that duty and is not intended by Siemens Healthcare to be used for any purpose in that regard. The treating physician bears the sole responsibility for the diagnosis and treatment of patients, including drugs and doses prescribed in connection with such use. The Operating Instructions must always be strictly followed when operating the MR System. The source for the technical data is the corresponding data sheets.

Point-of-Care MR Imaging and How We can Learn from Other Imaging Modalities. Thoughts on a Potential New Strategy

Gustav Andreisek, M.D., MBA

Section Head of MSK and MR Imaging, Institute of Diagnostic and Interventional Radiology, University Hospital Zurich, University of Zurich, Switzerland

Abstract

A new possible strategy in MR imaging (MRI) could be point-of-care MRI. Point-of-care imaging strategies are well-known from ultrasound. Point-of-care imaging is extremely focused and goal-directed. Ideal exams are those ones which can be performed easily and quickly. This article provides some thoughts on the background, advantages and limitations of this concept which could possibly be applied to MRI.

Key Points

- Point-of-care MRI could reduce examination time and thus be more cost-effective
- Point-of-care MRI may increase patient comfort and thus compliance

Background

One of the most frequently discussed drawbacks of MR imaging in medical literature is cost [1-7]. Although costs have come down massively over the past two decades, it still remains an imaging modality that costs more than other imaging modalities, such as ultrasound or X-ray. However, the term 'cost' needs closer consideration. When a radiologist-in-chief is asked about the 'costs of MRI', he would include the purchase price of the MR scanner and equipment as well as the daily running costs; a patient would think of the final bill sent by the imaging provider; the CEO of an insurance company would list some of the companies' reimbursement numbers and the sum paid to imaging providers; a referring physician would answer that he thinks there are high costs but that this is justified in this individual's case; and a politician would likely answer that the healthcare system of almost any country is struggling financially, and that overall costs need to come down. All these observations share a common basis – a desire for an 'improvement of costs', i.e. greater efficiency.

Efficiency in MRI can be influenced by several factors, but it is essential to acknowledge that a reduction in acquisition time per sequence, an increase in field strength, and an improvement in patient throughput will come to an end at some point. This is where a new strategy for MRI is needed.

A possible new strategy: some thoughts on point-of-care MR imaging

This new strategy could be point-of-care MR imaging. Point-of-care strategies in imaging are nothing new and indeed well-known from other modalities, such as ultrasound [8-10]. In general, 'point-of-care ultrasound' refers to the use of portable ultrasound devices at the patient's bedside. Typical characteristics for point-of-care strategies are the following [8]:

The exam should be

- performed for a clear-defined purpose in which it has been linked to improving patient outcomes
- focused and goal-directed
- easily recognizable
- learned easily
- quickly performed
- performed at the patient's bedside.

Theoretical basis of this strategy is that the diagnostic purpose is based on symptoms or sign-based examinations. Whereas all the listed requirements can be applied to ultrasound, adapting the last requirement to MRI is difficult. Nevertheless, whilst MRI at the patient's bedside is not possible, I observe every day in my clinical practice in a large European hospital that patients are brought to our MR imaging center in their beds and moved from their bed to the scanner's patient table for MR imaging. Since our in-house patients' transportation service is very well organized, patients will show up in the MR center roughly 15 minutes after our technologists called the nurses or activated the online call for this transportation service. In effect, this takes no longer than walking to the patient's bedside with a portable device.

One could therefore conclude that all the above requirements could be

Table 1

Region	Sequences	Duration [min]	Slices	Slice thickness	Field-of-view [mm]	Matrix	TR [ms]	TE [ms]
head	t1_se_sag	1:19	20	5	230x230	256x256	550	10
	t2_tse_tra	1:32	20	5	230x230	261x384	5000	99
	t2_tse_dark-fluid_tra	1:50	22	5	201x230	168x256	9000	92
	ep2d_diff_3scan_trace_p2	0:47	22	5	230x230	130x130	4500	80
c-spine	t2_tse_sag	1:26	15	3	240x240	240x320	3150	100
	t1_tse_sag	1:38	15	3	240x240	192x256	550	9
	TIRM_sag	2:18	15	3	240x240	192x256	350	40
	T2_me2d_tra	2:35	3	3	180x180	192x256	580	21
t-spine	t2_tse_sag	1:27	15	4	340x340	256x320	3700	90
	t1_tse_sag	0:53	15	4	340x340	256x320	570	9
	TIRM_sag	1:59	15	4	340x340	205x256	3550	41
	t2_tse_tra	1:29	15	4	200x200	230x256	3500	86
l-spine	t2_tse_sag	0:58	15	4	280x280	224x320	400	90
	t1_tse_sag	1:06	15	4	280x280	224x320	570	9
	TIRM_sag	2:11	15	4	280x280	224x320	3500	41
	t2_tse_tra_msma	1:51	15	4	200x200	230x256	3500	70
knee	pd_tse_cor	3:36	25	3	160x160	236x448	3200	35
	t2_tse_fs_sag	2:23	25	3	160x160	230x256	4300	72
	pd_tse_sag	2:08	25	3	160x160	256x320	3000	30
	pd_tse_fs_tra	2:38	30	3	140x140	218x256	4020	34
hip	t1_tse_cor	2:34	20	3	350x350	336x448	450	8
	pd_tse_fs_cor	2:50	20	3	350x350	336x448	2800	31
	t2_tse_tra	1:58	20	3	350x350	336x448	4000	85
shoulder	pd_tse_fs_cor	2:32	20	3	140x140	192x256	3500	25
	pd_tse_fs_tra	2:29	20	3	140x140	205x256	3000	34
	pd_tse_sag	2:23	20	3	140x140	256x320	3000	33

Example of possible protocols for point-of-care MRI with a maximum total acquisition time of under 10 minutes for each anatomic region. Please note that the point-of-care concept requires specifically tailored imaging protocols and the following might only be a basis for further specific adjustments.

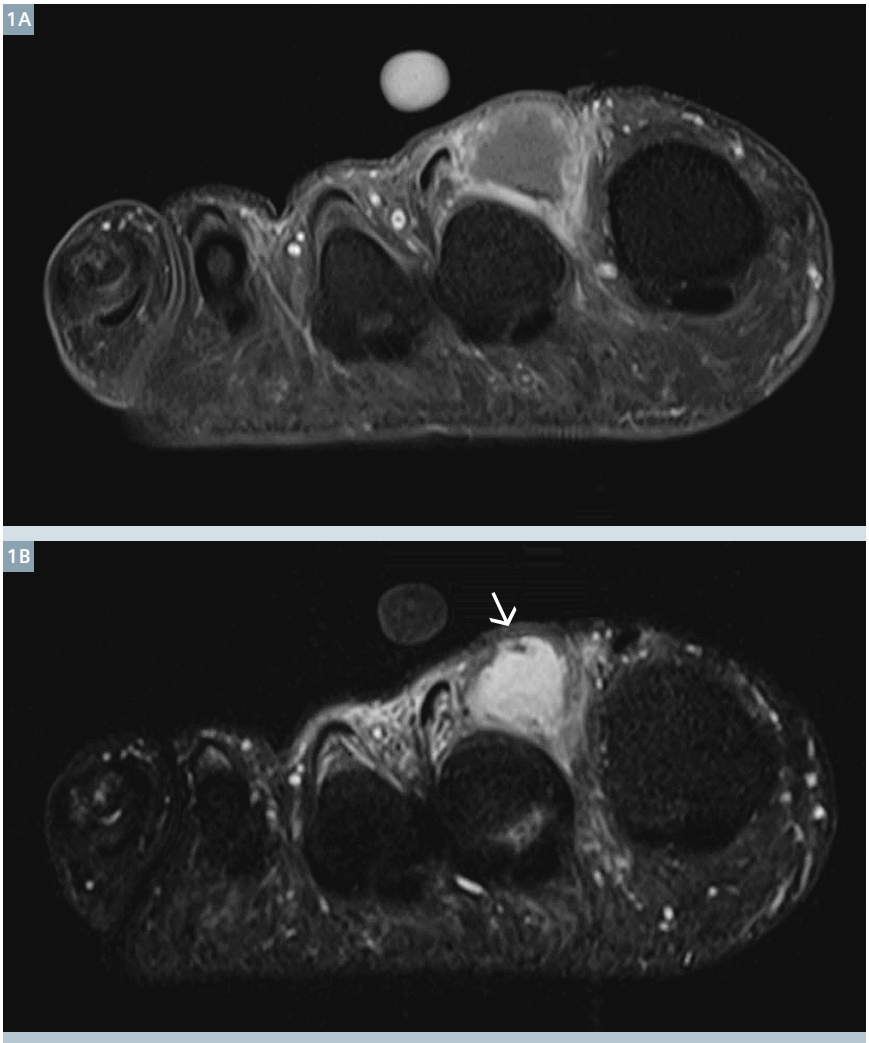
applied to MRI, although a further change in thinking about the core essentials of an MRI examination may be needed. In the past, we have always considered MRI a high-end modality, where we can solve all problems which other modalities could not solve. This was mainly driven by the inherent advantages of MRI over other modalities, such as its much better evaluation of soft tissue. Thus, MRI is performed virtually the same way anywhere in the world, as a means to gather as much information as possible from one single exam.

Let's take a simple example: A referral for 'suspicion of osteomyelitis of the fifth toe'. Typically, such a patient is placed in a supine position using a dedicated foot coil and a dedicated imaging protocol for the forefoot which usually includes all toes. However, strictly speaking, four of the five toes are not of interest and the clinician has not asked for them either. The clinicians have examined the patients and they know that it is the fifth digit that is affected as it presents as a painful, swollen red toe. Applying the point-of-care concept would mean that a tailored MR imaging protocol could be reduced to the fifth digit and since the question is only to confirm/rule out osteomyelitis, one sagittal and one axial fast T1-weighted sequence as well as one axial T2-weighted fast sequence could be acquired. Contrast might not be necessary to establish the diagnosis, but adding a sagittal fat suppressed T1-weighted sequence could do the job if desired. Overall, 3 to 4 sequences would be enough, and since the field-of-view can be limited to the fifth digit only,

between 5-10 slices each could be enough. Such an imaging protocol could be achieved within 6-8 min overall imaging time which means that the patients total in-room time might be under 10 minutes. In addition to greater cost efficiencies of this point-of-care strategy, there are also some advantages for the patient. A typical osteomyelitis patient might be an elderly diabetic who may or may not also have cardiovascular problems. Such a patient often suffers from shortness of breath and may have difficulties in lying supine for a longer period of time: A whole 30 minute forefoot protocol would be extremely uncomfortable. There is therefore less likelihood that a 6-8 minute exam would be hampered by motion artifacts as frequently seen with longer protocol durations. Since the point-of-care exam is very short, it could therefore dramatically improve the usefulness of the acquired images, as they will not be degraded due to motion.

The point-of-care strategy in MRI has some limitations:

1. It needs to be explained to the referring physicians that only the specific clinical question has been answered. There would no longer be the opportunity for incidental findings because the MRI exam would be focused on one single problem.
2. It may take time for both the radiologist and the clinicians to rid themselves of the feeling that something is missing in these exams. The list of sequences in the PACS system will be as short as the accompanying radiological report will be. The latter – as an extreme example – could be limited to "There are no signs of osteomyelitis in the fifth digit."
3. More preparatory work before individual examinations is needed to store tailored point-of-care protocols on the scanner next to the 'normal' protocols. However, the new software version *syngo* MR E11 and the various Dot-engines are the perfect platform, since point-of-care protocols can be integrated as own 'strategies' in the pre-existing protocols. These separate imaging paths can then be chosen by the radiologist or technologist in appropriate cases.
4. Staff need training in the new point-of-care strategy, and the patient-related processes outside the scan room need to be optimized as well. To take our osteomyelitis example, 5 to 6 patients could potentially be imaged within 1 hour and this needs very efficient processes within the MRI department.
5. Radiologists will eventually have to face a higher work-load, and efficient reporting tools and software are required to cope with the additional work load.
6. With reduced scan time, insurance companies and authorities will soon start reducing the amounts they reimburse for point-of-care MRI examinations, since currently it is the time that is reimbursed rather than the impact or true value of the imaging examination on the patient outcome.



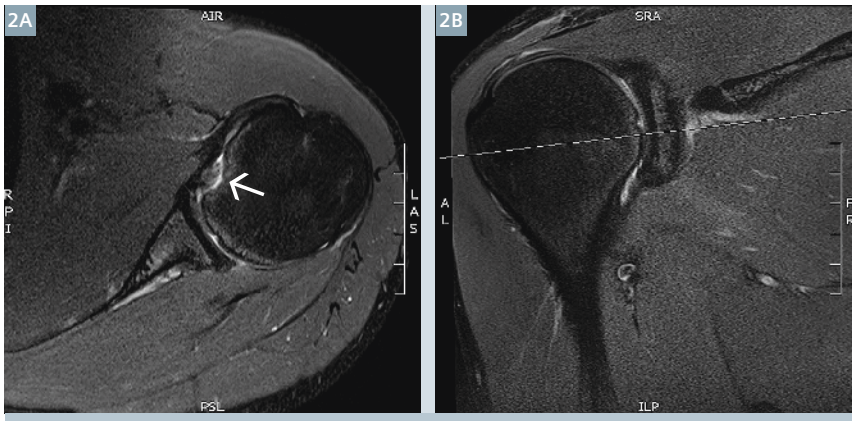
1 45-year-old male patient who was referred for MRI of the forefoot with the specific question to confirm an abscess between the first and second toe. Point-of-care MRI with axial fat suppressed contrast-enhanced T1-weighted **(1A)** and T2-weighted **(1B)** fast spin echo images confirmed the diagnosis of a local abscess (arrow). Total acquisition time was 8 min.

Future directions

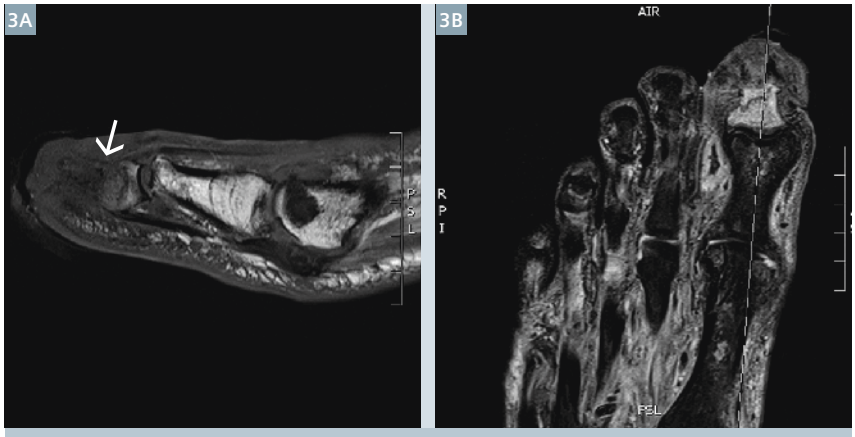
The strategy of point-of-care MRI might be applied to a proportion of MR examinations where a very specific clinical question is being asked.

Tailored protocols may include reduction of number of slices, reduction of number of sequences, smaller fields-of-view and a clear awareness that not everything that could be done is indeed being done. However, in my personal experience, there is no need to reduce image resolution or other parameters relevant for image quality. But whilst I still prefer to have the best image quality, I am happy to look at fewer images and less anatomy at the same time.

In conclusion, point-of-care MR imaging may represent a new strategy which might not only be more cost-efficient but which could also provide several advantages for the patients.



2 23-year-old male patient with a history of multiple shoulder dislocations and known multidirectional instability was referred for his fourth shoulder MRI to rule out an acute fracture after a new episode of dislocation. Point-of-care MRI with axial **(2A)** and coronal **(2B)** fat suppressed proton density-weighted fast spin echo images showed a reverse Hill-Sachs lesion (arrow) and some articular cartilage irregularities but no fracture was seen. Total acquisition time was 9 min.



3 75-year-old female patient was referred for MRI of the forefoot with a high clinical suspicion for osteomyelitis of the great toe. Point-of-care MRI with sagittal T1-weighted **(3A)** and coronal fat suppressed T2-weighted **(3B)** fast spin echo images confirmed the diagnosis of osteomyelitis (arrow). Total acquisition time was 7 min.

References

1 Ahern, C.H., et al., Cost-effectiveness of alternative strategies for integrating MRI into breast cancer screening for women at high risk. Br J Cancer, 2014. 111(8): p. 1542-51.
2 Vijayasarathi, A., et al., How Much Do Common Imaging Studies Cost? A Nationwide Survey of Radiology Trainees. AJR Am J Roentgenol, 2015. 205(5): p. 929-35.
3 Campbell, F., et al., Systematic review and modelling of the cost-effectiveness of cardiac magnetic resonance imaging compared with current existing testing pathways in ischaemic cardiomyopathy. Health Technol Assess, 2014. 18(59): p. 1-120.
4 Zhang, E., et al., Cost-utility analysis of nonalcoholic steatohepatitis screening. Eur Radiol, 2015. 25(11): p. 3282-94.
5 Levin, D.C., V.M. Rao, and L. Parker, Trends in the utilization of outpatient advanced imaging after the deficit reduction act. J Am Coll Radiol, 2012. 9(1): p. 27-32.
6 Curtis, L.H., et al., Geographic variation and trends in carotid imaging among medicare beneficiaries, 2001 to 2006. Circ Cardiovasc Qual Outcomes, 2010. 3(6): p. 599-606.
7 Smith-Bindman, R., D.L. Miglioretti, and E.B. Larson, Rising use of diagnostic medical imaging in a large integrated health system. Health Aff (Millwood), 2008. 27(6): p. 1491-502.
8 Kendall, J.L., S.R. Hoffenberg, and R.S. Smith, History of emergency and critical care ultrasound: the evolution of a new imaging paradigm. Crit Care Med, 2007. 35(5 Suppl): p. S126-30.
9 Shewmaker, D.M., O. Guderjahn, and T. Kummer, Identification of Peroneal Tenosynovitis by Point-of-Care Ultrasonography. J Emerg Med, 2015.
10 Paolini, S., et al., Rapid Short MRI Sequence Useful in Eliminating Stroke Mimics Among Acute Stroke Patients Considered for Intravenous Thrombolysis. J Neurol Disord, 2013. 1: p. 137.

Contact

Dr. Gustav Andreisek, M.D.
Institute of Diagnostic and Interventional Radiology
University Hospital Zurich, University of Zurich
Ramistrasse 100
8091 Zurich
Switzerland
gustav@andreisek.de



^{18}F-FDG PET/MR: Its Incremental Value in Assessing the Multiple Myeloma Patient

Jorge Oldan, M.D.; Hakan Ilaslan, M.D.; Shetal N. Shah, M.D.

Imaging Institute, Cleveland Clinic, Cleveland, Ohio, USA

Case summary

A 68-year-old female with previously serologically well-controlled IgG kappa, CD 20 positive multiple myeloma with lymphoplasmacytic morphology, on carfilzomib, prednisone, and pomalidomide, presented for follow-up. She complained of back, rib, and right hip pain, which appeared related to exercise, included muscle cramping, and had increased over the past few months. As there was concern this might signify refractory asecretory clones, a PET/MR scan was obtained to evaluate disease extent.

Imaging findings

Simultaneous Fludeoxyglucose F^{18} (^{18}F-FDG)[1] PET/MR scan from skull vertex to thighs including axial HASTE, T1-weighted FLASH, coronal T2w TSE and sagittal T2 of the spine was obtained. There is diffuse, abnormal heterogeneous bone marrow signal throughout the spine, pelvis, and proximal femurs with increased ^{18}F-FDG uptake with SUV_{max} of up to 4.4 in a 1.6 x 1.2 cm iliac lesion. There are multiple focal rib lesions as well (up to SUV_{max} 5.6 and 3 x 1.4 cm), and a 1.7 cm lesion within the right posterior L1 elements (SUV_{max} 5.2).

The spine in particular is diffusely T1-hypointense, with a heterogeneous appearance on T2-weighted images and focal areas of increased ^{18}F-FDG uptake corresponding to areas of increased T2 signal.

In addition, there is a solitary 1 cm hypermetabolic lesion in hepatic segment V (SUV_{max} 3.0) with mildly T1 and T2 hyperintense liver in the background of a diffuse T2 hypointense liver due to hemochromatosis.

Diagnosis

Multiple myeloma with diffuse involvement of the axial bone marrow and extra-medullary spread to the liver (confirmed by liver biopsy).

Discussion and conclusion

Our case demonstrates the diffuse variety of multiple myeloma within the axial skeleton as well as extramedullary spread on ^{18}F-FDG PET/MR. With this evidence of progression, prednisone was increased to her current regimen and rituximab added. Her disease continued to progress while on therapy, and she underwent palliative radiotherapy to sites of pain and had further chemotherapy. The patient eventually progressed clinically and died in less than a year after the scan was completed.

Multiple myeloma is a neoplasm resulting from monoclonal proliferation of mature plasma cells. It is relatively rare, representing 1.4% of all new cancer cases in the U.S., although it is the second most common hematologic malignancy after non-Hodgkin's lymphoma and the most common primary osseous malignancy in the elderly, with incidence of 24,050 and mortality of 11,090 in 2014 [1]. It presents with anemia (most common), bone pain, renal insufficiency, fatigue, hypercalcemia, and/or weight loss, and evolves from an asymptomatic malignant condition known as MGUS (monoclonal gammopathy of undetermined significance) at a rate of 1% per year [2]. 5-year survival rate remains low at 44.9% [1].

While one of the predominant staging systems for multiple myeloma (the Durie-Salmon Staging system or 'DS') assessed osseous involvement by plain radiography (along with serologic markers like hemoglobin, serum calcium, and serum and urine M protein), the revised 'DS Plus' incorporates the number of focal lesions over 5 mm in size as well as the distribution of the disease pattern (diffuse, focal, or variegated) based on MR or PET/CT [3] (Table 1).

Table 1: Durie-Salmon Plus (DS Plus) staging system

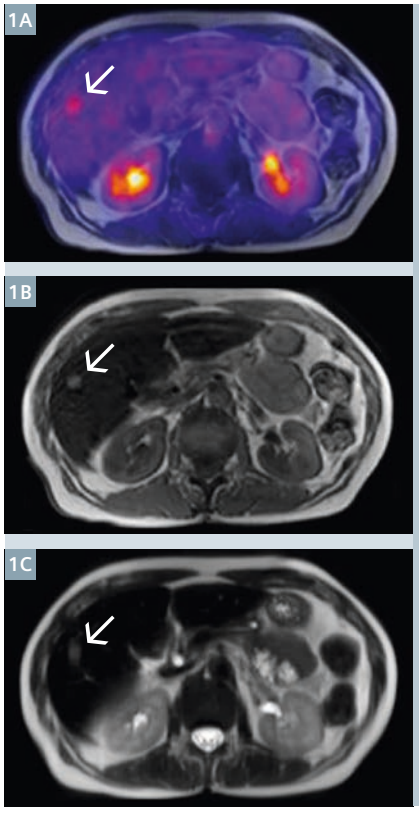
Durie-Salmon		PET/MR # of lesions
I: Hgb > 10 g/dL **AND** serum Ca < 10.5 mg/dL **AND** normal skeletal radiographs or solitary bone plasmacytoma **AND** low M-component production rates (IgG < 5 g/dL, IgA < 3 g/dL) **AND** urine light chain M-component on electrophoresis < 4 g/24h	Plus upstage	0–4
II: Fitting neither Stage I or Stage III		5–20
III: Hgb < 8.5 g/dL **OR** Serum Ca > 12 mg/dL **OR** Advanced lytic bone lesions **OR** High M-component production rates (IgG > 7 g/dL, IgA > 5 g/dL) **OR** Bence Jones Protein > 12g/24h		>20
B: Cr > 2.0 mg/dL		B: Cr > 2 and/or EMD on PET **OR** MRI
The stage I, II, or III may have an A or B modifier, B if the criteria for B (Cr >2 or extramedullary disease on PET or MRI) are met.		

[1] The full prescribing information for the Fludeoxyglucose F^{18} injection can be found at page 91.

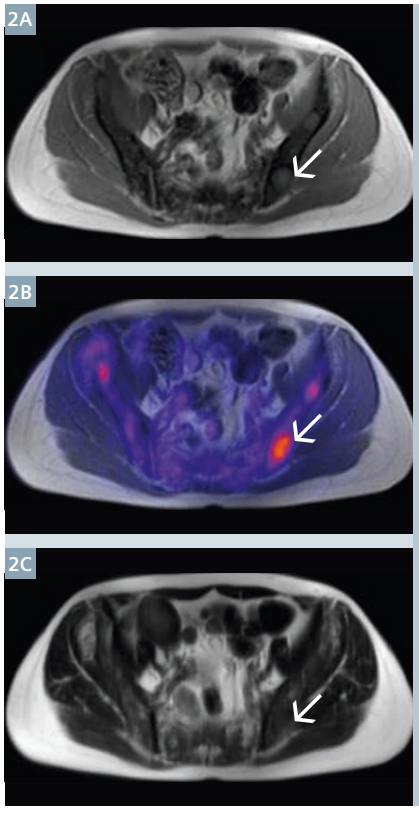
Presently, the International Myeloma Working Group states that PET can be used to confirm MGUS (which is PET negative) or exclude unsuspected and/or extramedullary myeloma (which would be PET positive), infection, and/or another malignancy [4]; it can also be used for therapy response assessment [5]. Because ^{18}F-FDG PET has been described as having limitation to assess diffuse spine involvement with false-positives with accompanying inflammation or infection, deposits of brown fat, postsurgical and vertebroplasty changes, or due to other malignancies [6], the addition of MR has proved valuable.

On radiography, multiple myeloma classically appears as 'punched-out' lytic lesions in the bones without surrounding reactive changes, or less commonly as diffuse osteopenia. Since between 10% and 20% of multiple myeloma patients have normal radiographs [7], MRI is useful in patients with classic symptoms and normal radiographs [8], and can detect complications such as cord compression, identifying size, level, and extent of tumor mass [2]. The pattern of marrow involvement on MRI can be described as focal, diffuse, or variegated [9], with a diffuse pattern correlating with a shorter survival time compared with focal or variegated [2]. In addition to detecting early bone involvement, ^{18}F-FDG can detect extramedullary disease and provides prognostic information. For example, a target lesion with SUV_{max} over 4.2 at baseline is a poor prognostic factor, and SUV_{max} over 3.5 correlates with increased risk of fracture [2]. ^{18}F-FDG PET can also assess treatment response [2] after chemotherapy or autologous stem cell treatment. Whereas PET/CT is more effective at detecting extramedullary disease, MRI is more sensitive in the marrow and has an overall increased contrast resolution in the viscera [2]; thus the potential for substantial synergy using PET/MR exists.

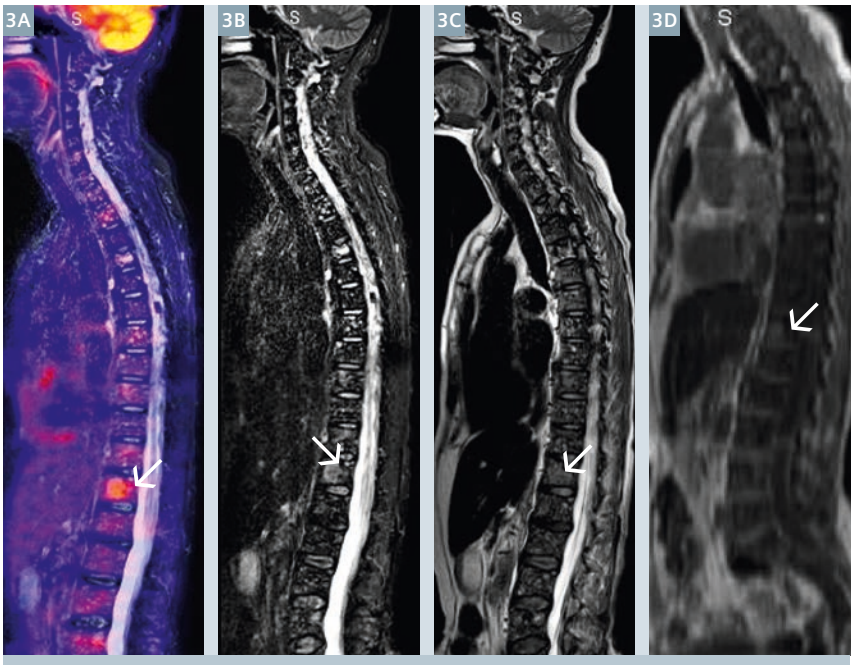
In our case, ^{18}F-FDG PET/MR detected both diffuse axial marrow involvement and extramedullary disease using PET/MR, finding a cause for the patient's bone pain and, unfortunately, an effective indicator of the patient's poor prognosis, including liver involvement and an SUV_{max} of 5.6 in a target lesion. PET/MR allows for one-stop evaluation of multiple myeloma patients using both advanced imaging modalities, and allows for close correlation of the findings on each – we were able to note ^{18}F-FDG activity of the liver lesion, and identify ^{18}F-FDG-avid marrow lesions corresponding to areas of marrow abnormality.



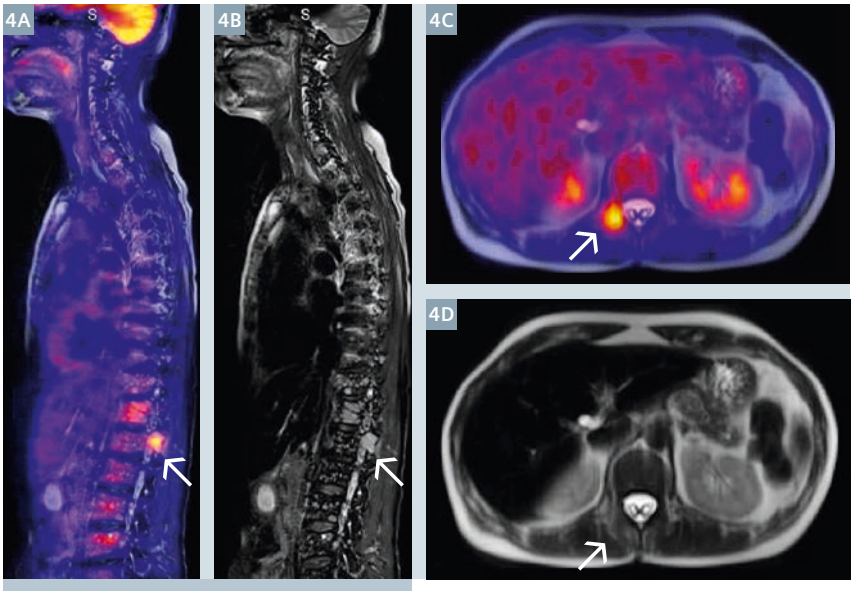
1 Fused ^{18}F-FDG-T1-weighted **(1A)**, T1-weighted **(1B)**, and T2-weighted HASTE **(1C)** MR images through the liver, demonstrating the 1 cm ^{18}F-FDG-avid (SUV_{max} 3.0) liver lesion in hepatic segment V (white arrows). Note the diffuse low intensity on T1 and T2 signal of the liver from hemochromatosis.



2 Axial T1-weighted **(2A)**, fused axial ^{18}F-FDG-T2-weighted **(2B)**, and axial T2-weighted **(2C)** MR images through the pelvis. Abnormal foci of marrow signal corresponding to areas of increased ^{18}F-FDG uptake (largest 1.6 x 1.1 cm, SUV_{max} 4.4) (white arrows). Myeloma deposits are more typically dark on T1, although in this patient hemochromatosis may have resulted in a dark marrow signal.



3 Fused sagittal ^{18}F-FDG-STIR **(3A)**, STIR **(3B)**, T2-weighted **(3C)**, and T1-weighted **(3D)** MR images. Note that the marrow has a heterogeneous appearance and is generally dark on both T1 and T2-weighted images (again, likely due to hemochromatosis), but areas of increased uptake (in particular the deposit in T12 vertebra) correspond to areas of increased signal intensity (white arrows).



4 Sagittal fused ^{18}F-FDG-STIR **(4A)**, fat saturated T2-weighted **(4B)**, axial fused ^{18}F-FDG-HASTE **(4C)** and axial HASTE **(4D)** MR images demonstrate the involvement of the posterior right T1 elements (white arrows). Note that while the disease is not well seen on axial images, PET/MR registration (always better with simultaneously acquired images such as these) allows for precise localization nevertheless.

References

1 SEER Stat Fact Sheets: myeloma. http://seer.cancer.gov/statfacts/html/mulmy.html. Published 2014. Accessed March 22, 2015.

2 Radiographics. 2015 Mar-Apr;35(2):438-54. doi: 10.1148/rg.352140112. MR Imaging and PET/CT in Diagnosis and Management of Multiple Myeloma. Ferraro R, Agarwal A, Martin-Macintosh EL, Peller PJ, Subramaniam RM.

3 Durie BG. The role of anatomic and functional staging in myeloma: description of Durie/Salmon plus staging system. Eur J Cancer. 2006 Jul;42(11):1539-43.

4 IMWG Criteria for the Diagnosis of Myeloma and Guidelines for the Diagnostic Work-Up of Myeloma. International Myeloma Foundation. https://myeloma.org/ArticlePage.action?tabId=0&menuId=0&articleId=2970&aTab=-1&gParentType=nugget&gParentId=18&parentIndexPageId=284. Accessed April 2, 2015.

5 Peller PJ. Multiple Myeloma. PET Clin. 2015 Apr;10(2):227-241.

6 Dimopoulos M, Terpos E, Comenzo RL, Tosi P, Beksac M, Sezer O, Siegel D, Lokhorst H, Kumar S, Rajkumar SV, Niesvizky R, Moulopoulos LA, Durie BG; IMWG. International myeloma working group consensus statement and guidelines regarding the current role of imaging techniques in the diagnosis and monitoring of multiple Myeloma. Leukemia. 2009 Sep;23(9):1545-56.

7 Durie BG, Kyle RA, Belch A, et al. Myeloma management guidelines: a consensus report from the Scientific Advisors of the International Myeloma Foundation. Hematol J 2003;4(6):379–398.

8 Dimopoulos M, Kyle R, Fermand JP, et al. Consensus recommendations for standard investigative workup: report of the International Myeloma Workshop Consensus Panel 3. Blood 2011;117(18):4701–4705.

9 Moulopoulos LA, Dimopoulos MA, Alexanian R, Leeds NE, Libshitz HI. Multiple myeloma: MR patterns of response to treatment. Radiology 1994;193(2):441–446.



Contact

Shetal N. Shah, M.D.
Cleveland Clinic Main Campus
Diagnostic Radiology / Nuclear Medicine
Mail Code JB3
9500 Euclid Avenue
Cleveland, OH 44195
USA
Phone: +1 216.445.8168

New 'ADC & b-value' Tool in *syngo*.via

Anja Fernandez Carmona; Klaus Mayer; Julien Gervais

Siemens Healthcare, Erlangen, Germany

Introduction

Diffusion-weighted imaging (DWI) is a key sequence in MRI, especially in the area of oncology imaging as it reveals the microscopic tissue architecture. High b-value images in particular deliver the most valuable clinical information, but they require long acquisition time and are often prone to distortion and ghosting artifacts.

The new *syngo*.via VB10 software allows you to generate ADC maps and computed b-value images from acquired DWI series. This can save valuable scan time while providing images of overall better accuracy [1].

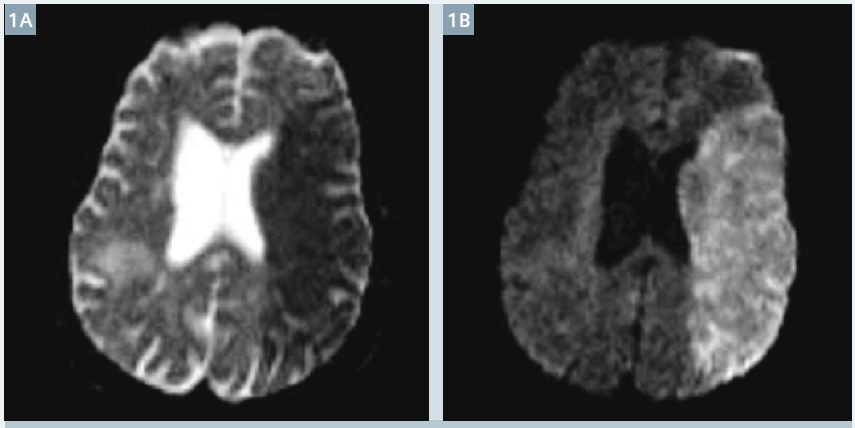
Additionally, with the Auto Preview functionality, the optimal b-value maximizing the contrast to better fit the pathology, the body region and the patient, can be simulated in real time.

Methodology

Background

The diffusion coefficient is a measure of the mobility of molecules within their environment.

In MRI, the ADC (apparent diffusion coefficient) is used: ADC maps show parametric images of the apparent diffusion coefficient of diffusion-weighted images.



1 ADC map **(1A)** and diffusion-weighted image **(1B)** show reduced diffusion in the left brain. *Reproduced with permission from: Praxiskurs MRT, Anleitung zur MRT Physik über klinische Bildbeispiele, W. Nitz.*

On ADC maps, a dark voxel represents a voxel with low ADC and low diffusion. In the diffusion-weighted images, it is the opposite, and low diffusion regions are represented by bright voxels (Fig. 1).

The evolution of the signal intensity in DWI images is described by an exponential function and is related to the b-value parameter of the sequence. This correlation is described by the formula:

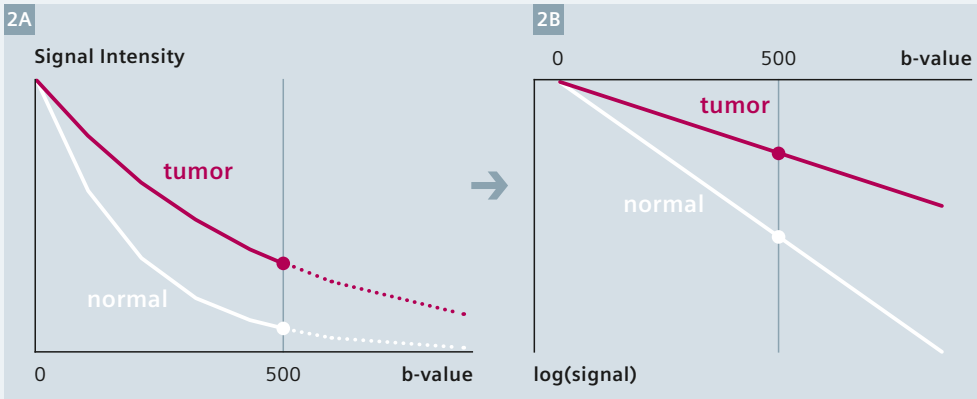
$$I(x,y) = \exp[-b \cdot D(x,y)]$$

where I is the signal intensity, b the b-value, and D the ADC coefficient.

A fitted linear regression model can be used to calculate the diffusion coefficient D for each voxel, as illustrated in Figure 2.

Consequently, with at least two b-values acquired, it is possible to compute the ADC for each voxel. Additionally, due to the linear correlation, it is then possible to extrapolate and generate DWI images of any other b-value.

The ADC map and computed b-value images can be generated 'inline' on the acquisition workplace of Siemens MR systems, making them immediately available for reading. This is an



2 Illustration of the signal intensity evolution in function of the b-value: exponential correlation for the signal intensity itself **(2A)**, linear correlation for the logarithm **(2B)**.

obvious advantage in terms of clinical workflow.

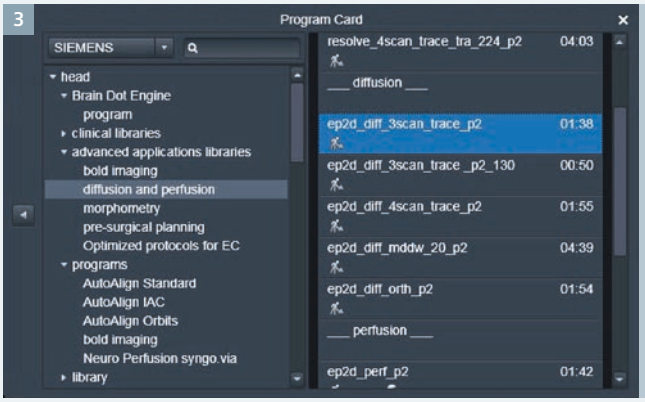
In some cases, the offline computation of the ADC maps can be beneficial, e.g. in case low b-value images have to be excluded from the map generation in order to reduce perfusion effects.

The offline and interactive approach is especially interesting for the gener-ation of computed b-value images. For example, there might be the need to compare with prior exams that have been acquired with a different protocol and different b-values. Additionally, the interactive aspect makes it possible to evaluate, in real-time, the signal evolution with different diffusion weighting, and find the b-value which best maximizes the contrast between the lesion and the surrounding tissue. This is adding an additional degree of freedom over the choice of the b-value [2].

Input series

The input series are diffusion-weighted images (trace-weighted images) acquired with a minimum of two different b-values. The maximum number of b-values is only limited by the scanning protocol. The typical diffusion sequence can be found in the program card of the Siemens protocol tree for the corresponding body region, as illustrated in Figure 3 for a head examination. The RESOLVE sequence (EPI segmented in the read-out direction), which reduces susceptibility and blurring artifacts, is compatible with the ADC & b-value tool.

Distortion corrected and filtered images can also be used, as long as the filter criterion is the same across all b-values.



3 Typical diffusion sequence for head examinations.

Tool activation and selection of the input series

The ADC & b-value tool is available in the lower right corner menu under 'Arithmetic Tools' as illustrated in Figure 4. This triggers the opening of the ADC & b-value card as a floating window (Fig. 5).

If the segment where the tool is activated already contains diffusion data, it is recognized and automatically loaded as input series. If the tool is activated in a segment which does not contain diffusion data, the input series can be selected via drag & drop from the series navigator.

As previously mentioned, the input series must have been acquired with a minimum of two b-values. If a series with less than two b-values is selected (or a non-diffusion series), the calculation cannot be performed.

The second b-value can be dropped afterwards with drag & drop into the input section.

The entire data in the input section can be replaced with new data from the series navigator and segment by holding the 'shift' key.



4 Activation of the ADC & b-value tool.



5 ADC & b-value card.

Computing ADC maps and extrapolated b-value images
The ADC & b-value card is divided into two sections: an upper part for the calculation of the ADC map, and a lower part for the generation of computed b-value images.

The typical sequence to generate ADC maps and computed b-value images is the following:

1. Select in the 'input series' section the b-value images to include in the calculation (Fig. 6):
   - Use the checkbox to select the b-value images to be included.
   - Use the 'Minus' icon to selectively delete single b-value images from this section.
2. Select the threshold for the ADC map calculation.

   The threshold is a parameter to reduce the noise in the resulting images. It is configurable and works as follow: For a specific voxel, if the signal intensity on the acquired b-value images selected for the calculation drops under the configurable threshold, its value is set to NULL and will be represented by a dark voxel in the ADC map. The configurable threshold has a value range of 0-1000 and is set by default to 10.
3. Check the name of the resulting series.

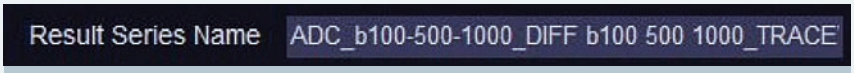
   After selection of the b-value images to include in the calculation, the default result series name is displayed in the 'Result Series Name' section (Fig. 7)

   The name is based on 'ADC_' and the information about the selected b-value images, plus the series description. The name can be modified.
4. Enable the computed b-value images.

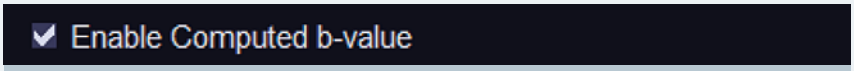
   The b-value images option can be switched on by clicking the 'Enable Computed b-value' check box (Fig. 8). If you do not wish to generate these images (but only ADC), the box should stay unchecked.



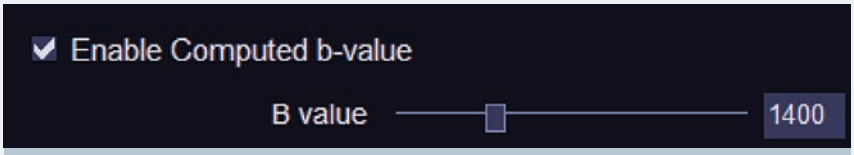
6 Selection of the b-value images.



7 Result Series Name.



8 'Enable Computed b-value' checkbox.



9 Slider bar or manual entry for b-value generation.



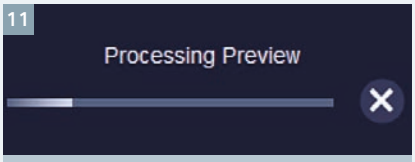
10 Selection of the target segments (here in a dual monitor setup). The orange arrow represents a potential drag & drop interaction by the user to modify the target segment of the computed b-value image.

5. Select the desired b-value for the computed image.

   The computed b-value images can be generated for b-values between 0 and 5000. The desired value can be selected by moving the slider bar or by typing in the value (Fig. 9).

   The result series name for the computed b-value is set per default by the system. The name is based on 'Calc_' plus the information about the desired b-value and the b-value images used as input (e.g. b1400_b50_400_800) plus the series description (e.g. ep2d_diff_tra_b50_400_TRACEW). The name can be modified.
6. Select the target segments and generate preview images.

   In the lower part of the card, the target segment is displayed. It represents the current layout setting (including dual monitor if appropriate) and the default position where the ADC map and the computed b-value image will be loaded. These positions can be modified by dragging & dropping the ADC and b-value icons to another segment (Fig. 10).



11 Progress bar.



12 Auto Preview functionality. The slider bar triggers a real-time update of the computed b-value image between b0 and b5000.

Clicking the 'Preview' button at the bottom of the card generates a preview of the ADC map and computed b-value series. The results are not stored when using the preview functionality.

During the calculation, a progress bar is displayed (Fig. 11). The computation can be canceled with the 'cancel' button.

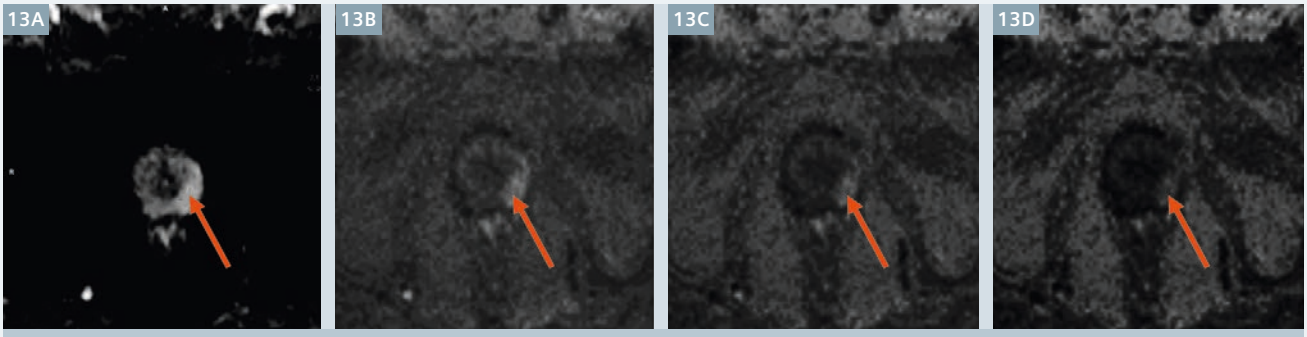
7. For interactive and real-time generation of computed b-value images, activate the 'Auto Preview' functionality (Fig. 12).

   Next to the b-value slider, the 'Auto Preview' check box can be activated. By moving the slider, the corresponding computed b-value image in the target segment is generated and updated in real-time. Thus, the influence of the b-value on the signal intensity can be seen interactively which may help to carve out specific lesions (cf. paragraph 'clinical cases').

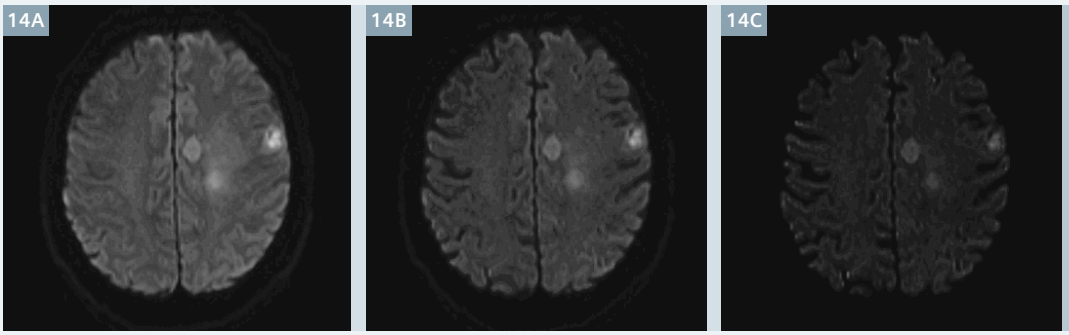
8. Save the results.

   When completing the case, click 'OK' to store the results in the series navigator and permanently save them with the patient data.

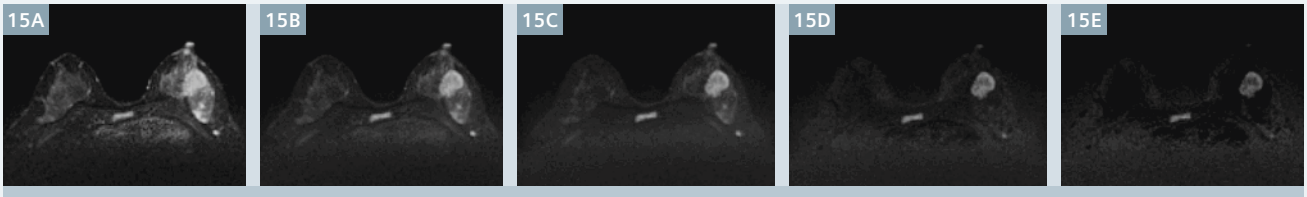
Clinical examples



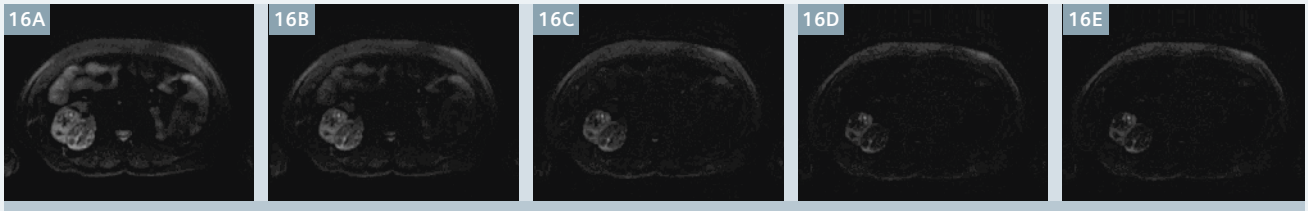
13 67-year-old man with prostate cancer. Acquired b800 **(13A)** and computed b1600 **(13B)**, b2000 **(13C)**, b2500 **(13D)** images.



14 58-year-old man with multiple brain lesions. Acquired b1000 **(14A)** and computed b1400 **(14B)**, b2200 **(14C)**.



15 41-year-old woman with breast tumor. Computed b500 **(15A)**, b800 **(15B)**, b1000 **(15C)**, b1400 **(15D)**, b1800 **(15E)** images show signal evolution in the lesion. Series are computed from RESOLVE diffusion series acquired with b0, b500, b1000.



16 62-year-old male patient with kidney tumor. Computed b600 **(16A)**, b800 **(16B)**, b1000 **(16C)**, b1200 **(16D)**, b1400 **(16E)** images show signal evolution in the kidney. Series are computed from standard diffusion series acquired with b50, b800.

Summary

This article describes the feature 'ADC & computed b-value' available in *syngo*.via VB10. This new tool provides an increased degree of freedom in the choice of the b-value for disease detection and characterization. This algorithm has been shown to save scan time and increase diffusion image quality. Easy to use and flexible with the Auto Preview functionality, it is standard with the *syngo*.MR General Engine and therefore included in the upgrade to *syngo*.via VB10.

Contact

Anja Fernandez Carmona
Siemens Healthcare
HC DI MR R&D SW VIA-APM
91050 Erlangen, Germany
Phone: +49 (9131) 84-3566
anja.fernandez_carmona@siemens.com

References

1 Feasibility study of computed vs measured high b-value (1400 s/mm²) diffusion-weighted MR images of the prostate, World J Radiol 2014 June 28; 6(6): 374-380.
2 Blackledge MD, Leach MO, Collins DJ, Koh DM. Computed diffusion-weighted MR imaging may improve tumor detection. Radiology 2011; 261: 573-581.
3 Source of brain image (first paragraph): Praxiskurs MRT, Anleitung zur MRT Physik über klinische Bildbeispiele, W.Nitz.
4 Rosenkrantz, et al. Computed diffusion-weighted imaging of the prostate at 3T: impact on image quality and tumour detection. European Radiology 2013; 23: 3170-7c.

syngo.via delta list for VB10

All improvements and new features of the new *syngo*.via are summarized in the *syngo*.via delta list for VB10.

Download it on your iPad:
www.siemens.com/vb10-epub

Download it on your PC:
www.siemens.com/vb10-pdf



Hybrid PET/MR Imaging with PSMA-Ligands: the Future Standard in the Diagnosis of Prostate Cancer?

Ali Afshar-Oromieh, M.D.[1,2]; Martin T. Freitag, M.D.[3]; Matthias C. Röthke, M.D.[3]; Jan P. Radtke, M.D.[3,4]; Heinz Peter Schlemmer, M.D.[3]

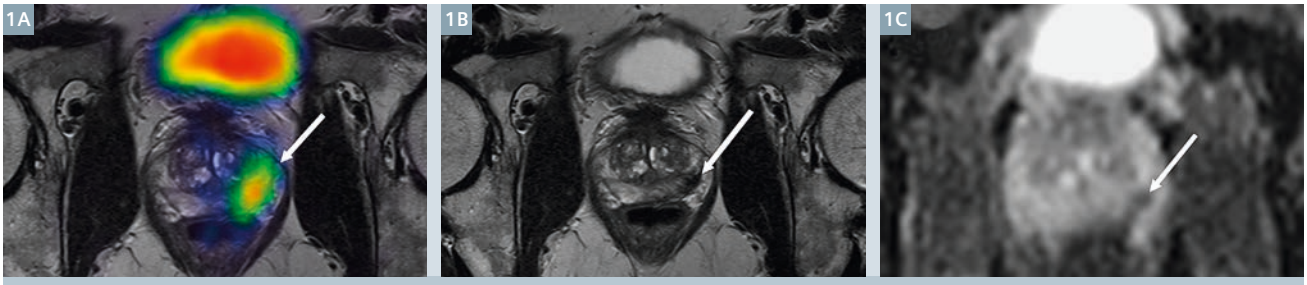
[1] Department of Nuclear Medicine, Heidelberg University Hospital, Heidelberg, Germany
[2] Clinical Cooperation Unit Nuclear Medicine, German Cancer Research Center (DKFZ), Heidelberg, Germany
[3] Department of Radiology (E010), German Cancer Research Center (DKFZ), Heidelberg, Germany
[4] Department of Urology, University Hospital Heidelberg, Germany

Prostate cancer (PCa) is the most frequent malignant tumor in men worldwide [1, 2]. Following initial therapy, mostly by surgery or radiation, biochemical relapse is rather common [3–6]. The search for tumor lesions at this constellation is challenging, since imaging modalities such as Computed Tomography (CT) and Magnetic Resonance Imaging (MRI) often revealed unsatisfying sensitivity and specificity [7].

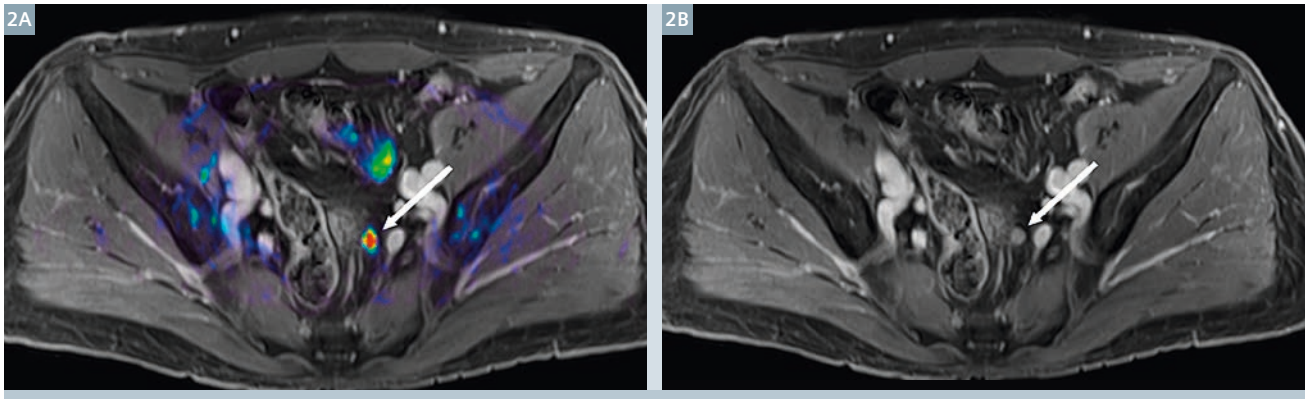
Research has therefore sought to find more sensitive and specific ways of diagnostic measures. The fact that prostate-specific membrane antigen (PSMA) is known to be overexpressed in most PCa offers the chance to develop ligands for this target. This has led to the introduction of the low-molecular-weight PSMA-ligand Glu-NH-CO-NH-Lys-(Ahx)-[^{68}Ga(HBED-CC)] (= ^{68}Ga-PSMA-11) in 2011 as a novel PET-tracer for diagnosing PCa. This compound was developed at the German Cancer Research Center Heidelberg, Germany [8, 9]. The first clinical application of ^{68}Ga-PSMA-11-PET/CT was conducted in May 2011 in the department of nuclear medicine at the Heidelberg University Hospital. This led to the rapid international spread of this novel imaging method. The growth can be explained by the hitherto existing results of PET/CT-imaging with ^{68}Ga-PSMA-11, which clearly demonstrate a significant increase in the diagnostic capabilities for the detection of PCa-related tissue [10–13]. A recently published study with a large patient cohort (n = 319) affirmed that ^{68}Ga-PSMA-11-PET/CT provides excellent sensitivity and specificity to detect PCa lesions [12]. Other groups have confirmed these findings [14].

When compared to CT, MRI provides a better method of soft tissue imaging due to its higher contrast-resolution and different functional sequences, both helping to clarify uncertain findings. Multiparametric MRI of the prostate has been proven as a powerful imaging tool for prostate cancer assessment [15]. It provides essential information for accurate prostate biopsy using TRUS/MR image-fusion guided biopsy systems, and is an integral part of follow-up during active surveillance and individualized therapy planning [16]. However, there are significant limitations in the early detection of cancer spreading into lymph nodes and bones, or of recurrent disease after curative intended treatment. These limitations can be overcome by adding the information from PSMA-PET, which yields complementary information compared to multiparametric MR. Consequently, the next step should therefore be a combination of PSMA-PET with MRI,

[1] The full prescribing information can be found at page 91.



1 Patient with prostate cancer (Gleason 9, cT3, PSA 26 ng/ml) presenting with focal T2w hypointensity, pathologic uptake in PSMA-PET and focal ADC decrease in the peripheral zone (white arrows). The PSMA-ligand is excreted via the urinary tract (in the upper part of 1A radioactive urine is visible within the bladder). **(1A)** PSMA-PET/MRI fusion with T2w high-resolution. **(1B)** T2w high-resolution TSE sequence. **(1C)** ADC map.



2 Patient with biochemical relapse after radical prostatectomy (Gleason 9, T2a, PSA at scan 3.6 ng/ml). PSMA-PET/MRI identifies a typical lymph node metastasis next to the left internal iliacal artery (white arrows). **(2A)** PSMA-PET/MRI fusion with **(2B)** T1w-CE-fatsat.

thus creating the best possible tool to detect, diagnose, stage and follow-up patients with suspected prostate cancer comprehensively and most accurately within 'one-stop-shopping'.

Siemens is the first company to have successfully developed a hybrid whole-body PET/MRI scanner allowing for simultaneous PET and MRI assessment. The objective of such hybrid scanners is a faster investigation and more accurate image fusion compared to separately conducted PET and MRI images.

As dedicated software to fuse separately acquired PET and MRI images already exists, some experts may argue that the development of hybrid PET/MRI scanners was a bit futile. Bearing in mind that very similar arguments were raised at the time of hybrid PET/CT scanner development, the ensuing years have clearly showed multiple advantages of those scanners: the image fusion was found to be more accurate when compared to the images that were reconstructed based on retroactive fusion of separately obtained PET and CT/MRI images. Human errors in the context of image fusion could also be avoided as no manipulation by humans is required. All this has resulted in saved time and resources. Furthermore, with regard to external radiation therapy, the development of hybrid PET/CT has enabled more accurate therapy approaches. In addition, PET/MRI allows parallel acquisition of PET and MRI, whereas for PET/CT the scans have to be conducted sequentially. At last, patients who undergo a PET/MRI scan are also exposed to less radiation compared to PET/CT.

After the development of hybrid whole-body PET/MRI scanners, multiple studies have been published which demonstrate the feasibility and the advantages of a PET/MRI hybrid system when using ^{18}F-FDG or ^{18}F-Choline. In 2013, our group began conducting PET/MRI with ^{68}Ga-PSMA-11 and the results were highly promising [9-12]. In fact, a subjectively easier evaluation of the images compared to PET/CT could be shown; an effect enabled by different diagnostic sequences and the higher resolution of MRI. The combination of the ^{68}Ga-PSMA-11-PET with multiparametric MRI provided images of a high diagnostic value not witnessed before (Figs. 1, 2). MRI has also helped to clarify unclear findings in PET/CT regarding PCa metastases (Fig. 3). The appearance of a reduced PET-signal around the urinary bladder in some patients was the only noticeable limitation compared to PET/CT [12]. However, there are strategies for reducing or even omitting the described effect, i.e. a sufficient hydration of the patients, voiding the bladder prior to acquisition and starting the examination with the pelvis when the bladder is less full. Further, a newly developed software offering two different types of scatter correction (relative and absolute scatter correction) can help to significantly reduce the described effect.

In summary, the authors strongly believe that hybrid ^{68}Ga-PSMA-PET/MRI has significant advantages over PET/CT and will create new options for the diagnosis and selective treatment of primary and recurrent PCa in the future.

Acknowledgements

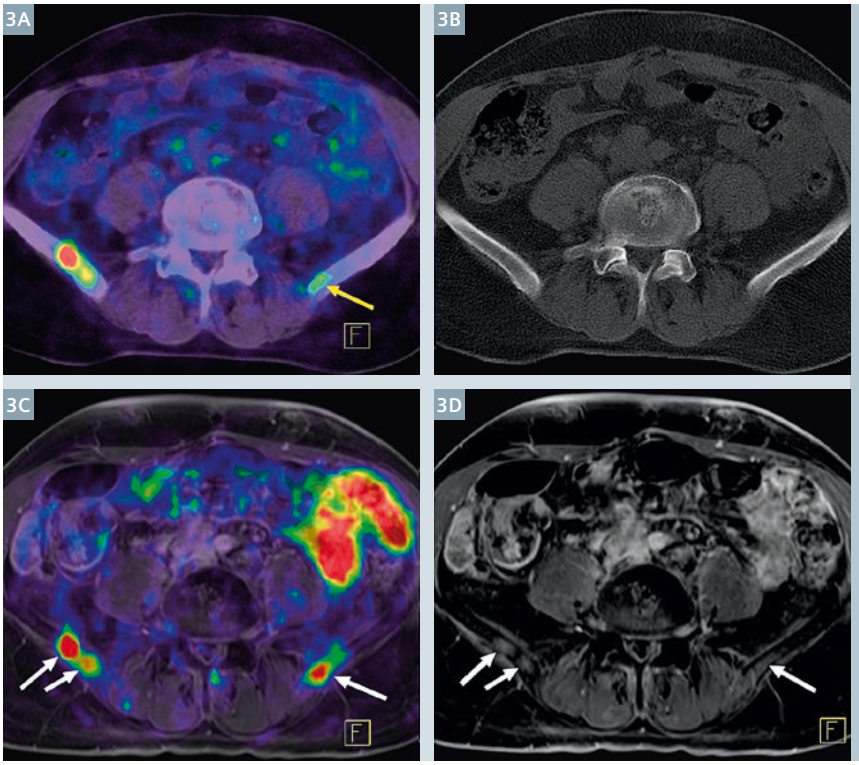
We express our gratitude to our staff, in particular to Regula Gnirs, René Hertel and Dr. Henrik Hetzheim.

Some of the Imaging Biomarkers referenced herein are not currently recognized by the US FDA as being safe and effective, and Siemens does not make any claims regarding their use.

The statements by Siemens' customers described herein are based on results that were achieved in the customer's unique setting. Since there is no 'typical' hospital and many variables exist (e.g., hospital size, case mix, level of IT adoption) there can be no guarantee that other customers will achieve the same results.

References

1 Jemal A, Bray F, Center MM, Ferlay J, Ward E, Forman D. Global cancer statistics. CA. Cancer J. Clin. 2011;61:69–90.
2 Siegel R, DeSantis C, Jemal A. Colorectal cancer statistics, 2014: Colorectal Cancer Statistics, 2014. CA. Cancer J. Clin. 2014;64:104–17.
3 Simmons MN, Stephenson AJ, Klein EA. Natural History of Biochemical Recurrence after Radical Prostatectomy: Risk Assessment for Secondary Therapy. Eur. Urol. 2007;51:1175–84.
4 Suardi N, Porter CR, Reuther AM, Walz J, Kodama K, Gibbons RP, et al. A nomogram predicting long-term



3 ^{68}Ga-PSMA-11-PET/CT **(3A, B)** and PET/MRI **(3C, D)** of a patient with rising PSA levels. This is an example of the potential of MRI to clarify even moderate PSMA-tracer accumulations as visible in the PET/CT (yellow arrow in 3A): while there is no correlation in CT, white arrows in 3D point to pathological MR-signals indicating bone metastases. **(3A)** PET/CT fusion, **(3B)** CT without contrast medium, **(3C)** PET/MRI fusion, **(3D)** MRI (contrast-enhanced T1w and fat saturation). *With kind permission of the European Journal of Nuclear Medicine and Molecular Imaging.*

biochemical recurrence after radical prostatectomy. Cancer. 2008;112:1254–63.
5 Boorjian SA, Thompson RH, Tollefson MK, Rangel LJ, Bergstralh EJ, Blute ML, et al. Long-Term Risk of Clinical Progression After Biochemical Recurrence Following Radical Prostatectomy: The Impact of Time from Surgery to Recurrence. Eur. Urol. 2011;59:893–9.
6 Han M, Partin AW, Pound CR, Epstein JI, Walsh PC. Long-term biochemical disease-free and cancer-specific survival following anatomic radical retropubic prostatectomy. The 15-year Johns Hopkins experience. Urol. Clin. North Am. 2001;28:555–65.
7 Sandler HM, Eisenberger MA. Assessing and Treating Patients With Increasing Prostate Specific Antigen Following Radical Prostatectomy. J. Urol. 2007;178:S20–4.
8 Eder M, Schäfer M, Bauder-Wüst U, Hull W-E, Wängler C, Mier W, et al. 68Ga-Complex Lipophilicity and the Targeting Property of a Urea-Based PSMA Inhibitor for PET Imaging. Bioconjug. Chem. 2012;23:688–97.
9 Schäfer M, Bauder-Wüst U, Leotta K, Zoller F, Mier W, Haberkorn U, et al. A dimerized urea-based inhibitor of the prostate-specific membrane antigen for 68Ga-PET imaging of prostate cancer. EJNMMI Res. 2012;2:23.
10 Afshar-Oromieh A, Haberkorn U, Schlemmer HP, Fenchel M, Eder M, Eisenhut M, et al. Comparison of PET/CT and PET/MRI hybrid systems using a 68Ga-labelled PSMA ligand for the diagnosis of recurrent prostate cancer: initial experience. Eur. J. Nucl. Med. Mol. Imaging. 2014;41:887–97.
11 Afshar-Oromieh A, Malcher A, Eder M, Eisenhut M, Linhart HG, Hadaschik BA, et al. PET imaging with a [68Ga]gallium-labelled PSMA ligand for the diagnosis of prostate cancer: biodistribution in humans and first evaluation of tumour lesions. Eur. J. Nucl. Med. Mol. Imaging. 2013;40:486–95.
12 Afshar-Oromieh A, Avtzi E, Giesel FL, Holland-Letz T, Linhart HG, Eder M, et al. The diagnostic value of PET/CT imaging with the 68Ga-labelled PSMA ligand HBED-CC in the diagnosis of recurrent prostate cancer. Eur. J. Nucl. Med. Mol. Imaging. 2014;1–13.
13 Afshar-Oromieh A, Zechmann CM, Malcher A, Eder M, Eisenhut M, Linhart HG, et al. Comparison of PET imaging with a 68Ga-labelled PSMA ligand and 18F-choline-based PET/CT for the diagnosis of recurrent prostate cancer. Eur. J. Nucl. Med. Mol. Imaging. 2014;41:11–20.
14 Eiber M, Maurer T, Souvatzoglou M, Beer AJ, Ruffani A, Haller B, et al. Evaluation of hybrid 68Ga-PSMA-ligand PET/CT in 248 patients with biochemical recurrence after radical prostatectomy. J. Nucl. Med. 2015;jnumed.115.154153.
15 Baco E, Ukimura O, Rud E, Vlatkovic L, Svindland A, Aron M, et al. Magnetic Resonance Imaging–Transectal Ultrasound Image-fusion Biopsies Accurately Characterize the Index Tumor: Correlation with Step-sectioned Radical Prostatectomy Specimens in 135 Patients. Eur. Urol. 2015;67:787–94.
16 Siddiqui M, Rais-Bahrami S, Turkbey B, et al. COmparison of mr/ultrasound fusion–guided biopsy with ultrasound-guided biopsy for the diagnosis of prostate cancer. JAMA. 2015;313:390–7.



Contact

Ali Afshar-Oromieh, M.D.
Heidelberg University Hospital
Department of Nuclear Medicine
INF 400
69120 Heidelberg
Germany
Phone: +49-6221-56-7732
Fax: +49-6221-42-2462
ali.afshar@med.uni-heidelberg.de

MR-Guided Biopsies of the Prostate in Supine Patient Position

Florian Schneider, M.D.[1]; Martin Requardt, Ph.D.[2]; Gregor Thörmer, Ph.D.[2]; Karl Engelhard, M.D.

[1] Diagnostic Radiology, Martha-Maria Hospital Nürnberg, Germany
[2] Siemens Healthcare, Magnetic Resonance, Erlangen, Germany

Introduction

Prompted by elevated PSA levels, more than a million men in the United States alone have to undergo transrectal ultrasound (TRUS)-guided prostate biopsy to clarify suspicion for prostate cancer per year [1]. Unlike pathways for other malignancies, biopsy of the prostate is performed by standardized, systematic but essentially random sampling [2]. The major limitation of this approach is that clinically *in*significant cancers are often identified by chance while, even more important, clinically *significant* cancers may remain undetected [3, 4]. As a result of this uncertainty, more than one-third of men whose first biopsy was negative are rebiopsied within 5 years [1].

Over recent years, multiparametric magnetic resonance imaging (mpMRI), combining the morphological assessment of T2-weighted (T2w) imaging with different functional imaging techniques such as diffusion-weighted imaging (DWI) and dynamic contrast enhanced imaging (DCE) has become a mature tool for localizing and visualizing suspicious foci in the prostate.

Consequently, advances are being made in the way that biopsies are performed, with the aim to integrate the additional information into the biopsy workflow: Cognitive registration, in-bore MR guided biopsy and MR/US fusion biopsies are the most commonly used techniques to improve prostate cancer detection with targeted biopsy.

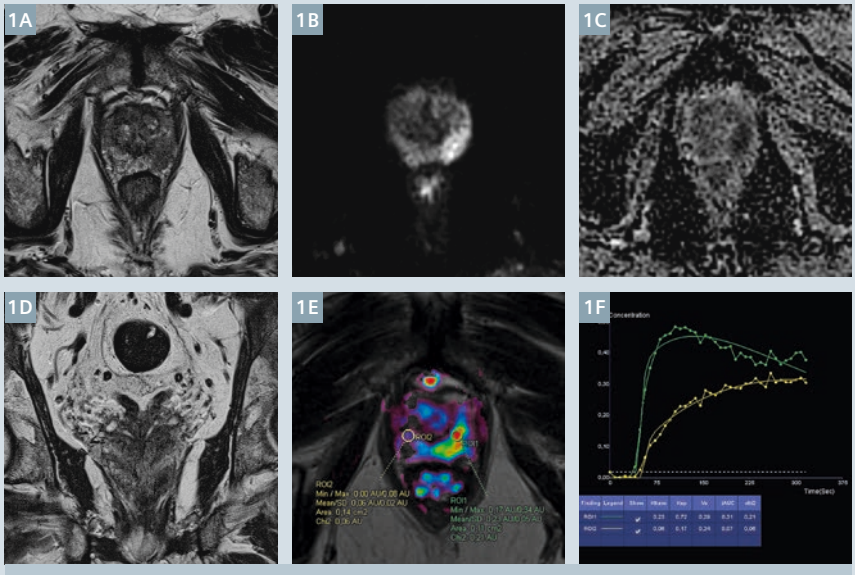
While both cognitive integration and MR/US fusion biopsies have been shown to improve the cancer detection rate [5], prostate biopsies performed under direct MR guidance are indicated in patients where MR imaging identified lesions that are either very small or located in areas difficult to reach with standard TRUS-guided biopsy. Another indication might be in patients showing a clear discrepancy between the histopathological findings of TRUS-biopsy and imaging results.

In the following, we report on our clinical experience with a customized approach and a simplified biopsy workflow for MR-guided prostate biopsies where the patient lies in supine position.

Case 1

Due to a contraindication for digital rectal examination and transrectal ultrasound because of rectal stenosis, a 72-year-old, biopsy-naive patient with continuously rising PSA levels (last: 12 ng/ml) was referred to our institution for diagnostic prostate MRI. Scans were performed with high-channel surface coils only using a MAGNETOM Skyra 3T system.

The protocol consisted of axial, coronal and sagittal T2-weighed TSE scans (TR 8300 ms, TE 107 ms, slice thickness 3.0 mm, FOV 160 mm, matrix 320, TA 3:11 min); axial diffusion-weighted imaging with RESOLVE (TR 4190 ms, TE 69 ms, slice thickness 3.0 mm, FOV 160 mm, matrix 114, TA 4:42 min) and axial DCE scans (TR 5.08 ms, TE 1.77 ms, slice thickness 3.5 mm, FOV 260 mm, matrix 192, TA 8:1 s, 35 repetitions).

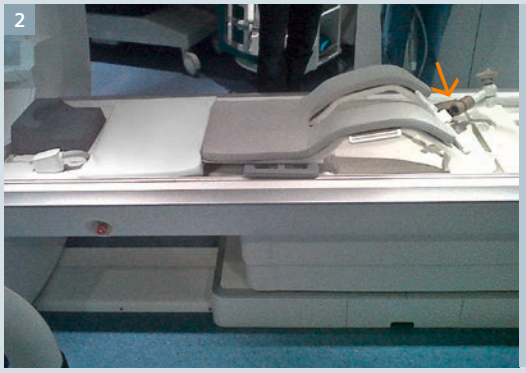


1 Transversal T2w TSE images **(1A)** demonstrating a suspicious lesion within the left peripheral zone with correspondingly increased signal in the b = 800 s/mm² image **(1B)**, diffusion restriction in the ADC map **(1C)**. The lesion can be confirmed in the coronal T2w images **(1D)**. The parametric map **(1E, K^{trans})** shows a clear focal lesion with a highly suspicious curve **(1F)**.

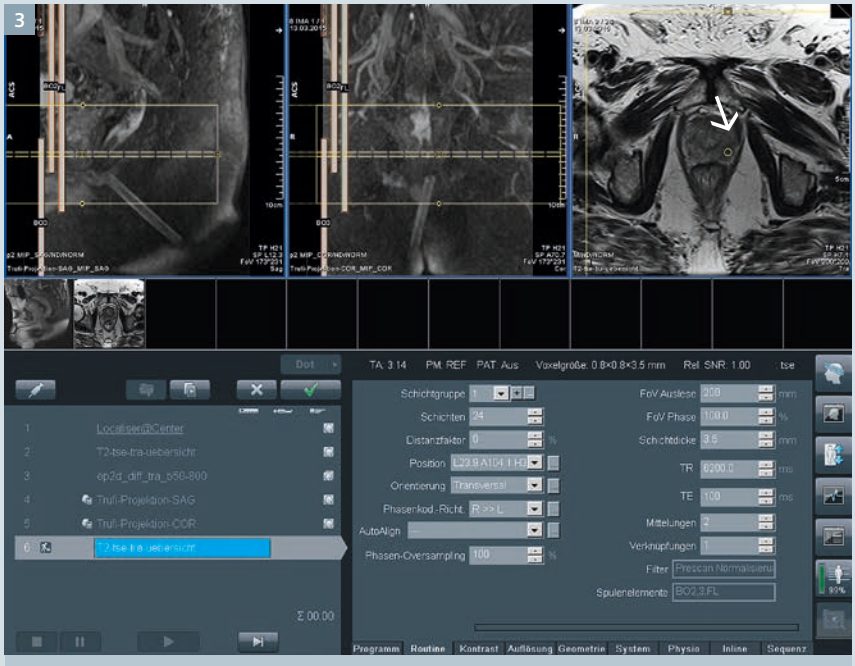
Dynamic contrast-enhanced images were post-processed using *syngo*.via Tissue 4D.

As illustrated in Figure 1, a lesion in the apical third of the prostate was visible in T2-weighted images as a hypointense, lenticular shaped structure extending more than 1.5 cm with corresponding diffusion-restriction and suspect, focal contrast uptake as well as wash-out in the DCE series. Consequently, the patient was referred to MRI-guided prostate biopsy of the highly suspicious areal in the gland.

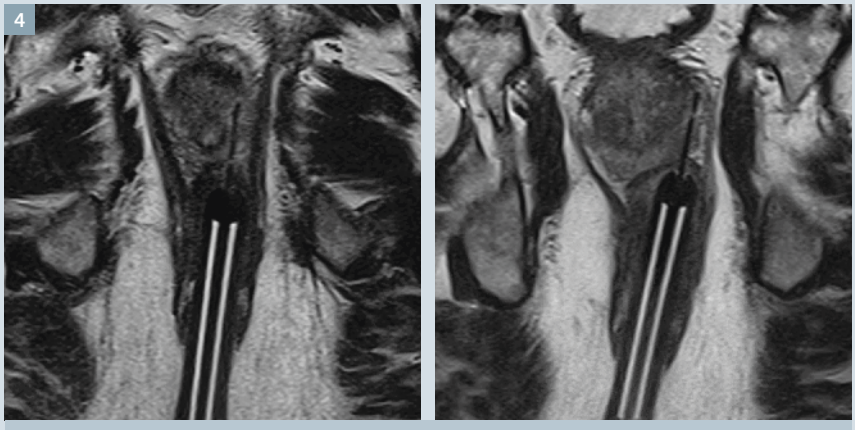
Biopsy was performed in a wide-bore MAGNETOM Aera 1.5T system with the patient in supine lithotomy position using a tailored positioning device (Fig. 2, Invivo Germany, Schwerin, Germany). Intra-procedural imaging was undertaken using a combination of a flexible 4-channel coil underneath the patients back and a standard 18-channel body coil positioned on the pelvis of the patient. First, a small, contrast-filled tube was inserted to the patient's rectum and fixated with a highly flexible MR-compatible arm. To define the target for biopsy, fast T2-weighted scans (TR 5000 ms, TE 100 ms, slice thickness 3.5 mm, FOV 200 mm, matrix 256, TA 1:45 min) were performed, while the position and orientation of the contrast-filled needle guide was imaged using a 3D fat suppressed TrueFISP sequence and visualized with a 3D maximum intensity projection (MIP) technique. By simply positioning the center mark of a slice block (Fig. 3, yellow circle) in the center of the lesion, the orientation of the needle guide with respect to the target was checked and the trajectory of the needle guide was iteratively corrected to point to the target. In the given case, only one iteration (repositioning of the needle guide, control scan) was necessary. After contentedly positioning the needle guide, the actual fully-automated biopsy device was inserted and two samples from slightly different positions were taken (Fig. 4). Histopathology revealed a 3 + 3 = 6 acinar adenocarcinoma.



2 Setup with the customized biopsy device. Patient will be positioned in supine position. A flexible arm (arrow) holds the contrast filled needle guide which is used to define the trajectory to the target and to insert the actual biopsy needle.



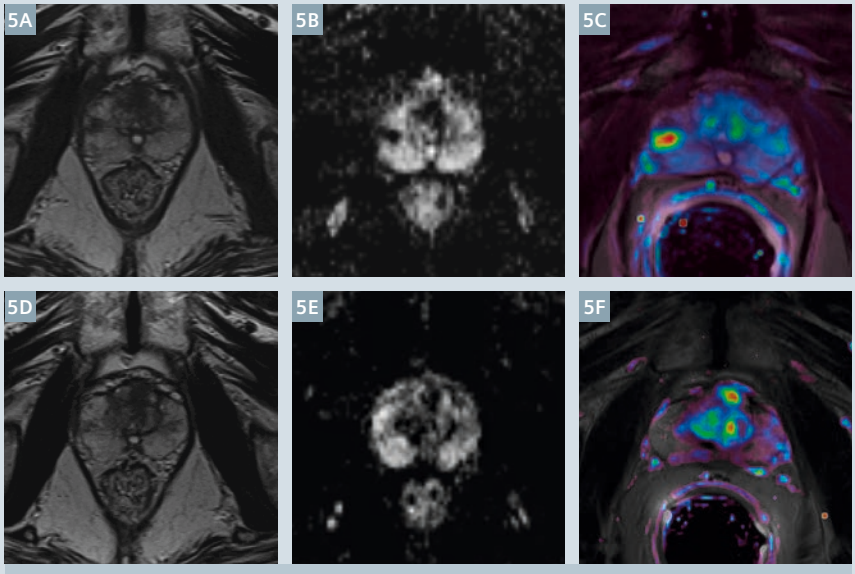
3 Control images to confirm the correct positioning of the needle guide. The center mark (yellow circle, right image) was positioned on the lesion to be biopsied. The left and middle images confirm that the contrast filled needle guide (visible as two bright lines) directly points to the target (yellow circle, arrow).



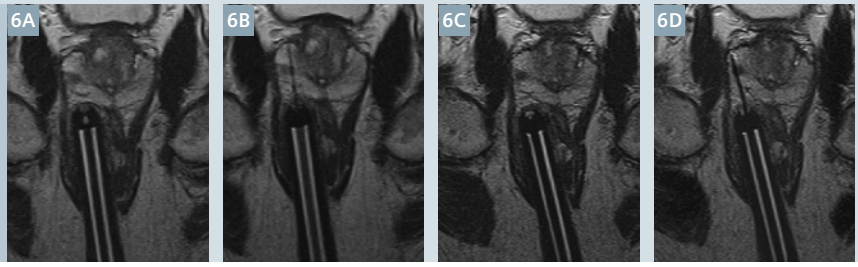
4 Fast, double-oblique T2w TSE control images confirming the right position of the needle in the lesion before tissue sampling.

Case 2

Patient presented at our department with constantly high PSA values (03/2015: 10.8 ng/ml; 04/2015: 13.0 ng/ml) with a referral for prostate MRI. Diagnostic multiparametric prostate MRI was performed on our 1.5T MAGNETOM Aera and revealed two relatively small lesions in the right and left peripheral zone (Fig. 5). The lesion in the right peripheral zone was selected for MR target biopsy due to better accessibility. During the MR-guided biopsy session, two samples were taken from different positions (Fig. 6). The one taken from the periphery revealed an acinar adenocarcinoma with a Gleason Score of 6 (3 + 3) while the other sample even showed a more aggressive pattern (Gleason Score 3 + 4 = 7).



5 Axial T2w TSE **(5A, D)**, ADC map **(5B, E)**, and K^{trans} maps **(5C, F)**.



6 After planning the biopsy trajectory **(6A)** the needle was inserted and an oblique control scan was performed. The control scan **(6B)** clearly shows that only the periphery of the lesion is targeted. After minimal repositioning of the needle guide **(6C)** the needle was reinserted and control scan shows optimal positioning of the needle in the lesion.

Summary

Targeted biopsies of the prostate under direct MRI-guidance are a reasonable complement to ultrasound biopsy techniques. As shown in the second case presented here, exact targeting of the most suspicious portion of a tumor is crucial for correct classification and consequently best therapy decisions. Especially in case of relatively small lesions, direct MR-guidance has clear advantages over fusion techniques which are always susceptible to intrinsic sources of registration errors.

The targeting procedure presented here, does not require any additional software equipment or extra planning PCs, since it is solely based on standard sequences and planning tools provided with the scanner. Biopsies in a supine position, as performed in Nuremberg, may further improve the acceptance and applicability of MR guided biopsies of the prostate especially in obese, dyspnoeic or elderly individuals.

References

1 Welch HG, Fisher ES, Gottlieb DJ, Barry MJ. Detection of prostate cancer via biopsy in the Medicare-SEER population during the PSA era. J Natl Cancer Inst 2007;99:1395–1400.

2 Churukanti G1, Siddiqui MM1. Prostate cancer: MRI-TRUS fusion biopsy versus 12-core systematic biopsy. Nat Rev Urol. 2015;12:369-71.

3 Sinnott M, Falzarano SM, Hernandez AV et al. Discrepancy in prostate cancer localization between biopsy and prostatectomy specimens in patients with unilateral positive biopsy: implications for focal therapy.Prostate 2012; 72: 1179–86.

4 Epstein JI, Feng Z, Trock BJ, Pierorazio PM. Upgrading and downgrading of prostate cancer from biopsy to radical prostatectomy: incidence and predictive factors using the modified Gleason grading system and factoring in tertiary grades. Eur Urol 2012; 61: 1019–24.

5 Sonn GA, et al. Targeted biopsy in the detection of prostate cancer using an office based magnetic resonance ultrasound fusion device. J Urol. 2013;189: 86-91.



Contact

Florian Schneider, M.D.
Martha-Maria Hospital
Radiology Department
Stadenstr. 58
90491 Nürnberg
Germany
Phone: +49 (0) 911 959-1151
Florian.M.Schneider@web.de

A Novel Model-Based MR Attenuation Correction Method for PET/MR Hybrid Imaging Considering Bone

Daniel H. Paulus[1]; Thomas Koesters[2,3]; Fernando Boada[2,3]; Kent P. Friedman[2]; Harald H. Quick[4,5]

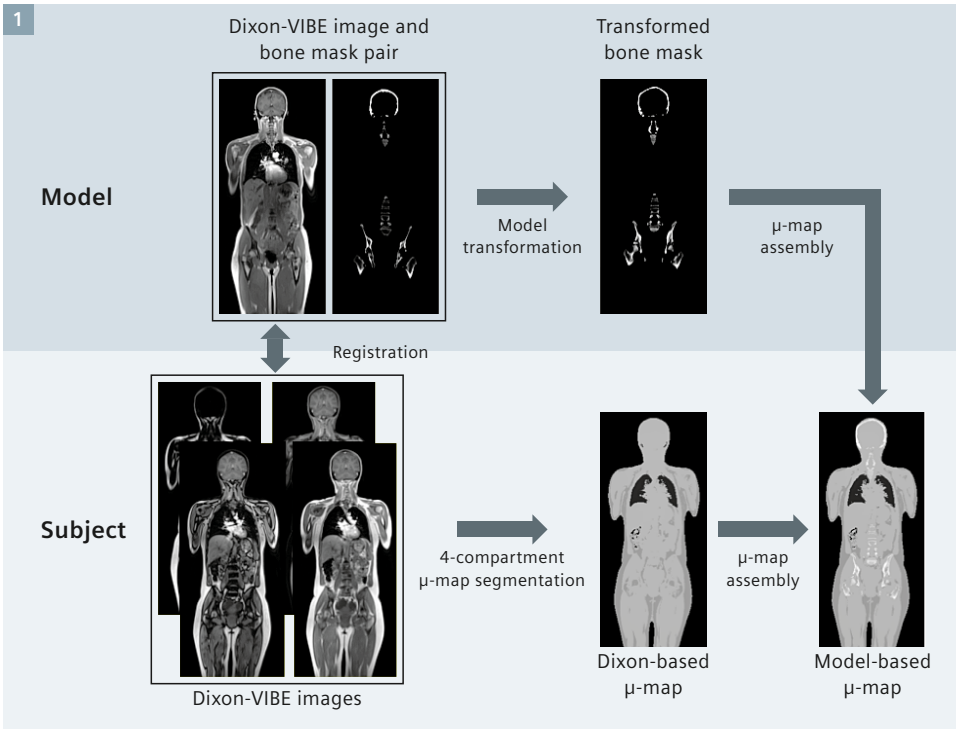
[1] Institute of Medical Physics, Friedrich-Alexander-University Erlangen-Nürnberg (FAU), Erlangen, Germany
[2] Bernard and Irene Schwartz Center for Biomedical Imaging, Department of Radiology, New York University School of Medicine, New York, NY, USA
[3] Center for Advanced Imaging Innovation and Research (CAI2R), New York, NY, USA
[4] Erwin L. Hahn Institute for MR Imaging, University Duisburg-Essen, Essen, Germany
[5] High Field and Hybrid MR Imaging, University Hospital Essen, Essen, Germany

Introduction

Whole-body hybrid PET/MR imaging has become a fast-growing research field in medical imaging, especially since the introduction of the first integrated whole-body PET/MRI system in 2010 [1, 2]. With an increasing role in clinical routine, it allows simultaneous data acquisition of metabolic information by the means of PET and anatomical information with excellent soft tissue contrast and further functional imaging parameters by the means of MR.

For accurate and quantitative PET images, appropriate attenuation correction (AC) is required. In hybrid PET/CT systems, CT images providing tissue attenuation as Hounsfield units (HU) can directly be transformed to attenuation coefficient maps (μ-maps) given in linear attenuation coefficients (LACs) at 511 keV by using a bilinear conversion [3]. In PET/MR hybrid imaging, PET AC is more challenging [4], since MR images provide mainly proton densities and cannot directly be converted to LACs at 511 keV.

Over recent years, image segmentation-based methods, on the basis of a fast 3-dimensional (3D) MR Dixon sequence are being used for AC in routine PET/MR hybrid imaging. This method provides up to 4 tissue classes including air, fat, lung, and soft tissue [5] assigned with predefined LACs. A short acquisition time, easy implementation, and robust performance have led this method to be used for several clinical PET/MRI studies [6–8], albeit there are certain limitations compared to CT-based AC. A limited MR imaging field-of-view might lead to image truncations in the μ-map and bone is not recognized by the MR Dixon sequence. Thus, LACs of bone are set to the soft tissue value in 4-compartment methods leading to a potential



1 Schematic drawing of the novel model-based algorithm that considers bone in whole-body PET/MRI AC. The model (upper part) consists of a set of MR image and bone mask pairs that are registered to the subject's (lower part) Dixon-VIBE images for each body bone individually. The transformation is applied to the bone segmentation for each body bone and added to the 4-compartment segmentation-based μ-map at all voxels of densities higher than soft tissue.

underestimation of PET standard uptake values (SUVs). This effect has been quantitatively evaluated by several groups and an SUV bias between -6.5% and -11.2% compared to CT AC was calculated for bone lesions [5, 9, 10]. However, all of the cited studies were based on PET/CT data sets, and CT images have been modified by thresholding to simulate a segmentation-based MR µ-map, before transforming to LACs at 511 keV.

For simultaneous PET/MR imaging of the head and brain new approaches have been proposed to include cortical bone information in the MR-based µ-map, such as atlas registration and pattern recognition [11] or pseudo CTs generated with an ultrashort echo time MR sequence [12]. These methods, however, have not yet been assigned to routine whole-body PET/MR imaging.

A novel prototype model-based AC method for PET/MR hybrid imaging has recently been introduced that considers major bones besides the head to improve whole-body PET/MRI AC [13]. In this study [13] the new method was compared to both the routine Dixon-based AC and the CT-based AC, and all reconstructions were based on only the PET/MRI raw data. This excludes inter-scanner biases that might otherwise occur, if PET raw data sets of different PET systems are used in quantitative comparisons. In this article, which is based on the study by Paulus et al. [13], the new model-based method is described and PET/MRI patient cases are demonstrated and quantitatively evaluated showing the benefit of adding cortical bone to the segmentation-based µ-map.

Materials and methods

Study population

This study was approved by the institutional review and ethical board. 20 patients (mean age, 54.8 ± 16.8 y, range 25–85 y, 19 female) first underwent a clinically indicated PET/CT examination (Biograph mCT, Siemens Healthcare, Knoxville, TN, USA) according to the standard clinical protocol, followed by a subsequent whole-body PET/MRI acquisition (Biograph mMR, Siemens Healthcare, Erlangen, Germany). MR/PET data sets were acquired on a Biograph mMR under the auspices of a NYU Langone Medical Center IRB approved-protocol. Written informed consent was obtained from all patients and no additional radiotracer was injected for the PET/MRI acquisition. An average activity of 541.7 ± 18.4 MBq was injected[1] and the PET/MRI acquisitions were performed 200.3 ± 48.8 min post injection. 14 patients were examined for 5 bed positions and 6 patients were examined for 3 bed positions where the head was not included into the PET/MRI protocol.

PET/MRI µ-maps

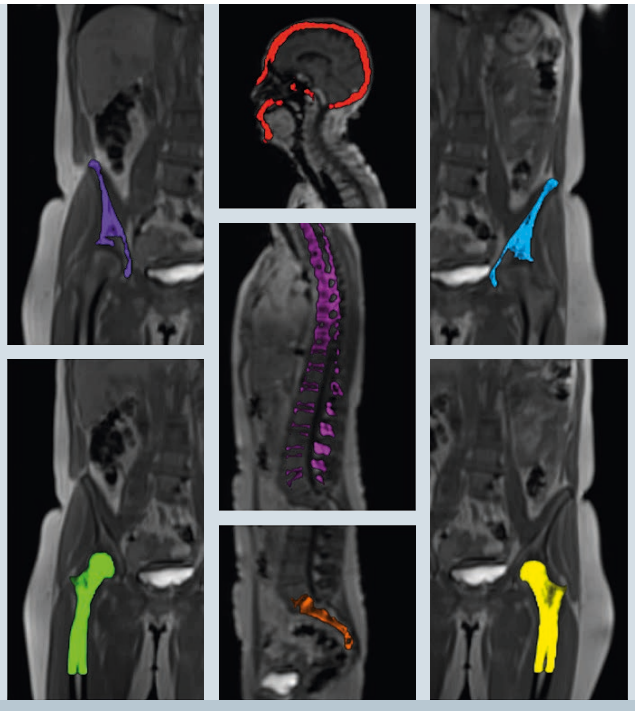
All PET reconstructions are based on emission data acquired with the PET/MRI system using identical parameters, like scanner hardware and identical reconstruction settings. Three different µ-maps were used for the PET reconstructions of each subject.

- **Standard MR-based µ-map**
  The routine MR-based segmentation AC (Dixon) was performed with a breath-hold 2-point 3D Dixon-VIBE (volume interpolated breath-hold examination) technique. The µ-map provides 4 different tissue classes including air, fat, lung, and soft tissue and was acquired with standard protocol parameters: Matrix 192 x 126 with 128 slices (coronal orientation); voxel size (2.60 x 2.60) mm², slice thickness 3.12 mm, TR = 3.6 ms, TE = 2.46 ms, flip angle 10°, and acquisition time 19 s per bed position.
- **Model-based µ-map**
  The novel method (Model), illustrated in Figure 1 is based on the regular 4-compartment segmentation from a Dixon sequence. Bone information is added to these µ-maps by using a model-based prototype bone segmentation algorithm[2] (Siemens Healthcare, Erlangen, Germany) [13] using continuous LACs for bone in cm^{-1} at the PET energy level of 511 keV. The model consists of the major body bones including left and right

[1] The full prescribing information for the Fludeoxyglucose F^{18} injection can be found at page 91.

[2] The product is still under development and not commercially available yet. Its future availability cannot be ensured.

2



2 An illustration of the major bones containing bone densities as continuous LACs in cm^{-1} at 511 keV used in the model-based AC. The bone information is superimposed with the subject's MR image demonstrating exact anatomical registration.

femur (upper part), left and right hip, spine (including sacrum), and skull (Fig. 2) with a corresponding pre-aligned MR image. At each major body bone, the MR image of the model is individually registered with the subject MR image.

The first step of the model algorithm is a learning-based approach to detect a set of landmarks surrounding each bone [14]. Subsequently, a more sophisticated deformable registration [15] is performed to bring the model to the subject space more precisely. Following the same transformations, the pre-aligned bone masks containing LAC in cm^{-1} are then brought to the subject space and added to the original Dixon-based µ-map at all voxels of densities higher than soft tissue. The average running time of the algorithm was between 2 and 3 minutes per whole-body data set.

- **CT-based µ-map**
  As a standard of reference quantification, CT-based AC (CT) was performed with the PET/MRI emission data. CT images derived from the PET/CT data of the same subject were non-rigidly registered to the anatomical Dixon-VIBE images and visually compared to ensure optimal anatomical alignment. The two-step registration framework was similar to the algorithm used for the Model method. It consists of a landmark-based rigid registration [14] and a deformable registration [15]. The CT images were transformed using the standard bilinear conversion [3] to provide LACs at 511 keV. Since PET/CT acquisitions were performed with patient's arms up and not with arms down as in PET/MRI, the arms were removed in the CT-based image and replaced with arm information of the Dixon-based µ-map.

Data processing
All µ-maps were post-processed with a maximum likelihood reconstruction of attenuation and activity (MLAA) algorithm [16] to add missing parts mainly of the arms. All PET images were reconstructed iteratively on the PET/MRI system with a 3D ordinary Poisson ordered-subsets expectation maximization (OP-OSEM) algorithm using 3 iterations and 21 subsets. The standard whole-body PET/MRI reconstruction parameters were used: Image matrix 172 x 172, pixel size 4.173 x 4.173 mm^2, slice thickness 2.031 mm, Gaussian filtering 4 mm.

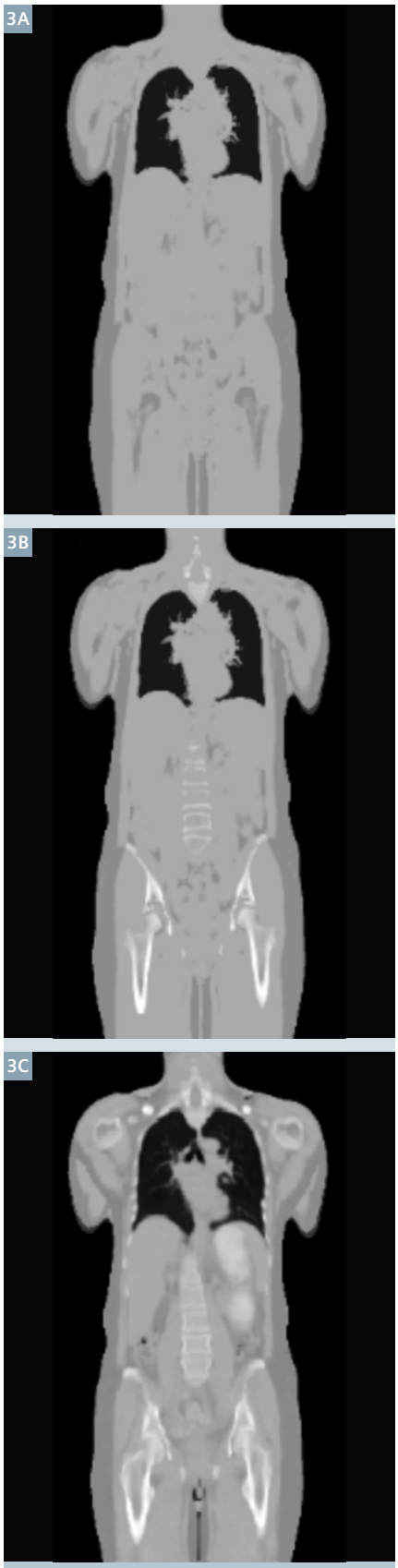
PET image analysis
PET images were superimposed with the corresponding MR images of a radial T1-weighted VIBE sequence used for MRI diagnosis in whole-body PET/MRI acquisitions. Based on the MR image, volumes of interest (VOIs) were manually drawn on normal tissue and the mean SUV (SUV_{mean}) was calculated for following regions: aorta/blood level, liver, spleen, femoral head left/right, iliac bones left/right, psoas muscles left/right, 3rd lumbar vertebra (L3), and subcutaneous fat. Additionally, VOIs of all identified soft-tissue lesions as well as bone lesions of all 20 subjects were drawn using a 50% maximum contour of the PET SUV. The CT-based reconstruction of each subject was used as the standard of reference.

The VOIs of one femoral head and one iliac bone of two patients were excluded from the analysis due to hip implants and resulting MR image artifacts. Furthermore, one femoral head VOI and two iliac bone VOIs were excluded due to lesions or metastases inside the VOIs. One spleen VOI is missing, since the patient underwent a splenectomy.

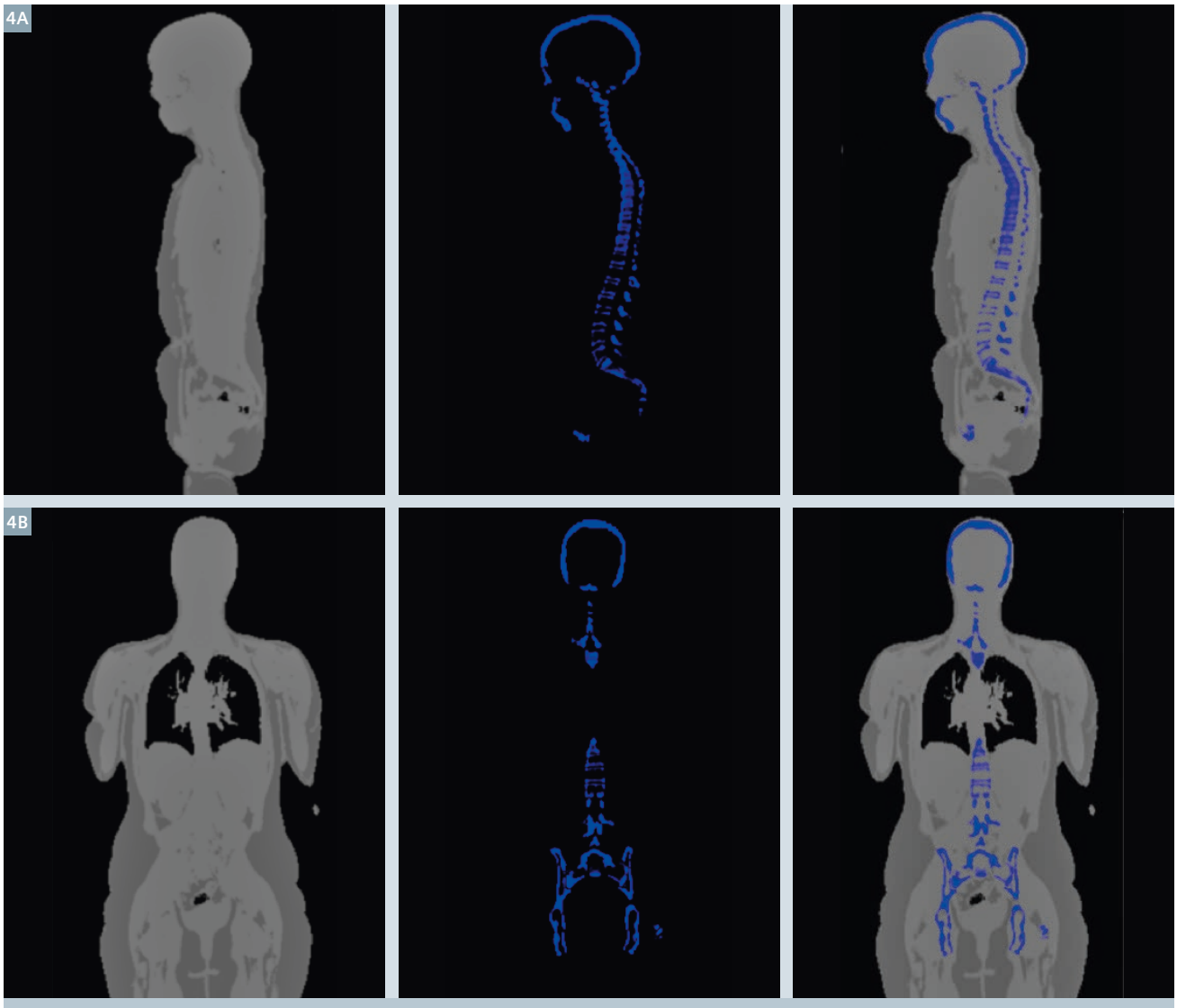
Results

Figure 3 shows all three different µ-maps of one subject in coronal view. The additional bone information that is added to the Dixon-based µ-map is illustrated in Figure 4.

The difference of background VOIs within all 20 patients depends very much on the tissue type. For soft tissue including aorta, liver, spleen, subcutaneous fat, and psoas muscles, the difference of the SUV_{mean} compared to CT is 2.4% for Dixon and 2.7% for Model. Cold-background VOIs of bony tissue were underestimated with Dixon by -46.5% ± 9.3% (femoral head), -20.0% ± 5.5% (iliac



3 Dixon **(3A)**, Model **(3B)**, and CT **(3C)** µ-map exemplarily shown for one patient.



4 Dixon-based segmentation μ-map (left), bone mask information (middle) and combined model-based μ-map (right) of one subject in sagittal **(4A)** and coronal **(4B)** view.

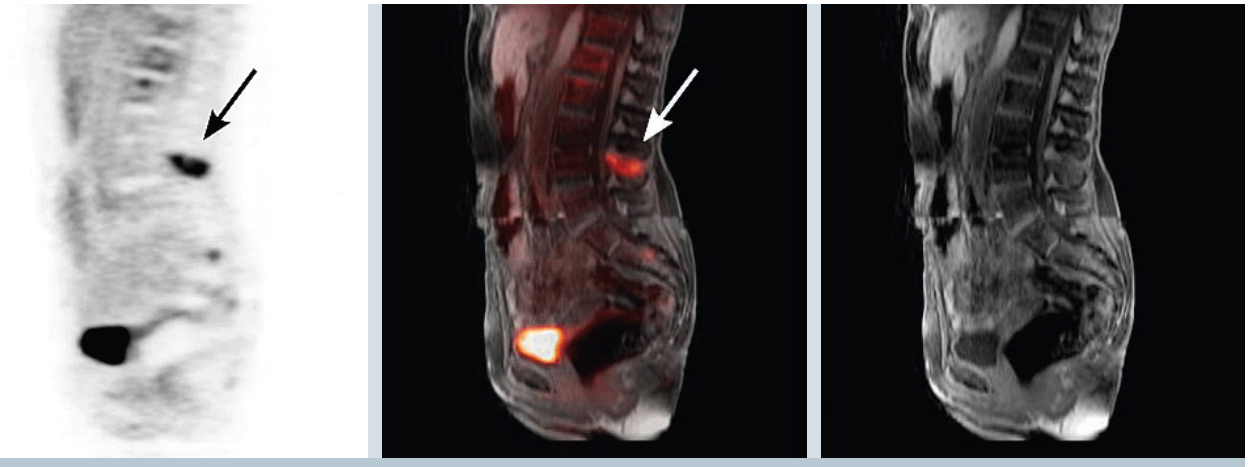
bones), and -9.9% ± 8.9% (L3). The bias is reduced with the new Model method to -4.9% ± 7.7% (femoral heads), -2.8% ± 4.6% (iliac bones), and -7.1% ± 7.8% (L3).

The SUV deviation between Dixon and Model is negligible for soft tissue lesions with a mean of 0.3% and a maximum of 1.5%. Compared to the CT-based AC, the deviation is 5.1% ± 5.1% and 5.2 ± 5.2% for the Dixon method and the Model method, respectively. In this way, lung lesions are excluded, where the segmentation μ-map differs from the CT μ-map in terms of LACs.

For bone lesions an underestimation of -7.3% ± 5.3% was calculated for Dixon compared to CT, which is reduced to -2.9% ± 5.8% with the new Model method.

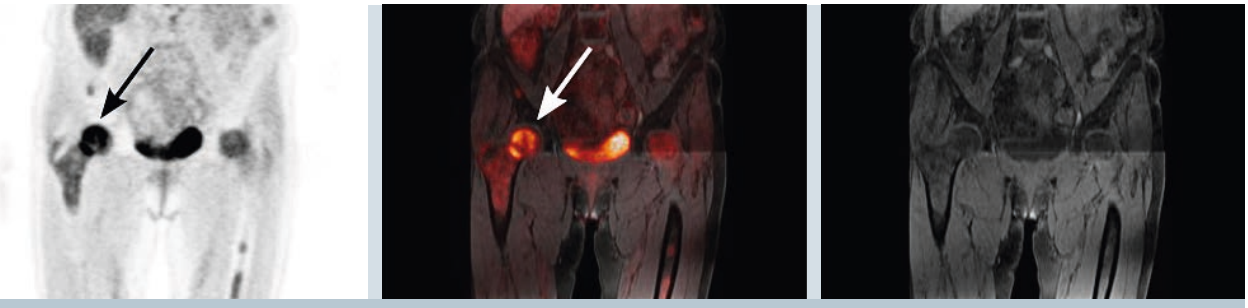
Figures 5 to 7 show the radial T1-weighted VIBE sequence used for MRI diagnosis, the PET image, and the superimposed PET/MR image of three different patients with bone lesions. The SUV comparison shows the improvement regarding PET quantification in bone lesions as a result of adding bone information to the Dixon segmentation-based μ-map. Case 1 has a spinous process bone metastasis showing an SUV_{mean} of 4.15 for the CT AC. The deviations with Dixon AC and Model AC compared to CT AC are -5.1% and -1.4%, respectively. Case 2 shows a bone metastasis in the right femoral head with an SUV of 5.51. The deviation of the SUV_{mean} with Dixon AC and Model AC compared to CT AC is -11.3% and -1.5%, respectively. In case 3, iliac bone metastases with a calculated SUV of 7.03 (right) and 8.99 (left) have been evaluated. The deviation of the SUV_{mean} with Dixon AC and Model AC compared to CT AC was -10.7% and -6.1% for the right side, respectively, and -10.8% and -5.0% for the left side, respetively.

5



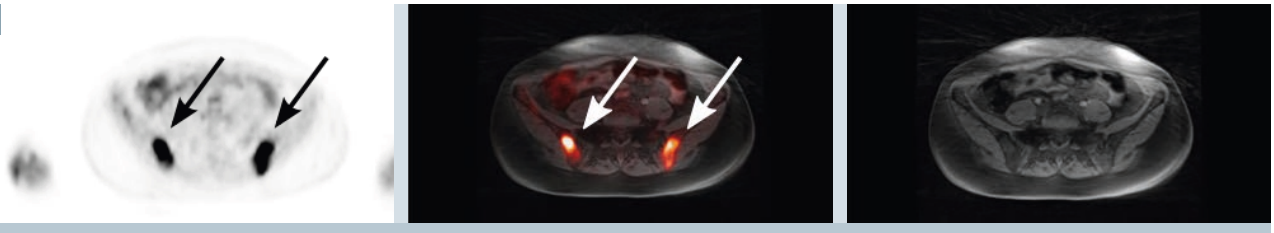
5 Sagittal PET image, superimposed PET/MR image, and diagnostic MR image of the radial T1-weighted VIBE sequence, showing a spinous process bone metastasis. The deviation of the SUV_{mean} with Dixon AC and Model AC compared to CT AC was -5.1% and -1.4%, respectively.

6



6 Coronal PET image, superimposed PET/MR image, and diagnostic MR image of the radial T1-weighted VIBE sequence, showing a bone metastasis in the right femoral head. The deviation of the SUV_{mean} with Dixon AC and Model AC compared to CT AC was -11.3% and -1.5%, respectively.

7



7 Transaxial PET image, superimposed PET/MR image, and diagnostic MR image of the radial T1-weighted VIBE sequence, showing iliac bone metastases (right and left). The deviation of the SUV_{mean} with Dixon AC and Model AC compared to CT AC was -10.7% and -6.1% for the right side, respectively, and -10.8% and -5.0% for the left side, respetively.

Discussion

On a dataset of 20 PET/MRI patients, it was shown that the new Model approach improved PET SUVs in bony regions when compared to CT-based AC and to Dixon MRI-based AC. The results of the study are comparable with previous whole-body hybrid imaging studies that have calculated an SUV underestimation for bony regions between -7% and -11% if bone is considered as soft tissue in the μ-map. The previous studies, however, were all based on PET/CT data [6, 10] and not PET/MRI data.

Unlike the relatively high impact in bony regions, the evaluation of SUVs of normal soft tissue shows that the Model as well as the Dixon approach have consistent results when compared to CT-based AC serving as standard of reference. This demonstrates the limited impact on SUVs in soft tissues that are not close to bone when corrected with μ-maps including bone information, as also shown by other groups [6, 13]. Furthermore, it shows that for these regions the routine Dixon μ-map performs virtually identically compared to the CT AC. This effect was also observable for soft tissue lesions.

The possibility should be considered that there are bone density variations in the same bone groups between patients. While the bias for patients without bone diseases is expected to be relatively small, bone density changes due to diseases might affect the PET quantification more. Due to abnormal decreased bone density SUVs might be overestimated in or near those bones, since LACs of the model are higher than the actual bone LACs. This however, remains true for most MRI-based AC methods including segmentation- and atlas-based AC. For better matching of bone densities, the model might be improved by grouping it into different ages, sex, and races.

In contrast to former whole-body PET/MRI AC studies, PET data of each patient within this study is based only on the emission raw data set of the PET/MRI system, which focuses the quantitative comparison to the differences of the μ-maps. Physiological aspects, like different patient positioning or tracer washout between PET/CT and PET/MRI scans, can therefore be excluded. The attenuation effect of local radiofrequency surface coils leading to a potential underestimation of -5% with a maximum up to -20% when neglected in AC [17,18] can also be excluded, since all PET reconstructions are performed with the same settings and raw data.

CT-based μ-maps of the body trunk were used as a standard of reference in this study. Due to the fact that patient positioning in PET/CT is performed with arms up, CT information of the patient arms was missing in these CT-based μ-maps. Since PET/MR imaging is performed with the arms resting beside the patient body, the MRI-based μ-maps contain the arms. Consequently, the missing information was added from the corresponding Dixon-based μ-map to the CT-based μ-map such that the different patient positioning (arms up vs. arms down) thus did not introduce additional bias. Furthermore, the effect of the arms for VOIs inside the body is expected to be small and is thus negligible.

The presented approach does not require any additional MRI sequences in the PET/MR imaging protocol, as needed in other methods such as the ultrashort echo time approach [12]. It is only based on the Dixon MRI sequence that is already acquired for the routine MRI-based AC. A data reconstruction run-time of about 2 to 3 minutes per whole-body case is short compared to other methods [11].

Conclusion

It is shown in 20 subjects that the new 5-compartment model improves the PET quantification compared to the current 4-compartment AC method, especially in bony tissue, bone lesions, and tissue close to bone. As the new method is based on the same Dixon MRAC acquisition, no additional scan time is required which is important given the generally long exam time of whole-body MR-PET scans.

Acknowledgments

This work was performed in collaboration with the Bernard and Irene Schwartz Center for Biomedical Imaging of New York University (NYU) and Siemens Healthcare GmbH. The authors would like to thank Matthias Fenchel, Christian Geppert, Yiqiang Zhan, Gerardo Hermosillo, and David Faul (all Siemens Healthcare GmbH) for their valuable participation and support.

References

1 Delso G, Furst S, Jakoby B, Ladebeck R, Ganter C, Nekolla SG, Schwaiger M, Ziegler SI. Performance measurements of the Siemens mMR integrated whole-body PET/MR scanner. J Nucl Med. 2011;52:1914–1922.
2 Quick HH. Integrated PET/MR. J Magn Reson Imaging. 2014;39:243-258.
3 Kinahan PE, Townsend DW, Beyer TT, Sashin D. Attenuation correction for a combined 3D PET/CT scanner. Med Phys. 1998;25:2046–2053.
4 Keereman V, Mollet P, Berker Y, Schulz V, Vandenberghe S. Challenges and current methods for attenuation correction in PET/MR. MAGMA. 2013;26:81–98.
5 Martinez-Moller A, Souvatzoglou M, Delso G, Bundschuh RA, Chefd'hotel C, Ziegler SI, Navab N, Schwaiger M, Nekolla SG. Tissue classification as a potential approach for attenuation correction in whole-body PET/MRI: evaluation with PET/CT data. J Nucl Med. 2009;50:520–526.
6 Drzezga A, Souvatzoglou M, Eiber M, Beer AJ, Fürst S, Martinez-Möller A, Nekolla SG, Ziegler S, Ganter C, Rummeny EJ, Schwaiger M. First clinical experience with integrated whole-body PET/MR: comparison to PET/CT in patients with oncologic diagnoses. J Nucl Med. 2012;53:845–855.
7 Wiesmüller M, Quick HH, Navalpakkam BK, Lell MM, Uder M, Ritt P, Schmidt D, Beck M, Kuwert T, von Gall CC. Comparison of lesion detection and quantitation of tracer uptake between PET from a simultaneously acquiring whole-body PET/MR hybrid scanner and PET from PET/CT. Eur J Nucl Med Mol Imaging. 2013;40:12–21.
8 Quick HH, von Gall CC, Zeilinger M, Wiesmüller M, Braun H, Ziegler S, Kuwert T, Uder M, Dörfler A, Kalender WA, Lell M. Integrated whole-body PET/MR hybrid imaging: clinical experience. Invest Radiol. 2013;48:280–289.
9 Samarin A, Burger C, Wollenweber SD, Crook DW, Burger IA, Schmid DT, von Schulthess GK, Kuhn FPPET/MR imaging of bone lesions--implications for PET quantification from imperfect attenuation correction. Eur J Nucl Med Mol Imaging. 2012;39:1154–1160.
10 Hofmann M, Bezrukov I, Mantlik F, Aschoff P, Steinke F, Beyer T, Pichler BJ, Schölkopf B. MRI-based attenuation correction for whole-body PET/MRI: quantitative evaluation of segmentation- and atlas-based methods. J Nucl Med. 2011;52:1392–1399.
11 Hofmann M, Steinke F, Scheel V, Charpiat G, Farquhar J, Aschoff P, Brady M, Bernhard Schölkopf B, Pichler BJ. MRI-based attenuation correction for PET/MRI: A novel approach combining pattern recognition and atlas registration. J Nucl Med. 2008;49:1875–1883.
12 Navalpakkam BK, Braun H, Kuwert T, Quick HH. Magnetic resonance-based attenuation correction for PET/MR hybrid imaging using continuous valued attenuation maps. Invest Radiol. 2013;48:323–332.
13 Paulus DH, Quick HH, Geppert C, Fenchel M, Zhan Y, Hermosillo G, Faul D, Boada F, Friedman KP, Koesters T. Whole-Body PET/MR Imaging: Quantitative Evaluation of a Novel Model-Based MR Attenuation Correction Method Including Bone. J Nucl Med. 2015;56:1061-1066.

14 Zhan Y, Zhou X, Peng Z, Krishnan A. Active scheduling of organ detection and segmentation in whole-body medical images. In: Metaxas D, Axel L, Fichtinger G, Székely G, eds. Medical Image Computing and Computer-Assisted Intervention–MICCAI 2008. Berlin, Germany: Springer; 2008:313–321.

15 Hermosillo G, Chefd'Hotel C, Faugeras O. Variational methods for multimodal image matching. Int J Comput Vis; 2002;50:329–343.

16 Nuyts J, Bal G, Kehren F, Fenchel M, Michel C, Watson C. Completion of a Truncated Attenuation Image From the Attenuated PET Emission Data. IEEE Trans Med Imaging. 2012;32:237–246.

17 Paulus DH, Braun H, Aklan B, Quick HH. Simultaneous PET/MR imaging: MR-based attenuation correction of local radiofrequency surface coils. Med Phys. 2012;39:4306–4315.

18 Kartmann R, Paulus DH, Braun H, Aklan B, Ziegler S, Navalpakkam BK, Lentschig M, Quick HH. Integrated PET/MR imaging: Automatic attenuation correction of flexible RF coils. Med Phys. 2013;40:082301.



Contact

Daniel H. Paulus, MSc
Institute of Medical Physics (IMP)
University of Erlangen-Nürnberg
Henkestr. 91, 91052 Erlangen,
Germany
daniel.paulus@imp.uni-erlangen.de



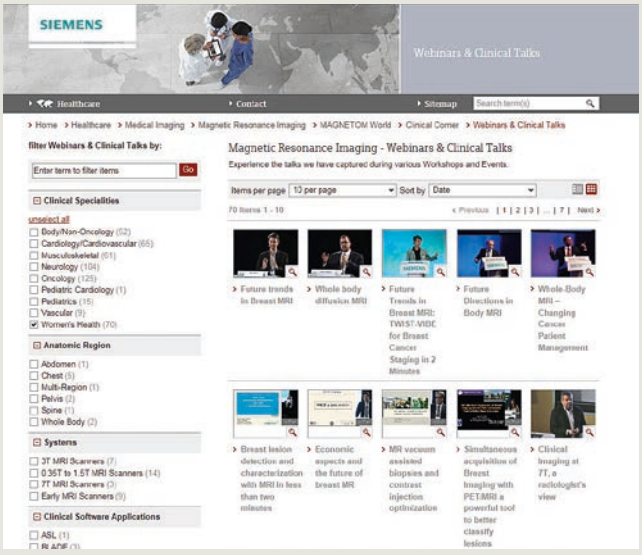
Contact

Prof. Harald H. Quick, Ph.D.
Director
Erwin L. Hahn Institute for MR Imaging
High Field and Hybrid MR-Imaging
University of Duisburg-Essen
Kokerei Zollverein
Kokereiallee 7, 45147 Essen, Germany
harald.quick@uni-due.de

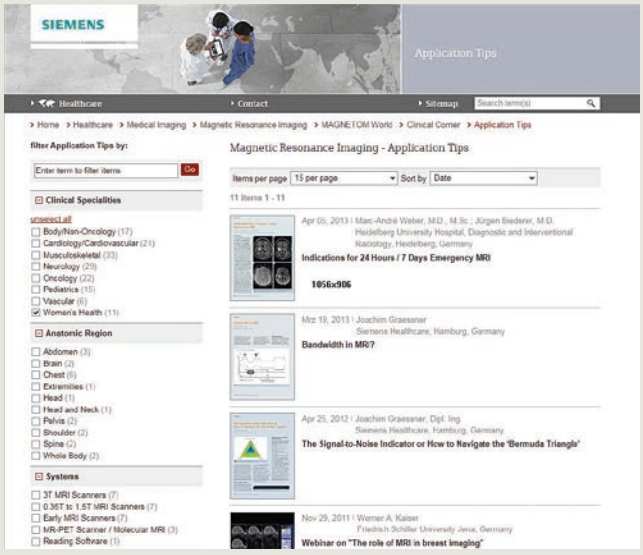
The MAGNETOM World

Your portal to protocols, talks, application tips and case studies

Siemens' global MRI community offers peer-to-peer support and information. Radiologists, physicists, and technologists, have all contributed with publications, presentations, training documents, case studies, and more – all freely available to you via this unique network.



Don't miss the >70 lectures and presentations by international and renowned experts in the field on Breast & Female Pelvis MR Imaging. These talks will allow you to be exposed to new ideas an alternative approaches.



The centerpiece of the MAGNETOM World Internet platform consists of MAGNETOM users' results. Here you will find protocols, case reports, articles and application tips allowing you to optimize your daily work.

Put the advantages of the MAGNETOM World to work for you!

www.siemens.com/magnetom-world

Breast MRI: Improved Image Quality with RESOLVE (readout-segmented echo-planar imaging, diffusion-weighted MRI)

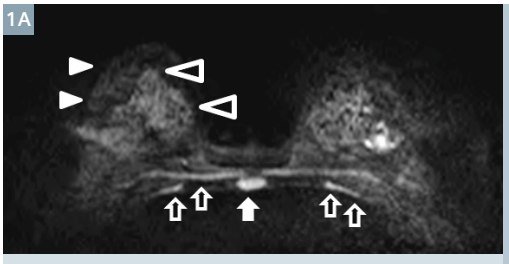
Sung Hun Kim, M.D.

Department of Radiology, Seoul St. Mary's Hospital, College of Medicine, The Catholic University of Korea, Seoul, Korea

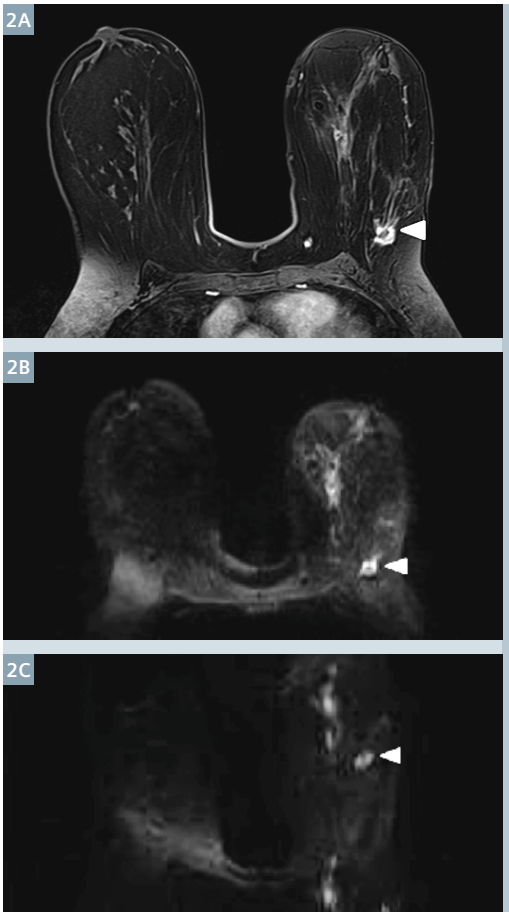
Diffusion-weighted imaging (DWI) allows measurement of the apparent diffusion coefficient (ADC) in breast tissue. Previous studies reported that ADCs could be an effective parameter in distinguishing between malignant and benign breast lesions [1], whereby low ADCs are associated with malignancy [2]. Conventional clinical DWI typically employs a single-shot echo-planar imaging (ss-EPI) sequence. However, due to its long echo-spacing, ss-EPI is afflicted with susceptibility artifacts, leading to geometric distortion, signal dropout, and image blurring [3]. RESOLVE (Siemens Healthcare, Erlangen, Germany), is a readout-segmented, multi-shot EPI (rs-EPI) sequence, in which only a subset of *k*-space points is acquired in the readout direction at each shot, instead of all *k*-space points in one shot. This allows for a substantial reduction in the echo spacing and in the time taken to traverse *k*-space in the phase-encoding direction, which leads to substantially reduced image degradation typically known in conventional DWI [4].

We compared the image quality based on standard ss-EPI and rs-EPI in 71 patients with 74 breast cancers and we found a significant improvement in image quality with RESOLVE for diffusion-weighted MR imaging of the breast [5]. Relative to conventional ss-EPI,

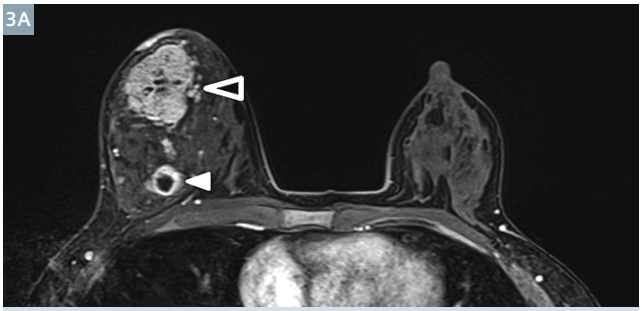
1. anatomical structure can be visualized more distinctly on images acquired with RESOLVE (Fig. 1),
2. lesion delineation is superior on RESOLVE and ghosting artifacts are less frequently present (Figs. 2, 3), and
3. geometric distortion are less common on RESOLVE (Fig. 4).

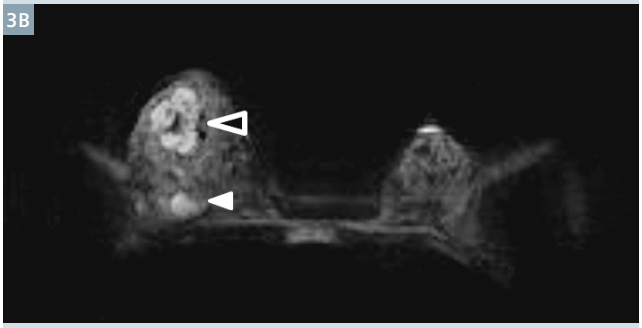


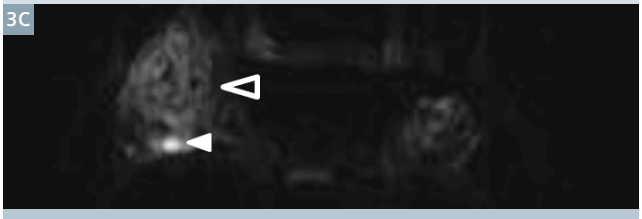
1 Sternum (arrow), fat-parenchymal differentiation (hollow arrowheads), chest wall (hollow arrows) can be visualized on both RESOLVE **(1A)** and conventional ss-EPI **(1B)**, but anatomy is better delineated on RESOLVE. Skin line (arrowheads) is only delineated on RESOLVE. Ghosting artifacts (stars) are apparent only on conventional ss-EPI.



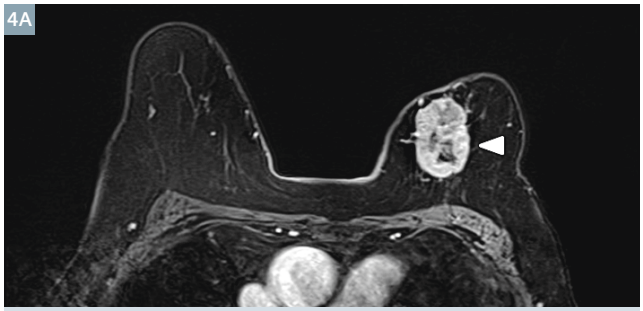
2 Left breast cancer is seen on the fat-suppressed T1-weighted contrast-enhanced image **(2A)**, RESOLVE **(2B)** and conventional ss-EPI image **(2C)**. The lesion is more clearly demonstrated on RESOLVE with high correspondence to the anatomical image. In the conventional ss-EPI image the lesion appeared to be located more anteriorly due to a ghosting artifact and there is only limited correspondence to the anatomical image.

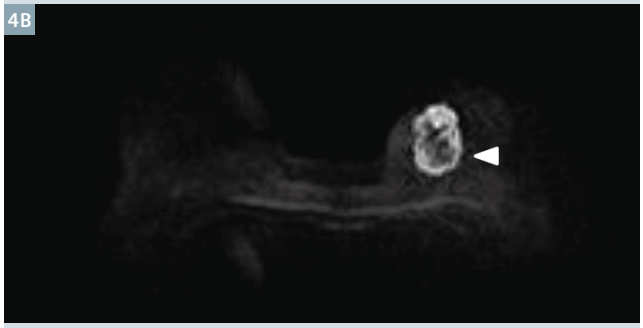


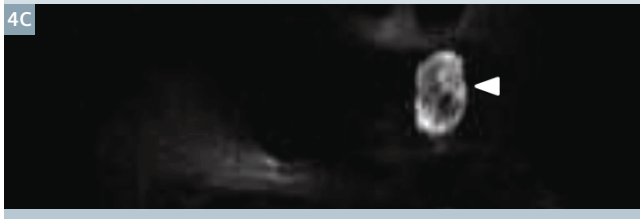




3 Two invasive ductal carcinomas are seen on the fat-suppressed T1-weighted contrast-enhanced **(3A)**, RESOLVE **(3B)** and conventional ss-EPI **(3C)** images. While the small, posteriorly located mass (solid arrowhead) is identifiable on both RESOLVE and conventional ss-EPI images, the larger mass (hollow arrowhead) is poorly defined on conventional ss-EPI.







4 Left breast cancer on fat-suppressed T1-weighted contrast-enhanced **(4A)**, RESOLVE **(4B)** and conventional ss-EPI **(4C)** images. As a result of the longer echo-train the conventional ss-EPI image shows a distinctive spatial distortion resulting in elongated anterior-posterior width of the mass. In contrast, the RESOLVE image shows very good accordance with the anatomical images.

There were also no significant differences in measured ADC values obtained with RESOLVE compared to ss-EPI.

In summary, RESOLVE showed improved overall image quality with no significant differences in ADCs relative to conventional ss-EPI. Given the distinct advantages of RESOLVE, it is now the standard sequence for diffusion within our routine clinical breast examinations.

References

1 Guo, Y., et al., Differentiation of clinically benign and malignant breast lesions using diffusion-weighted imaging. J Magn Reson Imaging, 2002. 16(2): 172-8.
2 Ei Khouli, R.H., et al., Diffusion-weighted imaging improves the diagnostic accuracy of conventional 3.0-T breast MR imaging. Radiology, 2010. 256(1): 64-73.
3 Yeom, K.W., et al., Comparison of Readout-Segmented Echo-Planar Imaging (EPI) and Single-Shot EPI in Clinical Application of Diffusion-Weighted Imaging of the Pediatric Brain. AJR Am J Roentgenol, 2013. 200(5): 437-43.
4 Porter, D.A. and R.M. Heidemann, High resolution diffusion-weighted imaging using readout-segmented echo-planar imaging, parallel imaging and a two-dimensional navigator-based reacquisition. Magn Reson Med, 2009. 62(2): 468-75.
5 Kim YJ, Kim SH, et al. Readout-segmented echo-planar imaging in diffusion-weighted MR imaging in breast cancer: comparison with single-shot echo-planar imaging in image quality. Korean J Radiol. 2014. 15(4): 403-10.



Contact

Sung Hun Kim, M.D.
Department of Radiology
Seoul St. Mary's Hospital College of Medicine
The Catholic University of Korea
505 Banpo-dong, Seocho-Gu, Seoul 137-701, Korea
Phone +82 (822) 2258-1455
Fax +82 (822) 2258-1457
rad-ksh@catholic.ac.kr

MRI for Parathyroid Imaging

Kambiz Nael, M.D.

Department of Radiology, Mount Sinai Hospital, New York, NY, USA

Background

Primary hyperparathyroidism (PHPT) is a common cause of hypercalcemia, with an estimated incidence of approximately 25 to 30 cases per 100,000 people. Approximately 85 to 90% of these cases are caused by single parathyroid adenomas (PTA), while multiglandular disease and parathyroid hyperplasia account for the remainder of cases with PHPT [1].

Diagnosis is often made by biochemical tests (serum Ca^{++} and PTH) in an appropriate clinical setting. Definitive treatment requires surgical excision, and preoperative localization with imaging is used to minimize the extent of surgery and complication rates [2].

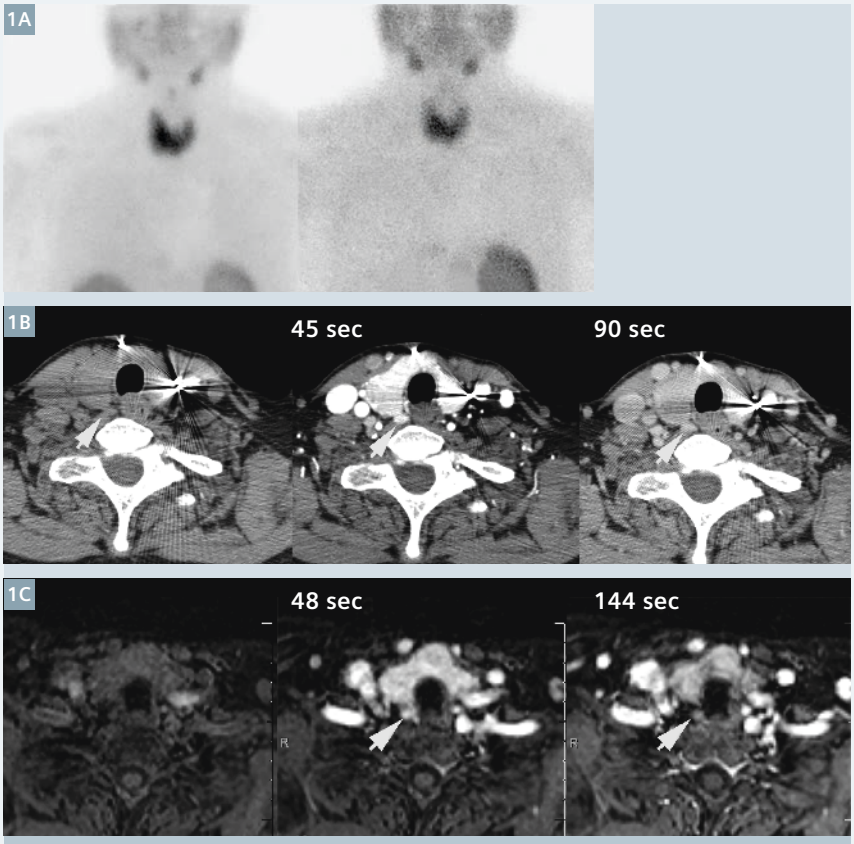
Traditionally, ultrasound and Technetium-99m (^{99m}Tc) Sestamibi scintigraphy have been used as first line tools to localize parathyroid adenomas. Ultrasound takes advantage of differential echogenicity of PTA compared to thyroid tissue, and scintigraphy takes advantage of physiologically differences in radiopharmaceutical uptake and retention. These tests can often be inconclusive, which has led to the development of other cross-sectional imaging such as dynamic multiphasic CT (4D CT) or dynamic MRI (Fig. 1).

Key points:

1. The MR technique described below has significantly improved on the traditional drawbacks of MR for parathyroid imaging including limited spatial and temporal resolution.
2. Four-dimensional (4D) contrast-enhanced MRI with high spatial and temporal resolution can be obtained for evaluation of parathyroid adenomas and has the potential to be used as a strong alternative imaging modality to Technetium (^{99m}Tc) Sestamibi or 4D CT without the need for radiation.
3. Multiparametric quantitative MR perfusion analysis can be used to distinguish parathyroid adenomas from subjacent thyroid tissue or lymph nodes.

Implications for patient care:

In patients with primary hyperparathyroidism, the described 4D DCE MRI technique provides additional means to accurately identify and characterize parathyroid adenomas without the need of radiation required for alternative imaging such as 4D CT or ^{99m}Tc-Sestamibi scan.



1 71-year-old woman with primary hyperparathyroidism (PHPT), who had left-sided parathyroidecotomy 3 years ago (note surgical clips on CT); now presenting with recurrent PHPT (PTH: 120 pg/mL, Ca^{++}: 10.6 mg/dL). **(1A)**: Tc-Sestamibi scan is negative. **(1B)**: 3-phase dynamic CT images including un-enhanced, arterial phase (45 sec) and venous phase (90 sec) images are shown, demonstrating a 5 mm arterial enhancing nodule (arrows) in the right tracheoesophegeal groove just posterior to the right thyroid lobe which shows washout on delayed phase. **(1C)**: Selected axial multiframe MR images from dynamic contrast-enhanced MR sequence are shown, demonstrating arterial enhancing PTA (arrows) that shows significant washout on delayed venous phase.

The main target of these cross-sectional studies is to exploit hypervascular nature of PTAs, a principle that was established in 1970s by the use of arterial catheter angiography [3, 4]. 4D CT has shown superior accuracy compared to scintigraphy [5] and has shown significant promise for identification and characterization of PTAs [6-8]. However there are two lingering problems associated with 4D CT:

1. Since continuous CT acquisition during the entire dynamic course of contrast through parathyroid glands is prohibited by the radiation dose, 4D CT provides only snapshots of contrast dynamic at certain time points (depending on the number of acquisitions). There are a variety of acquisition schemes using a combination of unenhanced and multiple post-contrast phases including 2 phases [9, 10], 2.5 phases [11, 12], 3 phases [8, 13] or 4 phases [14-17] with time interval ranging from 30 to 90 sec, each with strengths and limitations. However there is no consensus on the number and time-interval between CT acquisitions for an optimal 4D CT.
2. Radiation dose remains the main inherent disadvantage of CT. Despite using dose reduction techniques, effective radiation dose delivered by 4D CT ranges from 5.56 to 10.4 mSv [8, 18, 19] depending on the acquisition scheme used.

For these reasons, there remains a role for MRI to be explored in parathyroid imaging.

MRI technical considerations

MRI is an attractive alternative to both scintigraphy and 4D CT due to lack of radiation and has been used for the evaluation of PTAs with some success [20-22], though not with the same effectiveness as 4D CT. Fast image acquisition and high spatial resolution have long been significant advantages of CT and hence significant attention has been given to 4D CT for the detection of PTAs. Traditional technical limitations to localizing PTAs with MR have recently been addressed with modern MR technology. These include:

3. Limited spatial and temporal resolution for multiphase dynamic contrast enhanced (DCE) MR imaging over a large field-of-view required for parathyroid imaging. This limitation can be addressed by the use of fast imaging tools such as time-resolved angiography with stochastic trajectories (TWIST) [23] and improved parallel imaging technique such as Controlled Aliasing in Parallel Imaging Results in Higher Acceleration (CAIPIRINHA) [24].
4. Inhomogeneity of fat-suppression in the neck that is required for the detection of small parathyroid adenomas. Dixon fat-suppression technique [25] can significantly improve this shortcoming [26].

In our institution, using a modified MR sequence that incorporates Dixon fat saturation technique and fast imaging tools such as TWIST and CAIPIRINHA, we have established a 4D dynamic MRI protocol for the accurate identification and characterization of PTAs [27, 28].

How we do it?

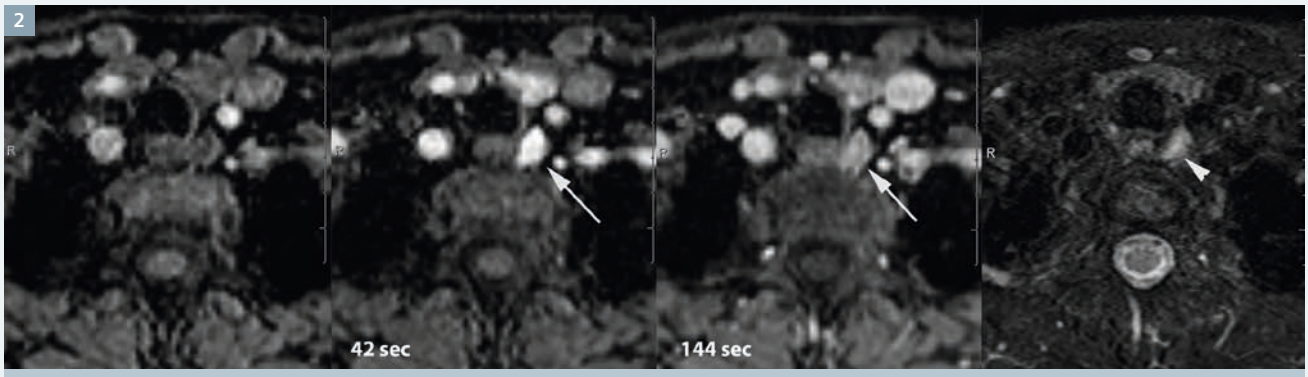
Image acquisition

In order to offset signal-to-noise (SNR) penalty associated with fast imaging tools such as TWIST and CAIPIRINHA, we use 3T MRI for our parathyroid imaging (MAGNETOM Skyra MRI system, Siemens Healthcare, Erlangen, Germany). A combination of 20-element head and neck coil is used for radiofrequency signal reception. Our MR imaging protocol includes axial T2w Fat sat, coronal STIR, coronal T1w pre contrast and 4D dynamic contrast-enhanced (DCE) sequences. 4D-DCE imaging is performed using a 3D VIBE (volumetric interpolated examination) sequence with the following parameters: (TR: 4.06 ms, 1st TE: 1.31 ms, 2nd TE: 2.54 ms, FA: 9°, matrix: 160 mm, FOV: 200 mm, 60 slices x 2 mm thick). The TWIST VIBE and Dixon fat/water separation are merged into one pulse sequence [29]. Bipolar readout gradients are used to produce two partial echoes at a first (TE: 1.31 ms) and a second (TE: 2.54 ms) echo time. Bipolar gradients allow for a shorter TR (4.6 ms) as well as less echo asymmetry. Integration of TWIST as an echo-sharing technique with sampling density of 33% results in x2 acceleration. In addition, CAIPIRINHA with accel-eration factor of 4 is incorporated, to increase net acceleration to a factor of 8.

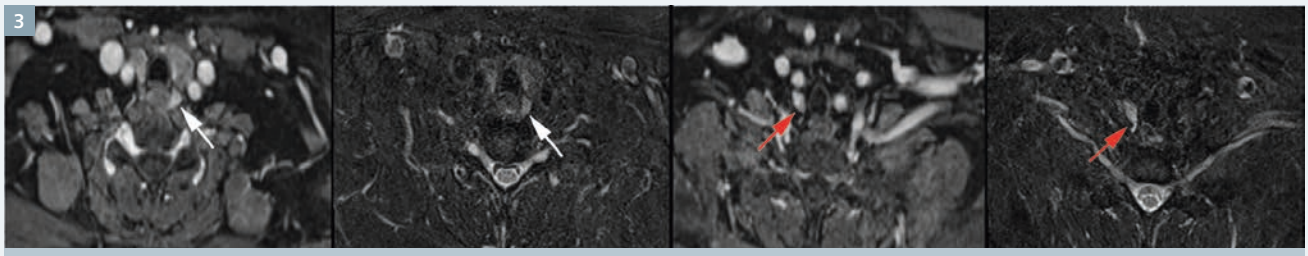
Using these combinations we acquire a 3D data set with voxel size of 1.3 x 1.3 x 2 mm^3 and temporal resolution of 6 seconds over a cranio-caudal coverage of 120 mm. This coverage is adequate to encompass from the inferior mandibular rim to the carina in most patients. We acquire 24 temporal frames for a total of 140 sec acquisition time. Four of these temporal frames (about 25 sec) are acquired before contrast injection to establish the baseline required for DCE analysis. A total of 0.1 mmol/kg of gadolinium is injected at 4 ml/sec.

Image analysis

Identification: For pre-operative localization, T2w fat-sat and 4D dynamic series are most scrutinized. The majority of PTAs are T2 hyperintense and should demonstrate early arterial enhancement (Fig. 2). Having high-spatial resolution voxels (1.3 x 1.3 x 2 mm^3) over a craniocaudal diameter of 12 cm (from mandibular rim to manubrium) allow for accurate examination of both native and ectopic adenomas as small as 3 mm. Having this data set every 6 seconds provides a true 4D capability for interrogation of contrast-enhancement cure of PTA over the course of image acquisition (144 sec). In contrast to 4D CT in which the number of acquisitions (ranging from 2 to 4) is limited by the prohibitive effect of radiation dose, using our 4D DCE MR, 24 time frames are acquired every 6 seconds to truly exploit the hypervascular nature of these lesions. This takes out the guesswork that is required in using 4D CT to capture the arterial phase. In our experience the majority of these PTAs are enhancing at the same time as, or one temporal frame before, the enhancement of thyroid bed (Fig. 2). The peak-enhancement of PTAs are often 6 to 12 seconds (1 to 2 temporal frames) before the peak-enhancement



2 55-year-old woman, with serum Ca^{++} of 12.2 and advanced osteoporosis as the result of her primary hyperparathyroidism (PHPT). Selected axial multiframe MR images from dynamic contrast-enhanced MR sequence are shown, demonstrating arterial enhancing PTA 42 seconds after contrast injection (arrows). This lesion is hyperintense on T2w images (arrowhead), which shows significant wash-out (40%) during later venous phase at 144 seconds post contrast injection.



3 68-year-old woman primary hyperparathyroidism (PHPT) who was found to have multiglandular disease involving all four parathyroid glands on pre-operative MRI, confirmed by surgical pathology. Selected axial images from 4D dynamic-contrast-enhanced series and corresponding T2w images show enlarged T2 hyperintense enhancing nodules of the left lower gland (white arrows) and right lower gland (red arrows) indicative of adenomatous enlargement seen with multiglandular hyperplasia. Note the excellent image quality of the 4D dynamic series that are obtained with voxel size of 1.3 x 1.3 x 2 mm^3 every 6 seconds. Also homogenous fat-saturation is achieved by using Dixon fat-saturation technique.

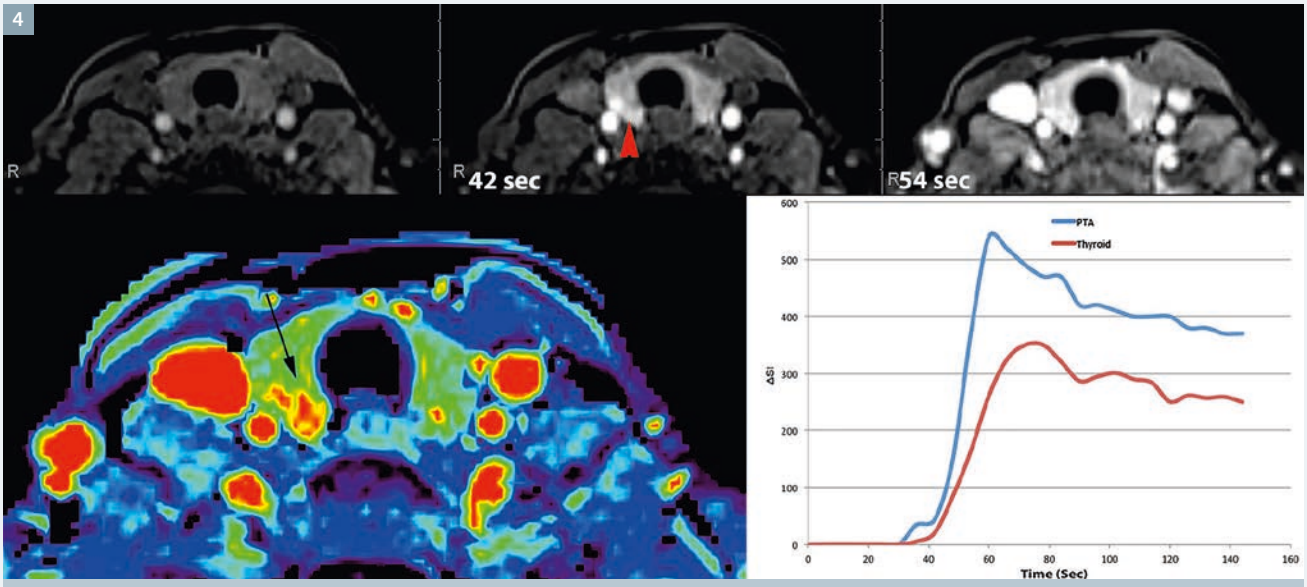
of the thyroid gland. In our experience, having a T2 hyperintense arterial enhancing nodule in the native parathyroid gland space or along the expected embryologic course of parathyroid glands such as tracheo-esophageal groove or superior mediastinum is extremely likely to be a PTA. Our preliminary data for pre-operative detection of PTA has shown a sensitivity close to 100% and positive-predictive value close to 1 for single PTA, while sensitivity drops to between 64 and 75% for multiglandular disease (Fig. 3) [28].

Characterization: The dynamic information inherent to this 4D DCE data set can be used to characterize PTA and differentiate them from PTA mimics such as cervical lymph nodes or subjacent thyroid tissue. This is particularly useful when you have a few PTA candidate lesions to narrow the differential diagnosis and provide the surgeon with the most likely lesion to be a true PTA [27] (Fig. 4).

The perfusion datasets are processed using commercially available FDA approved software (Olea Sphere, Olea Medical SAS, La Ciotat, France). Multiparametric quantitative perfusion parameters including peak enhancement, time-to-peak (TTP), wash-in and wash-out can be computed from the concentration-time curve. Multiparametric perfusion biomarkers can successfully exploit the hypervascular nature of PTAs, a feature that can be used to differentiate them from subjacent cervical lymph node and thyroid tissue. In our experience, TTP and wash-in, two characteristics of arterial enhancement, are significantly different in PTAs vs. cervical lymph nodes and thyroid tissue (Fig. 4). PTAs show significantly faster arterial enhancement with a mean TTP enhancement of 13 and 29 seconds earlier than thyroid tissue and normal cervical lymph node respectively. In addition the wash-in and wash-out values are significantly higher in PTAs. Using multiparametric MR perfusion and combined ROC analysis, the best overall model to distinguish PTA from cervical lymph node consists of a combination of TTP, wash-in and wash-out yielding an AUC of 0.96, superior to any individual or combination of other classifiers [27].

Conclusion

Dynamic 4D contrast-enhanced MRI with high temporal and spatial resolutions can now be obtained for pre-operative identification of PTAs, providing a strong alternative imaging modality to 4D CT without the need for radiation. Multiparametric MR perfusion can be used to exploit the hypervascular nature of PTAs to distinguish them from subjacent thyroid tissue or lymph nodes with high accuracy.



4 61-year-old woman with primary hyperparathyroidism (PTH: 118 pg/mL, Ca^{++}: 10.9 mg/dL) Note differential contrast enhancement of a small nodule in the posterior lobe of the right thyroid gland (red arrowhead) during the arterial phase 42 second after contrast injection and corresponding increased peak enhancement (arrow) on perfusion map in this surgically proven intrathyroid PTA. Note that on two imaging frames latter (54 sec), the nodule is less conspicuous due to increasing enhancement of the thyroid tissue. Contrast-time curve analysis from ROIs placed over the PTA and thyroid gland shows significantly faster and higher peak enhancement and higher wash-in and significant washout values in PTA in comparison to the thyroid gland.

Acknowledgement

I like to thank Kevin J. Johnson (Clinical Applications Scientist, Siemens Medical Solutions USA, Inc.) for his help and contribution for imaging protocol adjustment.

References

1 Heath H, 3rd, Hodgson SF, Kennedy MA. Primary hyperparathyroidism. Incidence, morbidity, and potential economic impact in a community. The New England journal of medicine. Jan 24 1980;302(4):189-193.
2 Chen H, Mack E, Starling JR. A comprehensive evaluation of perioperative adjuncts during minimally invasive parathyroidectomy: which is most reliable? Annals of surgery. Sep 2005; 242(3):375-380; discussion 380-373.
3 Doppman JL. Parathyroid localization: arteriography and venous sampling. Radiologic clinics of North America. Aug 1976;14(2):163-188.
4 Miller DL, Doppman JL. Parathyroid angiography. Annals of internal medicine. Dec 1987;107(6):942-943.
5 Mortenson MM, Evans DB, Lee JE, et al. Parathyroid exploration in the reoperative neck: improved preoperative localization with 4D-computed tomography. Journal of the American College of Surgeons. May 2008;206(5):888-895; discussion 895-886.
6 Day KM, Elsayed M, Beland MD, Monchik JM. The utility of 4-dimensional computed tomography for preoperative localization of primary hyperparathyroidism in patients not localized by sestamibi or ultrasonography. Surgery. Mar 2015;157(3):534-539.
7 Cham S, Sepahdari AR, Hall KE, Yeh MW, Harari A. Dynamic Parathyroid Computed Tomography (4DCT) Facilitates Reoperative Parathyroidectomy and Enables Cure of Missed Hyperplasia. Annals of surgical oncology. Feb 18 2015.
8 Kelly HR, Hamberg LM, Hunter GJ. 4D-CT for preoperative localization of abnormal parathyroid glands in patients with hyperparathyroidism: accuracy and ability to stratify patients by unilateral versus bilateral disease in surgery-naive and re-exploration patients. AJNR Am J Neuroradiol. Jan 2014;35(1):176-181.
9 Linda DD, Ng B, Rebello R, Harish S, Ioannidis G, Young JE. The utility of multidetector computed tomography for detection of parathyroid disease in the setting of primary hyperparathyroidism. Canadian Association of Radiologists journal = Journal l'Association canadienne des radiologistes. May 2012;63(2):100-108.
10 Gafton AR, Glastonbury CM, Eastwood JD, Hoang JK. Parathyroid lesions: characterization with dual-phase arterial and venous enhanced CT of the neck. AJNR Am J Neuroradiol. May 2012;33(5):949-952.
11 Kutler DI, Moquete R, Kazam E, Kuhel WI. Parathyroid localization with modified 4D-computed tomography and ultrasonography for patients with primary hyperparathyroidism. The Laryngoscope. Jun 2011;121(6):1219-1224.
12 Harari A, Zarnegar R, Lee J, Kazam E, Inabnet WB, 3rd, Fahey TJ, 3rd. Computed tomography can guide focused exploration in select patients with primary hyperparathyroidism and negative sestamibi scanning. Surgery. Dec 2008; 144(6):970-976; discussion 976-979.
13 Chazen JL, Gupta A, Dunning A, Phillips CD. Diagnostic accuracy of 4D-CT for parathyroid adenomas and hyperplasia. AJNR Am J Neuroradiol. Mar 2012; 33(3):429-433.
14 Starker LF, Mahajan A, Bjorklund P, Sze G, Udelsman R, Carling T. 4D parathyroid CT as the initial localization study for patients with de novo primary hyperparathyroidism. Annals of surgical oncology. Jun 2011;18(6):1723-1728.
15 Beland MD, Mayo-Smith WW, Grand DJ, Machan JT, Monchik JM. Dynamic MDCT for localization of occult parathyroid adenomas in 26 patients with primary hyperparathyroidism. AJR. American journal of roentgenology. Jan 2011;196(1):61-65.
16 Rodgers SE, Hunter GJ, Hamberg LM, et al. Improved preoperative planning for directed parathyroidectomy with 4-dimensional computed tomography. Surgery. Dec 2006;140(6):932-940; discussion 940-931.
17 Hunter GJ, Schellingerhout D, Vu TH, Perrier ND, Hamberg LM. Accuracy of four-dimensional CT for the localization of

abnormal parathyroid glands in patients with primary hyperparathyroidism. Radiology. Sep 2012;264(3):789-795.
18 Mahajan A, Starker LF, Ghita M, Udelsman R, Brink JA, Carling T. Parathyroid four-dimensional computed tomography: evaluation of radiation dose exposure during preoperative localization of parathyroid tumors in primary hyperparathyroidism. World journal of surgery. Jun 2012;36(6):1335-1339.
19 Madorin CA, Owen R, Coakley B, et al. Comparison of radiation exposure and cost between dynamic computed tomography and sestamibi scintigraphy for preoperative localization of parathyroid lesions. JAMA surgery. Jun 2013; 148(6):500-503.
20 Gotway MB, Reddy GP, Webb WR, Morita ET, Clark OH, Higgins CB. Comparison between MR imaging and 99mTc MIBI scintigraphy in the evaluation of recurrent of persistent hyperparathyroidism. Radiology. Mar 2001;218(3):783-790.
21 Lee VS, Spritzer CE, Coleman RE, Wilkinson RH, Jr., Coogan AC, Leight GS, Jr. The complementary roles of fast spin-echo MR imaging and double-phase 99m Tc-sestamibi scintigraphy for localization of hyperfunctioning parathyroid glands. AJR. American journal of roentgenology. Dec 1996;167(6):1555-1562.
22 Grayev AM, Gentry LR, Hartman MJ, Chen H, Perlman SB, Reeder SB. Presurgical localization of parathyroid adenomas with magnetic resonance imaging at 3.0 T: an adjunct method to supplement traditional imaging. Annals of surgical oncology. Mar 2012;19(3):981-989.
23 Song T, Laine AF, Chen Q, et al. Optimal k-space sampling for dynamic contrast-enhanced MRI with an application to MR renography. Magnetic resonance in medicine: official journal of the Society of Magnetic Resonance in Medicine / Society of Magnetic Resonance in Medicine. May 2009;61(5):1242-1248.
24 Breuer FA, Blaimer M, Heidemann RM, Mueller MF, Griswold MA, Jakob PM. Controlled aliasing in parallel imaging results in higher acceleration (CAIPIRINHA) for multi-slice imaging. Magnetic resonance in medicine : official journal of the Society of Magnetic Resonance in Medicine / Society of Magnetic Resonance in Medicine. Mar 2005;53(3):684-691.
25 Dixon WT. Simple proton spectroscopic imaging. Radiology. Oct 1984; 153(1):189-194.
26 Barger AV, DeLone DR, Bernstein MA, Welker KM. Fat signal suppression in head and neck imaging using fast spin-echo-IDEAL technique. AJNR Am J Neuroradiol. Jun-Jul 2006;27(6):1292-1294.
27 Nael K, Hur S.H, Bauer A, Khan R, Guerrero M. Multiparametric MR Perfusion in Characterization of Parathyroid Adenomas. Paper presented at: ASNR 53rd Annual Meeting; Apr 28, 2015; Chicago, IL.
28 Khan R Hur S.H, Guerrero M, Inampudi R, Nael K. 4D MRI at 3T to Preoperatively detect Single Parathyroid Adenoma and Multi-glandular Disease: A Feasibility Study. Paper presented at: ASNR 53rd Annual Meeting; Apr 28, 2015; Chicago, IL.
29 Le Y, Kroeker R, Kipfer HD, Lin C. Development and evaluation of TWIST Dixon for dynamic contrast-enhanced (DCE) MRI with improved acquisition efficiency and fat suppression. J Magn Reson Imaging. Aug 2012;36(2):483-491.



Contact

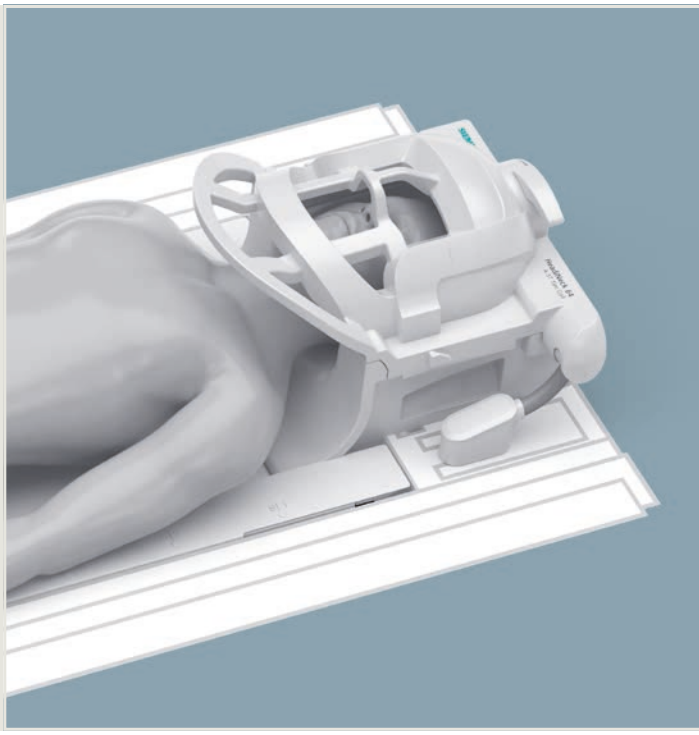
Kambiz Nael, M.D.
Assistant Professor of Radiology
Department of Radiology
Mount Sinai Hospital
1176 5th Avenue, Box 1235
New York, NY 10029, USA
kambiznael@gmail.com

"The Head/Neck 64 reveals previously hard-to-recognize, but pertinent, anatomical and disease-related details for a spectrum of pathologies within the brain, inner ear, orbits, skull base and neck, as well as the cervical spinal cord. This leads to improved insight into neuroanatomy relevant to an extended range of diseases and abnormalities. All this can be achieved, fortunately, at advanced speed and resolution."

Prof. Dr. med. Bernhard Schuknecht

Diagnostic, Vascular and Interventional Neuroradiology
Medizinisch Radiologisches Institut MRI Zurich
Klinik Bethanien, Zurich, Switzerland

The statements by Siemens' customers described herein are based on results that were achieved in the customer's unique setting. Since there is no 'typical' hospital and many variables exist (e.g., hospital size, case mix, level of IT adoption) there can be no guarantee that other customers will achieve the same results.



Reliable Imaging of Neurovasculature with Dot and T1 SPACE

Michel Paret[1]; Sylvain Doussin, Ph.D.[2]; Pr FG Barral, M.D.[3]; Dr C Boutet, M.D.[3]

[1] GIE IRMAS, Saint-Priest-en-Jarez, France
[2] Siemens Healthcare, Erlangen, Germany
[3] CHU Saint-Etienne, France

Research into the dissection of cervical-cerebral arteries is fundamental to clinical practice.

Any patient admitted to hospital with a suspected stroke should be given the benefit of an MRI. On the one hand this imaging technique allows the physician to diagnose whether the patient is suffering from a stroke, and on the other, it helps to establish the etiological diagnosis. It also affects the evolving prognosis of the patient because it allows the physician to decide on the best strategy for treating the patient. An MRI also allows the physician to detect early signs of vessel wall hematoma in a non-invasive way and to evaluate luminal abnormalities, if any.

Research into parietal hematoma

In the case of dissection of the cervical arteries, a morphological MRI is essential, since its aim is to look for a parietal hematoma.

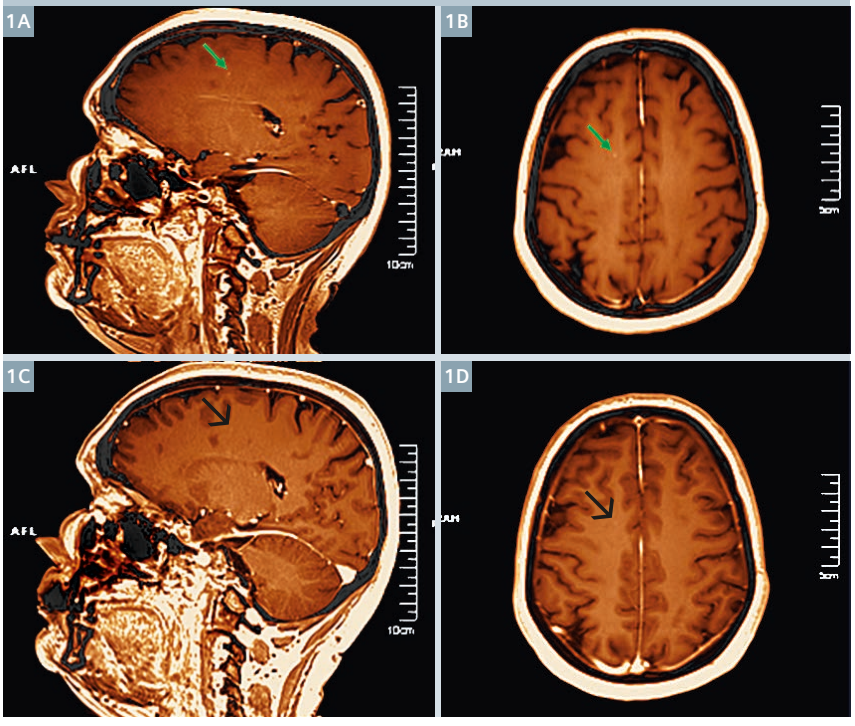
Different MRI techniques allow the physician to visualize this hematoma: in 2D or 3D, T1 or T2, with or without fat saturation. The flux, the voluntary or involuntary movements of the patient are the source of significant artifacts in this anatomical area.

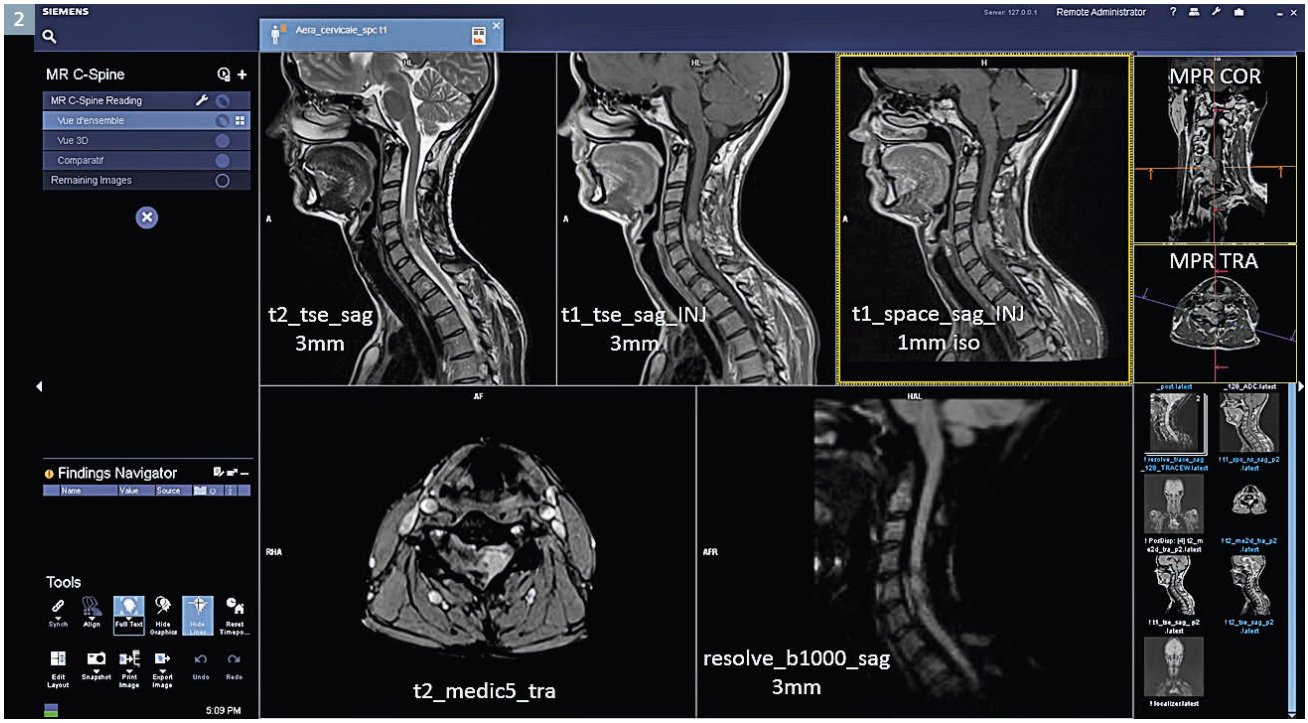
One protocol seems to be used for the most part: the 2D T1-weighted fat-saturated (FS) spin echo (SE) sequence with physiological synchronization of the pulse, carried out in a perpendicular direction on the vascular flow. At the sub-acute stage (about J3-J5), a rather eccentric hypersignal in the shape of a crescent surrounds the vessel lumen (presence of methemoglobin). At the acute stage, the wall appears thickened as an isosignal.

Cuvinciuc et al. [1] expressed interest in a 3D T1-weighted SPACE (Sampling Perfection with Application optimized Contrasts using different flip angle Evolution) sequence in contrast to a 2D T1w SE FS sequence. This 3D protocol, coupled with a fat saturation of the SPAIR type (SPectral Attenuated Inversion Recovery) and a Dark Blood technique offers robust data collection and good diagnostic sensitivity, even at the acute stage under difficult working conditions (a patient who does not cooperate).

This approach has been shown to have a higher sensitivity relative to the post-contrast T1 MPRAGE for the detection of brain lesions in multiple sclerosis (Fig. 1) [4, 5]. It also has a reliable role in the detection of tumors in the cervical region with its flexibility to enable reformatting in any plane (Fig. 2).

1 Multiple sclerosis brain lesions, color lookup table heart 16 bit.
(1A) t1_space_sag_INJ (green arrow),
(1B) t1_space_MPR TRA_INJ (green arrow),
(1C) t1_MPRAGE_sag_INJ 5' (black arrow),
(1D) t1_MPRAGE_MPR TRA_INJ 5' (black arrow).



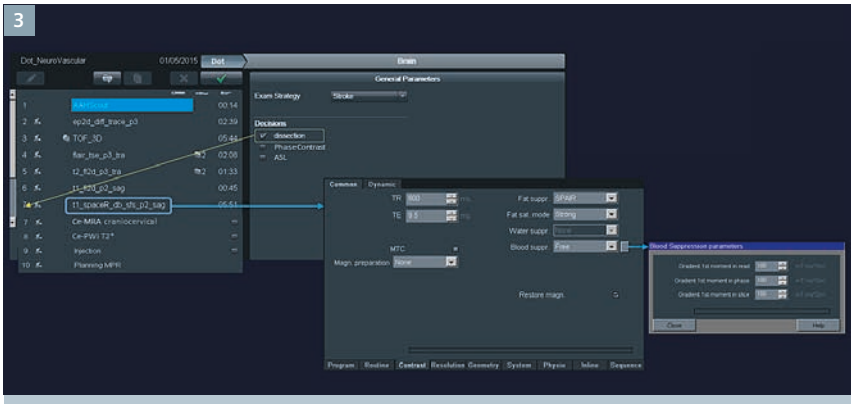


Acquisition protocol

Our doctors are often required to carry out these examinations in emergency cases. At our Regional Stroke Center, two MR systems are capable of collecting this type of data, a MAGNETOM Aera 1.5T and a MAGNETOM Spectra 3T.

In order to provide a service that can meet current demand, we have developed and programmed our own Dot engine from the standard Brain Dot Engine. Neurovascular imaging works in an identical way on the two systems so that we can offer a standardized treatment of patients. This Dot Engine has the same design and notably includes a 'dissection' decision (3D T1 SPACE Spair_db) (Fig. 3). The acquisition parameters are, however, specific to the individual system (contrast parameters, spatial and temporal resolution, etc.) (Fig. 4).

The Dot Engine complies with the official guidelines and enables all our 30 technologists, regardless of their level of experience, to carry out examinations without any difficulty and allows all our 70 radiologists to answer questions posed by our clinicians. For example, the slice positioning is set automatically using the AutoAlign Head>Brain function, the calculation of perfusion maps is automatic using Local AIF (arterial input function).



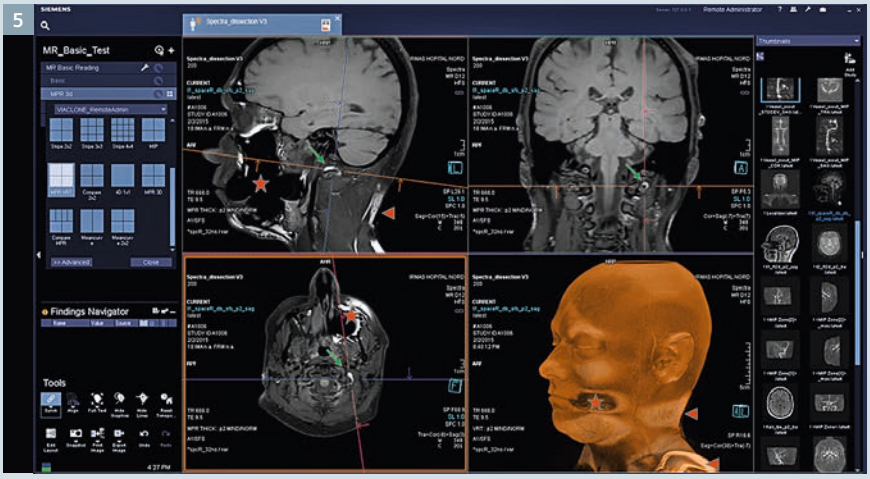
3 DotGO workflow for MAGNETOM Aera and MAGNETOM Spectra.

4 **Parameters 1.5T & 3T**

MR system	Slices per Slab	FOV (mm)	Voxel size	Fat suppr. (Contrast)	Blood suppr. (Contrast)	TR/TE (ms)	TA
Aera 1.5T	192 Excitation > Non-sel	256	1.0x1.0x1.0	SPAIR	Free 100 mT ms^2/m (In read, phase, slice)	550/7.2	5:34
Spectra 3T	192 Excitation > Non-sel	256	1.0x1.0x1.0	SPAIR	Free 100 mT ms^2/m (In read, phase, slice)	600/9.5 Restore pulse	5:51

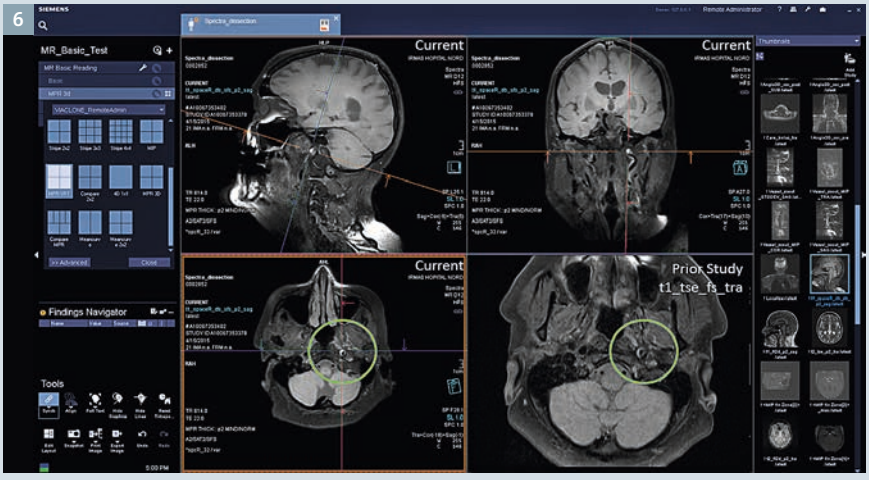
4 T1_space 3D dissection in sagittal orientation.

These examinations are visualized under *syngo*.via VB10A under a basic workflow with specific reading stages.



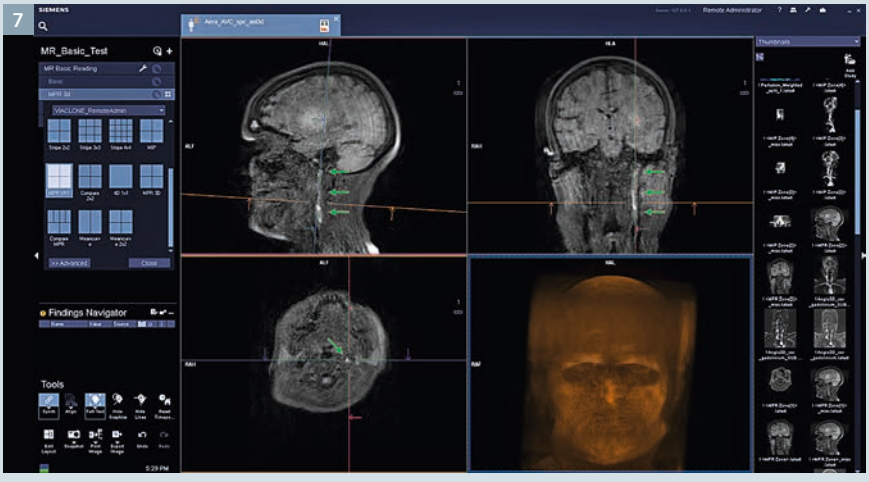
Case 1

45-year-old patient with a previous history of dissection left V3 segment (Fig. 5). Binocular diplopia with possible damage to right VI and of III on both sides. The T1 hyperintense signal of the left vertebral artery (green arrow) indicates a parietal hematoma at the sub-acute stage of dissection. Reliable acquisition protocol despite the presence of metallic dental materials (red star) and impaired spectral fat saturation (red arrow).



Case 2

80-year-old patient with a previous history of dissection of the left internal carotid (Fig. 6). Examination of the dissection. Prior study: carried out a classic T1w Spin Echo FS sequence with physiological synchronization of the pulse. Current study: carried out a T1-3D-space-SFS-db sequence without physiological synchronization. The SPACE protocol makes it easier to interpret the results because it is possible to evaluate the dissection in 3 dimensions with improved visualization of the dissection of the sub-petrous portion of the internal carotid (green circle).



Case 3

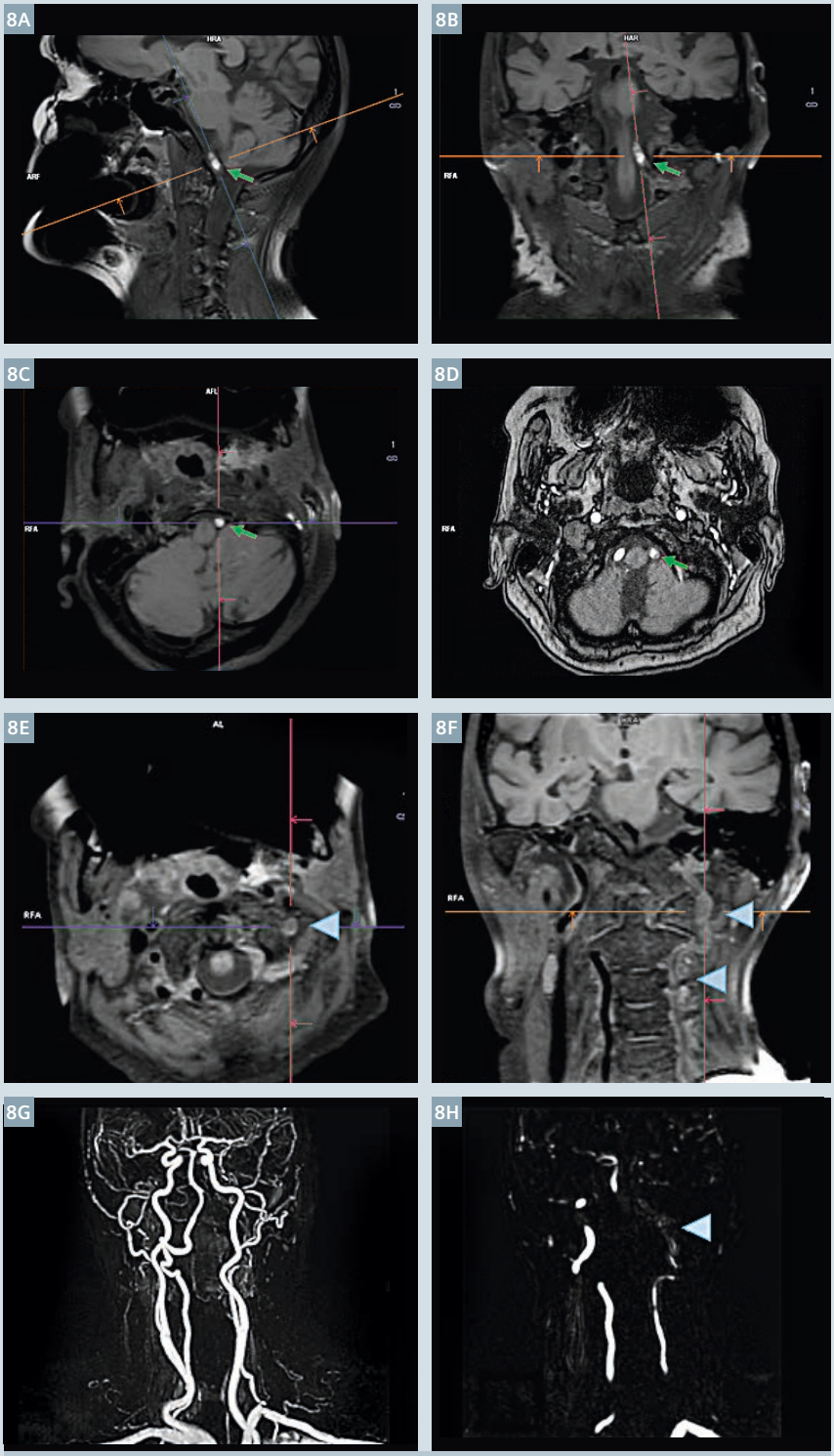
60-year-old patient, MRI examination of stroke of left middle cerebral artery (Fig. 7). The patient is not able to keep completely still. Despite patient motion, the T1-3D-space-SFS-db sequence demonstrates its capability and allows the physician to detect a significant T1 hyperintense signal of a sub-acute thrombus which is responsible for causing an occlusion of the left internal carotid artery.

Case 4

70-year-old patient, undergoing MRI examination of vertebral dissection in the course of a clinical examination presenting, among other things, an incomplete Wallenberg syndrome on the left side (Fig. 8). View of thrombosis of the left vertebral artery on the CT.

The CE-MRA sequence shows a left vertebral artery that is not opaque. On the T1-3D-space-SFS-db sequence a thrombosis is visible (Figs. 8A–C green arrow).

The MinIP Thin reconstruction (8H) shows a circulating thread on one portion with an image of very recent thrombosis as an isosignal (characteristic of the acute stage of a parietal hematoma) on the T1-3D-space-SFS-db sequence (blue arrow).



8 **(8A–C)** t1_space_sfs_db_sag (green arrow), slice 1
(8D) TOF (green arrow), slice 1
(8E–F) t1_space_sfs_db_sag (blue arrow), slice 2
(8G) Contrast-enhanced MR Angiography
(8H) MinIP Thin (blue arrow)

Conclusion

With its many benefits, (high reliability in the presence of metallic implants, 3D isotropic reconstruction, its high level of sensitivity, anatomical coverage, etc.), the SPACE T1 sequence has become an essential part of our hematoma research and in our evaluation of arterial wall pathologies.

The implementation and integration of a Dot strategy for neurovascular examinations enables a high degree of reproducibility amongst our MRI technologists within and between our sites. This, in turn, improves our efficiency in the treatment of our patients where time is a precious entity.

Acknowledgements

We would like to thank the team of stakeholders at GIE IRMAS (radiologists, technologists, doctors), and in particular our thanks go to Christophe Barles (MR Product Support Engineer Siemens Healthcare France) for the time he spent passing on his knowledge (technical, application, marketing etc.) on site, and at the Siemens France Users Clubs, which enabled us to share the same passion he has for MRI!

References

1 Victor Cuvinciuc, Magalie Viallon, Isabelle Momjian-Mayor, Roman Sztajzel, Vitor Mendes Pereira, Karl-Olof Lovblad, Maria Isabel Vargas: 3D fat-saturated T1 SPACE sequence for the diagnosis of cervical artery dissection. Neuroradiology (2013) 55:595–602.

2 Magalie Viallon, Victor Cuvinciuc, Benedicte Delattre, Laura Merlini, Isabelle Barnaure Nachbar, Seema Toso-Patel, Minerva Becker, Karl-Olof Lovblad, Sven Haller: State-of-the-art MRI techniques in neuroradiology: principles, pitfalls, and clinical applications. Neuroradiology (2015) 57:441-467.

3 Reichert M, Morelli JN, Runge VM, Tao A, von Ritschl R, von Ritschl A, Padua A, Dix JE, Marra MJ, Schoenberg SO, Attenberger UI: Contrast-enhanced 3-dimensional SPACE versus MP-RAGE for the detection of brain metastases: considerations with a 32-channel head coil. Invest Radiol. 2013 Jan;48(1):55-60.

4 B. Jeevanandham: To compare post contrast 3D T2 FLAIR, T1-SPACE and MP-RAGE sequences to select the ideal sequence for leptomeningeal abnormalities at 3 T MRI. ECR 2015.

5 Franz A. Fellner, Christine M. Fellner, Rene Chapot, Kaveh Akbari: MR Visualization of Spinal Dural Arterio-Venous Fistula Using T2-Weighted 3D SPACE – A Spin-Echo Technique. J. Biomedical Science and Engineering, 2015, 8, 327-332.

6 M. Edjlali, P. Roca, C. Rabrait, O. Naggara, and C. Oppenheim: 3D Fast Spin-Echo T1 Black-Blood Imaging for the Diagnosis of Cervical Artery Dissection. AJNR A3261 (oct-2012) 10.3174.

7 Chul-Ho Sohn, JiHoon Kim, Jaeseok Park, Kee-Hyun Chang, Seunghong Choi, and InSeong Kim: Contrast-Enhanced 3D Brain Black-Blood Imaging for Detection of Intracranial Arterial Unstable Plaque in Acute Ischemic Stroke Patients. ISMRM 2012.

8 Park J, et al. MRM 2007; 58:982.

9 Ling Zhanga, Eugene G. Kholmovski, Junyu Guob, Seong-Eun Kim Choi, Glen R. Morrell, and Dennis L. Parker: HASTE Sequence with Parallel Acquisition and T2 Decay Compensation: Application to Carotid Artery Imaging. Magn Reson Imaging. 2009 January; 27(1): 13–22.

10 Mara M. Kunst, Pamela W. Schaefer: Ischemic Stroke. Radiol Clin N Am 49 (2011) 1-26. enhanced MRI for screening patients at risk for malignant ventricular tachyarrhythmias. J Cardiovasc Magn Reson, 2004. 6(1): p. 84.

Contact

Michel Paret
MR Technologist
GIE IRMAS
110 avenue Albert Raimond
42270 Saint-Priest-en-Jarez, France
mparet@irmas.fr



Did you know that ...

" With DotGO it's going to be so much easier and quicker to build protocols on the fly and not interfere with taking table time away from the patients. Previously, to build a protocol from scratch would take 20 minutes. With DotGO, I was able to create a protocol in 45 seconds. Having consistency in our MRI protocols and examinations is extremely important. Our reputation is to provide the highest quality MRI examinations for our patients and referring physicians. DotGO will help us to do that."

Anthony Pavone

Zwanger-Pesiri Radiology
(New York, USA)

The statements by Siemens' customers described herein are based on results that were achieved in the customer's unique setting. Since there is no 'typical' hospital and many variables exist (e.g., hospital size, case mix, level of IT adoption) there can be no guarantee that other customers will achieve the same results.



More clinical articles, tips & tricks, talks on Siemens unique Dot engines at

www.siemens.com/magnetom-world-dot

How to get Inline Reconstructed Rotating MIPs with a 3D SPACE Measurement

Thomas Illigen

Application Specialist MR, Siemens Healthcare, Mannheim, Germany

In the Siemens software versions *syngo* MR E11 and D13, a measurement within the Abdomen Dot Engine offers a unique option to obtain inline reconstructed rotating maximum intensity projections (MIPs). Those are primarily intended to be generated for the high-resolution MR cholangiopancreatography (MRCP) visualization by a respiratory triggered 3D SPACE measurement.

Nevertheless it is possible to use this functionality outside the Abdomen Dot Engine and adapt it to other 3D SPACE protocols. In this article we will describe how to use this tool for lumbar spine myelography; however, you can do this for every 3D SPACE.

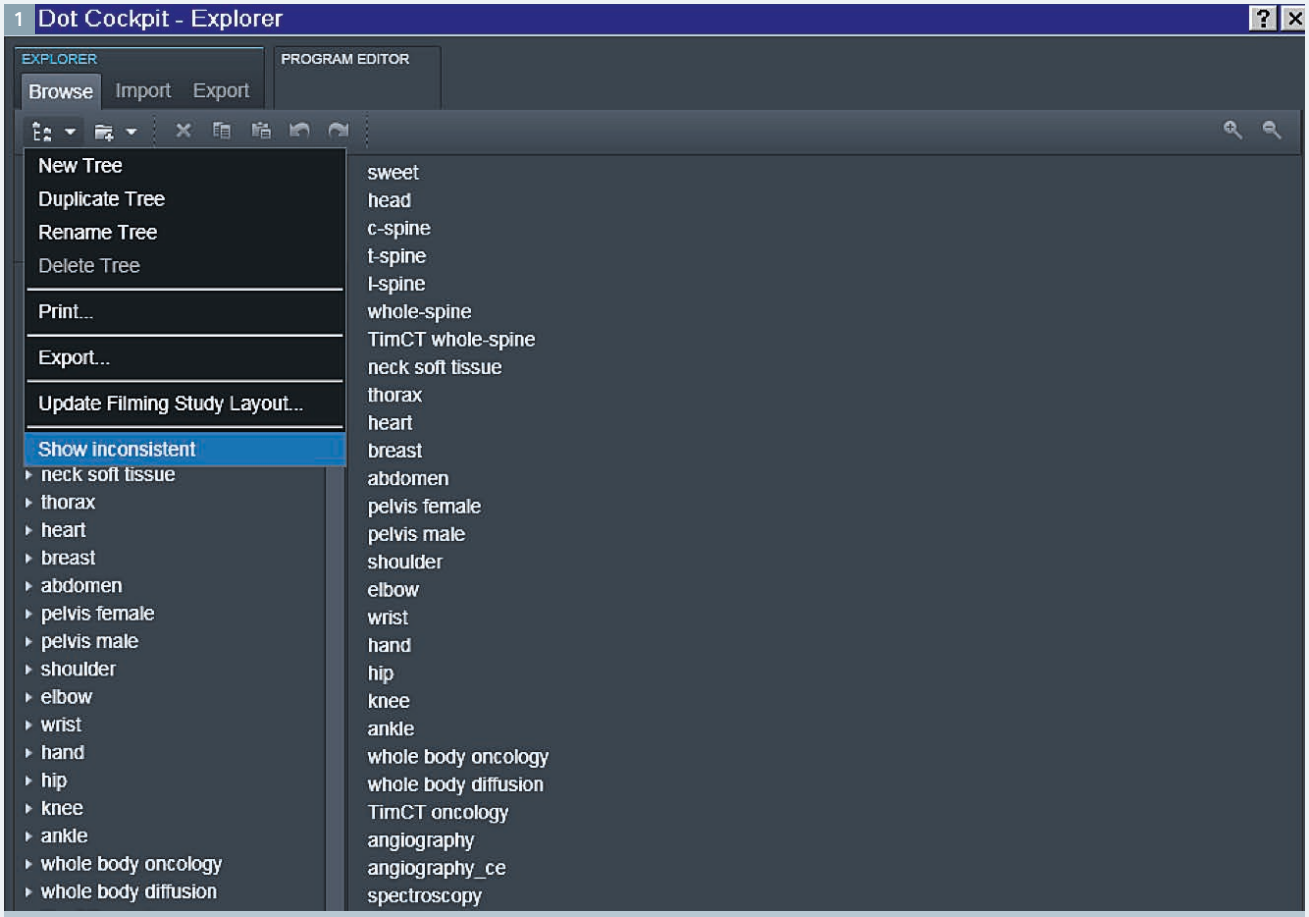
The functionality of the inline MIP reconstruction is linked to the GenericViews Dot AddIn for the said MRCP measurement. You will find it in the Abdomen Dot Engine under the name "t2_space_cor_trig".

Even if your MR system does not have the license for the Abdomen Dot Engine, you can still use it, it works independently from a Dot environment: only the AddIn is essential and must be kept.

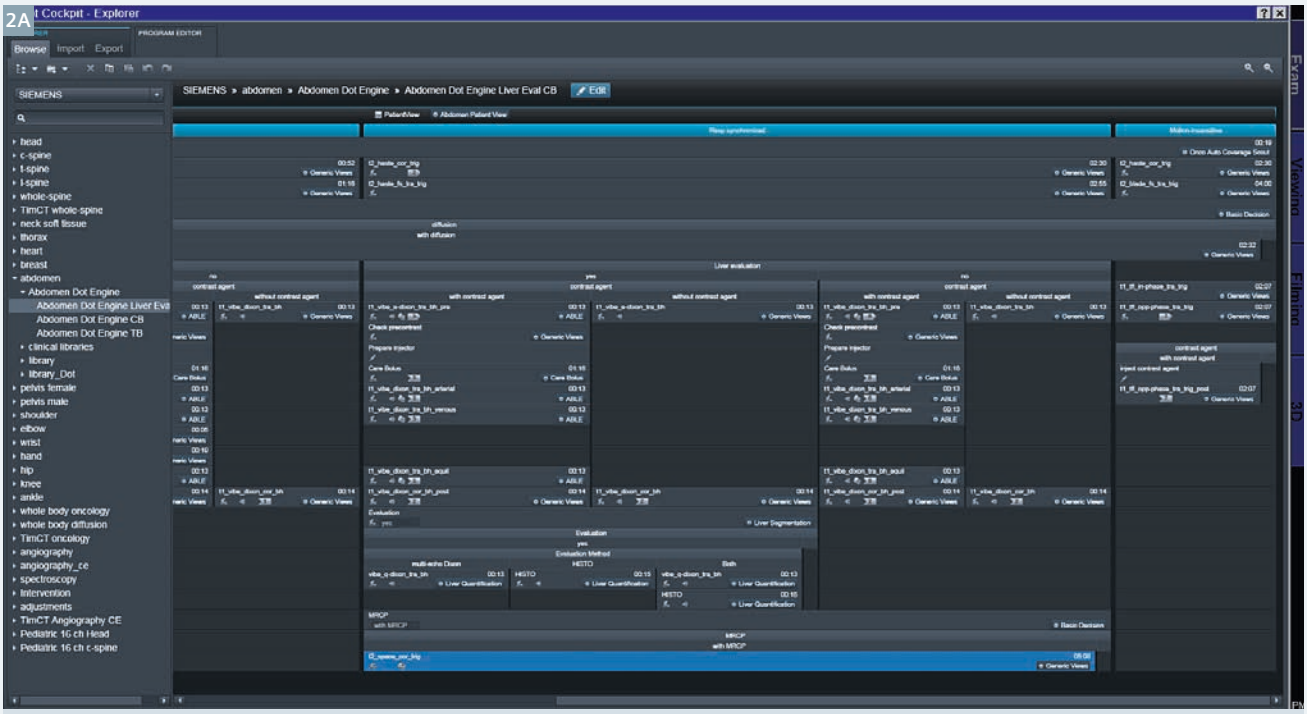
If you do not have a license for the Abdomen Dot Engine, you need to get access to unlicensed programs and protocols first. Open the Dot Cockpit, click on "Organize tree" and enable "Show inconsistent" (Fig. 1).

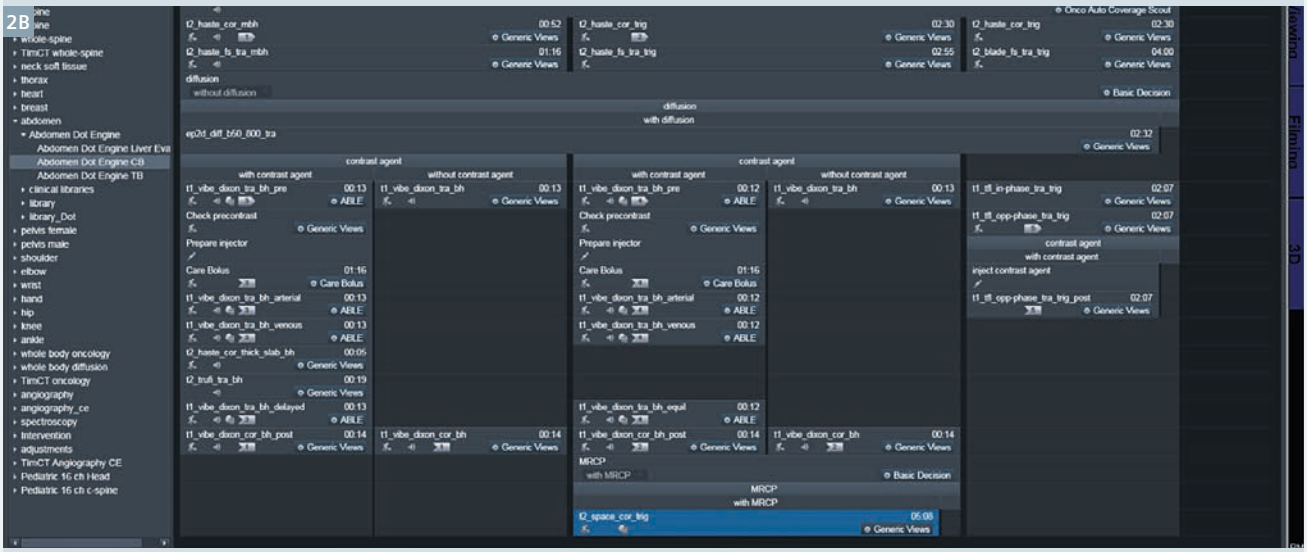
Select the Siemens tree, go to folder "abdomen" > "Abdomen Dot Engine".

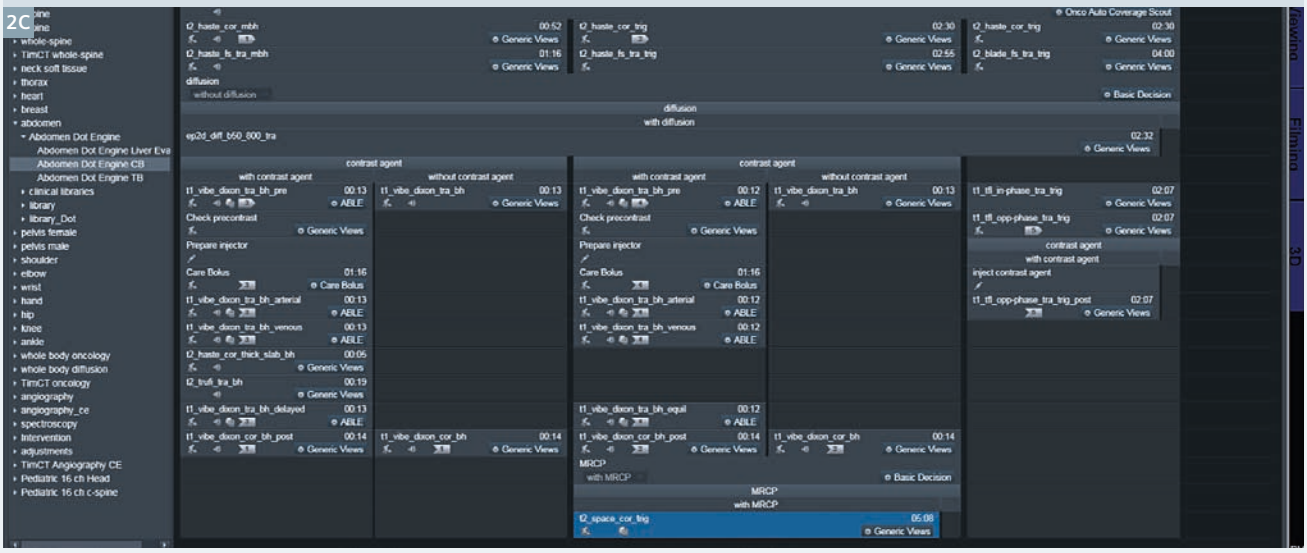
For all the Siemens Abdomen Dot Engines, the protocol can be found in the Dot strategy "Resp synchronized". It is in each case the bottommost protocol (Figs. 2A, B, C).

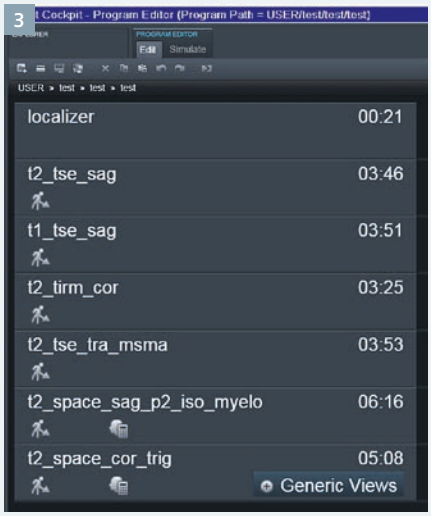


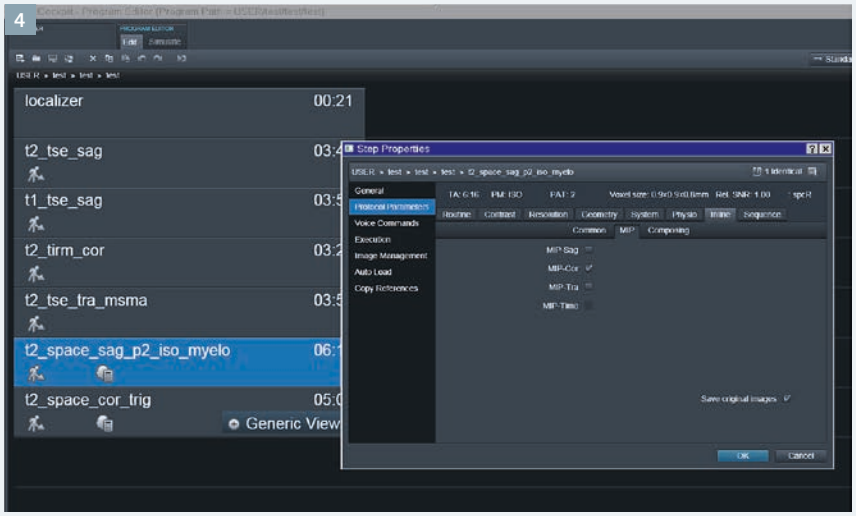
1 Open the Dot Cockpit, click on "Organize tree" and enable "Show inconsistent".


2A
t Cockpit - Explorer
Browse
Import
Export
SIEMENS
SIEMENS » abdomen » Abdomen Dot Engine » Abdomen Dot Engine Liver Eval CB
Edit
Abdomen Dot Engine Liver Eva
Abdomen Dot Engine CB
Abdomen Dot Engine TB


2B
Abdomen Dot Engine Liver Eva
Abdomen Dot Engine CB
Abdomen Dot Engine TB


2C
Abdomen Dot Engine Liver Eva
Abdomen Dot Engine CB
Abdomen Dot Engine TB





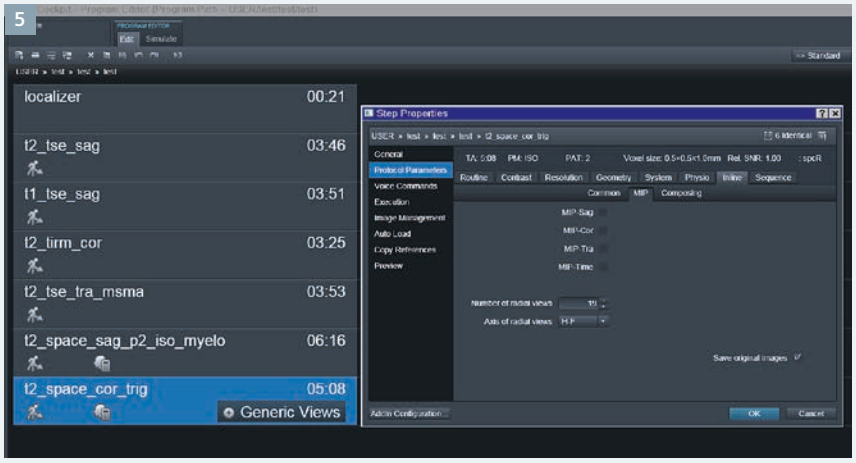
Copy the protocol "t2_space_cor_trig" to its designated place in the user tree (Fig. 3).

To use the inline MIP reconstruction with another 3D SPACE protocol, first set this protocol up, as it should be acquired. In this example, the default "t2_space_sag_p2_iso_myelo" was taken as pattern.

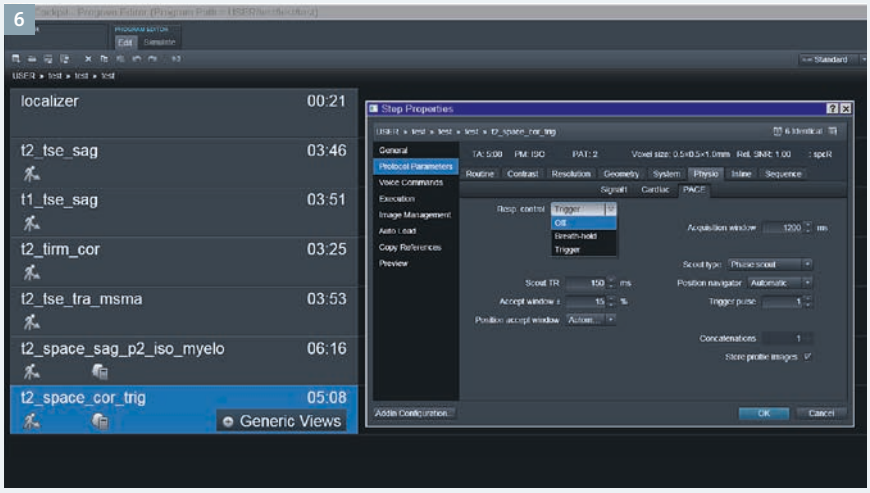
The standard protocol for lumbar myelography "t2_space_sag_p2_iso_ myelo" shows inline functionality "MIP-cor" (Fig. 4).

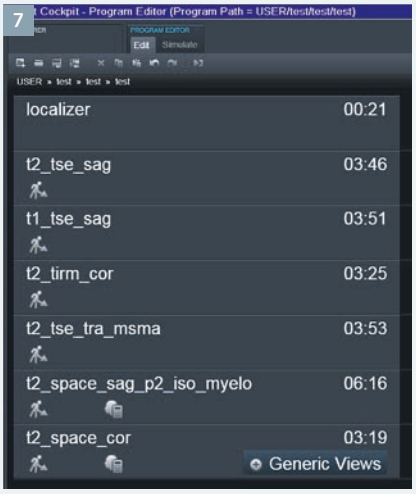
The MRCP-protocol "t2_space_cor_trig" shows inline functionality with radial views and the option to select a reconstruction axis of the radial views (Fig. 5).

The inline reconstruction is available in the protocol parameters. Nevertheless, you should not delete the Generic Views AddIn since this is essential, although it might not be directly obvious.



As a next step, you should ensure that the intended MRCP protocol has a respiratory trigger. For myelography a trigger is not intended, so the trigger should be set to "Off" (Fig. 6);





this will result in scan time reduction (Fig. 7).

Now you have to assimilate the protocol parameters.

Do NOT use the copy reference "Everything", because this will destroy the linked AddIn! Simply copying the AddIn is insufficient, too, since the inline functionality is implemented in the protocol parameters. You should therefore work step-by-step, starting with the copy reference "Measurement parameters" with the myelography protocol as origin and the former MRCP protocol as target.

"Copy phase encoding direction" should also be checked (Fig. 8).

If a pop-up window appears showing copy reference conflicts, just accept them.

The copy reference "Measurement parameters" performs changes according the geometry and resolution including field-of-view (FOV) read, FOV phase, slice thickness, orientation, position, phase- and slice oversampling, the number of slices per slab, base and phase resolution.

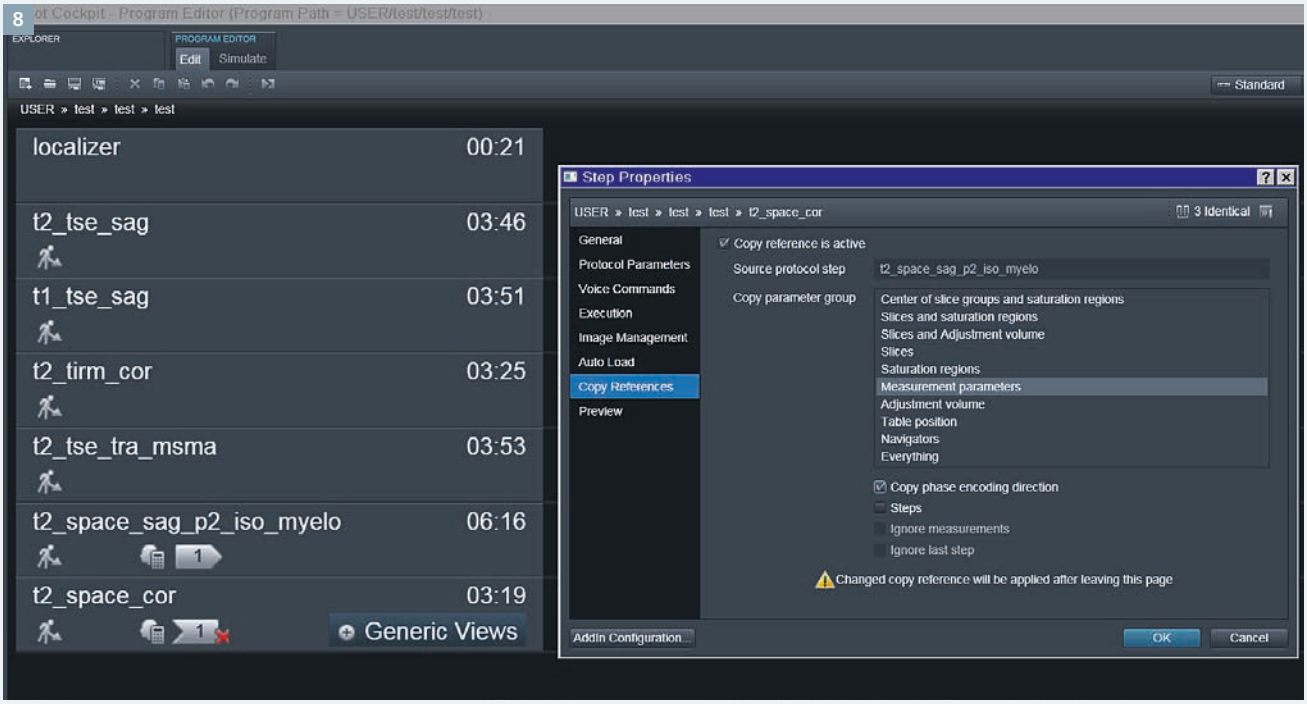
However, parameters affecting the contrast, such as TR, TE, number of averages, flip-angle, partial Fourier, fat-sat pulse, turbo-factor and bandwidth are not adapted, and these have to be changed manually.

Eventually the protocol might be renamed.

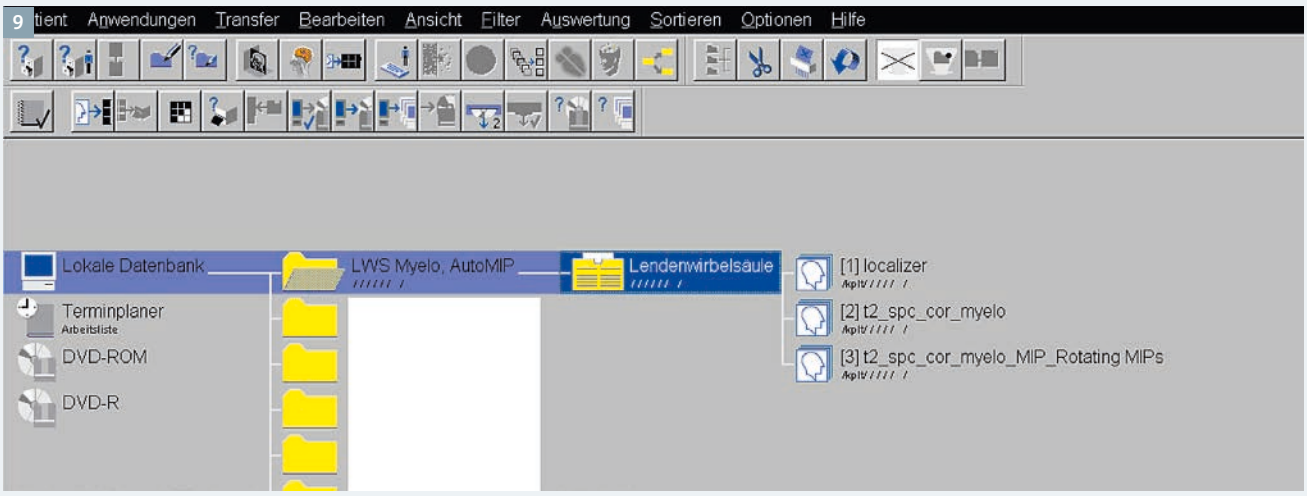
If you want to acquire coronal instead of sagittal, that's no problem, because the SPACE works fine in coronal orientation, too.

Having acquired the measurement, the inline calculated MIPs can be identified in the patient list by the measurement's name suffix "_Rotating MIPs" (Fig. 9).

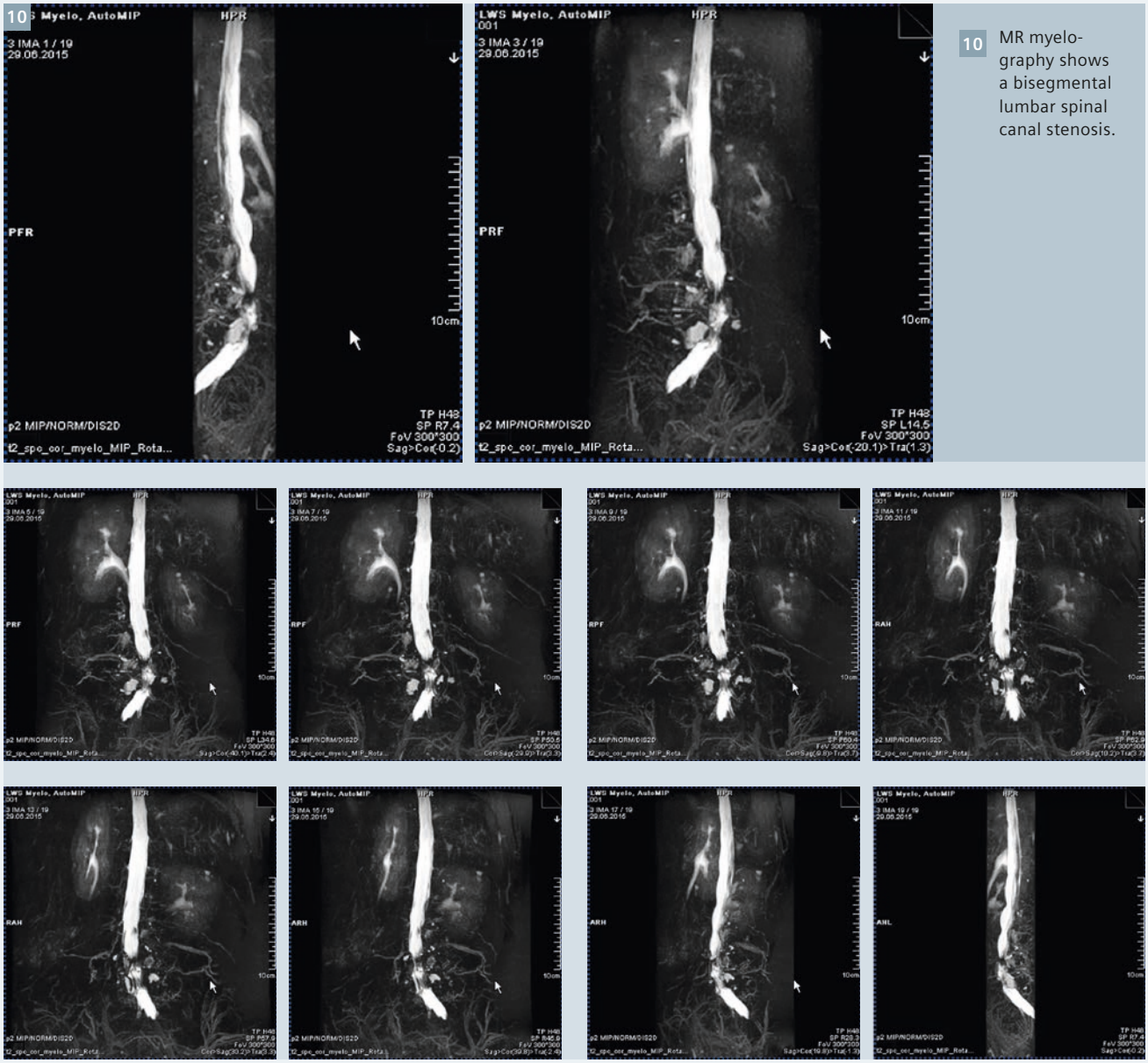
8



9



The following image collection shows inline reconstructed rotating MIPs (every second image). These images are courtesy of the Radiological Institute Hohenzollernstraße in Koblenz, Germany, where the inline reconstructed MIPs are used for lumbar myelography in clinical routine.



10 MR myelography shows a bisegmental lumbar spinal canal stenosis.



Contact

Thomas Illigen
Application Specialist MR
Siemens Healthcare GmbH
Customer Solutions, Region Germany, Central Region
HC CX DE MTE CS
Dynamostr. 4
68165 Mannheim
Germany
Phone: +49 174 2011898
thomas.illigen@siemens.com

Pediatric Pathologies that have Leukocoria as Presenting Sign: the Podium

Paolo Galluzzi; Sara Leonini; Alfonso Cerase; Alessandro Rossi

Neuroimaging and Neurointerventional Unit (NINT), Azienda Ospedaliera e Universitaria Senese, Siena, Italy

Abstract

Leukocoria is a condition in which the normal red reflex of the retina is replaced by a yellowish or grayish white color. Retinoblastoma is the most common cause of leuko-coria in the pediatric age, followed by persistent fetal vasculature and Coats' disease. Clinical and imaging signs and differential diagnosis features of these pathologies are evaluated.

Introduction

Leukocoria or cat's eye is a white, pink-white, or yellow-white reflex resulting from any white or light-colored intraocular retrolental abnormality (mass, membrane, retinal detachment, or retinal storage disease), that reflects incident light back through the pupil towards the observer (Fig. 1). Leukocoria is the most common presenting sign of retinoblastoma (RB), the highly malignant primary retinal cancer which is the most common intraocular tumor of childhood. Intraocular lesions presenting with leukocoria are usually diagnosed at ophthalmoscopy, however the detection and clinical differentiation between RB and other benign simulating lesions (so-called 'pseudoretinoblastoma') may be difficult [1-6]. Imaging therefore may play a pivotal role in the differential diagnosis.

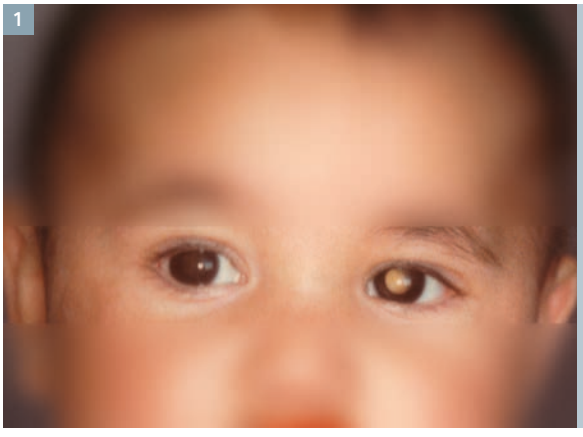
In addition to RB, which is the most frequent cause of leukocoria in children, the second and third most common ones are persistent fetal vasculature (PFV) and Coats' disease (CD), respectively.

Methods

The routine imaging protocol of children[1] with leukocoria in our institution takes about one hour. Our patients with leukocoria are studied in a 1.5T system (MAGNETOM Avanto, Siemens Healthcare, Erlangen, Germany) with a head coil and a surface coil for each eye (diameter 4 cm); our protocol includes pre-contrast T1, T2-weighted (transaxial) thin-slice (≤ 2 mm) imaging.

The measured voxel of the T1w sequences acquired with the orbit coils are 0.43 x 0.3 x 2 mm (TR 312 ms, TE 15 ms, FOV 75, base/phase resolution 256/80). Turbo spin echo (TSE) 3D T2-weighted images (TR 750 ms, TE 112 ms, FOV 170, base/phase resolution 256/100, slice thickness 0.7 mm) and have 0.7 x 0.7 x 0.7 isotropic voxels. Gradient-echo (GRE) 3D T2-weighted steady-state free precession sequences (TR 47 ms, TE 20 ms, FOV 180, base/phase resolution 384/93, slice thickness 1 mm) have voxels of 0.6 x 0.5 x 1 mm. Recently, GRE 3D T2-weighted imaging has been replaced by susceptibility-weighted imaging with the same slice thickness and with voxels of 0.7 x 0.5 x 1 mm (TR 46, TE 38, FOV 100, base/phase resolution 192/75). The study of the orbits also includes diffusion-weighted sequences (DWI) (TR 3200, TE 100, FOV 100, base/phase resolution 192/100, voxel size 1.2 x 1.2 x 2.6 mm), and post-contrast T1-weighted (sagittal oblique and transaxial, gadoteric acid (Dotarem, Guerbet, France)) without fat-saturation. 1 mm-thick fat-suppressed post-contrast T1-weighted Volumetric Interpolated Breathhold Examination (VIBE) images (TR 9.14, TE 4.39, FOV 75 mm, 2 averages, base/phase resolution 256/75, voxel size 0.4 x 0.3 x 1 mm) are also used to obtain volumetric imaging and to better evaluate orbital spread of the tumor. Dynamic Contrast Enhanced (DCE) images are also performed to evaluate contrast enhancement degree in early, medium and late phases. Imaging of the head includes pre-contrast sagittal T1 and T2-weighted, transaxial PD and T2-weighted (slice thickness ≤ 4 mm) and post-contrast 3D magnetization prepared rapid gradient echo (MPRAGE) sequences (TR 2070 ms,

[1] MR scanning has not been established as safe for imaging fetuses and infants under two years of age. The responsible physician must evaluate the benefit of the MRI examination in comparison to other imaging procedures.



1 Left eye leukocoria.

TE 3.52 ms, ST 1 mm, FOV 109 mm, base/phase resolution 384/75) of the whole brain, performed using the standard head coil.

All children are deeply sedated for the examinations to reduce motion artifacts.

Retinoblastoma

RB is a highly malignant primary retinal tumor arising from neuroectodermal cells (nuclear layer of the retina). Though rare, it is the most common intraocular tumor of childhood. The incidence of RB varies from 1 : 17,000 to 1 : 24,000 live births [7]. Most patients present before four years of age (mean age 24 months for unilateral and 12 months for bilateral cases) [8], but 30 to 40% of patients will have a germline mutation in the RB1 gene and present at an earlier age with multifocal, bilateral disease [9]. Patients with the genetic form of RB are at an increased risk for developing primary intracranial neuroectodermal tumors in the pineal or suprasellar region usually with a dismal prognosis, a condition termed 'trilateral retinoblastoma' [10-13].

RB was classified into five groups by Reese and Ellsworth [14] to provide a prognosis for local cure and vision of eyes treated with external beam radiotherapy (EBT). More recently, an international classification for intraocular RB (ABC) has been created for the purpose of clinical trials using chemotherapy [15] (Tables 1, 2).

The growth pattern of RB may be endophytic, from the retina into the vitreous, exophytic into the subretinal space and mixed, whereas the diffuse pattern with flat infiltration along the retina (so-called diffuse infiltrative retinoblastoma or DIRB) is uncommon [16].

It is not uncommon to observe an RB growing in an eye that is smaller than normal, but its occurrence in micro-ophthalmic eyes is extremely rare, with the exception of cases with a phthisis bulbi.

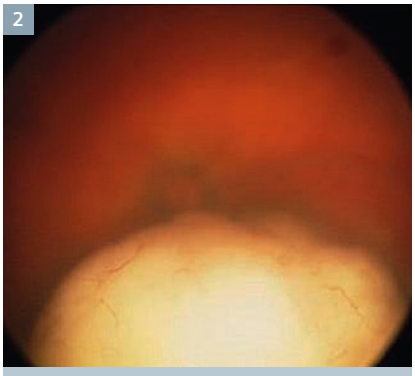
Diagnosis of RB is usually made by ophthalmoscopy (under general anesthesia). The more usual opthtalmoscopic appearance of RB is one or more pink-whitish tumor/s projecting

Table 1: Reese-Ellsworth Classification

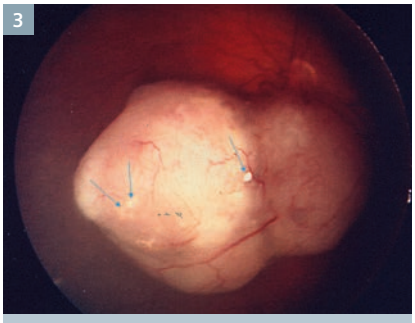
Group 1 (very favorable for saving [or preserving] the eye)
1A: one tumor, smaller than 4 disc diameters (DD), at or behind the equator
1B: multiple tumors smaller than 4 DD, all at or behind the equator
Group 2 (favorable for saving [or preserving] the eye)
2A: one tumor, 4 to 10 DD, at or behind the equator
2B: multiple tumors, with at least one 4 to 10 DD, and all at or behind the equator
Group 3 (doubtful for saving [or preserving] the eye)
3A: any tumor in front of the equator
3B: one tumor, larger than 10 DD, behind the equator
Group 4 (unfavorable for saving [or preserving] the eye)
4A: multiple tumors, some larger than 10 DD
4B: any tumor extending anteriorly (toward the front of the eye) to the ora serrata (front edge of the retina)
Group 5 (very unfavorable for saving [or preserving] the eye)
5A: tumors involving more than half of the retina
5B: vitreous seeding (spread of tumors into the gelatinous material that fills the eye)

Table 2: International Classification of Retinoblastoma

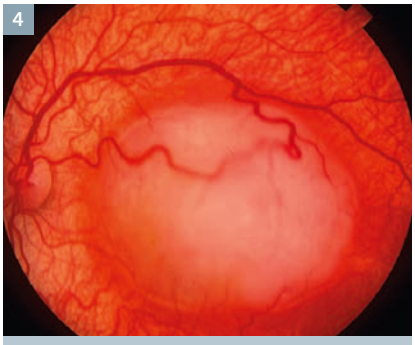
Group	Subgroup	Quick reference	Specific features
A	A	Small tumor	Retinoblastoma < 3 mm in size
B	B	Larger tumor	Retinoblastoma > 3 mm in size
		Macula	Macular retinoblastoma location (< 3 mm to foveola)
		Juxtapapillary	Juxtapapillary retinoblastoma location (< 1.5 mm to disc)
		Subretinal fluid	Clear subretinal fluid > 3 mm from margin
C		Focal seeds	Retinoblastoma with
	C1		Subretinal seeds < 3 mm from retinoblastoma
	C2		Vitreous seeds < 3 mm from retinoblastoma
	C3		Both subretinal and vitreous seeds > 3 mm from retinoblastoma
D		Diffuse seeds	Retinoblastoma with
	D1		Subretinal seeds > 3 mm from retinoblastoma
	D2		Vitreous seeds > 3 mm from retinoblastoma
	D3		Both subretinal and vitreous seeds > 3 mm from retinoblastoma
E	E	Extensive retinoblastoma	Extensive retinoblastoma occupying > 50% globe or Neovascular glaucoma
			Opaque media from hemorrhage in anterior chamber, vitreous or subretinal space
			Invasion of postlaminar optic nerve, choroid (2 mm), sclera, orbit, anterior chamber



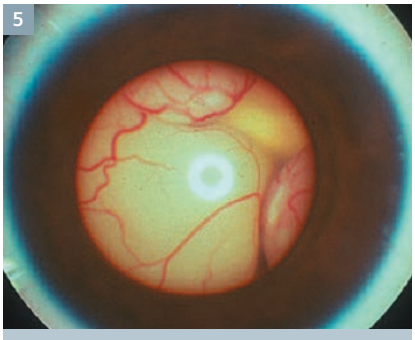
2 Whitish intraocular mass at ophthalmoscopy.



3 Superficial calcifications (arrows).



4 Feeder vessels in a large retinoblastoma.



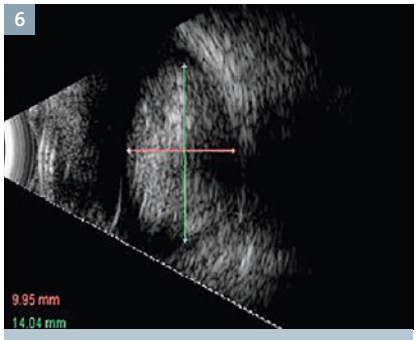
5 Bullous total retinal detachment.

into the vitreous (Fig. 2); calcifications and hypertrophic feeder vessels are more frequently encountered in medium-large size masses (Figs. 3, 4).

Intratumoral calcification and/or tumor seeding give additional support to an ophthalmoscopic diagnosis of RB. Tumoral mass development may result in retinal detachment (Fig. 5), choroidal and/or optic nerve infiltration, ciliary body invasion and anterior segment extension.

Solitary or multiple intraocular masses, often with calcification, whether or not associated with retinal detachment and vitreous seeding are readily visible by ultrasound (US). Particularly, at A-scan US the tumor shows high internal reflectivity and rapid attenuation of the normal orbital pattern, whilst B-scan US shows a round or irregular mass with high reflective echoes and a variable degree of calcification (i.e. shadowing) (Fig. 6). Ultrasound biomicroscopy (UBM) allows *in vivo* analysis of the anterior segment of the eye at microscopic resolution, providing a sensitive and reproducible visualization of the anterior retina, ciliary region, and anterior segment allowing a better staging of the advanced disease process, anterior to the ora serrata [17].

Both ophthalmoscopy and US may be limited by the presence of complex intraocular interfaces when vitreous opacities, subretinal fluid, and retinal detachment are present, have very limited ability to evaluate tumor extension into the optic nerve and may not detect the ocular wall and the extraocular space compared to MR imaging [18-22].



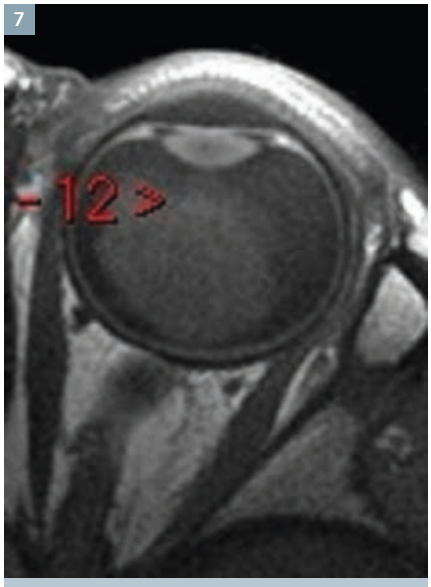
6 Large hyperechogenic mass with shadowing.

With 3D US, extrascleral extension and optic nerve invasion can be scrutinized with unique previously unavailable oblique and coronal sections, but shadowing can consistently reduce the reliability of this technique [23].

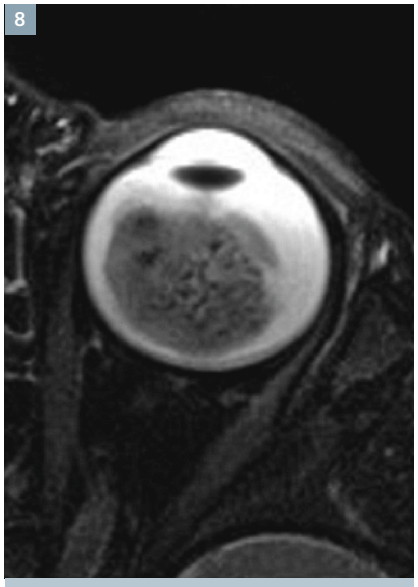
Ocular coherence tomography (OCT) is a valuable tool for assessment of cross-sectional retinal anatomy, with axial resolution to approximately 10 mm. Deeper tissues such as the choroid and sclera are imaged. OCT scans have also been used favorably during the management of RB [24-26]. On OCT, RB shows an optically dense appearance. Intralesional calcification can cause higher internal reflectivity (backscattering) and denser shadowing. There is abrupt transition of the normal retinal architecture to the retinal mass. OCT is also a useful test in monitoring reasons for visual loss following treatment of RB [24]. However, with the current clinical OCT platforms, it is very difficult to successfully image small children with RB without sedation.

Guidelines from European Retinoblastoma Imaging Collaboration (ERIC) to standardize MRI of the eye have been recently published [27].

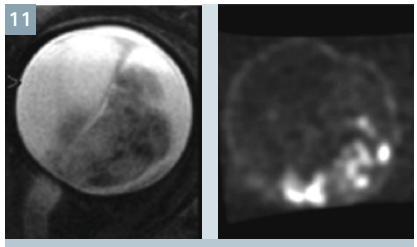
MRI demonstrates lesions that are slightly hyperintense to vitreous on T1-weighted sequences and hypointense to vitreous on T2-weighted sequences (Figs. 7-8), a feature that can be used to differentiate RB from PFV and CD that usually produce hyperintense abnormalities in both T1 and T2w images. Calcification is the most important differentiating feature of RB. The vast majority of RB appear nodular with calcifications. Only a few pathologic conditions other than RB show calcium deposits in extremely young children. These include microphthalmos with and without colobomatous cysts, choristoma, and cytomegalovirus (CMV) endophthalmitis [28-29]. In children older than three years of age, several additional lesions, such as astrocytoma of the retina, retinopathy of prematurity (ROP), toxocariasis, medulloepithelioma, and optic nerve drusen, may have calcifications, thus mimicking the appearance of RB. The common CT appearance of RB is that of a mild to moderate hyperdense lesion, very frequently



7 The mass is slightly hyperintense on T1-weighted image.



8 The mass is hypointense on T2-weighted image.



11 Correspondence between signal voids at MR (left side) and hyperdensities at *ex vivo* CT scan.

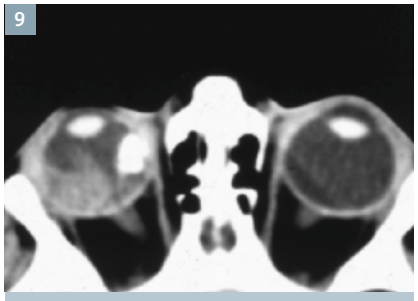


12 Susceptibility-weighted image (SWI) ameliorates the documentation of signal voids consistent with calcifications.

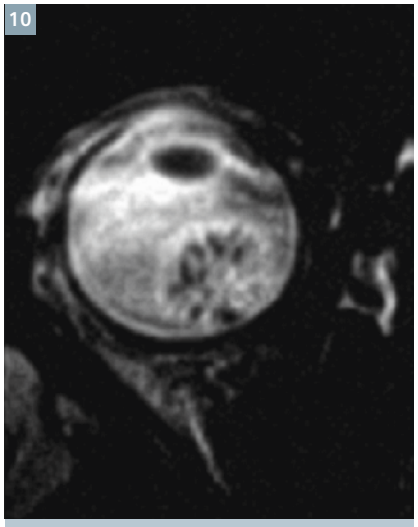
with calcifications and moderate to marked enhancement after contrast administration (Fig. 9). Our protocol does not include CT for assessment of intraocular tumors to avoid exposure of patients to ionizing radiation. A high-resolution gradient-echo T2-weighted sequence showed promising results regarding detection of calcifications [30] (Fig. 10). Galluzzi et al. [30] showed that when data from ophthalmoscopy, US and MRI are put together, no calcifications detected on CT were missed. More recently, signal-intensity voids indicating calcification on gradient-echo T2-weighted sequences were compared with *ex vivo* high-resolution CT: all calcifications visible on high-resolution CT could be matched with signal-intensity voids on MRI [31] (Fig. 11). Sensitivity of susceptibility-weighted imaging for detecting intratumoral calcifications is under evaluation (Fig. 12).

The tumor variably enhances with intravenous gadolinium contrast material (Fig. 13).

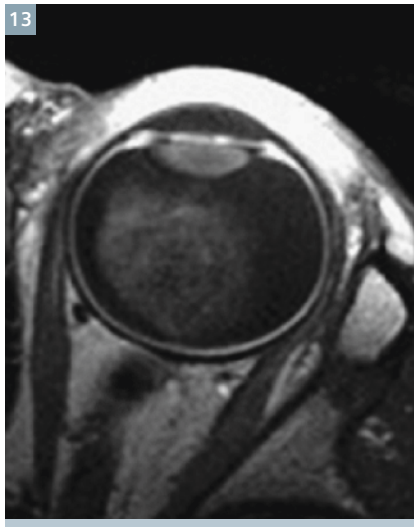
Diffuse infiltrating RB (DIRB) is a rare form of RB, generally presenting at a more advanced age than the typical unilateral form, and occurs more frequently in boys. It is consistently reported as being unilateral and sporadic [32-34]. Pseudo-inflammation is a common presenting sign (24% versus only 6% in the classic



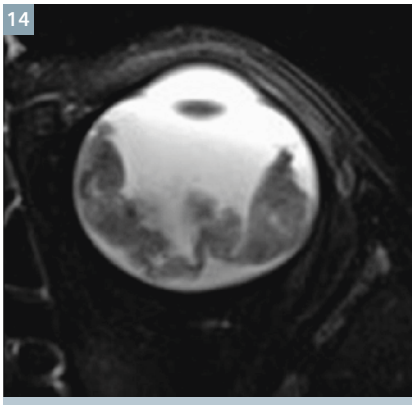
9 Contrast-enhanced CT scan showing enhancement of a partially calcified right eye mass.



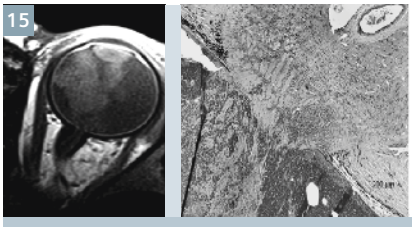
10 Intratumoral signal voids on gradient-echo 3D T2*-weighted image, consistent with calcifications.



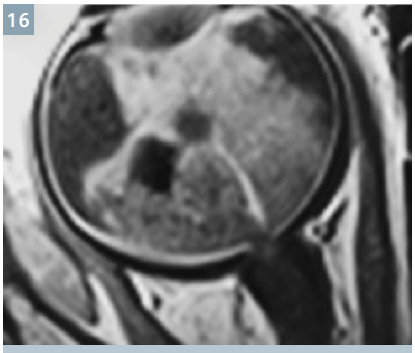
13 T1-weighted image after contrast administration showing moderate enhancement of the mass.



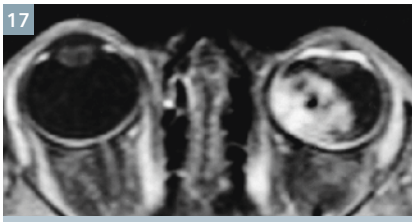
14 T2-weighted image of a diffuse infiltrating retinoblastoma (DIRB).



15 Histologically confirmed prelaminar optic nerve infiltration with interruption of choroido-retinal enhancement line at optic disc level.



16 T1-weighted contrast-enhanced image showing retrolaminar optic nerve infiltration.



17 T1-weighted contrast-enhanced image showing abnormal anterior segment enhancement of the left eye.

form), whereas leukocoria is relatively rare (24% versus 63% in the classic form), such as calcifications (14.3% of cases at histology) [33]. On clinical examination, pseudohypopyon is a suggestive sign, observed in 59% of cases [32]. On MR images it appears as an exophytic mass with relatively high signal intensity on T1-weighted sequences, low signal intensity on T2-weighted sequences, and moderate contrast enhancement. The detached retinal leaflets appeared to be diffusely thickened, irregular, and locally nodular, with possible contrast enhancement [32-34] (Fig. 14).

RB behaves aggressively, employing several modes of dissemination, but patients have a very high life expectancy, if the tumor is diagnosed early; the options for eye-preserving therapy have significantly improved over recent years [35-38].

As a consequence, more children are treated without histopathological confirmation and, what is more important, without assessment of risk factors for disease dissemination and prognosis.

Invasion of the optic nerve in RB is quite common. From there, neoplastic cells may then breach the pia to reach the subarachnoid space or spread into the intracranial optic pathways. Interruption of the normal linear enhancement at the optic nerve disk (choroidoretinal complex) supports a suggestion of prelaminar optic nerve invasion [39-41] (Fig. 15). Postlaminar nerve invasion is the presence of abnormal contrast-enhancement (enhancement ≥ 2 mm in diameter) in the distal nerve [42] (Fig. 16); when evaluating optic nerve enhancement we must pay attention to the presence of elevated intraocular pressure (IOP), that could lead to a false bulging of the tumor in the optic nerve head. The accuracy of MRI in detecting optic nerve invasion has been assessed in several studies [8, 27, 40, 42, 43, 44]. In a recent meta-analysis, De Jong et al. [45] reported the sensitivity and specificity of conventional MRI in detecting postlaminar nerve invasion to be 59% (95% CI, 37-78%) and 94% (95% CI, 84-98%), respectively.

Recent publications have suggested a limited correlation of MRI with histopathology and there is little agreement among radiologists' interpretations [46-49]. However, these authors used standard-resolution MRI with head coils; the use of surface coils is currently recommended [43, 44]. High-resolution MRI with surface coils excludes advanced optic nerve invasion with high negative predictive value and is recommended for the appropriate selection of RB patients eligible for primary enucleation. However, it cannot substitute for pathology in differentiating the first degrees of nerve invasion [50].

Postlaminar optic nerve or optic nerve meningeal sheath invasion should raise suspicion of leptomeningeal metastases.

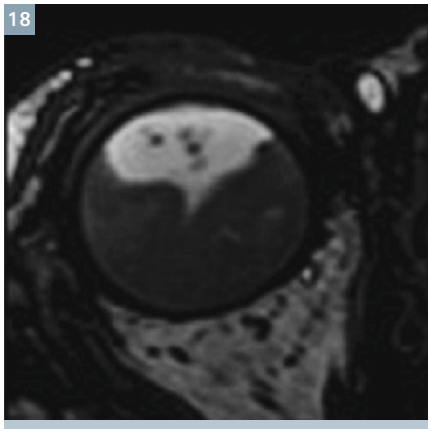
Invasion of the choroid and sclera may occur with subsequent extension into the orbit, conjunctiva, or eyelid. The risk of distant metastasis increases markedly with extraocular extension.

Discontinuity of the normal choroidal enhancement is the leading criterion for its infiltration. Massive choroidal invasion usually presents as focal choroidal thickening. Protrusion of enhancing tissue through the thickened choroid into the (low signal-intensity) sclera or beyond is a sign of scleral invasion or extraocular extension, respectively [40].

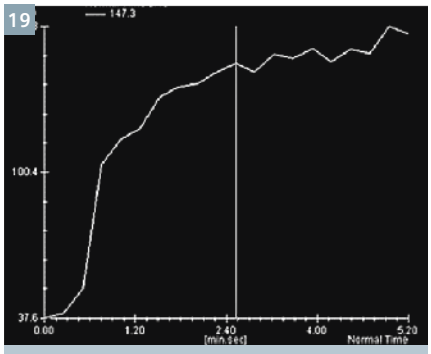
Anterior eye segment enhancement frequently occurs in RB and is usually a sign of iris angiogenesis, caused by the hyper-secretion of vascular endothelial growth factor (VEGF) in tumor growth-induced ischemia [51, 52] (Fig. 17). Tumor invasion into the anterior eye segment is an infrequent finding [40].

Vitreous seeding can be shown by MRI only if the tumoral flocculus are large enough to be detected and dedicated sequences are performed (Fig. 18).

DWI has been widely used in evaluation of orbital tumors in adults and children. In our protocol, DWI images of the eye(s) and the optic nerve(s) were acquired in the three orthogonal directions with b-factors of 0, 500, and 1000 mm^2/s and apparent diffusion coefficient (ADC) maps were automati-



18 T2-weighted 3D image showing small hypointense floccules of vitreal seeding.



19 Dynamic curve showing early enhancement with progressive growth.

cally generated. Preliminary results in RB consistently demonstrate low ADC within the tumor and a correlation between its value and prognostic parameters [53] (Fig. 19): actually, findings such as poorly differentiated or undifferentiated tumor, bilaterality, large size tumors, and optic nerve invasion are usually associated with a trend for lower ADC [54, 55].

There has been recent discussion of the potential for dynamic contrast-enhanced (DCE) MRI to non-invasively assess tumor angiogenesis and necrosis in RB concluding that the early phase of the DCE time curve positively correlates with microvascular density, while the presence of late enhancement correlates with necrosis [56] (Fig. 20).

Brain MRI can detect trilateral RB (i.e. PNET located mainly in the pineal gland, or rarely in the suprasellar area), leptomeningeal spread and



20 Restricted diffusion within the tumor.

congenital brain malformations (mainly in patients with 13q-deletion syndrome) [57, 58].

Persistent fetal vasculature (Persistent hyperplastic primary vitreous)

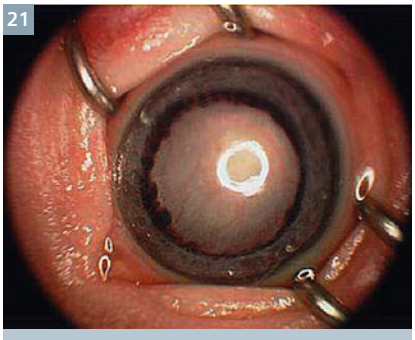
PFV (previously named persistent hyperplastic primary vitreous) is the second most common cause of leukocoria. It is a congenital, non-hereditary, failure of the embryonic primary vitreous to regress, resulting in continued proliferation and formation of a retrolental mass with cataract in the anterior segment. The primary vitreous is formed during the first month of development, extends from the posterior lens to the retina and contains branches of the hyaloid artery. The hyaloid blood system consists primarily of the hyaloid artery, a branch of the ophthalmic artery, and by the vasa hyaloidea propria. The hyaloid artery begins to regress during the formation of the avascular secondary vitreous at nine weeks. By the third month, the secondary vitreous, which ultimately forms the adult vitreous, fills most of the developing vitreous cavity. The primary vitreous becomes condensed into a narrow band (Cloquet's canal), running from the optic disc to the posterior aspect of the lens.

Usually, the primitive hyaloid system regresses completely: the posterior portion of the arterial system typically regresses at seven months of life, whilst the anterior one regresses at eight months of life. When the primitive mesenchymal tissue persists and continues to proliferate, a retrolental mass is formed. Commonly, patients have a combination of the anterior and posterior types of PFV. In the anterior type, findings include a shallow anterior chamber, elongated ciliary processes, enlarged iris vessels, cataracts, early onset glaucoma, and intralenticular hemorrhages (Fig. 21). There is also commonly degeneration of the lens fibers; this may manifest as an abnormal lental morphology at imaging and ultimately may lead to development of a cataract [59]. In the posterior type, findings include the classic retrolental fibrovascular mass, vitreous membrane, a remnant of the Cloquet canal, which carries the hyaloid artery, optic disc dysplasia, and a clear lens [60]. The retrolental mass may hinder the proper development of the retina and lead to variable degrees of microphthalmia. In older patients, calcification or even ossification of the lens may be observed [61].

PVF is unilateral in between 90%-98% of cases [61-63].

Rare bilateral cases of similar findings have been reported in the past in association with Norrie disease, Warburg syndrome, and other neurologic and systemic anomalies [61]. However, bilateral PFV may represent a separate clinical entity, with a unique underlying mechanism and several bilateral PFV have been recently described [64-67].

Retinal detachment is seen in 30%-56% of cases [61, 63]. Strands of glial tissue extending from the



21 Elongated ciliary processes in PFV.

retina into the vitreous are seen in about one third of cases [61].

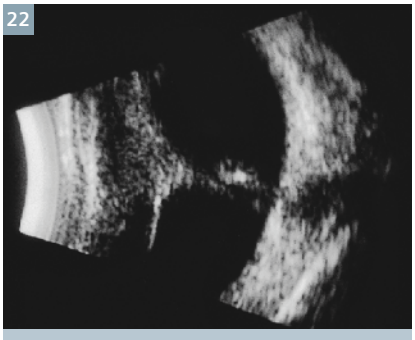
Vitreous hemorrhage from the fibrovascular tissue is common, especially in the first few months of life; hemorrhage and neovascular glaucoma are the most common complications necessitating enucleation.

The most typical finding of PFV is the retrolental fibrovascular mass [64, 68] caused by persistence of the primary vitreous that normally should regress [69].

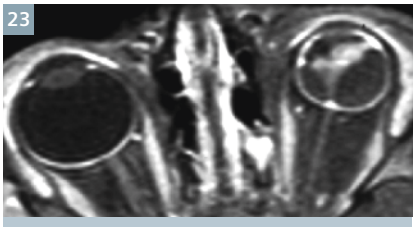
Patients with anterior type PFV can have a good visual outcome, whilst those with posterior type tend to have a poor one [64].

Imaging findings depend on the size, thickness, and vascularity of the retrolental fibrovascular mass. At US, the main finding is a contracting echogenic retrolental mass, with one or few hyperechoic band/s extending from the mass to the optic nerve head. This band corresponds to the Cloquet canal (Fig. 22). Sometimes, the hyaloid artery can be seen within this band with Doppler US. Mafee et al. initially described the relationship between leukocoria and CT findings of a funnel-shaped mass of fibrovascular tissue that occupies the retrolental space and the site of the Cloquet canal [70], extending from the area of the optic disc toward the posterior aspect of the lens [71]. Use of CT depicts well microphthalmos and frequently a retrolental focus of increased attenuation. A linear band or septum extending from the posterior aspect of the retrolental mass allows for a confident diagnosis of PFV, such as a layering attenuating hemorrhage in the globe. CT usually demonstrates tubular, cylindrical, triangular, or discrete intravitreal densities suggesting the presence of remnants of persistent hyaloid system or congenital non-attachment of the retina. A generalized increase in intravitreal density and enhancement of abnormal intravitreal tissue are both possible [70, 71]. CT may also detect the presence of calcifications, very rare in PFV; 3D gradient echo T2-weighted MR images and SWI MR images hopefully will replace CT in the calcification depiction also in this pathology. MRI usually depicts an inconstant contrast-enhancing mass behind the lens associated to retinal and/or posterior hyaloid detachment with hemorrhage and the abnormal lens in a microophthalmic eye (Fig. 23). Visualization of a vertical septum (Cloquet canal) between the optic disc and posterior lens is a diagnostic hallmark. Decubitus positioning may also show a gravitational effect on a fluid level within the globe, reflecting a sero-hematic fluid (Fig. 24). There may also be enhancement of the anterior chamber, which is thought to be related to elongation of the ciliary processes, possibly through the mechanism of leaky vessels [64].

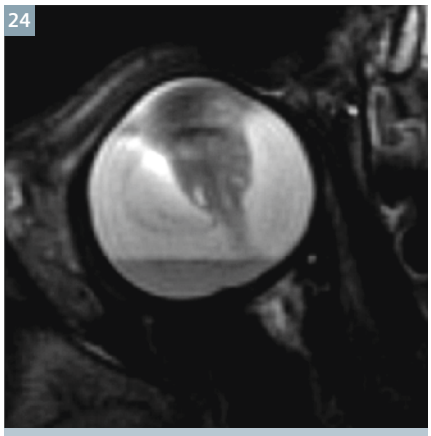
Anterior PFV is rarer than posterior PFV, and mixed type is by far the most frequent (Fig. 25). In the sporadic cases documented with MRI in the pertinent literature, anterior PFV showed a shallow anterior chamber, a flat lens, and an enhancement of the lens and of the ciliary body after intravenous gadolinium administration [60, 72].



22 Retrolental stalk along the Cloquet canal.



23 T1-weighted contrast-enhanced image showing retrolental mass in a microophthalmic left eye.



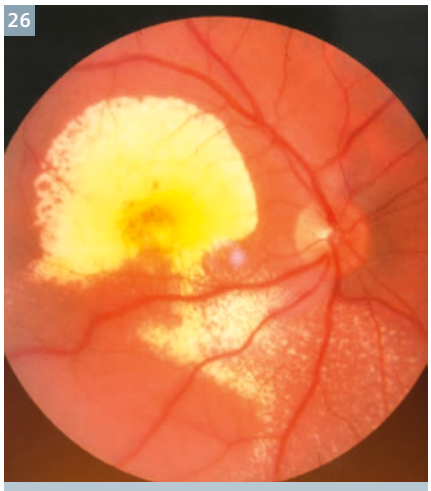
24 Fluid-fluid level due to intravitreal hemorrhage.



25 T2-weighted image of PFV with both anterior and posterior segments involvement.

Coat's disease

Since its original description in 1908, Coat's disease (CD) has been recognized as an idiopathic cause of severe vision loss with a remarkable diversity in clinical presentation and morphology. CD is a rare, probably congenital, nonfamilial, idiopathic vascular developmental disease of the retina, primarily caused by a defect at the endothelial cell level of the blood-retinal barrier, resulting in increasing amounts of yellowish intraretinal and subretinal exudate composed of blood components rich in cholesterol crystals, cholesterol- and pigment-laden macrophages, few erythrocytes, and minimal hemosiderin, final leakage of fluid into the vessel wall and perivascularly (Figs. 26, 27). The massive subretinal and intraretinal exudation often leads to thickening of the retina (heaviest in the outer sectors) and exudative retinal detachment [73, 74]. Some eyes develop retinal or choroidal neovascularization, which might result in hemorrhage. In up to 20% of all cases there is a fibrous submacular nodule that occasionally is calcified



26 Yellowish exudate at ophthalmoscopy.



27 Cholesterol crystals at histology.

or ossified. The clinical spectrum of CD is broad, ranging from asymptomatic perifoveal telangiectasis, to total exudative retinal detachment with poor visual prognosis, and may progress to neovascular glaucoma with eventual phthisis bulbi. Secondary changes also include rubeosis iridis, neovascular glaucoma, cataract, and uveitis. Shields et al. [75] proposed the most recent classification system in five stages:

Stage 1: retinal teleangectasia only

Stage 2: teleangectasia and exudation

Stage 3a: exudative subtotal retinal detachment

Stage 3b: exudative total retinal detachment

Stage 4: total retinal detachment and glaucoma

Stage 5: advanced end-stage disease

The vascular anomaly of CD, although present at birth, usually does not cause symptoms until the retina detaches and central vision is lost [76, 77]. Calcifications are very rare, although intraocular bone formation has been reported in advanced cases [78]. CD is unilateral in 80%-90% of patients, affecting 69%-85% of males. If bilateral, one eye is usually minimally affected [59, 79-81].

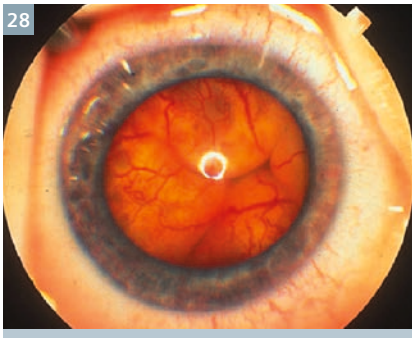
The disease usually appears in patients slightly older (4-8 years) than those affected by RB. Several exceptions to the usual age at presentation have been reported [77, 82, 83]. CD is isolated in the majority of cases, although associations with a variety of exudative retinopathies, as well as several conditions, have been described [59, 84-87].

Leukocoria and strabismus are the most common presenting signs of CD [73, 74, 77, 79, 88-91]. Progression to total retinal detachment, painful neovascular glaucoma, phthisis bulbi, and blindness, occurs in slightly more than half of untreated patients [83, 92]. Spontaneous remission has been sporadically reported [93].

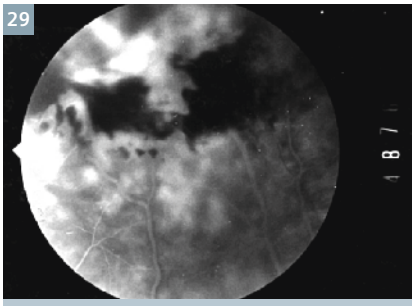
Misdiagnosing CD as RB may result in the enucleation of a potentially salvageable eye; conversely, mistaking a case of RB for CD delays the appropriate therapeutic intervention and increases the possibility of extraocular tumor spread, especially if intraocular surgery is performed.

Ophthalmoscopy can demonstrate a variety of findings, depending on the stage of the disease. In early stages, ophthalmoscopic examination reveals dilated and saccular aneurysmal changes in tortuous retinal vessels with exudates, and localized foci of retinal teleangiectasia [73]. With progression of the disease, the vascular abnormalities are associated with increasing amounts of yellow intraretinal and subretinal exudation. The ophthalmoscopic distinction of advanced CD from other diseases with bullous retinal detachment (such as RB) can be extremely difficult, if not impossible (Fig. 28); for instance, dilated retinal vessels and subretinal exudate with foamy macrophage may represent a so called 'Coat's reaction' to RB [74]. Furthermore, patients with advanced CD frequently manifest a clouded vitreous, which limits ophthalmoscopic findings. Fluorescein angiography plays a pivotal role in both diagnosis and assessment of disease progression, allowing clear visualization of the vascular changes which may be taking place [75]. It may show mildly irregular retinal vessels, sausage-like vascular beading, saccular outpouchings, or light-bulb dilations; leakage from the irregular-caliper retinal vessels may be demonstrated (Fig. 29).

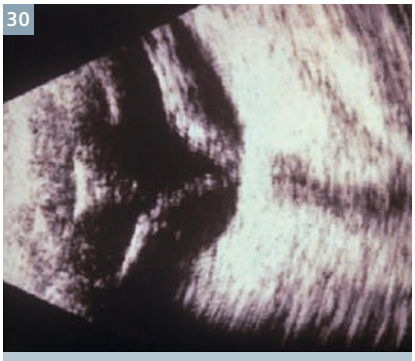
The ultrasonographic findings depend on the stage of the disease. In the early stages, US shows areas of retinal detachment, and excludes the presence of solid mass and calcification (both suggesting RB); documentation of teleangiectasia and retinal exudates are also possible in early stages. When the disease advances, some more characteristic echographic signs may help the right diagnosis: narrow or close V-shaped retinal detachment with looping of a thickened peripheral retina, poor retinal mobility, dense slowly moving



28 Bullous retinal detachment in Coat's disease.

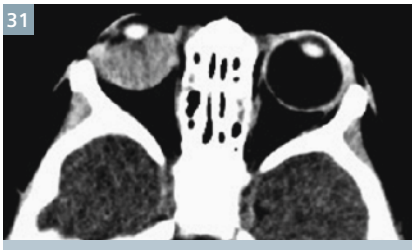


29 Leakage at fluorangiography.

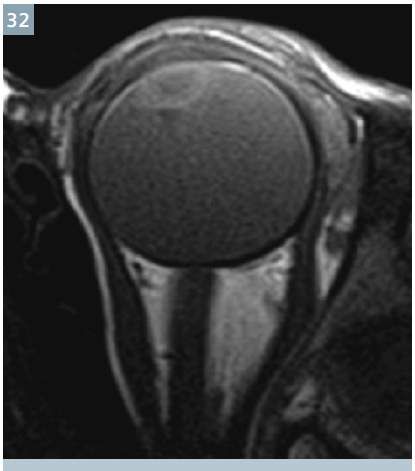


30 Funnel-shaped total retinal detachment at ultrasonography.

subretinal opacities, as well as the above described absence of solid mass and no evidence of calcification (Fig. 30). However, it is important to remember that looping of the peripheral retina may also be seen in advanced retinopathy of prematurity (ROP), and calcification has been described in longstanding CD [95]. Unfortunately, although ultrasonography is an essential component of the evaluation of patients with CD, it is of limited utility when diffuse vitreous infiltration, non-calcified masses, and complex interfaces are present. OCT is useful in identifying subtle macular edema or cystic changes, subretinal fluid, exudate, and hemorrhage, as well as assessment of the integrity of specific retinal layers [96].



31 CT scan showing diffuse hyperdensity in the right eye in high-grade Coat's disease. No calcifications are visible.



32 T1-weighted not-enhanced image showing diffuse hyperintense exudate in the affected eye.

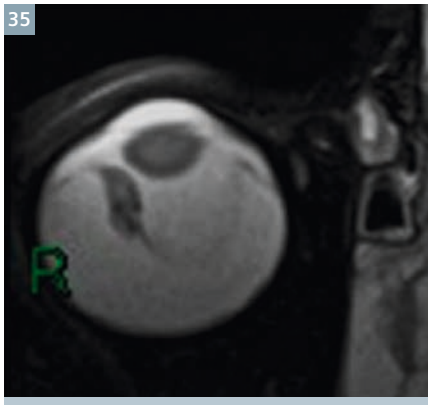
When clinical diagnosis is uncertain, CT and/or MR imaging are required. In the initial stages, imaging studies may be essentially normal or show very slight focal retinal thickening and exudate. In advanced stages, CT and MRI show a funnel-shaped retinal detachment with an underlying subretinal lipo-proteinaceous exudation. The exudate may occupy almost the entire globe and may obliterate the vitreous space in advanced cases. There is no calcification. The exudation appears hyperdense on CT (Fig. 31) and almost always as hyperintense signal on both T1w (Fig. 32), T2w (Fig. 33), and FLAIR (Fig. 34) images. This is in contrast



33 T2-weighted image showing hyperintense exudate and totally detached retina with some peripheral thickening.



34 FLAIR image clearly showing a hyperintense right eye.



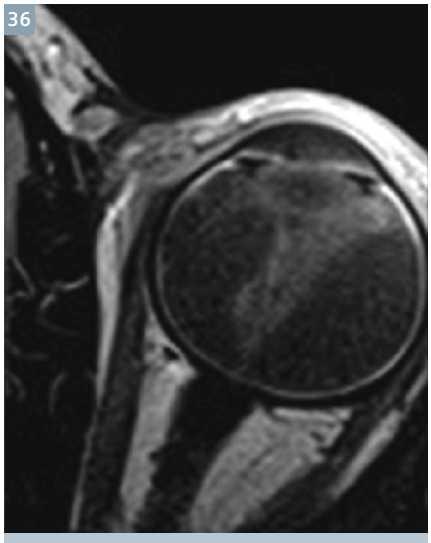
35 T2-weighted image showing a hypointense mass-like lesion in Coat's disease.

to RB, which is relatively hypointense on T2-weighted images. The presence of hemorrhage at different catabolic stages or fibrosis may confer a potentially confounding heterogeneous appearance, especially on T2-weighted images (Fig. 35). Post-contrast study usually shows an absence of enhancement in the subretinal region, and may document characteristic funnel-shaped enhancement of the detached leaves of the retina (Fig. 36), due to thickened retina with teleangectasia and microaneurysms, especially in the peripheral sections. Enhancement of the detached leaves of the retina, if present, may be very important in the differential diagnosis with RB, which enhances in a mass-like fashion. However, in extreme cases of advanced CD, a retrolental gliotic mass can occur simulating nodular RB.

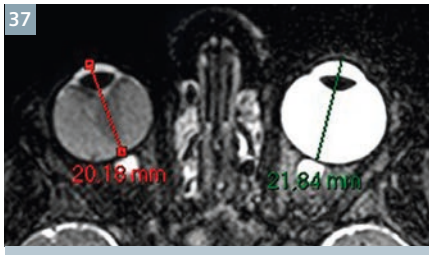
A case report with enhancement of the proximal optic nerve in T1-weighted contrast-enhanced images has been described in a child with elevated (58 mm Hg) intraocular pressure (IOP); the finding disappeared after normalization of IOP [97].

Proton MR spectroscopy of the exudate has demonstrated a peak at 1-1.6 ppm due to lipoproteinaceous material [98].

The main problem in differential diagnosis remains to differentiate advanced CD from RB, and usually requires the summation of various diagnosis aids, since both diseases may present with nonrhegmatogenous retinal detachment, teleangiectases, and subretinal collections.



36 T1-weighted contrast-enhanced image showing enhancement of thickened detached retina.



37 T2-weighted image showing the smaller diameter of the affected eye in Coat's disease.

Exceptions to the typical imaging features are seen in both CD and RB [73, 77, 99, 100]. Particularly, a retrolental contrast-enhancing gliotic mass simulating nodular RB can occur in extreme cases of advanced Coat's disease [101]. The rare DIRB may not show nodularity on any imaging studies [102]. DIRB may also simulate CD due to the diffuse pattern, rare presence of calcification and lack of underlying mass [2].

Furthermore, occasional reports of calcifications in CD have been well documented [73, 76, 99, 100]. In the chronic stages of CD, the MR signal intensity of subretinal fluid may become heterogeneous due to the combination of cholesterol crystals, hemorrhage in different stages of hemoglobin catabolism, PAS-positive material, and scarring [59, 77, 101], resulting in signal intensities which differ from the typical pattern.

A significantly smaller volume of the affected globe, always noted in CD, is an additional clue in the differential diagnosis with RB [82]; retinal vascular developmental abnormalities of CD may disturb the release of growth factors regulating the further development of secondary vitreous, and thus resulting in the disturbance of the growth of the affected globe (Fig. 37).

References

1 De Potter P, Flanders AE, Shields JA et Al: The role of fat-suppression technique and gadopentetate dimeglumine in magnetic resonance imaging evaluation of intraocular tumors and simulating lesions. Arch Ophthal- mol 112: 340-348, 1994.

2 Smirniotopoulos JG, Bargallo N, Mafee MF: Differential diagnosis of leuko- coria: radiologic-pathologic correlation. Radiographics 14: 1059-1079, 1994.

3 De Potter P, Shields JA, Shields CL: Tumors and pseudotumors of the retina. In: De Potter P, Shields JA, Shields CL (eds.). MRI of the eye and oRBit. Philadelphia: JB Lippincott Company 1995: 93-116.

4 Shields CL, Schoenberg E, Kocher K, Shukla SY, Kaliki S, Shields JA. Lesions simulating retinoblastoma (pseudoreti- noblastoma) in 604 cases: results based on age at presentation. Ophthal- mology. 2013;120(2):311-6.

5 Balmer A, Munier F. Differential diagnosis of leukocoria and strabismus, first presenting signs of retino- blastoma. Clin Ophthalmol. 2007;1(4):431-9.

6 Apushkin MA1, Apushkin MA, Shapiro MJ, Mafee MF. Retinoblastoma and simulating lesions: role of imaging. Neuroimaging Clin N Am. 2005 Feb;15(1):49-67.

7 Rao AA, Naheedy JH, Chen JY, Robbins SL, Ramkumar HL. A clinical update and radiologic review of pediatric oRBital and ocular tumors. J Oncol. 2013;2013:975908. doi: 10.1155/2013/975908. Epub 2013 Mar 12.

8 Schueler AO, Hosten N, Bechrakis NE, Lemke AJ, Foerster P, Felix R, Foerster MH, Bornfeld N.. High resolution magnetic resonance imaging of retino- blastoma. Br J Ophthalmol 2003 Mar;87(3):330-5.

9 Shields CL, Shields JA. Diagnosis and management of retinoblastoma. Cancer Control. 2004;11:317–327.

10 Kivela T. Trilateral retinoblastoma: a meta-analysis of hereditary retino- blastoma associated with primary ectopic intracranial retinoblastoma. J Clin Oncol. 1999;17:1829–1837.

11 Singh AD, Shields CL, Shields JA: Prognostic factors in retinoblastoma. J Pediatr Ophthalmol Strabismus 37: 134-141, 2000.

12 Finelli DA, Shurin SB, Bardenstein DS: Trilateral Retinoblastoma: Two Variations. Am J Neuroradiol 16: 166-170, 1995.

13 Provenzale JM, Weber AL, Klintworth GK et Al: Bilat- eral retinoblastoma with coexistent pinealoblastoma (trilateral retinoblastoma). Radiologic-pathologic corre- lation. Am J Neuroradiol 16: 157-165, 1995.

14 Reese A, Ellsworth R. Evaluation and current concept of retinoblastoma theraphy. Trans Am Acad Ophthalmolo Otorlaryngol 1963; 67: 164-172.

15 Murphree AL Intraocular retinoblastoma: the case for a new group classification. Ophthalmol Clin N Am 2005; 18: 41–53.

16 Shields CL, Ghassemi F, Tuncer S, Thangappan A, Shields JA. Clinical spectrum of diffuse infiltrating retino- blastoma in 34 consecutive eyes. Ophthalmology. 2008;115(12):2253-8.

17 Vasquez LM1, Giuliari GP, Halliday W, Pavlin CJ, Gallie BL, Héon E. Ultrasound biomicroscopy in the management of retinoblastoma. Eye 2011; 25: 141-147.

18 Mahajan A, Crum A, Johnson MH, Materin MA. Ocular neoplastic disease. Semin Ultrasound CT MR. 2011;32(1):28-37.

19 Rauschecker AM, Patel CV, Yeom KW, Eisenhut CA, Gawande RS, O'Brien JM, Ebrahimi KB, Daldrup-Link HE. High- resolution MR imaging of the oRBit in patients with retinoblastoma. Radio- graphics. 2012;32(5):1307-26.

20 Roth DB, Scott IU, Murray TG et Al: Echography of retinoblastoma: histo- pathologic correlation and serial evalu- ation after globe-conserving radio- therapy or chemotherapy. J Pediatr Ophthalmol Strabismus 38: 136-143, 2001.

21 Razek AA, Elkhamary S. MRI of retino- blastoma. Br J Radiol. 2011;84(1005):775-84.

22 Kaufman LM, Mafee MF, Song CD: Retinoblastoma and simulating lesions. Radiol Clin North Am 36: 1101- 1117, 1998.

23 Finger PT, Harbour W, Karcioglu Z. Risk factors for metastasis of retinoblastoma. Surv Ophthalmol 2002;47:1–36.

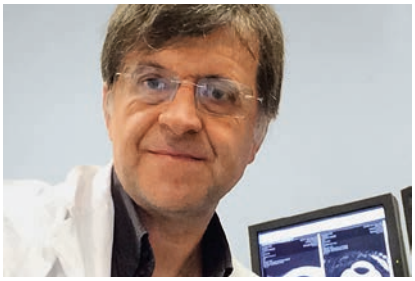
24 Shields CL1, Materin MA, Shields JA. Review of optical coherence tomography for intraocular tumors. Curr Opin Ophthalmol. 2005 Jun;16(3):141-54.

25 Villegas VM1, Hess DJ, Wildner A, Gold AS, Murray TG. Retinoblastoma. Curr Opin Ophthalmol. 2013;24(6):581-8.

26 Yousef YA, Schroff M, Halliday W, Gallie BL, Héon E. Detection of optic nerve disease in retinoblastoma by use of

spectral domain optical coherence tomography. J AAPOS 2012; 16: 481-483.
27 de Graaf P, Göricke S, Rodjan F, Galluzzi P, Maeder P, Castelijns JA, Brisse HJ; European Retinoblastoma Imaging Collaboration (ERIC). Guidelines for imaging retinoblastoma: imaging principles and MRI standardization. Pediatr Radiol. 2012 Jan;42(1):2-14.
28 Brennan RC, Wilson MW, Kaste S, Helton KJ, McCarville MB. US and MRI of pediatric ocular masses with histopathological correlation. Pediatr Radiol. 2012;42(6):738-49.
29 Tuncer S, Oray M, Yildirim Y, Camcioglu Y, Tugal-Tutkun I. Bilateral intraocular calcification in necrotizing cytomegalovirus retinitis. Int Ophthalmol (2014) 34:1119–1122.
30 Galluzzi P, Hadjistilianou T, Cerase A, et al. Is CT still useful in the study protocol of retinoblastoma? AJNR Am J Neuroradiol. 2009;30:1760–1765.
31 Rodjan F, de Graaf P, van der Valk P, Hadjistilianou T, Cerase A, Toti P, de Jong MC, Moll AC, Castelijns JA, Galluzzi P; on behalf of the European Retinoblastoma Imaging Collaboration. Detection of Calcifications in Retinoblastoma Using Gradient-Echo MR Imaging Sequences: Comparative Study between In Vivo MR Imaging and Ex Vivo High-Resolution CT. AJNR Am J Neuroradiol. 2015 Feb;36(2):355-60.
32 Brisse HJ, Lumbroso L, Fréneaux PC, Validire P, Doz FP, Quintana EJ, Berges O,Desjardins LC, Neuenschwander SG. Sonographic, CT, and MR imaging findings in diffuse infiltrative retinoblastoma: report of two cases with histologic comparison. AJNR Am J Neuroradiol. 2001 Mar;22(3):499-504.
33 Bhatnagar R, Vine AK: Diffuse Infiltrating Retinoblas- toma. Ophthalmology 98: 1657-1661, 1991.
34 Mansour AM, Greenwald MJ, O'Grady R: Diffuse Infil- trating Retinoblastoma. J Ped Ophthalmol Strabismus 36: 152-54, 1989.
35 Shields CL, Fulco EM, Arias JD, Alarcon C, Pellegrini M, Rishi P, Kaliki S, Bianciotto CG, Shields JA. Retinoblastoma frontiers with intravenous, intra-arterial, periocular, and intravitreal chemotherapy. Eye (Lond). 2013;27(2):253-64.
36 Abramson DH, Gobin YP, Marr BP, Dunkel IJ, Brodie SE. Intra-arterial chemotherapy for retinoblastoma. Ophthalmology. 2012;119(8):1720-1; author reply 1721.
37 Venturi C, Bracco S, Cerase A, Cioni S, Galluzzi P, Gennari P, Vallone IM, Tinturini R, Vittori C, De Francesco S, Caini M, D'Ambrosio A, Toti P, Renieri A,Hadjistilianou T. Superselective ophthalmic artery infusion of melphalan for intraocular retinoblastoma: preliminary results from 140 treatments. Acta Ophthalmol. 2013;91(4):335-42.
38 Bracco S, Leonini S, De Francesco S, Cioni S, Gennari P, Vallone IM, Piu P, Galimberti D, Romano DG, Caini M, De Luca M, Toti P, Galluzzi P, Hadjistilianou T, Cerase A. Intra-arterial chemotherapy with melphalan for intraocular retinoblastoma. Br J Ophthalmol. 2013;97(9):1219-21.
39 de Graaf P, Knol DL, Moll AC, Imhof SM, Schouten-van Meeteren AY, Castelijns JA. Eye size in retinoblastoma: MR imaging measurements in normal and affected eyes. Radiology. 2007;244(1):273-80.
40 de Graaf P, Barkhof F, Moll AC, et al. Retinoblastoma: MR imaging parameters in detection of tumor extent. Radiology. 2005;235:197–207.
41 de Graaf P, Moll AC, Imhof SM, van der Valk P, Castelijns JA. Retinoblastoma and optic nerve enhancement on MRI: not always extraocular tumour extension. Br JOphthalmol. 2006;90(6):800-1.
42 Brisse HJ, Guesmi M, Aerts I, et al. Relevance of CT and MRI in retinoblastoma for the diagnosis of postlaminar invasion with normal-size optic nerve: a retrospective study of 150 patients with histological comparison. Pediatr Radiol. 2007;37:649–656.
43 Lemke AJ, Kazi I, Mergner U et al (2007) Retinoblastoma-MR appearance using a surface coil in comparison with histopathological results. Eur Radiol 17:49–60.
44 Ainbinder DJ, Haik BG, Frei DF, Gupta KL, Mafee MF (1996) Gadolinium enhancement: improved MRI detection of retinoblastoma extension into the optic nerve. Neuroradiology 38:778–781.
45 de Jong MC, de Graaf P, Noij DP, Göricke S, Maeder P, Galluzzi P, Brisse HJ, Moll AC, Castelijns JA; European Retinoblastoma Imaging Collaboration (ERIC). Diagnostic performance of magnetic resonance imaging and computed tomography for advanced retinoblastoma: a systematic review and meta-analysis. Ophthalmology 2014 ;121(5):1109-18.
46 Wilson MW, Rodriguez-Galindo C, Billups C, Haik BG, Laningham, F, Patay Z (2009) Lack of correlation between the histologic and magnetic resonance imaging results of optic nerve involvement in eyes primarily enucleated for retinoblastoma. Ophthalmology 116: 1558–1563.
47 Song KD, Eo H, Kim JH, Yoo SY, Jeon TY (2012) Can preoperative MR imaging predict optic nerve invasion of retinoblastoma? Eur J Radiol 81:4041–4045.
48 Lee BJ, Kim JH, Kim DH, Park SH, Yu YS (2012) The validity of routine brain MRI in detecting post-laminar optic nerve involvement in retinoblastoma. Br J Ophthalmol 96:1237–1241.
49 Chawla B, Sharma S, Sen S et al (2012) Correlation between clinical features, magnetic resonance imaging, and histopathologic findings in retinoblastoma: a prospective study. Ophthalmology 119:850–856.
50 Brisse HJ, de Graaf P, Galluzzi P, Cosker K, Maeder P, Göricke S, Rodjan F, de Jong MC, Savignoni A, Aerts I, Desjardins L, Moll AC, Hadjistilianou T, Toti P, van der Valk P, Castelijns JA, Sastre-Garau X; on behalf of the European Retinoblastoma Imaging Collaboration (ERIC). Assessment of early-stage optic nerve invasion in retinoblastoma using high-resolution 1.5 Tesla MRI with surface coils: a multicentre, prospective accuracy study with histopathological correlation. Eur Radiol. 2014 Nov 30.
51 Galluzzi P, Cerase A, Hadjistilianou T, De Francesco S, Toti P, Vallone IM, Filosomi G, Monti L, Bracco S, Gennari P, Ginanneschi C, Venturi C. Retinoblastoma: Abnormal gadolinium enhancement of anterior segment of eyes at MR imaging with clinical and histopathologic correlation. Radiology. 2003;228(3):683-90.
52 de Graaf P, van der Valk P, Moll AC, Imhof SM, Schouten-van Meeteren AY, Knol DL, Castelijns JA. Contrast-enhancement of the anterior eye segment in patients with retinoblastoma: correlation between clinical, MR imaging, and histopathologic findings. AJNR Am J Neuroradiol. 2010;31(2):237-45.
53 de Graaf P, Pouwels PJ, Rodjan F, Moll AC, Imhof SM, Knol DL, Sanchez E, van der Valk P, Castelijns JA. Single-shot turbo spin-echo diffusion-weighted imaging for retinoblastoma: initial experience. AJNR Am J Neuroradiol. 2012;33(1):110-8.
54 Sepahdari AR, Kapur R, Aakalu VK, Villablanca JP, Mafee MF. Diffusion-weighted imaging of malignant ocular masses: initial results and directions for further study. AJNR Am J Neuroradiol. 2012;33(2):314-9.
55 Abdel Razek AA, Elkhamary S, Al-Mesfer S, Alkatan HM. Correlation of apparent diffusion coefficient at 3T with prognostic parameters of retinoblastoma. AJNR Am J Neuroradiol. 2012;33(5):944-8.
56 Rodjan F, de Graaf P, van der Valk P, Moll AC, Kuijer JP, Knol DL, Castelijns JA, Pouwels PJ. Retinoblastoma: value of dynamic contrast-enhanced MR imaging and correlation with tumor angiogenesis. AJNR Am J Neuroradiol. 2012;33(11):2129-35.
57 Rodjan F, Graaf P, Moll AC, et al. Brain abnormalities on MR imaging in patients with retinoblastoma. AJNR Am J Neuroradiol. 2010;31:1385–1389.
58 Rodjan F, de Graaf P, Brisse HJ, Göricke S, Maeder P, Galluzzi P, Aerts I, Alapetite C, Desjardins L, Wieland R, Popovic MB, Diezi M, Munier FL, Hadjistilianou T, Knol DL, Moll AC, Castelijns JA. Trilateral retinoblastoma: neuroimaging characteristics and value of routine brain screening on admission. J Neurooncol. 2012;109(3):535-44.

59 Edward DP, Mafee MF, Garcia-Valenzuela E, Weiss RA. Coats' disease and persistent hyperplastic primary vitreous—role of MR imaging and CT. Radiol Clin North Am 1998; 36 (6) 1119-1131.
60 Castillo M, Wallace DK, Mukherji SK. Persistent hyperplastic primary vitreous involving the anterior eye. AJNR Am J Neuroradiol 1997;18(8):1526–15281998; 36(6):1119–1131.
61 Haddad R, Font RL, Reeser F. Persistent hyperplastic primary vitreous: a clinico-pathologic study of 62 cases and review of the literature. Surv Ophthalmol 1978;23(2):123–134.
62 Reese AB. Persistent hyperplastic primary vitreous. Trans Am Acad Ophthalmol Otolaryngol 1955;59(3):271–295.
63 Pollard ZF. Persistent hyperplastic primary vitreous: diagnosis, treatment and results. Trans Am Ophthalmol Soc 1997;95:487–549.
64 Kumar A, Jethani J, Shetty S, Vijayalakshmi P. Bilateral persistent fetal vasculature: a study of 11 cases. J AAPOS 2010;14(4): 345–348.
65 Jain TO. Bilateral persistent hyperplastic primary vitreous. Indian J Ophthalmol 2009; 57:53-54.
66 Galal AH, Kotoury AIS, Azzab AA. Bilateral persistent hyperplastic primary vitreous: An Egyptian family supporting a rare autosomal dominant heritance. Genet Couns 2006; 17: 441-447.
67 Sanghvi DA, Sanghvi CA, Purandare NC. Bilateral persistent hyperplastic primary vitreous. Australas Radiol 2005; 49: 72-74.
68 Pediatric Orbit Tumors and Tumorlike Lesions: Neuroepithelial Lesions of the Ocular Globe and Optic Nerve. Chung EM, Specht CS, Schroeder JW. Radiographics 2007; 27 (4):1159-1187.
69 Shastry BS. Persistent hyperplastic primary vitreous: congenital malformation of the eye. Clin Experiment Ophthalmol 2009;37(9): 884–890.
70 Goldberg MF, Mafee MF. Computed tomography for diagnosis of persistent hyperplastic primary vitreous (PHPV). Ophthalmology 1983. 90 (5) :442-451.
71 Mafee MF, Goldberg MF. Persistent hyperplastic primary vitreous (PHPV): role ot computed tomography and magnetic resonance. Radiol Clin North Am.1987 25 (4): 683-692.
72 Sun MH, Kao LY, Kuo YH. Persistent hyperplastic primary vitreous: magnetic resonance imaging and clinical findings. Chang Gung Med J. 2003;26(4):269-76.
73 Chang M, Mc Lean IW, Merritt JC: Coat's disease: a study of 62 histologically confirmed cases. J Pediatr Ophthalmol Strabismus 21: 163-168, 1984.
74 Kremer I, Nissehorn I, Ben-Sira I: Cytologic and biochemical examination of the subretinal fluid in the diagnosis of Coat's disease. Acta Ophthalmol (Copenh) 1989; 67: 342- 346.
75 Shields JA, Shields CL, Honavar SG, Demirci H, Cater J: Classification and management of Coats disease: the 2000 Proctor Lecture. Am J Ophthalmol 2001;131:572–583.
76 Mafee MF: Imaging of the globe. In: Valvassori GE, Mafee MF, Carter BL. Imaging of head and neck. Thieme: 216-246, 1995.
77 Haik BG: Advanced Coat's disease. Tr Am Ophth Soc 89: 371-475, 1991.
78 Steidl SM, Hirose T, Sang D t Al: Difficulties in exclud- ing the diagnosis of retinoblastoma in cases of advanced Coat's disease; a clinicopathologic report. Ophthalmo- logica 210: 336-340, 1996.
79 Woods AC, Duke JR. Coats's disease. I. Review of the literature, diagnostic criteria, clinical findings, and plasma lipid studies. Br J Ophthalmol 1963;47:385–412.
80 Shields JA, Shields CL. Review: Coats disease—the 2001 LuEsther T. Mertz lecture. Retina 2002;22(1):80–91.
81 Egerer I, Tasman W, Tomer TT. Coats disease. Arch Ophthalmol 1974;92(2):109–112.
82 Galluzzi P, Venturi C, Cerase A et al: Coat's disease: smaller volume of the affected globe. Radiology 221: 64- 69, 2001.
83 Kirath H, Eldem B. Management of moderate to ad- vanced Coat's disease. Ophthalmologica 212: 19-22, 1998.
84 Solomon A, Banin E, Anteby I et al: Retinitis pigmen-tosa, Coat's disease and uveitis. European Journal of Ophthalmology 9: 202-205, 1999.
85 Park DH, Kim IT. Patient with Parry-Romberg syndrome complicated by Coats' syndrome Jpn J Ophthalmol. 2008 ; 52(6):520-2.
86 Crow YJ, McMenamin J, Haenggeli CA, Hadley DM, Tirupathi S, Treacy EP, Zuberi SM, Browne BH, Tolmie JL, Stephenson JB. Coats' plus: a progressive familial syndrome of bilateral Coats' disease, characteristic cerebral calcification, leukoencephalopathy, slow pre- and post-natal linear growth and defects of bone-marrow and integument Neuropediatrics 2004, 35(1); 10-19.
87 Romaniello R1, Arrigoni F, Citterio A, Tonelli A, Sforzini C, Rizzari C, Pessina M, Triulzi F, Bassi MT, Borgatti R. Cerebroretinal microangiopathy with calcifications and cysts associated with CTC1 and NDP mutations. J Child Neurol. 2013,28(12):1702-8.
88 Coats G: Forms of retinal disease with massive exudation. R Lond Ophthalmol Hosp Res 17: 440-525, 1908.
89 Gomez Morales A: Coat's disease: natural history and results of treatment. Am J Ophthalmol 60: 855-865, 1965.
90 Tripathi R, Ashton N: Electron microscopical study of Coat's disease. Br J Ophthalmol 55: 289-301, 1971.
91 Spitznas M, Joussen F, Wessing A et Al: Coat's disease. An epidemiologic and fluorescein angiographic study. Albrecht Graefes Arch Klin Ophthalmol 195: 241-250, 1975.
92 Char DH: Coat's syndrome: long term follow up. Br J Ophthalmol 84: 37-39, 2000.
93 Deutsch TA, Rabb MF, Jampol LM: Spontaneous regression of retinal lesions in Coat's disease. Can J Ophthalmol 17: 169-172, 1982.
94 Jaffe MS, Shields JA, Canny CL et Al: Retinoblastoma simulating Coat's disease: a clinicopathologic report. Ann Ophthalmol 9: 863-868, 1977.
95 Atta HR, Watson N: Echographic Diagnosis of Advanced Coat's Disease. Eye 6: 80-85, 1992.
96 Sigler EJ, Randolph JC, Calzada JI, Wilson MW, Haik BG. Current management of Coats disease. Surv Ophthalmol. 2014;59(1):30-46.
97 Dhoot DS, Weissman LJ, Landon RE, Evans M, Stout T. Optic nerve enhancement in Coats disease with secondary glaucoma. Journal of AAPOS. 2009; 13 (3): 301-302.
98 Eisenberg L, Castillo M, Kwock L, Mukherji SK, Wallace DK. Proton MR spectroscopy in Coats disease. AJNR Am J Neuroradiol 1997;18(4):727–729.
99 Senft SH, Hidayat AA, Cavender JC: Atypical presentation of Coat's disease. Retina 14: 36-38, 1994.
100 Pe'er J: Calcifications in Coat's disease. Am J Ophthalmol 106: 742-743, 1988.
101 Shields JA, Shields CL: Intraocular tumors: a text and atlas. Philadelphia, Saunders vol 341, pp. 356-359, 1992.
102 Villablanca JP, Mafee MF, Kaufman LM et Al: Facies to remember. Retinoblastoma, Coat's disease, and toxocariasis. Int J Neuroradiol 4: 41-50, 1998.

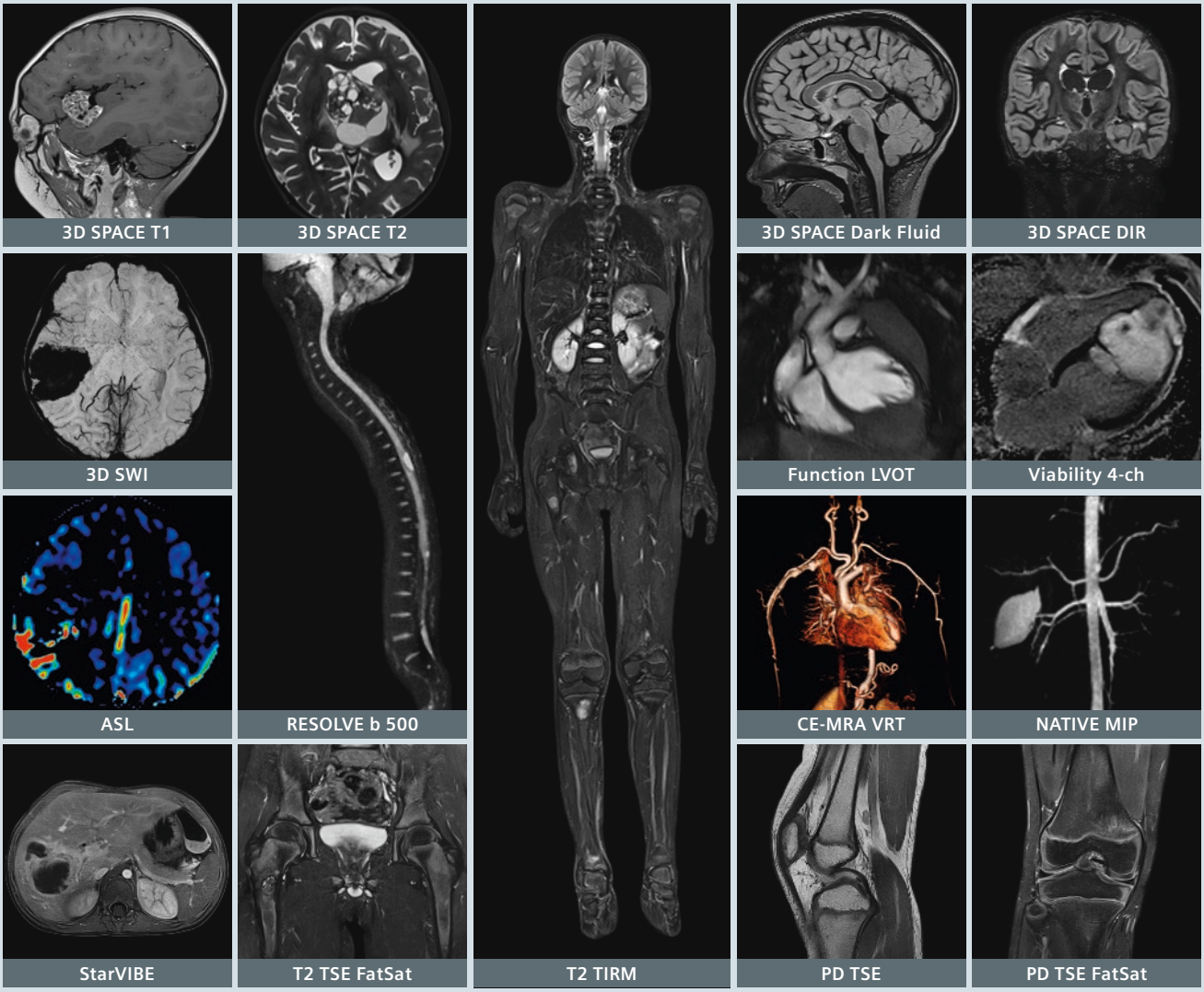


Contact

Paolo Galluzzi
Neuroimaging and Neuro-interventional Unit (NINT)
Azienda Ospedaliera e Universitaria Senese
Siena
Italy
galluzzip@libero.it

Siemens Pediatric* MRI

Caring for our youngest and most vulnerable



Images courtesy of:
Children's Hospital, Boston, USA; National Center for Child Health and Development, Tokyo, Japan; University Children's Hopsital Beider Basel, Basel, Switzerland; The Royal Children's Hospital, Melbourne, Australia; Children's Healthcare of Atlanta of Scottish Rite, Atlanta, USA; Children's MRI Centre & RCH 3T, Victoria, Australia; Cook Children's Hospital, Ft. Worth, USA; University Hospital Saarland, Homburg, Germany

Siemens offers innovative applications for pediatric MR imaging to answer all clinical questions:

- **Quiet Suite** for complete, quiet examinations for Neurology and Orthopedics
- **StarVIBE** for motion-insensitive, contrast-enhanced T1-weighted imaging
- **SPACE** for advanced 3D imaging capabilities, including SPACE DIR
- **ASL 2D** and **ASL 3D** for contrast-free perfusion evaluation of the brain
- **SWI** for the visualization of intra-venous deoxygenated blood and extravascular blood products
- **BLADE** for motion insensitive imaging throughout the body, in all directions
- **RESOLVE** for high-resolution, anatomy-true DWI and DTI of the brain and spine
- **REVEAL** for high quality, efficient diffusion-weighted imaging of the whole body
- **TWIST** for high temporal resolution MR angiography with low contrast dose
- **NATIVE** for contrast-free MR angiography
- **GRAPPA** and **CAIPIRINHA** with Tim 4G coils for faster imaging and minimal loss of SNR

*MR scanning has not been established as safe for imaging fetuses and infants less than two years of age. The responsible physician must evaluate the benefits of the MR examination compared to those of other imaging procedures.

Image Gallery MAGNETOM Amira



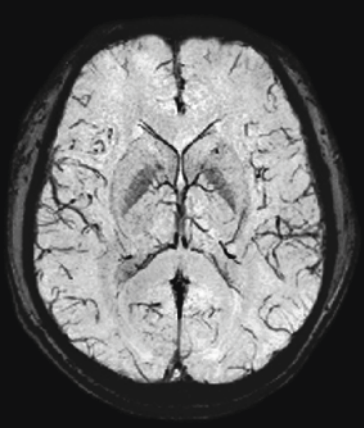
MAGNETOM Amira is the latest addition to Siemens 1.5T MRI portfolio. It is designed to provide answers to present day challenges including enhanced clinical capabilities while maintaining patient comfort and keeping ownership costs low.

Powered by the latest *syngo* MR E11 software and high density Tim 4G coils, MAGNETOM Amira delivers high quality images for all routine and advanced application.

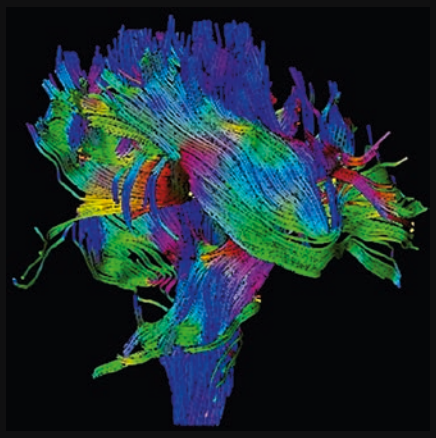
Here is a small collection of images from our clinical collaborators and early adopters around the world.



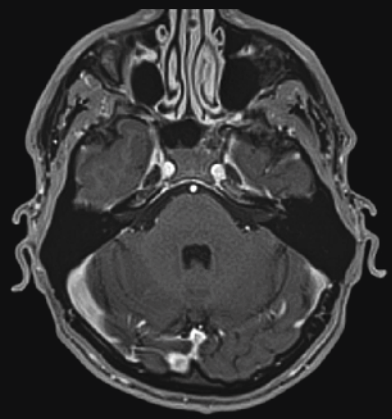
3D T1 SPACE, GRAPPA 2



3D SWI minIP, Quiet, GRAPPA 2

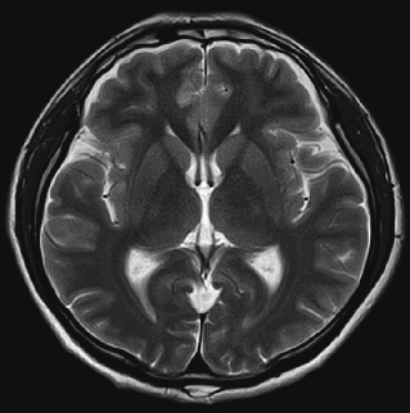


Diffusion, Fibertracking, 20 directions, GRAPPA 2

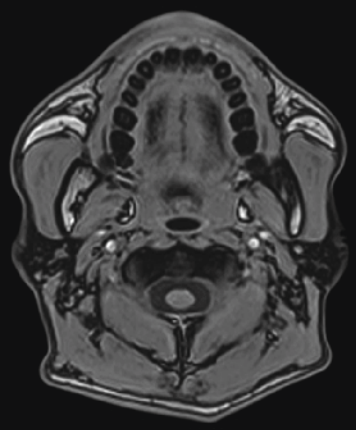


3D StarVIBE FatSat

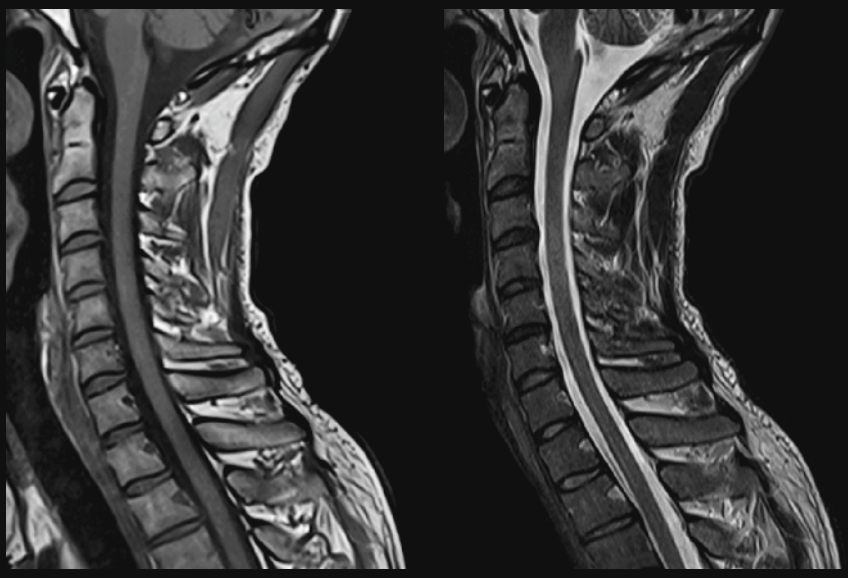
Courtesy of Radiologische Gemeinschaftspraxis, Halle, Germany



T2 TSE, Quiet, with BLADE



3D VIBE, opposed phase, GRAPPA 2



T1 TSE, Quiet

Courtesy of Radiologische Gemeinschaftspraxis, Halle, Germany



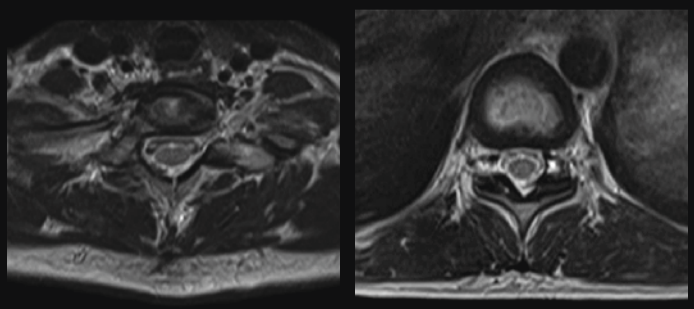
3D FLASH CE-MRA, MIP, GRAPPA 3

Courtesy of Radiologische Gemeinschaftspraxis, Halle, Germany



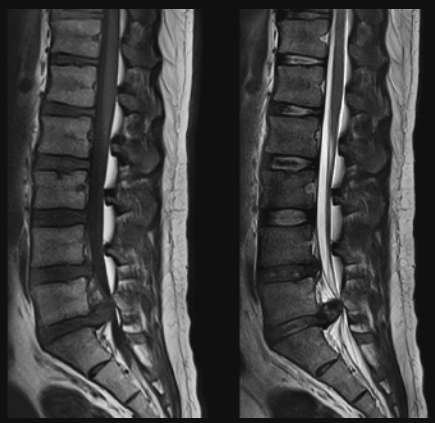
T1 TSE, GRAPPA 2 | T2 TSE, GRAPPA 2 | T2 TIRM, GRAPPA 2

Courtesy of Munakata Shukokai Sogo Hospital, Fukuoka, Japan



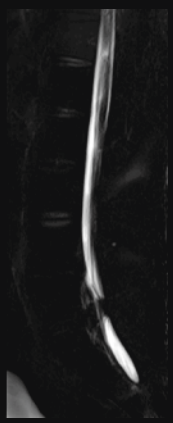
T2 TSE

Courtesy of Munakata Shukokai Sogo Hospital, Fukuoka, Japan

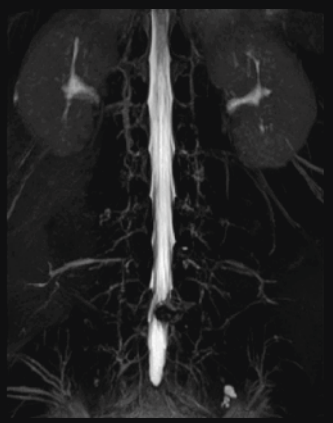


T1 TSE, GRAPPA 2 | T2 TSE, GRAPPA 2

Courtesy of Munakata Shukokai Sogo Hospital, Fukuoka, Japan



Myelography, T2 HASTE FatSat, thick slab, GRAPPA 2



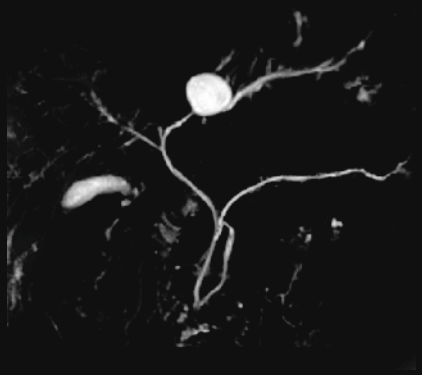
Myelograohy, 3D T2 SPACE FatSat, MIP, GRAPPA 2

Courtesy of Munakata Shukokai Sogo Hospital, Fukuoka, Japan



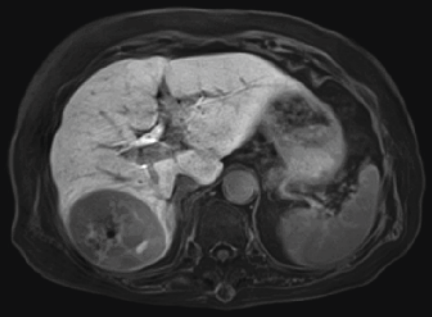
3D VIBE Dixon water, CAIPIRINHA 4

Courtesy of Radiologiezentrum, Schwabmuenchen, Germany



MRCP, 3D T2 SPACE FatSat, MIP, GRAPPA 2

Courtesy of Radiologische Gemeinschaftspraxis, Halle, Germany

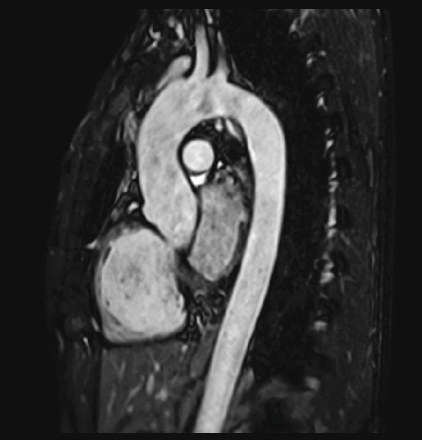


3D StarVIBE SPAIR

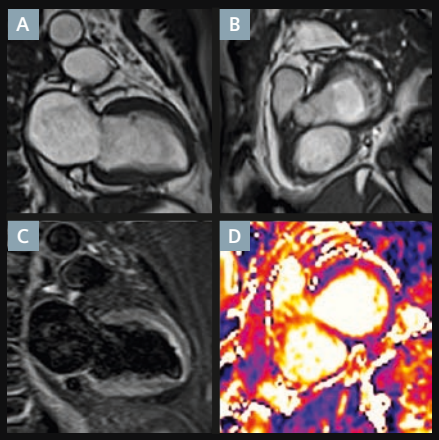
Courtesy of Munakata Shukokai Sogo Hospital, Fukuoka, Japan



T2 TIRM, GRAPPA 2,
3 steps composed



3D TrueFISP FatSat, MPR, GRAPPA 2

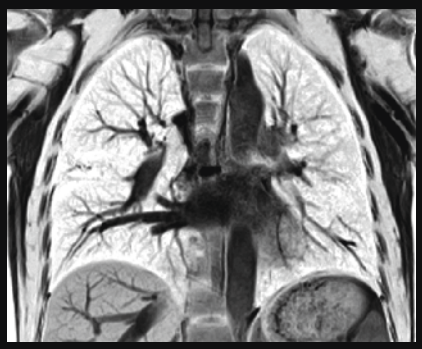


A, B: TrueFISP cine, GRAPPA 2

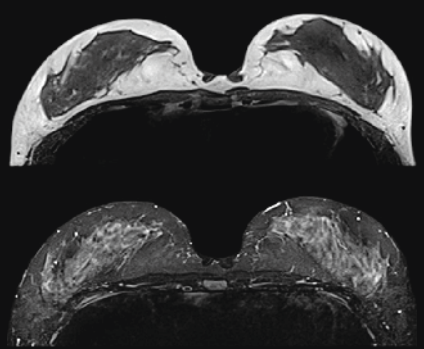
C: T2 TIRM Dark Blood

D: MyoMap T2, TrueFISP, GRAPPA 2

Courtesy of Radiologische Gemeinschaftspraxis, Halle, Germany

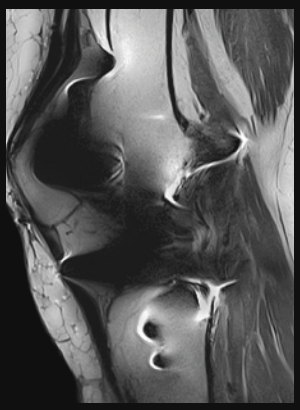


3D SPACE IR, thin MIP, inverted, GRAPPA 2

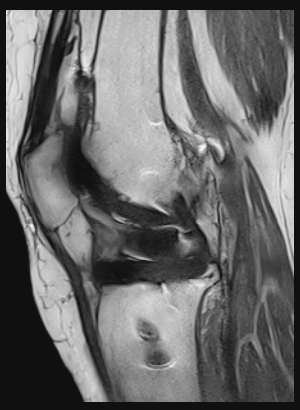


Upper row:
3D T1 FLASH, GRAPPA 3

Bottom row:
T2 TIRM, GRAPPA 3

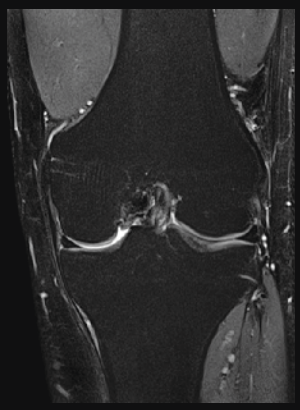


PD TSE, without metal artifact reduction, GRAPPA 2

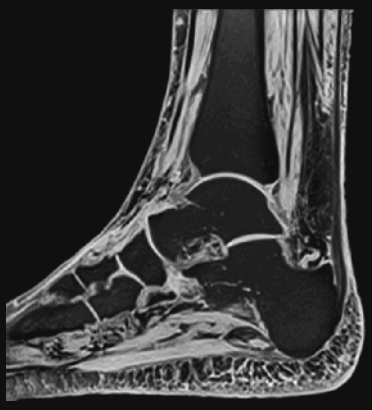


PD TSE, with WARP, SEMAC, GRAPPA 3

Courtesy of Radiologische Gemeinschaftspraxis, Halle, Germany



PD TSE FatSat, GRAPPA 2



3D VIBE water excitation

Courtesy of Radiologische Gemeinschaftspraxis, Halle, Germany



QISS, TrueFISP FatSat, MIP, GRAPPA 3, 9 steps composed



3D FLASH CE-MRA, MIP, GRAPPA 2, 3 steps composed



TWIST, 3D FLASH CE-MRA dynamic, MIP, GRAPPA 3

Courtesy of Radiologiezentrum, Schwabmuenchen, Germany

Standard Tim 4G coils



Head & Neck 16 *



Spine 18



Body 13



Flex Large 4 and Flex Small 4 *

Optional Tim 4G coils



Shoulder large and small *



Hand/Wrist *



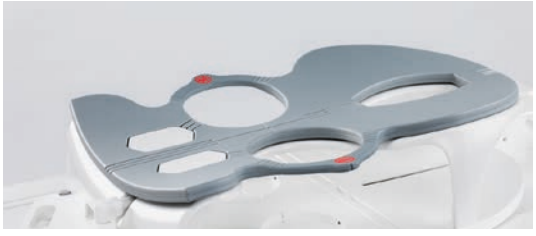
Breast 18 *



iTX Extremity 18



Foot/Ankle 16 *



4-Channel BI Breast coil *



Peripheral Angio 16

*Coils exchangeable with MAGNETOM Aera

Self-Navigated Free-Breathing High-Resolution 3D Cardiac Imaging: A New Sequence for Assessing Cardiovascular Congenital Malformations

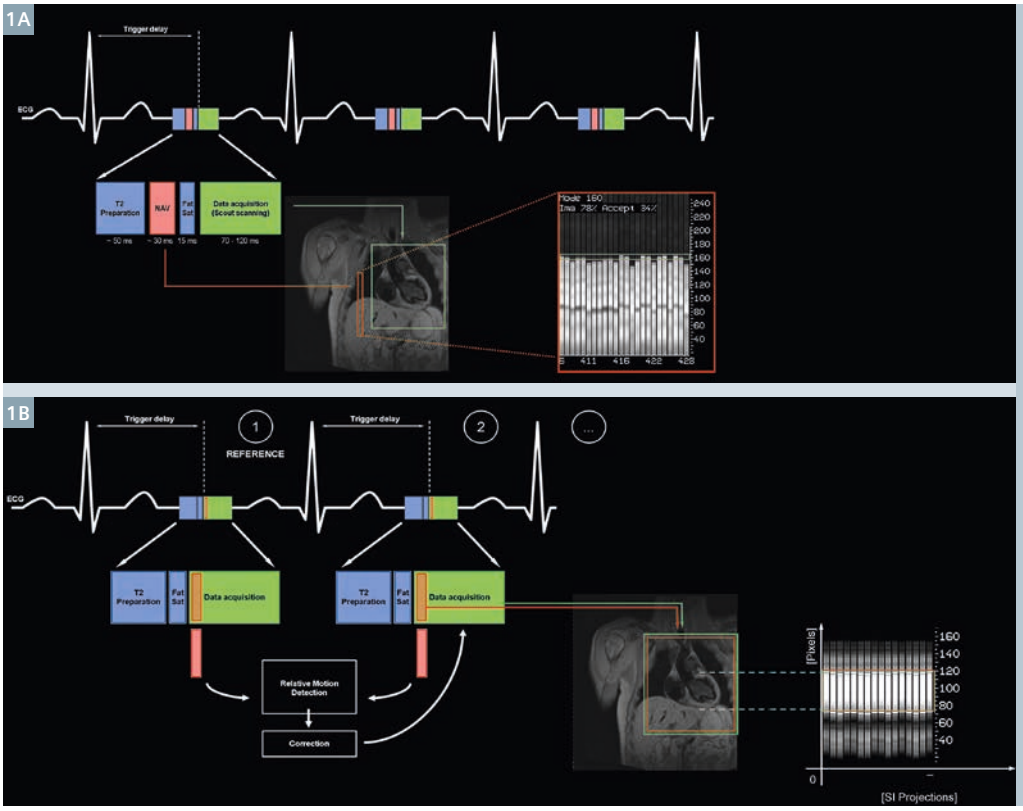
Pierre Monney, M.D.[1]; Davide Piccini[2]; Grégoire Berchier[1]; Tobias Rutz, M.D.[1]; Gabriella Vincenti[1]; Milan Prša, M.D.[3]; Nicole Sekarski, M.D.[3]; Matthias Stuber, Ph.D.[4]; Juerg Schwitter, M.D.[1]

[1] Division of Cardiology and Cardiac MR Center, University Hospital of Lausanne (CHUV), Lausanne, Switzerland
[2] Advanced Clinical Imaging Technology, Siemens Healthcare IM BM PI, Lausanne, Switzerland
[3] Unit of Pediatric Cardiology, Department of Pediatrics, University Hospital Lausanne (CHUV), Lausanne, Switzerland
[4] Department of Radiology, University Hospital (CHUV) and University of Lausanne (UNIL) / Center for Biomedical Imaging, (CIBM), Lausanne, Switzerland

Introduction

Congenital cardiac malformations occur in 9.1 per 1,000 live births [1] and range from simple defects including bicuspid aortic valve or isolated restrictive ventricular septal defect, to complex malformations requiring surgical correction or palliation early in life. While the neonatal mortality with such complex malformations remained stable, an important increase in life expectancy has been achieved with the advances in surgical treatment and the majority of the patients can nowadays reach adulthood [2].

As a consequence of this increase in life expectancy, the population of adult patients with congenital heart disease is growing [3]. Despite an optimal surgical correction or palliation, a regular follow-up of these patients is mandatory as they remain at higher risk for long-term cardiac complications including arrhythmia and heart failure [4, 5]. Cardiac imaging plays an important role in the follow-up of these patients to assess the morphology and function of the cardiac chambers and the valves, and to assess the integrity of any surgically implanted material. While echocardiography is used as the first-line imaging modality for initial diagnosis and follow-up assessments, cardiac magnetic resonance (CMR) is the



1 (**1A**) To consistently acquire data at the same respiratory position, a narrow acceptance window is defined, corresponding to the end-expiration, and only data acquired within this window are utilized in the final image reconstruction, while all other data segments are rejected and reacquired later during the scan. (**1B**) The position of the heart at the beginning of each data segment is compared with a reference position, i.e. the position of the ventricular blood-pool at the very first data segment, and automatically corrected for respiratory motion before the data are sent to the reconstruction pipeline.

modality of choice for the assessment of the right ventricle, the pulmonary arteries and veins, and for imaging extracardiac shunts or conduits [5].

Several consensus papers from scientific societies provide recommendations for standard CMR protocols adapted to the different cardiac malformations [6-9]. Three-dimensional whole-heart acquisitions are now routinely performed, especially for more complex malformations, as they allow the acquisition of a full volume of data during one single imaging sequence, including the heart and the intrathoracic vessels. This volume of data can be explored freely and specific 2D images can be extracted in any plane orientation during post-processing.

As CMR acquisitions are relatively slow and a high spatial resolution is required, the acquisition has to be segmented over several heartbeats. Additionally, the amount of data is so large that it cannot be acquired during one single breath-hold and respiratory motion compensation is needed for an adequate data acquisition during free-breathing.

Self-navigation: a new concept for respiratory motion compensation

Initially developed for coronary artery visualization, three-dimensional whole-heart navigator-based acquisitions have been used for over a decade to also assess the complex anatomy of congenital cardiac malformations [10]. These sequences rely on diaphragmatic respiratory navigation, where a pencil-beam navigator, usually placed on the dome of the right hemi-diaphragm, detects the respiratory position of the liver-lung interface along the superior-inferior direction for every heartbeat [11]. To consistently acquire data at the same respiratory position, a narrow acceptance window is defined, corresponding to the end-expiration, and only data acquired within this window are utilized in the final image reconstruction, while all other data segments are rejected and reacquired later during the scan (Fig. 1A). However, respiratory motion of the right hemidiaphragm and the heart are not tightly coupled, in particular during irregular breathing, when this correlation changes. As a result, data quality, especially during longer scans, can be inadequate if patients start to breath irregularly. In addition, with the navigator approach, acquisition duration is unpredictable and scan efficiency is typically in the order of 40% [12].

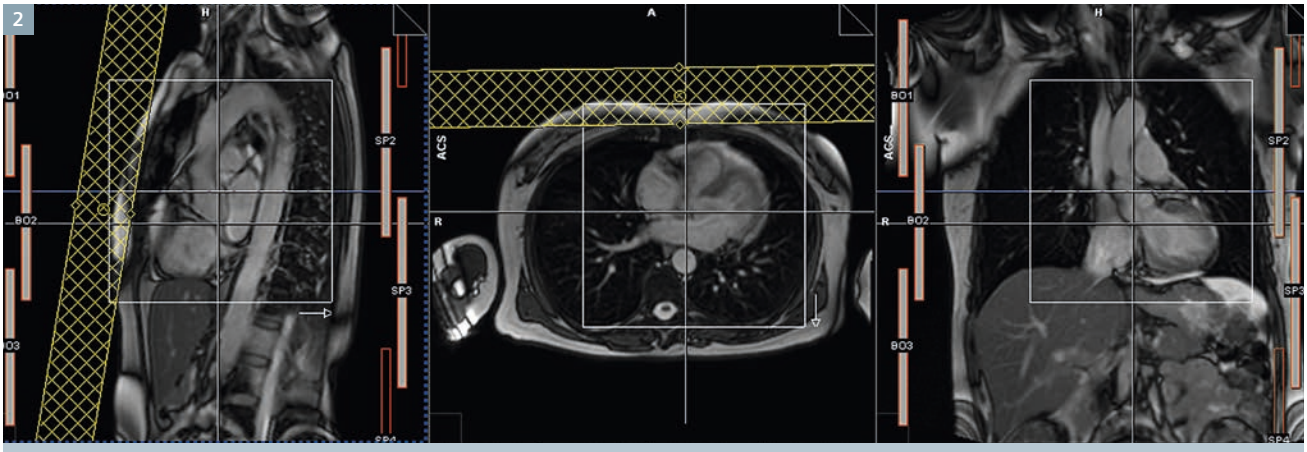
In order to address these limitations, respiratory self-navigation has been developed for coronary artery imaging [13-15]. With this strategy, the position of the heart itself is monitored over time and this approach should therefore also be robust in cases of irregular breathing. In addition, the respiratory motion information is extracted directly from the ventricular blood-pool signal throughout the respiratory cycle, so that navigator placement is not needed [13]. The prototype imaging sequence consists of a segmented 3D radial acquisition, intrinsically robust against motion, undersampling and foldover artifacts, with T2 and fat-saturation pre-pulses, and a balanced Steady-State Free Precessing (bSSFP) readout. The arrangement of the radial lines in *k*-space follows a spiral phyllotaxis pattern [16], with the first radial line of each acquired data segment (at each heartbeat) being consistently oriented in the superior-inferior direction, allowing for a 1D-detection of the cardiac displacement during the respiratory cycle. The position of the heart at the beginning of each data segment is thus compared with a reference position, i.e. the position of the ventricular blood-pool at the very first data segment, and automatically corrected for respiratory motion before the data are sent to the reconstruction pipeline (Fig. 1B). With this acquisition scheme, the respiratory motion correction reliably tracks the heart position and scan efficiency is typically 100%.

Characteristics of the sequence and planning strategy

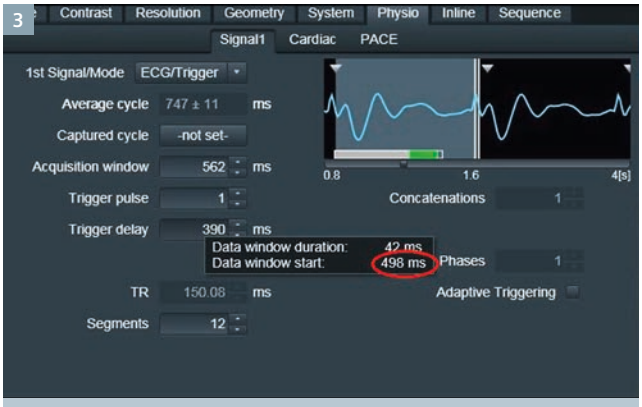
With the current version of this prototype sequence[1], a cubic field-of-view of 180-240 mm^3 is acquired with a 3D isotropic spatial resolution of 0.9-1.15 mm^3. Other important imaging parameters are TR 3.1 ms, TE 1.65 ms, matrix size (192)^3, receiver bandwidth 898 Hz/pixel, and RF excitation angle of 90°-115°. The trigger delay is selected to match one of the quiescent periods of the cardiac cycle – either mid-diastole or end-systole – previously identified on a standard four-chamber cine acquisition of the heart. The temporal resolution is adapted to the duration of the quiescent cardiac period, and may range from 18 to over 100 ms. A higher temporal resolution (= a lower number of lines per segment) has to be compensated by a higher number of heartbeats (= a higher number of shots) to ensure an adequate filling of the *k*-space. As a rule of thumb, we made sure that a minimum of 20% of the Nyquist sampling of *k*-space lines (= number of shots x number of lines per segment) were acquired, corresponding to a 6 to 12-minute scan duration, depending on the heart rate of the patient. The Nyquist undersampling ratio can be easily assessed by a tooltip that pops up when hovering the mouse pointer over the 'Radial Views' parameter in the Resolution tab.

The self-navigated 3D whole-heart acquisition is easy to use, as it avoids the placement of a pencil-beam navigator on the right hemi-diaphragm. The planning of the sequence is performed in two steps: 1) the *coil-localizer sequence* (allowing an automated selection of the receiver coils that will best detect the blood-pool signal for respiratory navigation) [17], and 2) the *data acquisition sequence*. The coil-localizer sequence is first selected, and the planning is simply using the axial, sagittal and coronal localizers. On each of these orthogonal planes, the cubic volume of acquisition is displayed as a square field-of-view, which has to be cen-

[1] The product is still under development and not commercially available yet. Its future availability cannot be ensured.



2 The cubic field-of-view is simply placed on the heart, while keeping the left ventricular blood-pool roughly in the center. A saturation band is placed on the anterior thoracic fat to reduce striking artifacts.



3 The trigger delay is selected, such that the data window start matches the onset of the quiescent period previously identified.

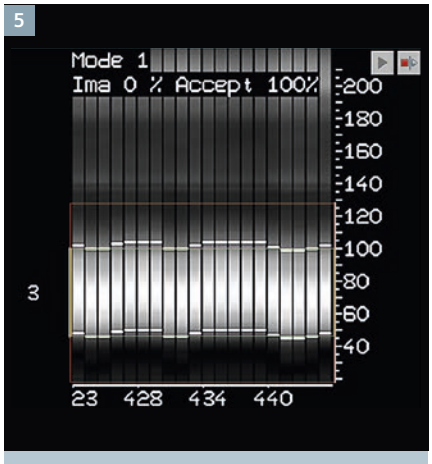


4 Depending on the duration of the quiescent period, the duration of the acquisition window can be modified, together with the number of heartbeats of acquisition (shots per slice), in order to keep the number of acquired *k*-space profiles over the above mentioned 20% of the Nyquist limit.

tered on the left ventricular blood-pool. A saturation band is placed on the anterior thoracic fat to reduce striking artifacts (Fig. 2). The coil-localizer sequence is started without a breath-hold, typically lasting a total of about 10 sec. The data acquisition sequence is then opened, and the positions of the acquisition volume and of the saturation band are simply copied from the coil-localizer sequence. The trigger delay is selected, such that the data window start matches the onset of the quiescent period previously identified (Fig. 3). Depending on the duration of the quiescent period, the duration of the acquisition window can be modified, together with the number of heartbeats of acquisition (shots per slice), in order to keep the number of acquired *k*-space profiles over the above mentioned 20% of the Nyquist limit (Fig. 4). The sequence is then started during free-breathing, and the quality of respiratory tracking can be checked in real time throughout the data acquisition, using the inline monitor (Fig. 5).

Experience in patients with congenital heart disease

Early experience with 3D self-navigated cardiac imaging was gained from small series of volunteers aiming at the visualization of the coronary arteries [13-15]. These early



5 The quality of respiratory tracking can be checked in real time throughout the data acquisition, using the inline monitor.

studies reported a good performance of the sequence with an image quality that was equal or better than that obtained with conventional diaphragm navigation [13]. The first single-center experience on patients was also reported for coronary artery assessment [14]. 78 patients were included, and the self-navigated 3D sequence was used with a spatial resolution of 1.15 x 1.15 x 1.15 mm^3. The proximal segments of the coronary arteries were visualized in 92% of cases and the distal segments in 56%. When compared to invasive coronary angiography (available for comparison in 31 patients), the sensitivity and specificity for the detection of a significant coronary artery stenosis were 65% and 85%, respectively.

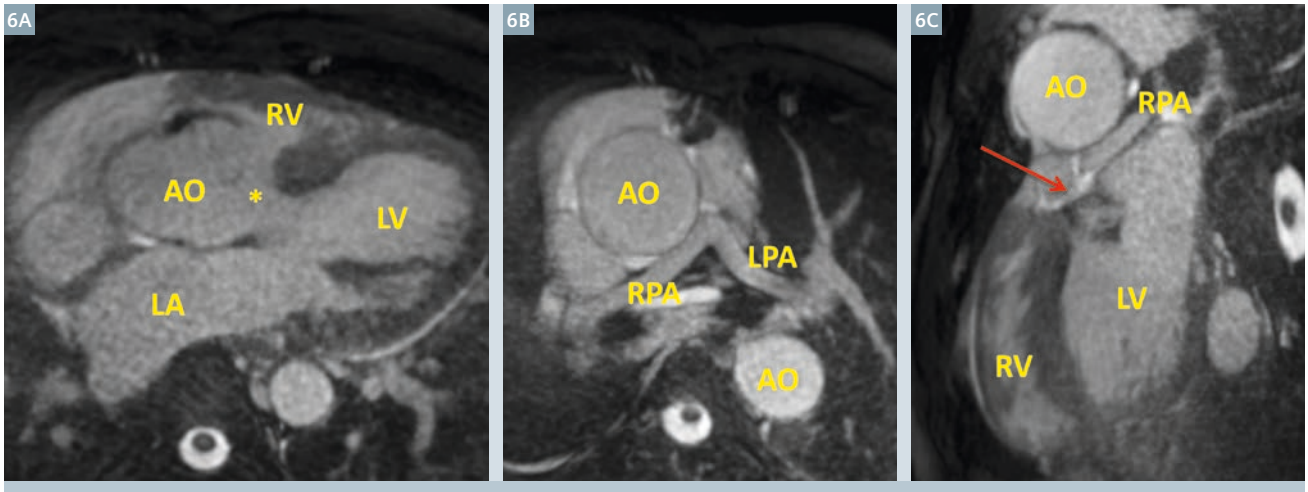
The first experience using the sequence for the characterization of congenital heart malformations was recently reported in a single-center series of 105 patients [18]. All examinations were performed on a 1.5T MAGNETOM Aera (Siemens Healthcare, Erlangen, Germany). The cohort included patients with ages ranging from 2 to 56 years (55% were males), and 44% had a complex cardiac malformation. The majority of the datasets (87%) were acquired after intravenous contrast injection (Gadovist, Bayer Schering Pharma, Zurich, Switzerland). While no direct head-to-head comparison with the conventional 3D whole-heart imaging sequence using diaphragm navigation was performed, this study aimed to assess the diagnostic performance and the image quality obtained with the new self-navigated sequence.

Using the 3D whole-heart self-navigated sequence alone, the systematic segmental anatomy of the heart and great vessels was correctly described in 93% to 96% of cases (by two different readers) and 93% to 95% of the residual uncorrected defects were correctly identified. Images were of diagnostic quality in 90% of cases and 70% were of good to excellent quality. Injection of intravenous contrast before image acquisition was associated with an improvement in image quality, resulting in a diagnostic image quality in 94% and a good to excellent image quality in 77% of the contrast-enhanced datasets. The origin and proximal course of the coronary arteries were visualized in 93%, 87% and 98% of the cases for the left anterior descending, left circumflex and right coronary artery, respectively, and all four patients of the cohort with an abnormal course of the coronary arteries were correctly identified. Finally, the measurement of the great arteries' diameters were very robust with a high intra-observer (coefficient of variation 3.5%) and inter-observer (coefficient of variation 5.0%) agreement.

27% of the patients were of pediatric[2] age (age <16) and the performance of the self-navigated 3D sequence also showed good results in this population. Despite the fact that fewer datasets were of good to excellent quality in children, a diagnostic image quality was obtained as frequently as in adult patients. This slight reduction in image quality might be attributed to a shorter quiescent period of the cardiac cycle with higher heart rates, or to the fact that dephasing artifacts, which may occur with high-velocity flows, more severely obscured the small vascular structures of pediatric patients.

Figure 6 shows 2D images reconstructed from a 3D whole-heart dataset acquired with self-navigation in a 47-year-old man with unoperated pulmonary atresia with a ventricular septal defect (VSD). 6A shows a large anterior mal-alignment VSD (*) with an overriding aorta. The branch pulmonary arteries are hypoplastic (6B) and there is fibrous atresia of the main pulmonary artery, located immediately behind the left atrial appendage (arrow on 6C).

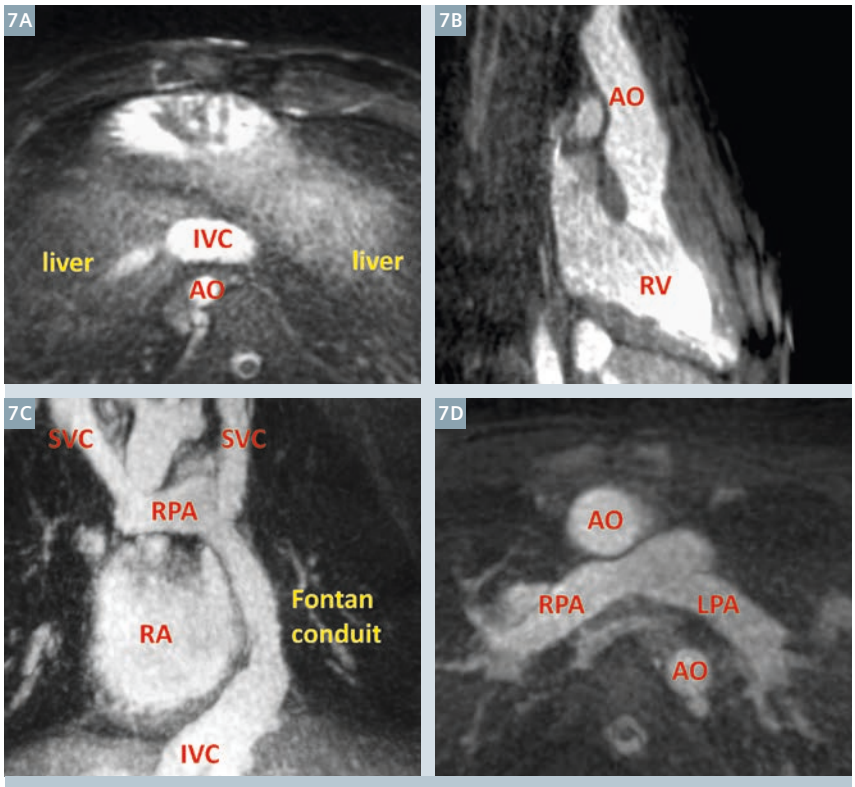
[2] MR scanning has not been established as safe for imaging fetuses and infants under two years of age. The responsible physician must evaluate the benefit of the MRI examination in comparison to other imaging procedures.



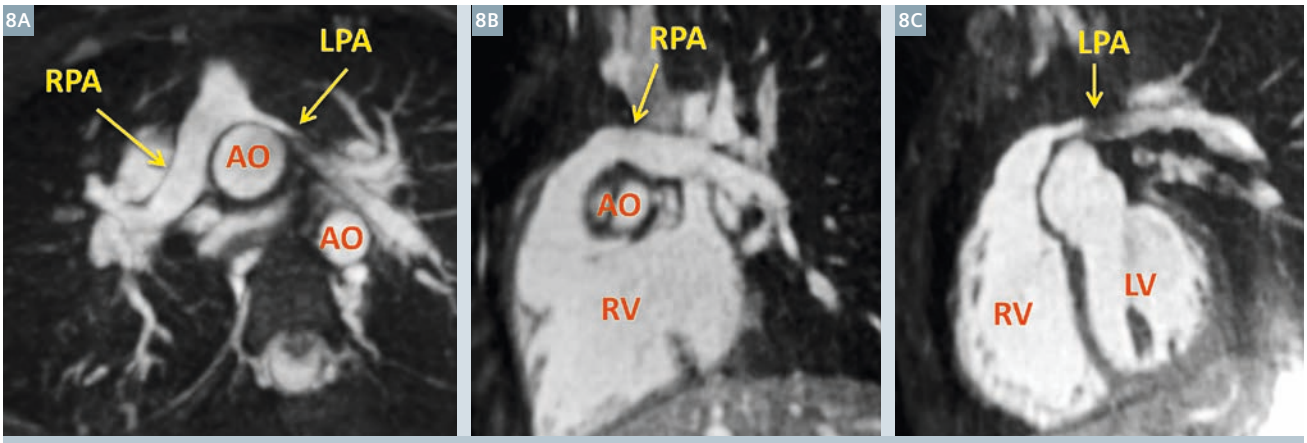
6 2D images reconstructed from a 3D whole-heart dataset acquired with self-navigation in a 47-year-old man with unoperated pulmonary atresia with a ventricular septal defect (VSD). **6A** shows a large anterior mal-alignment VSD (*) with an overriding aorta. The branch pulmonary arteries are hypoplastic (**6B**) and there is fibrous atresia of the main pulmonary artery, located immediately behind the left atrial appendage (arrow on **6C**).

Another example of complex cardiac anatomy is presented in Figure 7. This 27-year-old patient was born with right atrial isomerism, complete atrio-ventricular septal defect, total anomalous pulmonary venous return (TAPVR) and a single ventricle of right ventricular morphology. He underwent surgical correction of the TAPVR, followed by a bilateral Glenn operation and an extracardiac Fontan operation. 7A shows a large central liver and no spleen. The inferior vena cava (IVC) is located anterior to the descending aorta (AO). 7B shows the single ventricle with the typical characteristics of a right ventricle, connected to the ascending aorta. The systemic venous return is presented on 7C: both the right-sided superior vena cava (SVC) and the persistent left SVC are connected to the pulmonary arteries (bilateral Glenn), whereas the IVC is connected to the left pulmonary artery through an extracardiac conduit. 7D shows the normal-sized branch pulmonary arteries.

Good performance of the 3D self-navigated cardiac sequence is also demonstrated in children [18], as shown in the example presented in Figure 8. This 6-year-old patient, born with d-transposition of the great arteries, underwent an arterial switch operation. To connect the aorta to the left ventricle and the



7 This 27-year-old patient was born with right atrial isomerism, complete atrio-ventricular septal defect, total anomalous pulmonary venous return (TAPVR) and a single ventricle of right ventricular morphology. He underwent surgical correction of the TAPVR, followed by a bilateral Glenn operation and an extracardiac Fontan operation. **7A** shows a large central liver and no spleen. The inferior vena cava (IVC) is located anterior to the descending aorta (AO). **7B** shows the single ventricle with the typical characteristics of a right ventricle, connected to the ascending aorta. The systemic venous return is presented on **7C**: both the right-sided superior vena cava (SVC) and the persistent left SVC are connected to the pulmonary arteries (bilateral Glenn), whereas the IVC is connected to the left pulmonary artery through an extracardiac conduit. **7D** shows the normal-sized branch pulmonary arteries.



8 This 6-year-old patient, born with d-transposition of the great arteries, underwent an arterial switch operation. To connect the aorta to the left ventricle and the pulmonary artery to the right ventricle, the main pulmonary artery has to be displaced anteriorly to the ascending aorta by the surgeon. **8A** shows the typical anterior position of the main pulmonary artery with the branch pulmonary arteries running on either side of the aorta. In this patient, the right pulmonary artery is of normal size (**8B**) while the left pulmonary artery appears compressed by the ascending aorta. Flow acceleration in the LPA induces dephasing of the spins and appears as a low-signal artifact in the vessel (**8C**).

pulmonary artery to the right ventricle, the main pulmonary artery has to be displaced anteriorly to the ascending aorta by the surgeon. 8A shows the typical anterior position of the main pulmonary artery with the branch pulmonary arteries running on either side of the aorta. In this patient, the right pulmonary artery is of normal size (8B) while the left pulmonary artery appears compressed by the ascending aorta. Flow acceleration in the LPA induces dephasing of the spins and appears as a low-signal artifact in the vessel (8C).

Abnormal origin or course of the coronary arteries can be successfully detected with this sequence, as shown in Figure 9. This 4-year-old patient is known for a surgically corrected tetralogy of Fallot, associated with a coronary abnormality. As shown on 9A, all 3 coronary arteries originate from a single main stem connected to the right coronary sinus of the aortic root. On 9B, the course of the left anterior descending artery (LAD) is anterior to the main pulmonary artery. The left circumflex artery (LCx) has a proximal course between the aorta and the atria (9C), while the right coronary artery (RCA) has a normal course around the tricuspid annulus (9D). Such morphology – especially the presence of a LAD running anterior to the main pulmonary artery, is associated with a risk of coronary artery damage during the surgical correction of the right ventricular outflow tract obstruction. A precise identification of the coronary anatomy in these patients is therefore essential.

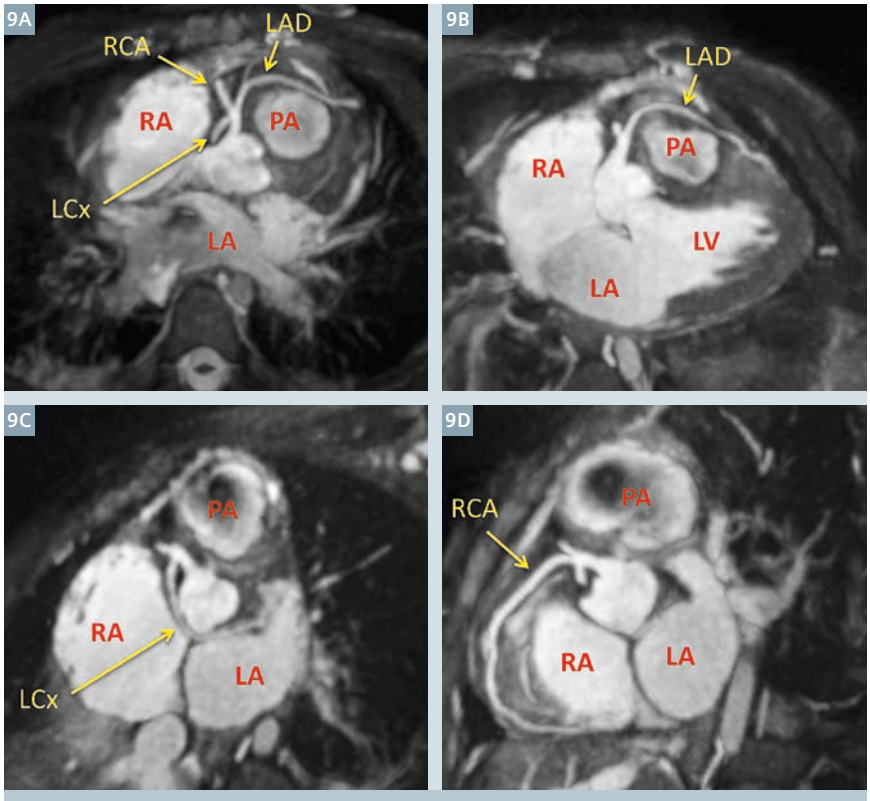
Discussion and conclusion

The self-navigated 3D cardiac imaging sequence is characterized by a great ease of use and a low operator interaction. The radial acquisition scheme renders the sequence immune to foldover artifacts and a high isotropic resolution is obtained over a relatively large field-of-view. The temporal resolution can be individually adapted to the heart rate, i.e. the duration of the quiescent period of the cardiac cycle, resulting in a 6 to 12 min acquisition duration, which can be known *a priori*.

With these characteristics, the sequence can be easily added to the standard imaging protocol of patients with congenital cardiac malformations. The performance of the sequence was considered very good in this population with a diagnostic image quality obtained in 94% of contrast-enhanced datasets and 93 to 96% of residual defects correctly detected. Despite the fact that very young children <2 years old were not included in the reported study, the performance of this sequence was good in the pediatric population[2] as well [18].

Further improvements are likely to be implemented to this sequence in the future, including the development of 3D rather than 1D respiratory motion compensation algorithms [19, 20], or strategies to selectively remove *k*-space lines associated with extreme respiratory positions [21], which were shown to further improve image quality.

In conclusion, the 3D self-navigated cardiac imaging sequence is characterized by its high robustness while providing high temporal and high isotropic spatial resolution. It may serve as an attractive tool for the three-dimensional assessment of congenital heart malformations in adults and children.



9 This 4-year-old patient has surgically corrected tetralogy of Fallot, associated with a coronary abnormality. As shown on **9A**, all 3 coronary arteries originate from a single main stem connected to the right coronary sinus of the aortic root. On **9B**, the course of the left anterior descending artery (LAD) is anterior to the main pulmonary artery. The left circumflex artery (LCx) has a proximal course between the aorta and the atria (**9C**), while the right coronary artery (RCA) has a normal course around the tricuspid annulus (**9D**).

Acknowledgement

The authors would like to thank all the members of the Center for Cardiac Magnetic Resonance of the

[2] MR scanning has not been established as safe for imaging fetuses and infants under two years of age. The responsible physician must evaluate the benefit of the MRI examination in comparison to other imaging procedures.

CHUV (CRMC, Prof Juerg Schwitter MD) and of the Center for Cardiovascular MR Research (CVMR, Prof Matthias Stuber PhD), as well as the MR technologists team at the CHUV for their active and excellent collaboration during this study. An important acknowledgement also goes to our colleagues from the pediatric cardiology unit and from the adult congenital heart disease clinic at the CHUV, Lausanne. Finally, we want to thank the Siemens Healthcare MR cardio team of Edgar Müller in Erlangen.

References

1 van der Linde D, Konings EE, Slager MA, et al. Birth prevalence of congenital heart disease worldwide: a systematic review and meta-analysis. Journal of the American College of Cardiology 2011;58:2241-7.

2 Wren C, O'Sullivan JJ. Survival with congenital heart disease and need for follow up in adult life. Heart 2001;85:438-43.

3 Marelli AJ, Mackie AS, Ionescu-Ittu R, Rahme E, Pilote L. Congenital heart disease in the general population: changing prevalence and age distribution. Circulation 2007;115:163-72.

4 Bouchardy J, Therrien J, Pilote L, et al. Atrial arrhythmias in adults with congenital heart disease. Circulation 2009;120:1679-86.

5 Baumgartner H, Bonhoeffer P, De Groot NM, et al. ESC Guidelines for the management of grown-up congenital heart disease (new version 2010). European heart journal 2010;31:2915-57.

6 Kilner PJ, Geva T, Kaemmerer H, Trindade PT, Schwitter J, Webb GD. Recommendations for cardiovascular magnetic resonance in adults with congenital heart disease from the respective working groups of the European Society of Cardiology. European heart journal 2010;31:794-805.

7 Kilner P, Valsangiacomo Buechel E, Schwitter J. Congenital Heart Diseases in Adults. In: Schwitter J, ed. CMR Update. 2. Edition ed. Lausanne, Switzerland: Schwitter, J. www.herz-mri.ch; 2012:136-55.

8 Fratz S, Chung T, Greil GF, et al. Guidelines and protocols for cardiovascular magnetic resonance in children and adults with congenital heart disease: SCMR expert consensus group on congenital heart disease. Journal of cardiovascular magnetic resonance : official journal of the Society for Cardiovascular Magnetic Resonance 2013;15:51.

9 Valsangiacomo Buechel ER, Grosse-Wortmann L, Fratz S, et al. Indications for cardiovascular magnetic resonance in children with congenital and acquired heart disease: an expert consensus paper of the Imaging Working Group of the AEPC and the Cardiovascular Magnetic Resonance Section of the EACVI. European heart journal cardiovascular Imaging 2015;16:281-97.

10 Sorensen TS, Korperich H, Greil GF, et al. Operator-independent isotropic three-dimensional magnetic resonance imaging for morphology in congenital heart disease: a validation study. Circulation 2004;110:163-9.

11 Wang Y, Rossman PJ, Grimm RC, Riederer SJ, Ehman RL. Navigator-echo-based real-time respiratory gating and triggering for reduction of respiration effects in three-dimensional coronary MR angiography. Radiology 1996;198:55-60.

12 Kato S, Kitagawa K, Ishida N, et al. Assessment of coronary artery disease using magnetic resonance coronary angiography: a national multicenter trial. J Am Coll Cardiol 2010;56:983-91.

13 Piccini D, Littmann A, Nielles-Vallespin S, Zenge MO. Respiratory self-navigation for whole-heart bright-blood coronary MRI: methods for robust isolation and automatic segmentation of the blood pool. Magnetic resonance in medicine 2012;68:571-9.

14 Piccini D, Monney P, Sierro C, et al. Respiratory self-navigated postcontrast whole-heart coronary MR angiography: initial experience in patients. Radiology 2014;270:378-86.

15 Stehning C, Bornert P, Nehrke K, Eggers H, Stuber M. Free-breathing whole-heart coronary MRA with 3D radial SSFP and self-navigated image reconstruction. Magnetic resonance in medicine 2005;54:476-80.

16 Piccini D, Littmann A, Nielles-Vallespin S, Zenge MO. Spiral phyllotaxis: the natural way to construct a 3D radial trajectory in MRI. Magnetic resonance in medicine 2011;66:1049-56.

17 Piccini D, Marechal B, Coppo S, et al. Automated and Subject-Specific Coil Selection for Respiratory Self-Navigation in Coronary MRA. Proc Intl Soc Mag Reson Med. Milan2014:2503.

18 Monney P, Piccini D, Rutz T, et al. Single centre experience of the application of self navigated 3D whole heart cardiovascular magnetic resonance for the assessment of cardiac anatomy in congenital heart disease. Journal of cardiovascular magnetic resonance : official journal of the Society for Cardiovascular Magnetic Resonance 2015;17:55.

19 Henningsson M, Prieto C, Chiribiri A, Vaillant G, Razavi R, Botnar RM. Whole-heart coronary MRA with 3D affine motion correction using 3D image-based navigation. Magnetic resonance in medicine 2014;71:173-81.

20 Pang J, Sharif B, Arsanjani R, et al. Accelerated whole-heart coronary MRA using motion-corrected sensitivity encoding with three-dimensional projection reconstruction. Magnetic resonance in medicine 2014.

21 Chaptinel J, Piccini D, Coppo S, Bonanno G, Schwitter J, Stuber M. Optimized Data Selection for 3D Radial Self-Navigated Whole-Heart Coronary MRA. MRA Club; 2013; New York City, New York, USA.



Pierre Monney



Juerg Schwitter

Contact

Professor Juerg Schwitter
Médecin Chef Cardiologie
Directeur du Centre de la RM Cardiaque du CHUV
Centre Hospitalier Universitaire Vaudois – CHUV
Rue du Bugnon 46, 1011 Lausanne, Switzerland
Phone: +41 21 314 0012
jurg.schwitter@chuv.ch
www.cardiologie.chuv.ch

Further reading

For more images and quantitative analyses on this study, please refer to the newly published paper in Reference 18.



Advertisement



A smart addition to your team

Make a smart move with Bayer's new MR SMART Injection System.

The Medrad® MRXperion™ MR Injection System delivers improved efficiencies, personalized care and reproducible quality... all backed by on-site field service and VirtualCare® Remote Support for maximum uptime and patient throughput.

- Automated fluid delivery and streamlined workflow
- Modality worklist* connectivity and protocol storage/retrieval
- Accurate procedure data recording and reporting

Learn more and schedule a personalized demo today!

radiology.bayer.com

*Requires Certegra® @ Point of Care software.

MEDRAD® MRXperion™
MR Injection System

© 2015 Bayer
Bayer, the Bayer Cross, MEDRAD®, Certegra®, VirtualCare® and MRXperion™ are trademarks of the Bayer group of companies.

PP-MRX-US-0021 October 2015

Utility of Delayed Enhanced Cardiac MRI in the Assessment of Cardiomyopathies

Mohamad G. Ghosn, Ph.D.[1]; Kongkiat Chaikriangkrai, M.D.[1]; Itamar Birnbaum, M.D.[2]; Gary McNeal, MS (BME)[3]; Dipan J. Shah, M.D.[1]

[1] Houston Methodist Hospital, Houston, TX, USA
[2] Baylor College of Medicine, Houston, TX, USA
[3] Siemens Healthcare, Malvern, PA, USA

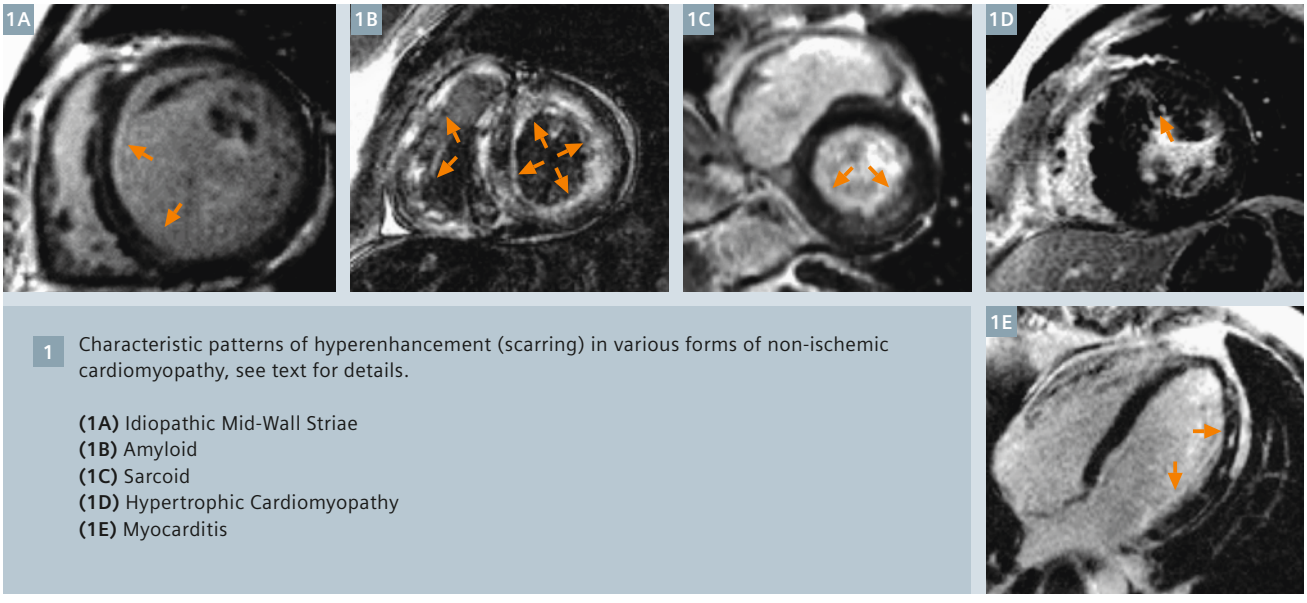
Introduction

Heart failure (HF) is a major public health problem in the United States, with over 5 million individuals afflicted, and well over 600,000 new cases diagnosed each year resulting in a direct and indirect cost in the United States of nearly $35 billion annually [1]. While coronary artery disease (CAD) is the leading cause of left ventricular (LV) dysfunction, anywhere from a third to a half of all patients have LV dysfunction in the absence of significant epicardial CAD [2]. Most of these patients are labeled with the general diagnosis of idiopathic non-ischemic cardiomyopathy (NICMP), as no direct discernable etiology of their myocardial dysfunction is evident. Identification of the specific etiology of HF in these patients with NICMP can have important prognostic implications [3]. However the traditional imaging modalities such as echocardiography, nuclear scintigraphy, or coronary angiography are limited in their ability to specifically evaluate the myocardium and to perform tissue characterization. In fact even the utility of endomyocardial biopsy is uncertain because of frequent non-specific findings, and the inherent invasiveness and small but finite risk of the procedure [4].

In recent years, delayed contrast enhancement (DE) cardiac magnetic resonance (CMR) has emerged as a powerful non-invasive technique for direct assessment of myocardial structure and tissue characterization. Studies have demonstrated its ability to detect both irreversible acute ischemic injury and chronic myocardial infarction (MI) with a high level of accuracy [5-8]. Using this same technique in patients with NICMP has enabled the detection of unique patterns of myocardial scarring which aid in identifying a specific etiology of NICMP and therefore help provide additional prognostic information and occasionally drastically alter patient management. The focus of this article will be to describe the potential role of DE-CMR in assessment of patients with cardiomyopathy.

Idiopathic dilated cardiomyopathy

An early study by McCrohon et al. [9] studied a population of 90 patients with heart failure and LV dysfunction consisting of 63 with idiopathic dilated cardiomyopathy and 27 with ischemic cardiomyopathy. Of the 27 patients with ischemic cardiomyopathy, all had a history of myocardial infarction and all had a myocardial hyperenhancement pattern involving the subendocardium. Of the 63 patients with idiopathic dilated cardiomyopathy, 59% had no hyperenhancement, 13% had hyperenhancement involving the subendocardium (similar to that found in ischemic cardiomyopathy) and 28% had hyperenhancement in



1 Characteristic patterns of hyperenhancement (scarring) in various forms of non-ischemic cardiomyopathy, see text for details.

(1A) Idiopathic Mid-Wall Striae
(1B) Amyloid
(1C) Sarcoid
(1D) Hypertrophic Cardiomyopathy
(1E) Myocarditis

an unusual pattern, primarily involving the ventricular midwall with subendocardial sparing.

In a recent study we evaluated 45 patients with symptomatic heart failure and evidence of significant LV systolic dysfunction (LVEF < 35% on invasive ventriculography or echocardiography). 28 patients had ischemic cardiomyopathy and 17 had idiopathic dilated cardiomyopathy. In this study, hyperenhancement patterns consistent with prior myocardial infarction were identified; linear midwall striae with increased image intensity were not scored as hyperenhanced regions. Interestingly, the findings demonstrated that all patients with ischemic cardiomyopathy had hyperenhancement, whereas only 12% of patients with idiopathic dilated cardiomyopathy had hyperenhancement. When we tested clinical parameters for their utility in distinguishing ischemic from non-ischemic cardiomyopathy, we found that the best discriminator was the presence of hyperenhancement on DE-MRI which had a 100% sensitivity, 88% specificity, and 96% overall accuracy for the detection of ischemic disease.

In this study, 100% of patients with ischemic cardiomyopathy had evidence of hyperenhancement, despite the fact that only 50% had clinical history of myocardial infarction. This finding is consistent with necropsy studies that have demonstrated that virtually all patients with congestive heart failure and significant coronary artery disease have gross myocardial scarring at autopsy, even in those without clinical history of MI, angina, or Q-waves [10, 11]. Conversely, we observed in patients with idiopathic dilated cardiomyopathy that hyperenhancement was uncommon. This finding is also consistent with previous studies. Roberts et al. [12] found grossly visible scars at cardiac necropsy in 14% of patients with idiopathic dilated cardiomyopathy. Uretsky et al. [13] evaluated chronic heart failure patients at autopsy and found old infarcts in 12% of patients without coronary artery disease. A number of mechanisms may be responsible for myocardial infarction in patients without coronary artery disease, including coronary vasospasm, thrombosis with spontaneous lysis superimposed on minimal atherosclerosis, or coronary emboli. Regardless of the mechanism, myocardial infarction in the absence of coronary artery disease is rare, and the findings in this study suggest that DE-MRI may be useful in distinguishing ischemic from non-ischemic cardiomyopathy non-invasively. One caveat, however, should be noted. The non-CAD cohort in the study by McCrohon [9] included only patients with idiopathic dilated cardiomyopathy, as patients with other forms of non-ischemic cardiomyopathy, such as hypertrophic cardiomyopathy, myocarditis, and infiltrative cardiomyopathy, were excluded at the time of enrollment.

Hypertrophic cardiomyopathy

Hypertrophic cardiomyopathy (HCM) is the most frequently occurring genetic cardiomyopathy [14]. Several studies have described DE-MRI findings in patients with hypertrophic cardiomyopathy (HCM). Choudhury et al. [15] enrolled 21 patients who were thought to be representative of the majority of community patients with HCM, since they were identified by routine outpatient screening procedures and were generally asymptomatic or minimally symptomatic. Patients with concomitant CAD were excluded. In this study, cine MRI demonstrated that the maximum LV end-diastolic wall thickness averaged 25 ± 8 mm, and the LV ejection fraction was preserved (70 ± 11%). DE-MRI demonstrated that hyperenhancement was found in the majority of patients (81%), and hyperenhancement mass was on average 8 ± 9% of the left ventricular mass. The pattern of hyperenhancement, however, was peculiar. Hyperenhancement occurred only in hypertrophied regions, was patchy with multiple foci, and predominately involved the middle third of the ventricular wall. Additionally, all patients with hyperenhancement had involvement at the junctions of the interventricular septum and the RV free wall. On a regional basis, there was a modest correlation between the extent of hyperenhancement and end-diastolic wall thickness ($r = 0.36$, $p < 0.0001$). No region with end-diastolic wall thickness < 10 mm had any hyperenhancement. There was also a significant but inverse correlation between the extent of hyperenhancement and systolic wall thickening ($r = -0.21$, $p < 0.0001$).

Although a number of pathophysiological processes are evident in hypertrophic cardiomyopathy, Choudhury et al. interpreted hyperenhancement in HCM as specifically representing myocardial scarring. The rationale for this assumption is discussed at length in an editorial [16] and data by Moon et al. [17] suggests that this assumption is valid. In a patient that underwent heart transplantation after *in vivo* DE-MRI, followed by detailed histological analysis of the explanted heart, there was a significant relationship, regionally, between the extent of hyperenhancement and the amount of myocardial fibrosis ($r = 0.7$, $p < 0.0001$) but not disarray.

Moon et al. [18] performed DE-MRI in 53 patients selected from a dedicated HCM clinic. Overall, hyperenhancement was found in 79% of patients, a figure quite similar to that found by Choudhury et al. This study, however, also compared DE-MRI findings to the presence of clinical risk factors for sudden death in HCM (e.g. non-sustained ventricular tachycardia, syncope, family history of premature cardiac death, etc.), and to progressive adverse LV remodeling. Interestingly, the authors observed that there was a greater extent of hyperenhancement in patients with two or more risk factors for sudden death (15.7% vs. 8.6%, $p = 0.02$) and in patients with progressive remodeling (28.5% vs. 8.7% of LV mass, $p < 0.001$).

Since hyperenhancement was observed in approximately 80% of patients in both the study by Choudhury et al. and Moon et al., the presence of hyperenhancement in itself cannot be indicative of an adverse prognosis. However, it is possible that the amount of hyperenhancement – indicative of the amount of

scarring – may be an important prognostic determinant. This hypothesis is currently being tested in observational clinical trials.

Myocarditis

Clinical manifestation of myocarditis or inflammatory cardiomyopathy varies with a broad spectrum of symptoms ranging from asymptomatic signs to myocardial infarction and cardiogenic shock. Myocarditis can occasionally lead to sudden death and may progress to dilated cardiomyopathy in up to 10% of patients [19]. Endomyocardial biopsy is considered as gold standard for diagnosis. It is an invasive procedure and has limited sensitivity and specificity. A noninvasive and effective diagnostic imaging modality is CMR. Cine imaging shows wall motion abnormalities that are matched by areas of scar on DE-CMR. The scar pattern frequently involves the epicardial myocardium of the lateral wall.

Mahrholdt et al. [19] performed DE-MRI in 32 patients who were diagnosed with myocarditis by clinical criteria. Hyperenhancement was found in 28 of 32 patients (88%). Of the 21 patients in whom myocardial biopsy was obtained from the region of hyperenhancement, histopathological analysis revealed active myocarditis in 19. Hyperenhancement was usually observed in a patchy distribution originating primarily from the epicardial quartile of the wall with one or several foci with a predilection for the lateral free wall. The pattern and distribution of hyperenhancement found in this study are consistent with that of myocardial lesions found in postmortem evaluations in patients with myocarditis [20]. The potential mechanism for hyperenhancement in myocarditis was postulated to be similar to that for coronary artery disease: either acute necrosis with cell membrane rupture for acute lesions, or myocardial scarring and fibrosis for chronic lesions. If true, this mechanism would imply that the presence, location, and total extent of irreversible myocardial damage that occurs in a patient with myocarditis could be determined noninvasively by DE-MRI.

Amyloid

Cardiac involvement is seen with primary amyloidosis (AL) and is an example of infiltrative cardiomyopathy [24]. Cardiac amyloid is associated with a poor prognosis with a median survival of 6 months [24, 25]. Diagnosis of cardiac involvement requires multiple endomyocardial biopsies, each biopsy specimen has a 55% sensitivity for the detection of amyloid protein [26]. CMR is a noninvasive diagnostic tool that can identify patients and guide biopsies to areas of scarring for improved sensitivity. Cine CMR shows a restrictive morphology. DE-CMR shows early diffuse heterogeneous enhancement and this proves difficult to null the myocardial signal at standard inversion time (TI). This leads to difficulty in distinguishing normal from abnormal myocardium. Inversion time scout images are obtained over a range of TI times to identify the TI time corresponding to the null point of the blood-pool and the myocardium. Amyloid protein deposits in the intercellular spaces and this plays a major role in the pattern of hyperenhancement seen on DE-CMR. According to Maceira et al. there was 97% concordance in diagnosis of cardiac amyloid by combining the presence of late gadolinium enhancement and an optimized T1 threshold (191 ms at 4 minutes) between myocardium and blood. DE-CMR pattern shows scar in the subendocardium and mid wall distributions [27].

Sarcoidosis

Myocardial involvement is evident in about 5% of patients with sarcoidosis, however, autopsy studies have shown up to 50% of cases of noncaseating granulomas in fatal sarcoidosis [28]. In one study by Smedema et al. CMR was performed for evaluation of cardiac sarcoidosis in 58 patients with biopsy proven pulmonary sarcoidosis and it showed a DE-CMR pattern mostly involving basal and lateral segments in 19 patients [29]. In 8 of the 19 patients patchy scar was present. The sensitivity and specificity of CMR were 100% and 78%, and the positive and negative predictive values were 55% and 100%, respectively, with an overall accuracy of 83%. Sudden cardiac death is a leading cause of mortality in this population [30]. We hypothesize that the presence and extent of hyperenhancement on DE-CMR may be directly related to the risk of sudden cardiac death in this population.

Risk stratification for sudden death

Scarred myocardium is an established anatomical and electrophysiological substrate for the occurrence of ventricular tachyarrhythmias and sudden death in patients with CAD [31]. The ability of DE-MRI to accurately detect the presence and extent of scarred myocardium may make it uniquely suited to noninvasively identify individuals with substrate for sudden death. Some recent pilot data comparing DE-MRI findings to results at electrophysiological study (EPS) suggests that this hypothesis is valid [32]. For example, of the total of 58 patients studied, 18 were determined to be at high risk for sudden death by EPS (inducible monomorphic ventricular tachycardia), and all 18 had myocardial scarring on DE-MRI. Conversely, none of the 22 patients without scarring had inducible monomorphic VT. On multivariate analysis, scar size by DE-MRI was found be the best independent predictor of inducibility at EPS.

Earlier in this section, we noted that hyperenhancement can be observed in patients with non-ischemic cardiomyopathy, particularly in those with hypertrophic and infiltrative forms of disease. Although there is currently less evidence linking scarred myocardium to sudden death in patients without CAD, there is reason to believe that scar tissue can serve as substrate for malignant ventricular tachyarrhythmias in these patients as well [16]. Therefore, we hypothesize that DE-MRI will provide important prognostic information for patients with a wide range of myocardial disorders. Studies are currently underway to evaluate for a relationship between sudden cardiac death and the presence, extent, or morphology of myocardial scar.

Conclusion

Delayed enhancement CMR is proving to be an invaluable tool in the evaluation of patients with cardiomyopathy. Although a number of studies have been performed in the past decade, significant work still remains to be done. The utility of CMR on evaluation of cardiomyopathies is yet to be fully explored; the authors speculate that CMR will be an integral part of the evaluation of these patients for years to come.

References

1 Rosamond, W., et al., Heart Disease and Stroke Statistics 2008 Update. A Report From the American Heart Association Statistics Committee and Stroke Statistics Subcommittee. Circulation, 2007.

2 Fox, K.F., et al., Coronary artery disease as the cause of incident heart failure in the population. Eur Heart J, 2001. 22(3): p. 228-36.

3 Felker, G.M., et al., Underlying causes and long-term survival in patients with initially unexplained cardiomyopathy. N Engl J Med, 2000. 342(15): p. 1077-84.

4 Hunt, S.A., et al., ACC/AHA 2005 Guideline Update for the Diagnosis and Management of Chronic Heart Failure in the Adult: a report of the American College of Cardiology/American Heart Association Task Force on Practice Guidelines (Writing Committee to Update the 2001 Guidelines for the Evaluation and Management of Heart Failure): developed in collaboration with the American College of Chest Physicians and the International Society for Heart and Lung Transplantation: endorsed by the Heart Rhythm Society. Circulation, 2005. 112(12): p. e154-235.

5 Kim, R.J., et al., Relationship of MRI delayed contrast enhancement to irreversible injury, infarct age, and contractile function. Circulation, 1999. 100(19): p. 1992-2002.

6 Fieno, D.S., et al., Contrast-enhanced magnetic resonance imaging of myocardium at risk: distinction between reversible and irreversible injury throughout infarct healing. J Am Coll Cardiol, 2000. 36(6): p. 1985-91.

7 Hillenbrand, H.B., et al., Early assessment of myocardial salvage by contrast-enhanced magnetic resonance imaging. Circulation, 2000. 102(14): p. 1678-83.

8 Kim, R.J., et al., The use of contrast-enhanced magnetic resonance imaging to identify reversible myocardial dysfunction. N Engl J Med, 2000. 343(20): p. 1445-53.

9 McCrohon, J.A., et al., Differentiation of heart failure related to dilated cardiomyopathy and coronary artery disease using gadolinium-enhanced cardiovascular magnetic resonance. Circulation, 2003. 108(1): p. 54-9.

10 Schuster, E.H. and B.H. Bulkley, Ischemic cardiomyopathy: a clinicopathologic study of fourteen patients. Am Heart J, 1980. 100(4): p. 506-12.

11 Boucher, C.A., et al., Cardiomyopathic syndrome caused by coronary artery disease. III: Prospective clinicopathological study of its prevalence among patients with clinically unexplained chronic heart failure. Br Heart J, 1979. 41(5): p. 613-20.

12 Roberts, W.C., R.J. Siegel, and B.M.n. McManus, Idiopathic dilated cardiomyopathy: analysis of 152 necropsy patients. Am J Cardiol, 1987. 60(16): p. 1340-55.

13 Uretsky, B.F., et al., Acute coronary findings at autopsy in heart failure patients with sudden death: results from the assessment of treatment with lisinopril and survival (ATLAS) trial. Circulation, 2000. 102(6): p. 611-6.

14 Maron, B.J., Hypertrophic cardiomyopathy: a systematic review. JAMA, 2002. 287(10): p. 1308-20.

15 Choudhury, L., et al., Myocardial scarring in asymptomatic or mildly symptomatic patients with hypertrophic cardiomyopathy. J Am Coll Cardiol, 2002. 40(12): p. 2156-64.

16 Kim, R.J. and R.M. Judd, Gadolinium-enhanced magnetic resonance imaging in hypertrophic cardiomyopathy: in vivo imaging of the pathologic substrate for premature cardiac death? J Am Coll Cardiol, 2003. 41(9): p. 1568-72.

17 Moon, J.C., et al., The histologic basis of late gadolinium enhancement cardiovascular magnetic resonance in hypertrophic cardiomyopathy. J Am Coll Cardiol, 2004. 43(12): p. 2260-4.

18 Moon, J.C., et al., Toward clinical risk assessment in hypertrophic cardiomyopathy with gadolinium cardiovascular magnetic resonance. J Am Coll Cardiol, 2003. 41(9): p. 1561-7.

19 Mahrholdt, H., et al., Cardiovascular magnetic resonance assessment of human myocarditis: a comparison to histology and molecular pathology. Circulation, 2004. 109(10): p. 1250-8.

20 Shirani, J., L.J. Freant, and W.C.n. Roberts, Gross and semiquantitative histologic findings in mononuclear cell myocarditis causing sudden death, and implications for endomyocardial biopsy. Am J Cardiol, 1993. 72(12): p. 952-7.

21 Moon, J.C., et al., Gadolinium enhanced cardiovascular magnetic resonance in Anderson-Fabry disease. Evidence for a disease specific abnormality of the myocardial interstitium. Eur Heart J, 2003. 24(23): p. 2151-5.

22 Moon, J.C., et al., The histological basis of late gadolinium enhancement cardiovascular magnetic resonance in a patient with Anderson-Fabry disease. J Cardiovasc Magn Reson, 2006. 8(3): p. 479-82.

23 Beer, M., et al., Impact of enzyme replacement therapy on cardiac morphology and function and late enhancement in Fabry's cardiomyopathy. Am J Cardiol, 2006. 97(10): p. 1515-8.

24 Falk, R.H., R.L. Comenzo, and M. Skinner, The systemic amyloidoses. N Engl J Med, 1997. 337(13): p. 898-909.

25 Falk, R.H., Diagnosis and management of the cardiac amyloidoses. Circulation, 2005. 112(13): p. 2047-60.

26 Pellikka, P.A., et al., Endomyocardial biopsy in 30 patients with primary amyloidosis and suspected cardiac involvement. Arch Intern Med, 1988. 148(3): p. 662-6.

27 Maceira, A.M., et al., Cardiovascular magnetic resonance in cardiac amyloidosis. Circulation, 2005. 111(2): p. 186-93.

28 Sharma, O.P., A. Maheshwari, and K. Thaker, Myocardial sarcoidosis. Chest, 1993. 103(1): p. 253-8.

29 Smedema, J.P., et al., The additional value of gadolinium-enhanced MRI to standard assessment for cardiac involvement in patients with pulmonary sarcoidosis. Chest, 2005. 128(3): p. 1629-37.

30 Virmani, R., J.C. Bures, and W.C. Roberts, Cardiac sarcoidosis; a major cause of sudden death in young individuals. Chest, 1980. 77(3): p. 423-8.

31 Hurwitz, J.L. and M.E.n. Josephson, Sudden cardiac death in patients with chronic coronary heart disease. Circulation, 1992. 85(1 Suppl): p. I43-9.

32 Klem, I., et al., The utility of contrast enhanced MRI for screening patients at risk for malignant ventricular tachyarrhythmias. J Cardiovasc Magn Reson, 2004. 6(1): p. 84.



Mohamad G. Ghosn



Dipan J. Shah

Contact

Dipan J. Shah, M.D., FACC
Associate Professor
The Methodist Hospital Research Institute
Director, Cardiac Magnetic Resonance Imaging
Methodist DeBakey Heart and Vascular Center
The Methodist Hospital
6565 Fannin St
Houston, TX 77030, USA
Phone: +1 713-332-2539
DJShah@HoustonMethodist.org

Case Report: Acute Myocardial Syndrome in a 37-Year-Old Patient with Severe Renal Impairment

S. A. Mohiddin; A. S. Herrey

Institute of Cardiovascular Science, University College London;
The Inherited Cardiovascular Diseases Unit and Cardiac Imaging Department, The Barts Heart Centre, London, UK

A 37-year-old lady was admitted to our institution with chest pain and pain in her left arm, but no shortness of breath. Preceding the admission she had experienced symptoms of an acute upper respiratory tract infection.

Her past medical history included hypertension, hypothyroidism, hyperprolactinaemia, focal sclerosing glomerulosclerosis with stage IV chronic kidney disease, eGFR 17 mL/min, treated tuberculosis and three first trimester miscarriages.

On admission, her hs- troponin T was > 7,000 ng/L (normal < 30 ng/L). Her ECG was largely unchanged from a previous one taken in 2013 meeting LVH criteria, but otherwise unremarkable.

Her echocardiogram showed low-normal left ventricular systolic function with akinesis of the mid inferior and mid infero-septal segments with an estimated EF of 55%.

On coronary angiography, her coronary arteries were unobstructed.

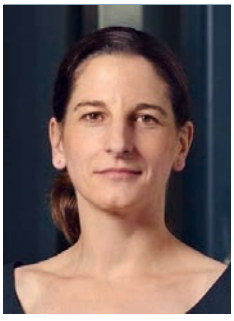
To confirm the working diagnosis of myocarditis, she underwent Cardiovascular Magnetic Resonance (CMR) imaging on our MAGNETOM Aera 1.5T (Siemens Healthcare, Erlangen, Germany). In view of her severe renal impairment, no gadolinium contrast was given.

This was reported as showing normal biventricular size, mild systolic impairment with hypokinesis of the antero-septum, infero-septum and inferior wall. Non-contrast tissue characterisation with T1 and T2 mapping identified markedly increased T1 and T2 values matching (and extending beyond) the regional wall motion abnormalities, confirming the diagnosis of florid acute myocarditis.

Subsequently, her troponin levels were falling and she was discharged pain free a few days later.

A month later, her EF on echo had normalised with mild residual inferior hypokinesis and her troponin was normal at 18 n/L. Her repeat CMR, however, showed persistent myocardial inflammation, but with falling T2 values.

In summary, non-contrast myocardial mapping in this case was used to establish and confirm a diagnosis of myocarditis and also to monitor progress.



Contact

Anna S. Herrey
Institute of Cardiovascular Science
University College London
The Barts Heart Centre
16-18 Westmoreland Street
London W1G 8PH
UK
anna.john@doctors.org.uk

Panel 1

The T1 maps (MOLLI) show extensive interstitial expansion in the septum and the inferior wall on the first scan. On the second (F_UP) scan, there is incomplete resolution in the inferior wall and limited change in the septum.

a) On the two-chamber view (T1_MOLLI_2cha and F_UP_T1_MOLLI_2cha) there is increased signal in the inferior wall.

b) In a four-chamber orientation (T1_MOLLI-4cha and F_UP_T1_MOLLI_4cha), there is increased signal in the septum.

c) In the short axis views (T1_MOLLI_mid-SAX and F_UP_T1_MOLLI_mid_SAX), both increased signal can be seen in the septum and the inferior wall.

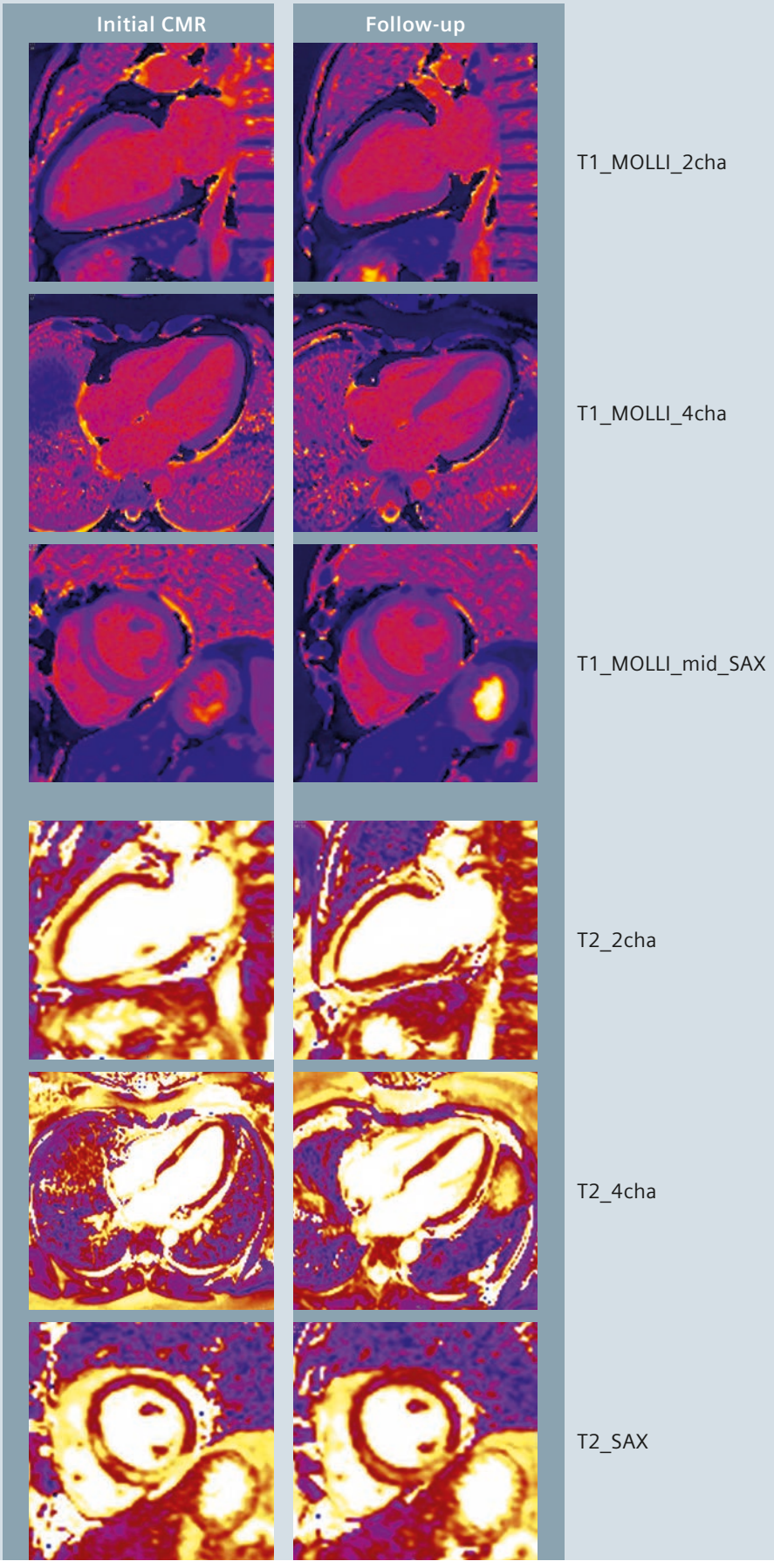
Panel 2

The matching T2 maps confirm myocardial oedema matching the areas of high native T1 values. The florid changes seen in the initial scan are less impressive at follow-up (F_UP), but still present.

a) High T2 signal is seen in the two-chamber view in the inferior wall (T2-4cha and F_UP_T2_4cha).

b) In the four-chamber orientation, there is increased signal in the mid septum.

c) The short axis view confirms similar changes in septum and inferior wall compared to the T1 maps.



Case Report: Detection of Myocardial Changes in a Patient Undergoing Chemotherapy

Arash Seratnahaei, M.D.; Vincent L. Sorrell, M.D., FACP, FACC, FASE; David Powell, Ph.D.; Peter A. Hardy, Ph.D.; Bruce Spottiswoode, Ph.D.; Steve W. Leung, M.D., FACC

University of Kentucky Medical Center, Gill Heart Institute, Lexington, KY, USA

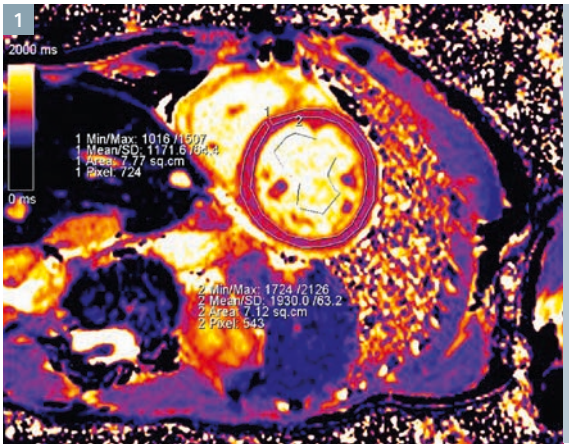
Patient history

46-year-old female presented with progressive dyspnea on exertion. She was found to have acute myeloid leukemia, and underwent 7+3 chemotherapy induction with daunorubicin. The initial chemotherapy was not effective, and thus re-induction with high dose cytarabine and idarubicin was given. Prior to chemotherapy, she had a normal left ventricular ejection fraction (LVEF) (>55%) by echocardiography. Three weeks after chemotherapy, her repeat LVEF by echo was reduced to 40-50% with a possible thrombus in the LV apex. She underwent cardiac magnetic resonance (CMR) imaging for the assessment of left ventricular function and apical thrombus.

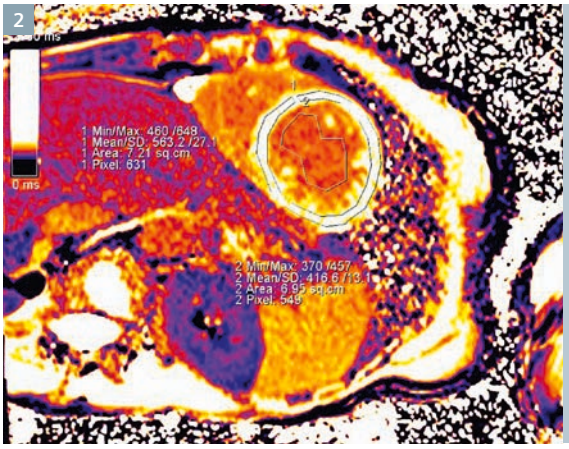
Sequences details

All images have been acquired using a MAGNETOM Aera 1.5T scanner with software version *syngo* MR D13. Mid-ventricular short axis MOdified Look Locker Inversion Recovery (MOLLI) images were acquired during diastole for T1 determination using an 11 heart-beat, 5(3)3, SSFP readout sequence. Imaging parameters were: Field-of-view 300 mm, slice thickness 8 mm, TR 335.62 ms, TE 2.7 ms, matrix 256 × 168 pixels resulting in a resolution of 1.2 x 1.2 mm, TI start = 130 ms, TI increment = 80 ms.

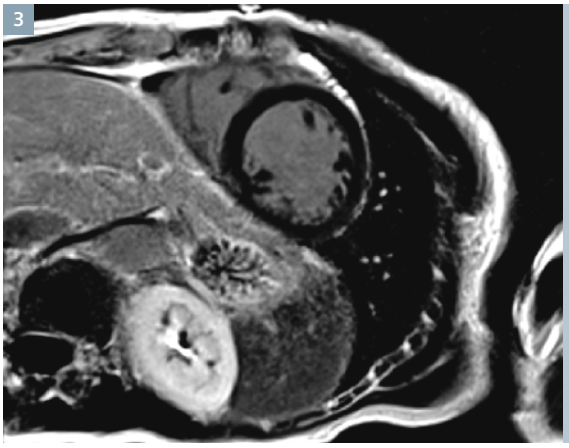
Then, a total dose of 0.2 mmol/kg gadopentetate dimeglumine (MAGNEVIST, Bayer HealthCare Pharmaceuticals, Leverkusen, Germany) was injected at 4 mL/second. Ten minutes after contrast injection, late gadolinium enhancement (LGE) images were acquired with a phase-



1 Native T1 mapping (MOLLI 5(3)3) in the mid-ventricular short axis demonstrating an elevated native T1 time in the myocardium.



2 Post contrast T1 mapping (MOLLI 4(1)3(1)2) in the mid-ventricular short axis was used for calculation of extracellular volume fraction.



3 Late gadolinium enhancement phase-sensitive inversion recovery mid-ventricular short axis image demonstrating no enhancement.

sensitive inversion recovery gradient-echo imaging sequence for the assessment of focal myocardial fibrosis. Finally, 18 minutes after contrast injection, post-contrast MOLLI T1 mapping 4(1)3(1)2 was repeated in identical prescription as native T1 mapping.

Native and post-contrast blood T1 times were measured on a region-of-interest manually drawn in the center of the blood-pool. Native and post-contrast T1 times were measured on the T1 maps as shown in figures 1 and 2.

The partition coefficient lambda (λ) and extracellular volume fraction (ECV) were calculated in the following manner:

$$\lambda = \frac{1/T1\,\text{myocardium postcontrast} - 1/T1\,\text{myocardium precontrast}}{1/T1\,\text{blood postcontrast} - 1/T1\,\text{blood precontrast}}$$

$$ECV = \lambda\,(1\text{-Hematocrit})$$

Imaging findings

CMRI confirmed the LVEF was reduced at 40% with global hypokinesis. LGE images did not demonstrate any focal fibrosis or left ventricular thrombus. Native myocardial T1 time was 1171 ms, and 1930 ms for the blood-pool. Post-contrast myocardial T1 was 563 ms, and 417 ms for the blood-pool. Hematocrit, on the morning of the scan, was 26.9%. Calculated ECV was 35.9%, which is elevated. Heart rate was 65 bpm during native T1 mapping and post-contrast T1 mapping. Based on the T1 mapping, the patient appears to have edema or acute inflammatory response that was not detected with traditional CMR imaging.

The quantitative analysis of native T1 mapping (Fig. 1) shows higher T1 value, while the quantitative analysis of the post-contrast T1 mapping (Fig. 2) shows shorter T1 value. LGE (Fig. 3) shows no evidence of fibrosis or scar.

Comments (Discussion)

Endomyocardial biopsy is the 'gold' standard for myocardial disease evaluation. However, this is an invasive procedure and its accuracy is limited by sampling error and carries a risk of morbidity and mortality. Therefore, non-invasive testing is the preferred the technique for myocardial tissue evaluation. CMR provides several methods for non-invasive myocardial tissue characterization. For evaluation of the myocardial ECV, T1 mapping before and after gadolinium-based contrast administration has become an emerging technique. Native T1 mapping reveals acute myocardial inflammation, while the combination of native and post-contrast T1 mapping provides information regarding expansion of the myocardial extracellular volume fraction. Increased ECV is seen in focal or diffuse fibrosis/scar or edema [1].

Anthracycline-based chemotherapy has a well-documented history of causing cardiac dysfunction, which limits its use. Both short-term and long-term cardiac dysfunction has been described [2]. Long-term effects are cumulative dose dependent and include irreversible LV systolic dysfunction. In contrast, short-term effects have been described in small case series. These effects can occur immediately or within a few weeks of chemotherapy administration and include pericarditis, arrhythmias, and acute LV systolic dysfunction [2, 3]. In this patient, the native T1 is elevated indicating acute myocardial edema. If the native T1 time was within the normal range, the calculated ECV would have been within the normal range as well. The elevated ECV appears to be driven mainly by the edema, rather than diffuse fibrosis. This case highlights the ability of CMR with T1 mapping to identify acute myocardial edema in a patient who had recently received anthracycline-based chemotherapy. Although the patient's LGE images appear normal, the overall extracellular volume fraction is elevated.

References

1 White SK, Sado DM, Flett AS, Moon JC. Characterising the myocardial interstitial space: the clinical relevance of non-invasive imaging. Heart 2012;98:773–9.

2 Dazzi H, Kaufmann, Follath. Anthracycline-induced acute cardiotoxicity in adults treated for leukaemia. Analysis of the clinico-pathological aspects of documented acute anthracycline induced cardiotoxicity in patients treated for acute leukaemia at the University Hospital of Zurich, Switzerland, between 1990 and 1996. Ann Oncol 2001; 12(7): 963-6.

3 Bristow MR, Thompson PD, Martin RP, et al. Early anthracycline cardiotoxicity. Am J Med 1978; 65(5): 823-32.



Contact

Steve W. Leung, M.D., FACC
University of Kentucky Medical Center
Division of Cardiovascular Medicine
Gill Heart Institute
326 Charles T. Wethington Building
Lexington, KY 40536
USA
Phone: +1 859-323-8040
steve.leung@uky.edu

Case Report: QISS MRA at 3T

Anna-Maria Lydon, PgDip MRI, DCR(R)[1]; Associate Professor Andrew Holden, MBChB, FRANZCR[2]; Dr. Jacobus Kritzinger, MBChB, FRCPC[2]

[1] Centre for Advanced MRI, Faculty of Medical & Health Sciences, University of Auckland; New Zealand
[2] Auckland City Hospital, New Zealand

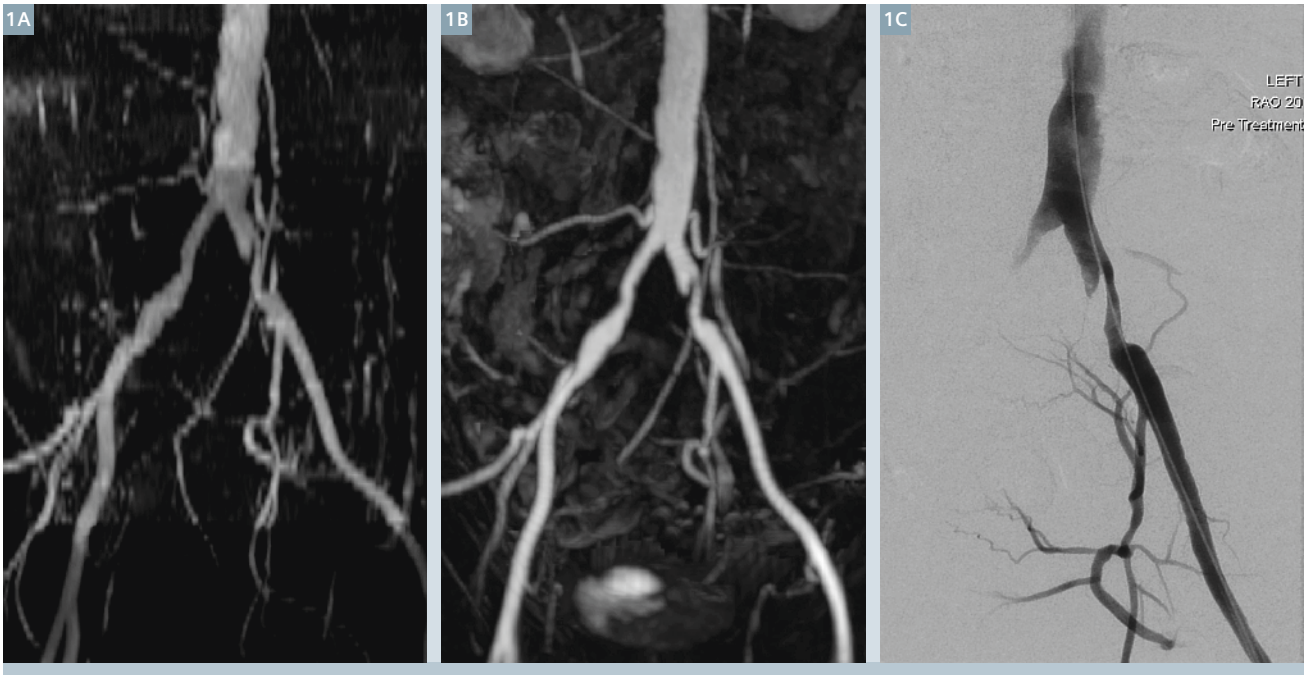
Quiescent Interval Single-Shot (QISS) MR Angiography (MRA) has been shown to be a robust technique for non-contrast MRA of the peripheral vasculature at 1.5T. At 3T, early versions of the sequence offered greater signal-to-noise ratio (SNR) than at 1.5T, but were occasionally compromised by inversion pulse insufficiency due to B_1 inhomogenieties. This gave rise to poor venous suppression particularly in the abdominal and pelvic region. We had the opportunity to try a WIP version of the QISS MRA sequence with a modified FOCI pulse which was hoped to overcome aforementioned B_1 inhomogeneities and improve venous suppression whilst maintaining small vessel visualisation on 3T.

We present a case of a 69-year-old male who was referred with short distance left leg claudication, and reduced left femoral pulse, query iliac artery disease. He had a history of smoking 10 cigarettes per day. The patient was imaged on the 3T MAGNETOM Skyra (Siemens Healthcare, Erlangen, Germany) using the peripheral matrix coil in combination with the spine and body matrix coils. ECG gating was achieved using the Siemens wireless PMU.

At the time of imaging the patient had a heart rate of 68 bpm and a recent eGfr of 70 ml/min / 1.73 m^2.

QISS MRA sequences using TrueFISP readout were acquired as a vessel scout technique as this provides an excellent overview for planning subsequent contrast-enhanced (CE) MRA imaging. The standard QISS MRA was used which consists of 1 x 1 x 3 mm contiguous axial slices, single slice per RR interval, flip angle 90°, iPat 3, 40 slices per station. We acquired the abdominal stations during quiet respiration as we found our elderly population cope with this better than with breath-holds and there is no time penalty between techniques.

As per our standard protocol subsequent CE-MRA imaging was performed using diluted 20 ml Multihance (Gadobenate dimeglumine) + 10 ml 0.9% NaCl, followed by 0.9% NaCl flush. A test bolus of 1.5 mls contrast @ 2 ml/s followed by 20 ml 0.9% NaCl was sampled using a dynamic 2D FLASH single



1 QISS MRA CE-MRA DSA

slice positioned at the level of the aortic bifurcation to determine the arrival time of the contrast in the abdominal aorta. Next the tibial arteries were imaged using time-resolved TWIST MRA sequence using 4 ml diluted contrast and a 20 ml NaCl flush delivered @ 2 ml/s. Finally, the full peripheral arterial tree is imaged from above the renal arteries to the pedal arteries using 22-23 ml diluted contrast delivered as follows:

Dual-phase contrast injection:
10 ml @ 2 ml/s, followed by
13 ml @ 1.5 ml/s then an NaCl flush of 20 ml @ 1 ml/s.

Findings included a high-grade stenosis of the mid left common iliac artery. There was also a mild-moderate stenosis of the proximal right common iliac artery. Femoral and popliteal arteries were of normal calibre. There was three vessel run-off to each calf, with severe disease of the left anterior tibial artery and vessel occlusion by mid-calf.

Follow-up DSA confirmed QISS MRA and CE-MRA findings, and the left common iliac artery lesion was treated by angioplasty and stenting with an 8 x 40 mm self-expanding stent, post dilated to 7 mm.

In this case QISS images correlated excellently with the CE-MRA images and subsequent DSA imaging as seen below. We have found that the optimized FOCI pulse is particularly effective in the aorto-iliac region and this case demonstrates very nicely how this new version of the sequence (now product) performs compared to CE-MRA and also DSA.

Acknowledgements

We would like to thank Dr Robert Edelman (Northwestern University, Chicago, IL, USA) and Shivraman Giri (Siemens Healthcare, USA) for providing us with this version of the WIP for evaluation. We would also like to thank Benjamin Schmitt (Siemens Healthcare, Australia) for his support.

Contact

Anna-Maria Patricia Lydon, PgDip MRI, DCR(R)
Charge MRI Technologist
The University of Auckland
Centre for Advanced MRI
Private Bag 92019
Auckland 1142, New Zealand
Phone: +64 9 923 9512
a.lydon@auckland.ac.nz

Learn more!

Quantification and speed. What else drives CMR into broader clinical use? Don't miss the talks of experienced and renowned experts at:

www.siemens.com/magnetom-world



Emerging Contributions of CMR in Cardiology

Dudley Pennell

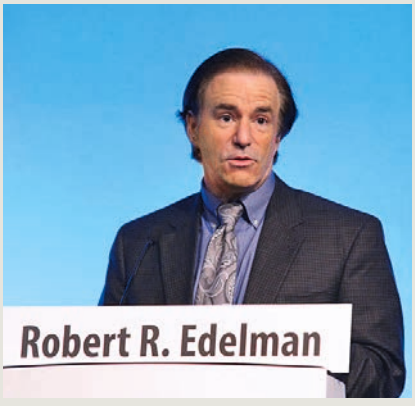
Royal Brompton & Harefield (London, UK)



Need for Speed in CMR

James Carr

Northwestern Memorial Hospital (Chicago, IL, USA)



Advances in Non-CE MR Angiography

Robert R. Edelman

NorthShore University HealthSystem (Evanston, IL, USA)

Quiescent Interval Single-Shot (QISS) Lower Extremity MRA for the Diagnosis of Peripheral Artery Disease: Case Presentations

Akos Varga-Szemes[1]; Thomas M. Todoran[2]; Shivraman Giri[3]; Stephen R. Fuller[1]; U. Joseph Schoepf[1]

[1] Division of Cardiovascular Imaging, Department of Radiology and Radiological Science, Medical University of South Carolina, Charleston, SC, USA
[2] Division of Cardiology, Department of Medicine, Medical University of South Carolina, Charleston, SC, USA
[3] Siemens Healthcare, Chicago, IL, USA

Introduction

Peripheral artery disease (PAD) affects 12%–14% of the general population and its prevalence increases with patient age [1]. While segmental Doppler pressures and pulse volume recording are the most appropriate techniques for screening symptomatic patients, more sophisticated non-invasive imaging techniques may be necessary for further anatomic evaluation and treatment planning, especially before revascularization [2, 3]. The American College of Radiology (ACR) rates both CT angiography (CTA) and MR angiography (MRA) as "usually appropriate" diagnostic approaches for claudication with suspected vascular etiology [2]. Because many patients with PAD suffer from several comorbidities including renal insufficiency, the administration of either iodinated or gadolinium-based contrast media may be of concern given the increased risk of contrast-induced nephropathy or nephrogenic systemic fibrosis (NSF), respectively [4, 5].

These concerns with the risks of contrast media administration in combination with recent technical advances have led to an increased interest in non-contrast MRA techniques. Although many approaches to non-contrast MRA have been evaluated [6], most of them have limited clinical utility in patients with PAD due to either technical issues (e.g. long acquisition time) or overestimation of mild to moderate stenosis [7, 8].

Quiescent-interval single-shot (QISS) MRA is a recently introduced, robust non-contrast MRA technique [9]. QISS MRA at 1.5 and 3T has shown promising results with reported diagnostic accuracies close to or equal to contrast-enhanced MRA [10-14]. Here, we illustrate some of the benefits of QISS MRA over other modalities through two clinical cases and also provide a brief overview of the literature available for this technology.

Discussion

These cases demonstrate certain benefits of QISS MRA over CTA. As emphasized by ACR guidelines, the two major shortcomings limiting image interpretation of CTA in PAD patients are the relatively difficult acquisition timing following contrast administration due to reduced flow in the stenotic vessels and reduced lumen visibility due to heavily calcified atheromatous lesions [2]. As we have shown, QISS MRA is able to overcome both of these limitations to provide reliable findings comparable to invasive DSA.

The QISS MRA technique was first introduced in 2010 by Edelman et al. [9]. This ECG-triggered technique employs initial saturation pulses followed by a 2D single-shot balanced steady-state free precession readout with a quiescent interval between them.

Case 1

A 55-year-old male was referred for evaluation and treatment of intermittent claudication despite adherence to a regular walking program. The patient was a former smoker and his medical history included hyperlipidemia, hypertension, coronary artery disease, PAD, and ANCA-positive vasculitis. Physical examination revealed diminished femoral and popliteal pulses bilaterally. Posterior tibial and dorsalis pedis pulses were Dopplerable. His ankle-brachial index (ABI) was 0.78 in the right leg and 0.91 in the left leg at rest, while ABI severely decreased post exercise (0.53 and 0.52, respectively). In preparation for revascularization the patient was referred for a lower extremity run-off CTA. CTA demonstrated moderate to severe bilateral iliac and superficial femoral artery stenosis. The evaluation of calf vessels was inconclusive as the slower flow in the stenotic vessels delayed the arrival of contrast and thus acquisition occurred before peak enhancement was reached in these vessels. Prior to intervention, the patient underwent a non-contrast QISS MRA on a 1.5T MAGNETOM Avanto scanner. QISS MRA successfully visualized each arterial segment, including those poorly visualized on CTA. In addition to visualizing the stenosis already found on CTA, QISS MRA was able to delineate infrapopliteal run off to the feet. There was total occlusion of the right peroneal artery and total occlusion of the left anterior tibial and posterior tibial arteries. These findings were confirmed by invasive digital subtraction angiography (DSA).


CTA
QISS
DSA

Two saturation pulses are used: one to suppress the background signal, and one applied inferior to the slice to suppress the venous blood signal. The quiescent interval before the readout allows the inflow of unsaturated arterial spins into the imaging plane. Due to its design, the flow sensitivity of QISS MRA is negligible compared to other non-contrast techniques such as time-of-flight, 3D fast spin echo based approaches, and



ungated ghost MRA [10]. Additionally, single-shot 2D TrueFISP acquisition makes this technique relatively insensitive to patient motion.

Novel technological innovations in development promise to further facilitate the clinical implementation of QISS MRA. QISS MRA can be performed without ECG gating by employing prospective self-navigation based on the detection of the acceleration of blood flow during systole with a reference-less phase contrast navigator [15]. Highly undersampled radial *k*-space readout enables the acquisition of multiple 2D slices in a single cardiac cycle shortening the acquisition time of a complete lower extremity runoff MRA to about 2 minutes [16]. High-resolution QISS MRA provides 1.5 mm section thickness and thus more detailed visualization of the vascular anatomy [17]. Quiescent interval low angle shot MRA provides superior image quality for the external carotid arteries compared to 2D time-of-flight with an average acquisition time of less than 6 minutes [18].

The diagnostic accuracy of non-contrast QISS MRA has been evaluated with non-invasive contrast-enhanced MRA as a reference standard, showing a segment-based sensitivity and specificity of 89.7% and 96.5%, respectively [11]. A subgroup analysis in patients who also underwent DSA showed substantial agreement between QISS MRA and DSA [12]. Similarily high sensitivity (98.6%) and specificity (96%) were reported for QISS MRA versus contrast-enhanced MRA in patients with PAD by Klasen et al. [13]. QISS MRA demonstrated superior specificity for detecting hemodynamically significant arterial stenosis in the lower extremities compared to subtracted 3D fast spin echo MRA and was also found to provide higher image quality and diagnostic accuracy in the abdominal and pelvic regions [19].

While the majority of initial QISS MRA studies were performed at 1.5T [9, 11, 12], QISS MRA has also shown good diagnostic accuracy at higher field strength. 3T QISS MRA has high sensitivity (100%) in the presence of adequate image quality for the detection of peripheral artery stenosis when compared to the DSA as a reference standard [14]. Later studies have confirmed the feasibility of QISS MRA at 3T and reported high diagnostic performance and high image quality, especially in the distal segments [20-22].

Conclusion

Past studies have shown that QISS MRA provides high diagnostic accuracy for the detection of hemodynamically significant arterial stenosis of the lower extremities at both 1.5 and 3T. QISS MRA seems to be a feasible alternative for patients in whom contrast media administration is contraindicated, especially in the light of the new ACR guidelines widening the population considered at risk for NSF to patients with eGFR <40 ml/min/1.73m^2 [23]. Furthermore, QISS MRA may avoid the timing-related difficulties of contrast-enhanced CTA and better visualize heavily calcified arteries. Finally, its relative insensitivity to blood-flow and patient motion simplify the patient workflow by requiring minimal user input during the acquisition.

References

1 Hiatt WR, Hoag S, Hamman RF. Effect of diagnostic criteria on the prevalence of peripheral arterial disease. The San Luis Valley Diabetes Study. Circulation. 1995;91(5):1472-9.

2 Expert Panel on Vascular Imaging, Dill KE, Rybicki FJ, et al. ACR Appropriateness Criteria® Claudication - Suspected Vascular Etiology. Available at https://acsearch.acr.org/docs/69411/Narrative/. American College of Radiology. Accessed 10/19/2015.

3 Norgren L, Hiatt WR, Dormandy JA, et al. Inter-society consensus for the management of peripheral arterial disease. Int Angiol. 2007;26(2):81-157.

4 Davenport MS, Khalatbari S, Cohan RH, Dillman JR, Myles JD, Ellis JH. Contrast material-induced nephrotoxicity and intravenous low-osmolality iodinated contrast material: risk stratification by using estimated glomerular filtration rate. Radiology. 2013;268(3):719-28.

5 Kuo PH, Kanal E, Abu-Alfa AK, Cowper SE. Gadolinium-based MR contrast agents and nephrogenic systemic fibrosis. Radiology. 2007;242(3):647-9.

6 Miyazaki M, Lee VS. Nonenhanced MR angiography. Radiology. 2008;248(1):20-43.

7 Lim RP, Hecht EM, Xu J, et al. 3D nongadolinium-enhanced ECG-gated MRA of the distal lower extremities: preliminary clinical experience. J Magn Reson Imaging. 2008;28(1):181-9.

8 Haneder S, Attenberger UI, Riffel P, Henzler T, Schoenberg SO, Michaely HJ. Magnetic resonance angiography (MRA) of the calf station at 3.0 T: intraindividual

Case 2

A 65-year-old man was referred for evaluation and treatment of intermittent claudication. Relevant past medical history included hyperlipidemia, hypertension, carotid artery disease, subclavian artery disease, and PAD. Physical examination was remarkable for normal femoral pulses, diminished popliteal pulses and Dopplerable posterior tibial and dorsalis pedis pulses bilaterally. The patient's ABI in the right leg (0.72) was consistent with moderate ischemia, while ABI in the left leg (0.95) was within normal limits at rest. The patient was referred for a lower extremity CTA to plan for revascularization. This demonstrated occluded right superficial femoral, popliteal, anterior tibial, and peroneal arteries and left popliteal, peroneal, anterior tibial, and posterior tibial arteries. Complete lumen visibility was limited due to the presence of heavy calcification, especially in the superficial femoral arteries. As a result, the length of the occlusion could not be determined. Non-contrast QISS MRA (1.5T MAGNETOM Avanto) was performed and was able to sufficiently visualize the entire lower extremity runoff including the heavily calcified segments. QISS MRA provided superior image quality in the calves, visualizing the three vessel runoff in the right calf and the proximal total occlusion of all three left calf vessels filling via collaterals. QISS MRA findings were confirmed with subsequent DSA results.

comparison of non-enhanced ECG-gated flow-dependent MRA, continuous table movement MRA and time-resolved MRA. Eur Radiol. 2011;21(7):1452-61.
9 Edelman RR, Sheehan JJ, Dunkle E, Schindler N, Carr J, Koktzoglou I. Quiescent-interval single-shot unenhanced magnetic resonance angiography of peripheral vascular disease: Technical considerations and clinical feasibility. Magn Reson Med. 2010;63(4):951-8.
10 Offerman EJ, Hodnett PA, Edelman RR, Koktzoglou I. Nonenhanced methods for lower-extremity MRA: a phantom study examining the effects of stenosis and pathologic flow waveforms at 1.5T. J Magn Reson Imaging. 2011;33(2):401-8.
11 Hodnett PA, Koktzoglou I, Davarpanah AH, et al. Evaluation of peripheral arterial disease with nonenhanced quiescent-interval single-shot MR angiography. Radiology. 2011;260(1):282-93.
12 Hodnett PA, Ward EV, Davarpanah AH, et al. Peripheral arterial disease in a symptomatic diabetic population: prospective comparison of rapid unenhanced MR angiography (MRA) with contrast-enhanced MRA. AJR Am J Roentgenol. 2011;197(6):1466-73.
13 Klasen J, Blondin D, Schmitt P, et al. Nonenhanced ECG-gated quiescent-interval single-shot MRA (QISS-MRA) of the lower extremities: comparison with contrast-enhanced MRA. Clin Radiol. 2012;67(5):441-6.
14 Hansmann J, Morelli JN, Michaely HJ, et al. Nonenhanced ECG-gated quiescent-interval single shot MRA: Image quality and stenosis assessment at 3 tesla compared with contrast-enhanced MRA and digital subtraction angiography. J Magn Reson Imaging. 2014;39(6):1486-93.
15 Offerman EJ, Koktzoglou I, Glielmi C, Sen A, Edelman RR. Prospective self-gated nonenhanced magnetic resonance angiography of the peripheral arteries. Magn Reson Med. 2013;69(1):158-62.
16 Edelman RR, Giri S, Dunkle E, Galizia M, Amin P, Koktzoglou I. Quiescent-inflow single-shot magnetic resonance angiography using a highly undersampled radial k-space trajectory. Magn Reson Med. 2013;70(6):1662-8.
17 Thierfelder KM, Meimarakis G, Nikolaou K, et al. Non-contrast-enhanced MR angiography at 3 Tesla in patients with advanced peripheral arterial occlusive disease. PLoS One. 2014;9(3):e91078.
18 Koktzoglou I, Murphy IG, Giri S, Edelman RR. Quiescent interval low angle shot magnetic resonance angiography of the extracranial carotid arteries. Magn Reson Med. 2015.
19 Ward EV, Galizia MS, Usman A, Popescu AR, Dunkle E, Edelman RR. Comparison of quiescent inflow single-shot and native space for nonenhanced peripheral MR angiography. J Magn Reson Imaging. 2013;38(6):1531-8.
20 Knobloch G, Gielen M, Lauff MT, et al. ECG-gated quiescent-interval single-shot MR angiography of the lower extremities: initial experience at 3 T. Clin Radiol. 2014;69(5):485-91.
21 Amin P, Collins JD, Koktzoglou I, et al. Evaluating peripheral arterial disease with unenhanced quiescent-interval single-shot MR angiography at 3 T. AJR Am J Roentgenol. 2014;202(4):886-93.
22 Wagner M, Knobloch G, Gielen M, et al. Nonenhanced peripheral MR-angiography (MRA) at 3 Tesla: evaluation of quiescent-interval single-shot MRA in patients undergoing digital subtraction angiography. Int J Cardiovasc Imaging. 2015;31(4):841-50.
23 ACR Committee on Drugs and Contrast Media. ACR Manual on Contrast Media. Version 10.1. 2015.



Contact

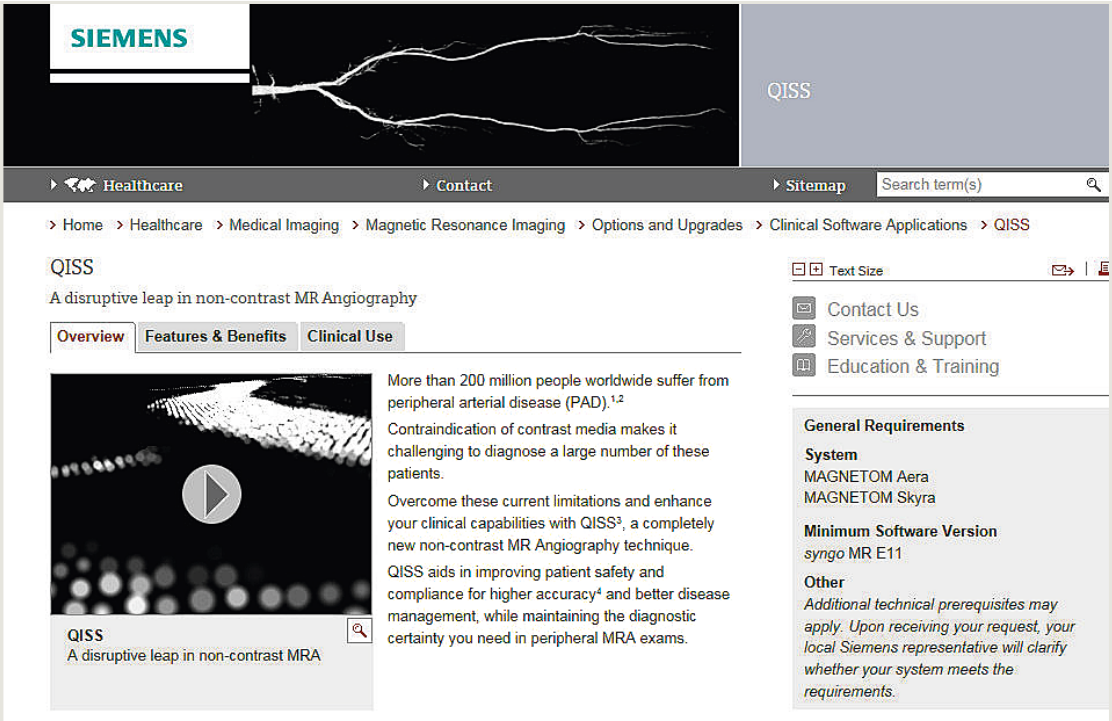
Akos Varga-Szemes, M.D., Ph.D.
Division of Cardiovascular Imaging
Department of Radiology and Radiological Science
Medical University of South Carolina
25 Courtenay Drive, MSC 226
Charleston, SC 29425, USA
Phone +1 843-876-0097
Fax +1 843-876-3157
vargaasz@musc.edu

Try QISS on your system

A free-of-charge 90 day trial license is available for QISS.

For further details, product overviews, image galleries, case studies and general requirements visit us at:

www.siemens.com/mri-options-overview



Using Remote Assist to Expand Your Expertise

Gary Smith

Siemens Healthcare, Great Britain and Ireland

What is Remote Assist?

Siemens Remote Assist (RA) is an application that allows you to share your MR workspace with the Application Specialist who is not on site. With your permission, the system is connected via an encrypted broadband connection – with Siemens Remote Service ensuring secure data transfer.

The Remote Assist application allows Application Specialists to troubleshoot scanning problems and offer you real-time assistance with difficult tasks at short notice. The Remote Assist application also allows your institution to grow its potential by participating in an application session to set up a new service. In this article we will take a look at an institution that wanted to set up a pulmonary angiogram service. Instead of booking a day of applications training, the training was done remotely; this led to less disruption for the institution and its patients, and a faster response time from the applications team.

How it works

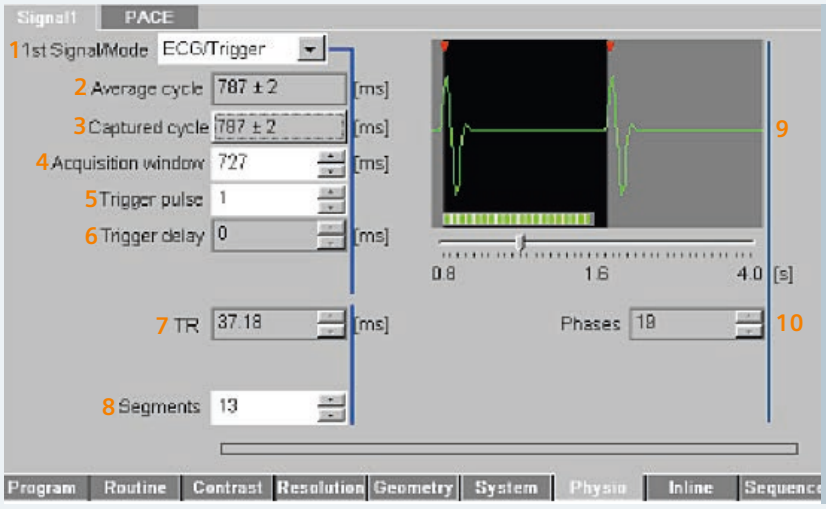
Using Siemens Remote Assist provides real-time image quality assessment, protocol optimization and workflow enhancements. The Application Specialist will ask you to go to Options > Service > Remote Assistance. The Siemens Application Specialist will then give you a 6 digit security number. Once entered, you are logged on and both parties then share the MR screen. The Application Specialist gives visual guidance with a red cursor and may take control of the console with your permission. To allow full access, you need to select the RA icon at the bottom of the screen and follow the instructions.

Guidance over the phone, with additional on-screen support, is usually all that is necessary to provide a strong training session. Verbal and visual reinforcement of the training can lead to a better outcome for your team and your patients.

Organizing the RA session

An RA session can be organized whenever it is required through the Customer Care Centre – for instance to answer questions concerning an application or image review. If you wish to participate in a longer session to improve or grow your service, preparation is helpful. Contact the Customer Care Centre and organize for your Application Specialist to call you and discuss your application needs.

During this phone call, the Application Specialist may dial onto the scanner to look at the available software and applications. There should be a discussion of the desired outcomes. By remotely organizing and remotely performing the training, you can improve the efficiency of your department. There should be no need for scanner down time, as software checks and organization are done remotely. RA is also less intrusive, as no one is on site, and additionally, there is more room for further staff members to attend the session.



1

1. Trigger type
2. Average R-R cycle
3. The captured R-R cycle to be used as trigger.
4. Acquisition window. The time you have to perform your pulse sequence.
5. Trigger pulse. 1 = every pulse. 2 = every other pulse.
6. Trigger delay
7. TR
8. Segments lines of raw data collected in a phase. Affects your TR.
9. Graphic of ECG and pulse sequence. Green segments will be collected, red will cause a trigger to miss.
10. Number of phases to be scanned.

When preparing for a RA session, you should ensure that a suitable date and enough time are allotted to staff and system to ensure the best possible training environment. If you are setting up a new service, it may be better to involve more than one patient as training participant. Ideally, all stakeholders involved in this service growth should be available, i.e. radiographers who will be performing the study and training of others, and clinicians who will be interested in image quality. With this setup, the new service can be ready to start right after finishing the RA session.

Performing the RA session

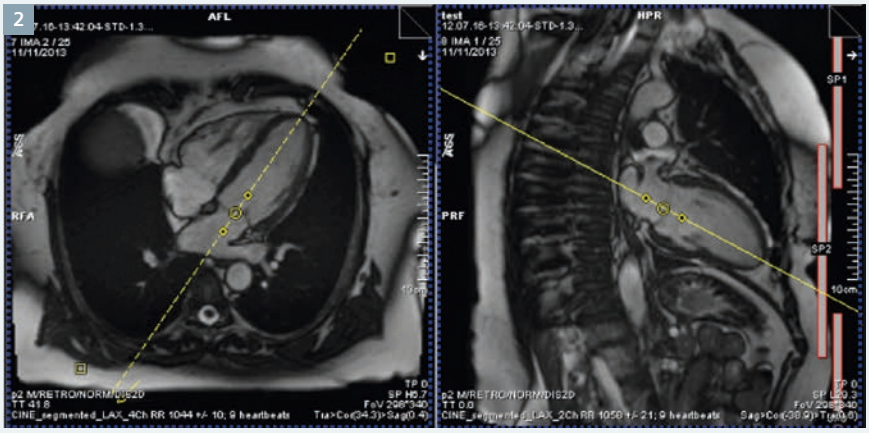
In this example, the user had many years of advanced scanning experience and wanted to start a pulmonary angiogram service. It had clinical help from another site. It had also performed angiograms before. The user was interested in acquiring additional knowledge concerning test bolus angiograms and wanted some basic cardiac sequences to allow for optimum positioning.

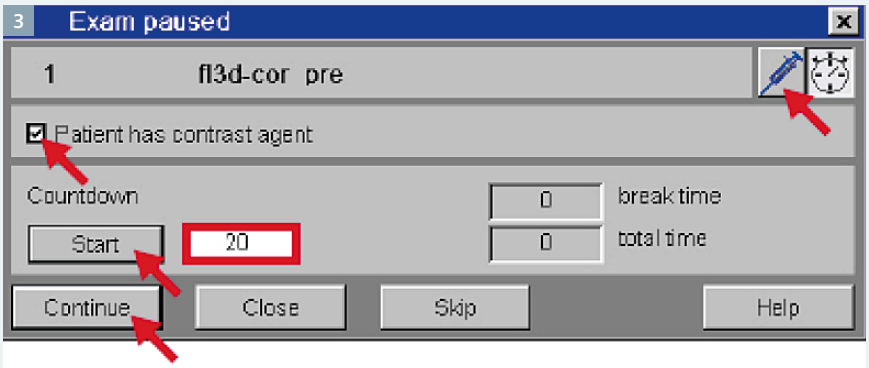
The RA was organized as above and two patients were booked for the session. All software required for the session had been checked for updates and system integration to ensure a best possible system preparation.

At the start of the session, ECG gating was taught. Positioning of electrodes was done by staff on site.

The Physio page was explained (Fig. 1).

To localize the pulmonary arteries, cardiac planes for 2-chamber, 4-chamber and coronal RVOT (right ventricular outflow tract) views of the heart were shown (Fig. 2). Dark blood and bright blood scanning was also explained. The angiography workflow was created using the base angiography series in the Siemens default tree. The field-of-view (FOV) and coverage were altered. Increasing the slices in the 3D slab gave more signal which could be used to accelerate the scan using iPat. The workflow was tested including the





test-bolus stage to practice breathing patterns with the patient, and to assess image quality before administrating contrast media. Using the rerun functionality in the workflow allows you to restart the workflow.

The scan sequence for the Angio follows.

Test Bolus (2 ml of contrast media given at the same flow rate with the saline flush as the primary dose).

3D angio pre-contrast (breath-hold).

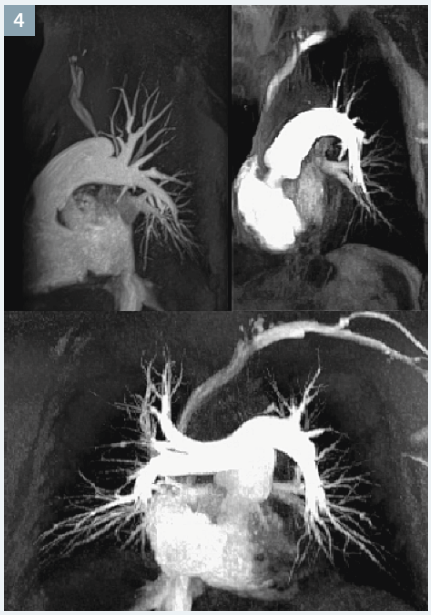
Pause (enter contrast details here to ensure subtraction).

3D angio post-contrast (in Properties set up wait for user to start flag man on B level software arrow on D and E level. This gives you the pop-up shown in Figure 3. You are offered the possibility to set the countdown to delay the scan. You can also set AutoStart in the properties of D and E level software. AutoStart will start the measurement after the countdown has finished.

Once you run the test bolus sequence, you get a set of images with time stamps at the bottom. You can then simply take that time stamp and enter it into the countdown clock to set your timing. To improve your timing, you can load the data into mean curve – or use the Angio Dot Engine.

To perform a mean curve, open the application mean curve. Drag and drop the test bolus sequence from the browser to the top-left box. There are a set of tools on the right that change scaling and sorting to normal time. Draw a region-of-interest (ROI) over an artery and then select curve calculation. You now have the timing of the test bolus. You can look at when the contrast arrives: The real bolus will be longer so it will peak later, so you can offset your scan by using the time to center (TTC) parameter on the Angio tab. Therefore, if arrival time is 18 seconds, you can set a TTC to 2 seconds to offset your measurement over the peak of the primary dose.

Once the timing is calculated, run your pre-contrast scan. When the pause opens for the post-contrast scan, enter your time into the countdown. Start the contrast and timer at the same time. About 8 seconds



before the end give your breath-hold instructions. If you use AutoStart, the scan will start by itself – if not, hit continue at 0 seconds. The image quality obtained is shown. This was reviewed by the radiologists. (Fig. 4) Image quality (IQ) was evaluated and then requirements were considered. A second patient was scanned by the user. The workflow was repeated again without any verbal assistance from the Application Specialist to ensure that the service could continue on its own. IQ was then checked with this different patient.

Once this was all finished, the protocols were saved and any options for image loading were set using the Find function and properties.

Conclusion

Remote Assist can give you quick answers to applications and IQ issues. However, it is also a useful tool for training, offering you a direct, hands-on approach, while the Application Specialist provides verbal and on-screen guidance. You should therefore perhaps consider an RA session the next time you prepare to expand your service lines.

Availability

Remote Assist is provided only in combination with a standard service contract (Performance Plan TOP, PLUS, PRO) or in combination with an Education Plan, which can either be offered standalone or as an optional element of a service contract.

With Siemens Education Plans, a package of User Services will be tailored to your training and education needs. Based on your goals, your package can include classroom or on-site trainings, hands-on workshops, e-learnings and Webinars, remote trainings, or consulting services.

Educations Plans are available in three service levels:

- **Routine Plan** for basic image quality and patient safety; ideal for continuous on-boarding of new staff. In addition to on-site training, this plan offers Remote Assist for direct application assistance.
- **Expertise Plan** to enhance clinical expertise, improve patient outcome and quality of care, and strengthen employee satisfaction. In addition to classroom training, you can choose from a variety of clinical workshops.
- **Excellence Plan** helps you stand out as a center of excellence. The primary goal is to improve existing routines and daily performance; the focus is on consulting and optimization.

An Education Plan runs for multiple years, and it will typically be linked to one of your Siemens imaging systems. With the Multi-Modality Option, you can expand the Education Plan to include trainings for other Siemens imaging systems. With an Education Plan, you can be confident that your clinical staff will be well-trained and will remain consistently at the forefront of your system's lifecycle. Siemens User Services offers your staff the opportunity to get the most out of your equipment – to use your imaging systems to their fullest potential and to create the best possible outcome for your patients.

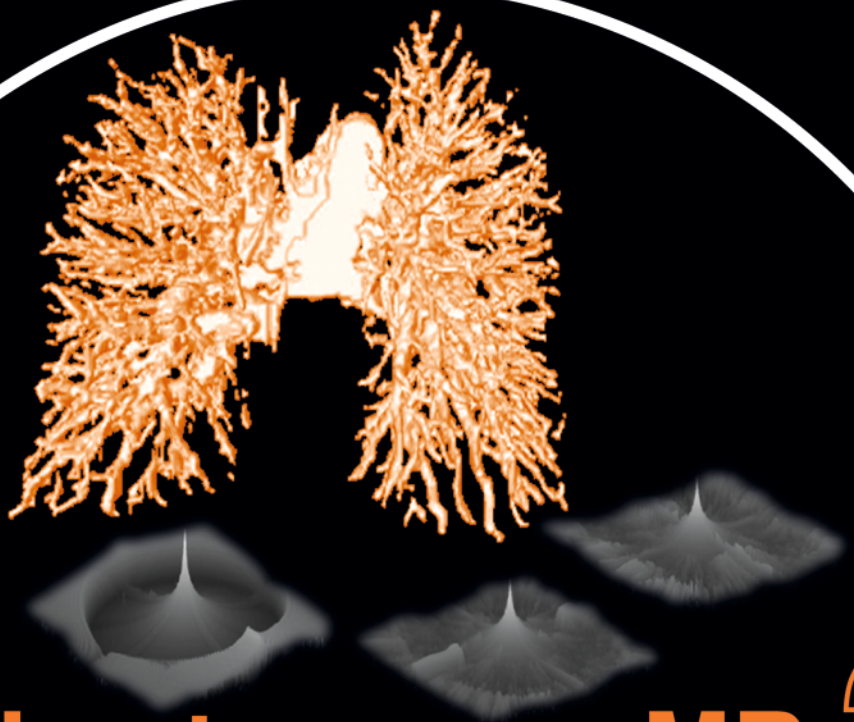


Contact

Gary Smith
Siemens Healthcare
HC CX NWE GB CX-CS BD AM IE MR
Chapel Lane
Dublin
Ireland
Phone: +353 (1) 8132192
smithgary@siemens.com

Advertisement

ESMRMB
European Society for Magnetic Resonance in Medicine and Biology



Lectures on MR 2016

Educational courses, exercises, and practical demonstrations on MR physics and engineering

Simultaneous multi-slice/ multiband imaging
January 18–20, Nijmegen/NL

Acquisition strategies for hyperpolarised spin systems: Spectral, spatial and temporal
February 24–26, Munich/DE

Quantitative MRI for characterising brain tissue microstructure
June 6–8, Leipzig/DE
NEW!

Create your own echo: How to generate, calculate and manipulate echoes
June 20–22, Tübingen/DE

RF coils: Design, build and characterise your own
June 21–23, L'Aquila/IT

Non-Cartesian MRI: Implementation and application
August 25–28, Würzburg/DE
NEW!

RF pulses: Design and applications
September 8–10, Krakow/PL

In vivo MR spectroscopy: From basics to advanced methods
September 26–28, Vienna/AT
NEW!

www.esmrmb.org

HIGHLIGHTS OF PRESCRIBING INFORMATION

These highlights do not include all the information needed to use Fludeoxyglucose F 18 Injection safely and effectively. See full prescribing information for Fludeoxyglucose F 18 Injection.
Fludeoxyglucose F 18 Injection, USP
For intravenous use
Initial U.S. Approval: 2005

RECENT MAJOR CHANGES

Warnings and Precautions (5.1, 5.2)	7/2010
Adverse Reactions (6)	7/2010

INDICATIONS AND USAGE

Fludeoxyglucose F18 Injection is indicated for positron emission tomography (PET) imaging in the following settings:

- Oncology: For assessment of abnormal glucose metabolism to assist in the evaluation of malignancy in patients with known or suspected abnormalities found by other testing modalities, or in patients with an existing diagnosis of cancer.
- Cardiology: For the identification of left ventricular myocardium with residual glucose metabolism and reversible loss of systolic function in patients with coronary artery disease and left ventricular dysfunction, when used together with myocardial perfusion imaging.
- Neurology: For the identification of regions of abnormal glucose metabolism associated with foci of epileptic seizures (1).

DOSAGE AND ADMINISTRATION

Fludeoxyglucose F 18 Injection emits radiation. Use procedures to minimize radiation exposure. Screen for blood glucose abnormalities.

- In the oncology and neurology settings, instruct patients to fast for 4 to 6 hours prior to the drug's injection. Consider medical therapy and laboratory testing to assure at least two days of normoglycemia prior to the drug's administration (5.2).
- In the cardiology setting, administration of glucose-containing food or liquids (e.g., 50 to 75 grams) prior to the drug's injection facilitates localization of cardiac ischemia (2.3).

Aseptically withdraw Fludeoxyglucose F 18 Injection from its container and administer by intravenous injection (2).

The recommended dose:

- for adults is 5 to 10 mCi (185 to 370 MBq), in all indicated clinical settings (2.1).
- for pediatric patients is 2.6 mCi in the neurology setting (2.2).

Initiate imaging within 40 minutes following drug injection; acquire static emission images 30 to 100 minutes from time of injection (2).

DOSAGE FORMS AND STRENGTHS

Multi-dose 30mL and 50mL glass vial containing 0.74 to 7.40 GBq/mL (20 to 200 mCi/mL) Fludeoxyglucose F 18 Injection and 4.5mg of sodium chloride with 0.1 to 0.5% w/w ethanol as a stabilizer (approximately 15 to 50 mL volume) for intravenous administration (3).

CONTRAINDICATIONS

None

WARNINGS AND PRECAUTIONS

- Radiation risks: use smallest dose necessary for imaging (5.1).
- Blood glucose adnormalities: may cause suboptimal imaging (5.2).

ADVERSE REACTIONS

Hypersensitivity reactions have occurred; have emergency resuscitation equipment and personnel immediately available (6).
To report SUSPECTED ADVERSE REACTIONS, contact PETNET Solutions, Inc. at 877-473-8638 or FDA at 1-800-FDA-1088 or www.fda.gov/medwatch.

USE IN SPECIFIC POPULATIONS

Pregnancy Category C: No human or animal data. Consider alternative diagnostics; use only if clearly needed (8.1).

- Nursing mothers: Use alternatives to breast feeding (e.g., stored breast milk or infant formula) for at least 10 half-lives of radioactive decay, if Fludeoxyglucose F 18 Injection is administered to a woman who is breast-feeding (8.3).
- Pediatric Use: Safety and effectiveness in pediatric patients have not been established in the oncology and cardiology settings (8.4).

See 17 for PATIENT COUNSELING INFORMATION

Revised: 1/2011

FULL PRESCRIBING INFORMATION: CONTENTS*

1 INDICATIONS AND USAGE
1.1 Oncology
1.2 Cardiology
1.3 Neurology
2 DOSAGE AND ADMINISTRATION
2.1 Recommended Dose for Adults
2.2 Recommended Dose for Pediatric Patients
2.3 Patient Preparation
2.4 Radiation Dosimetry
2.5 Radiation Safety – Drug Handling
2.6 Drug Preparation and Administration
2.7 Imaging Guidelines
3 DOSAGE FORMS AND STRENGTHS
4 CONTRAINDICATIONS
5 WARNINGS AND PRECAUTIONS
5.1 Radiation Risks
5.2 Blood Glucose Abnormalities
6 ADVERSE REACTIONS
7 DRUG INTERACTIONS
8 USE IN SPECIFIC POPULATIONS
8.1 Pregnancy
8.3 Nursing Mothers
8.4 Pediatric Use
11 DESCRIPTION
11.1 Chemical Characteristics
11.2 Physical Characteristics
12 CLINICAL PHARMACOLOGY
12.1 Mechanism of Action
12.2 Pharmacodynamics
12.3 Pharmacokinetics
13 NONCLINICAL TOXICOLOGY
13.1 Carcinogenesis, Muta-genesis, Impairment of Fertility
14 CLINICAL STUDIES
14.1 Oncology
14.2 Cardiology
14.3 Neurology
15 REFERENCES
16 HOW SUPPLIED/STORAGE AND DRUG HANDLING
17 PATIENT COUNSELING INFORMATION

* Sections or subsections omitted from the full prescribing information are not listed.

FULL PRESCRIBING INFORMATION

1 INDICATIONS AND USAGE

Fludeoxyglucose F 18 Injection is indicated for positron emission tomography (PET) imaging in the following settings:

1.1 Oncology

For assessment of abnormal glucose metabolism to assist in the evaluation of malignancy in patients with known or suspected abnormalities found by other testing modalities, or in patients with an existing diagnosis of cancer.

1.2 Cardiology

For the identification of left ventricular myocardium with residual glucose metabolism and reversible loss of systolic function in patients with coronary artery disease and left ventricular dysfunction, when used together with myocardial perfusion imaging.

1.3 Neurology

For the identification of regions of abnormal glucose metabolism associated with foci of epileptic seizures.

2 DOSAGE AND ADMINISTRATION

Fludeoxyglucose F 18 Injection emits radiation. Use procedures to minimize radiation exposure. Calculate the final dose from the end of synthesis (EOS) time using proper radioactive decay factors. Assay the final dose in a properly calibrated dose calibrator before administration to the patient [see Description (11.2)].

2.1 Recommended Dose for Adults

Within the oncology, cardiology and neurology settings, the recommended dose for adults is 5 to 10 mCi (185 to 370 MBq) as an intravenous injection.

2.2 Recommended Dose for Pediatric Patients

Within the neurology setting, the recommended dose for pediatric patients is 2.6 mCi, as an intravenous injection. The optimal dose adjustment on the basis of body size or weight has not been determined [see Use in Special Populations (8.4)].

2.3 Patient Preparation

- To minimize the radiation absorbed dose to the bladder, encourage adequate hydration. Encourage the patient to drink water or other fluids (as tolerated) in the 4 hours before their PET study.
- Encourage the patient to void as soon as the imaging study is completed and as often as possible thereafter for at least one hour.
- Screen patients for clinically significant blood glucose abnormalities by obtaining a history and/or laboratory tests [see Warnings and Precautions (5.2)]. Prior to Fludeoxyglucose F 18 PET imaging in the oncology and neurology settings, instruct patient to fast for 4 to 6 hours prior to the drug's injection.
- In the cardiology setting, administration of glucose-containing food or liquids (e.g., 50 to 75 grams) prior to Fludeoxyglucose F18 Injection facilitates localization of cardiac ischemia

2.4 Radiation Dosimetry

The estimated human absorbed radiation doses (rem/mCi) to a newborn (3.4 kg), 1-year old (9.8 kg), 5-year old (19 kg), 10-year old (32 kg), 15-year old (57 kg), and adult (70 kg) from intravenous administration of Fludeoxyglucose F 18 Injection are shown in Table 1. These estimates were calculated based on human[2] data and using the data published by the International Commission on Radiological Protection[4] for Fludeoxyglucose ^{18} F. The dosimetry data show that there are slight variations in absorbed radiation dose for various organs in each of the age groups. These dissimilarities in absorbed radiation dose are due to developmental age variations (e.g., organ size, location, and overall metabolic rate for each age group). The identified critical organs (in descending order) across all age groups evaluated are the urinary bladder, heart, pancreas, spleen, and lungs.

Table 1. Estimated Absorbed Radiation Doses (rem/mCi) After Intravenous Administration of Fludeoxyglucose F-18 Injection[a]

Organ	Newborn (3.4 kg)	1-year old (9.8 kg)	5-year old (19 kg)	10-year old (32 kg)	15-year old (57 kg)	Adult (70 kg)
Bladder wall[b]	4.3	1.7	0.93	0.60	0.40	0.32
Heart wall	2.4	1.2	0.70	0.44	0.29	0.22
Pancreas	2.2	0.68	0.33	0.25	0.13	0.096
Spleen	2.2	0.84	0.46	0.29	0.19	0.14
Lungs	0.96	0.38	0.20	0.13	0.092	0.064
Kidneys	0.81	0.34	0.19	0.13	0.089	0.074
Ovaries	0.80	0.8	0.19	0.11	0.058	0.053
Uterus	0.79	0.35	0.19	0.12	0.076	0.062
LLI wall *	0.69	0.28	0.15	0.097	0.060	0.051
Liver	0.69	0.31	0.17	0.11	0.076	0.058
Gallbladder wall	0.69	0.26	0.14	0.093	0.059	0.049
Small intestine	0.68	0.29	0.15	0.096	0.060	0.047
ULI wall **	0.67	0.27	0.15	0.090	0.057	0.046
Stomach wall	0.65	0.27	0.14	0.089	0.057	0.047
Adrenals	0.65	0.28	0.15	0.095	0.061	0.048
Testes	0.64	0.27	0.14	0.085	0.052	0.041
Red marrow	0.62	0.26	0.14	0.089	0.057	0.047
Thymus	0.61	0.26	0.14	0.086	0.056	0.044
Thyroid	0.61	0.26	0.13	0.080	0.049	0.039
Muscle	0.58	0.25	0.13	0.078	0.049	0.039
Bone surface	0.57	0.24	0.12	0.079	0.052	0.041
Breast	0.54	0.22	0.11	0.068	0.043	0.034
Skin	0.49	0.20	0.10	0.060	0.037	0.030
Brain	0.29	0.13	0.09	0.078	0.072	0.070
Other tissues	0.59	0.25	0.13	0.083	0.052	0.042

[a] MIRDOSE 2 software was used to calculate the radiation absorbed dose. Assumptions on the biodistribution based on data from Gallagher et al.1 and Jones et al.2

[b] The dynamic bladder model with a uniform voiding frequency of 1.5 hours was used. *LLI = lower large intestine; **ULI = upper large intestine

2.5 Radiation Safety – Drug Handling

- Use waterproof gloves, effective radiation shielding, and appropriate safety measures when handling Fludeoxyglucose F 18 Injection to avoid unnecessary radiation exposure to the patient, occupational workers, clinical personnel and other persons.
- Radiopharmaceuticals should be used by or under the control of physicians who are qualified by specific training and experience in the safe use and handling of radionuclides, and whose experience and training have been approved by the appropriate governmental agency authorized to license the use of radionuclides.
- Calculate the final dose from the end of synthesis (EOS) time using proper radioactive decay factors. Assay the final dose in a properly calibrated dose calibrator before administration to the patient [see Description (11.2)].
- The dose of Fludeoxyglucose F 18 used in a given patient should be minimized consistent with the objectives of the procedure, and the nature of the radiation detection devices employed.

2.6 Drug Preparation and Administration

- Calculate the necessary volume to administer based on calibration time and dose.
- Aseptically withdraw Fludeoxyglucose F 18 Injection from its container.
- Inspect Fludeoxyglucose F 18 Injection visually for particulate matter and discoloration before administration, whenever solution and container permit.
- Do not administer the drug if it contains particulate matter or discoloration; dispose of these unacceptable or unused preparations in a safe manner, in compliance with applicable regulations.
- Use Fludeoxyglucose F 18 Injection within 12 hours from the EOS.

2.7 Imaging Guidelines

- Initiate imaging within 40 minutes following Fludeoxyglucose F 18 Injection administration.
- Acquire static emission images 30 to 100 minutes from the time of injection.

3 DOSAGE FORMS AND STRENGTHS

Multiple-dose 30 mL and 50 mL glass vial containing 0.74 to 7.40 GBq/mL (20 to 200 mCi/mL) of Fludeoxyglucose F 18 Injection and 4.5 mg of sodium chloride with 0.1 to 0.5% w/w ethanol as a stabilizer (approximately 15 to 50 mL volume) for intravenous administration.

4 CONTRAINDICATIONS

None

5 WARNINGS AND PRECAUTIONS

5.1 Radiation Risks

Radiation-emitting products, including Fludeoxyglucose F 18 Injection, may increase the risk for cancer, especially in pediatric patients. Use the smallest dose necessary for imaging and ensure safe handling to protect the patient and health care worker [see Dosage and Administration (2.5)].

5.2 Blood Glucose Abnormalities

In the oncology and neurology setting, suboptimal imaging may occur in patients with inadequately regulated blood glucose levels. In these patients, consider medical therapy and laboratory testing to assure at least two days of normoglycemia prior to Fludeoxyglucose F 18 Injection administration.

6 ADVERSE REACTIONS

Hypersensitivity reactions with pruritus, edema and rash have been reported in the postmarketing setting. Have emergency resuscitation equipment and personnel immediately available.

7 DRUG INTERACTIONS

The possibility of interactions of Fludeoxyglucose F 18 Injection with other drugs taken by patients undergoing PET imaging has not been studied.

8 USE IN SPECIFIC POPULATIONS

8.1 Pregnancy

Pregnancy Category C

Animal reproduction studies have not been conducted with Fludeoxyglucose F 18 Injection. It is also not known whether Fludeoxyglucose F 18 Injection can cause fetal harm when administered to a pregnant woman or can affect reproduction capacity. Consider alternative diagnostic tests in a pregnant woman; administer Fludeoxyglucose F 18 Injection only if clearly needed.

8.3 Nursing Mothers

It is not known whether Fludeoxyglucose F 18 Injection is excreted in human milk. Consider alternative diagnostic tests in women who are breast-feeding. Use alternatives to breast feeding (e.g., stored breast milk or infant formula) for at least 10 half-lives of radioactive decay, if Fludeoxyglucose F 18 Injection is administered to a woman who is breast-feeding.

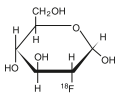
8.4 Pediatric Use

The safety and effectiveness of Fludeoxyglucose F 18 Injection in pediatric patients with epilepsy is established on the basis of studies in adult and pediatric patients. In pediatric patients with epilepsy, the recommended dose is 2.6 mCi. The optimal dose adjustment on the basis of body size or weight has not been determined. In the oncology or cardiology settings, the safety and effectiveness of Fludeoxyglucose F 18 Injection have not been established in pediatric patients.

11 DESCRIPTION

11.1 Chemical Characteristics

Fludeoxyglucose F 18 Injection is a positron emitting radiopharmaceutical that is used for diagnostic purposes in conjunction with positron emission tomography (PET) imaging. The active ingredient 2-deoxy-2-[^{18}F]fluoro-D-glucose has the molecular formula of $C_6H_{11}{}^{18}FO_5$ with a molecular weight of 181.26, and has the following chemical structure:



Fludeoxyglucose F 18 Injection is provided as a ready to use sterile, pyrogen free, clear, colorless solution. Each mL contains between 0.740 to 7.40GBq (20.0 to 200 mCi) of 2-deoxy-2-[^{18}F]fluoro-D-glucose at the EOS, 4.5 mg of sodium chloride and 0.1 to 0.5% w/w ethanol as a stabilizer. The pH of the solution is between 4.5 and 7.5. The solution is packaged in a multiple-dose glass vial and does not contain any preservative.

11.2 Physical Characteristics

Fluorine F 18 decays by emitting positron to Oxygen O 16 (stable) and has a physical half-life of 109.7 minutes. The principal photons useful for imaging are the dual 511 keV gamma photons, that are produced and emitted simultaneously in opposite direction when the positron interacts with an electron (Table 2).

Table 2. Pricipal Radiation Emission Data for Fluorine F18

Radiation/Emission	% Per Disintegration	Mean Energy
Positron (b+)	96.73	249.8 keV
Gamma (±)*	193.46	511.0 keV

*Produced by positron annihilation

From: Kocher, D.C. Radioactive Decay Tables DOE/TIC-I 1026, 89 (1981)

The specific gamma ray constant (point source air kerma coefficient) for fluorine F 18 is 5.7 R/hr/mCi (1.35 x 10-6 Gy/hr/kBq) at 1 cm. The half-value layer (HVL) for the 511 keV photons is 4 mm lead (Pb). The range of attenuation coefficients for this radionuclide as a function of lead shield thickness is shown in Table 3. For example, the interposition of an 8 mm thickness of Pb, with a coefficient of attenuation of 0.25, will decrease the external radiation by 75%.

Table 3. Radiation Attenuation of 511 keV Photons by lead (Pb) shielding

Shield thickness (Pb) mm	Coefficient of attenuation
0	0.00
4	0.50
8	0.25
13	0.10
26	0.01
39	0.001
52	0.0001

For use in correcting for physical decay of this radionuclide, the fractions remaining at selected intervals after calibration are shown in Table 4.

Table 4. Physical Decay Chart for Fluorine F18

Minutes	Fraction Remaining
0*	1.000
15	0.909
30	0.826
60	0.683
110	0.500
220	0.250

*calibration time

12 CLINICAL PHARMACOLOGY

12.1 Mechanism of Action

Fludeoxyglucose F 18 is a glucose analog that concentrates in cells that rely upon glucose as an energy source, or in cells whose dependence on glucose increases under pathophysiological conditions. Fludeoxyglucose F 18 is transported through the cell membrane by facilitative glucose transporter proteins and is phosphorylated within the cell to [18F] FDG-6-phosphate by the enzyme hexokinase. Once phosphorylated it cannot exit until it is dephosphorylated by glucose-6-phosphatase. Therefore, within a given tissue or pathophysiological process, the retention and clearance of Fludeoxyglucose F 18 reflect a balance involving glucose transporter, hexokinase and glucose-6-phosphatase activities. When allowance is made for the kinetic differences between glucose and Fludeoxyglucose F 18 transport and phosphorylation (expressed as the ‚lumped constant" ratio), Fludeoxyglucose F 18 is used to assess glucose metabolism. In comparison to background activity of the specific organ or tissue type, regions of decreased or absent uptake of Fludeoxyglucose F 18 reflect the decrease or absence of glucose metabolism. Regions of increased uptake of Fludeoxyglucose F 18 reflect greater than normal rates of glucose metabolism.

12.2 Pharmacodynamics

Fludeoxyglucose F 18 Injection is rapidly distributed to all organs of the body after intravenous administration. After background clearance of Fludeoxyglucose F 18 Injection, optimal PET imaging is generally achieved between 30 to 40 minutes after administration.

In cancer, the cells are generally characterized by enhanced glucose metabolism partially due to (1) an increase in activity of glucose transporters, (2) an increased rate of phosphorylation activity, (3) a reduction of phosphatase activity or, (4) a dynamic alteration in the balance among all these processes. However, glucose metabolism of cancer as reflected by Fludeoxyglucose F 18 accumulation shows considerable variability. Depending on tumor type, stage, and location, Fludeoxyglucose F 18 accumulation may be increased, normal, or decreased. Also, inflammatory cells can have the same variability of uptake of Fludeoxyglucose F 18.

In the heart, under normal aerobic conditions, the myocardium meets the bulk of its energy requirements by oxidizing free fatty acids. Most of the exogenous glucose taken up by the myocyte is converted into glycogen. However, under ischemic conditions, the oxidation of free fatty acids decreases, exogenous glucose becomes the preferred myocardial sub strate, glycolysis is stimulated, and glucose taken up by the myocyte i s metabolized immediately instead of being converted into glycogen. Under these conditions, phosphorylated Fludeoxyglucose F 18 accumulates in the myocyte and can be detected with PET imaging.

In the brain, cells normally rely on aerobic metabolism. In epilepsy, the glucose metabolism varies. Generally, during a seizure, glucose metabolism increases. Interictally, the seizure focus tends to be hypometabolic.

12.3 Pharmacokinetics

Distribution: In four healthy male volunteers, receiving an intravenous administration of 30 seconds in duration, the arterial blood level profile for Fludeoxyglucose F 18 decayed triexponentially. The effective half-life ranges of the three phases were 0.2 to 0.3 minutes, 10 to 13 minutes with a mean and standard deviation (STD) of 11.6 (±) 1.1 min, and 80 to 95 minutes with a mean and STD of 88 (±) 4 min.

Plasma protein binding of Fludeoxyglucose F 18 has not been studied.

Metabolism: Fludeoxyglucose F 18 is transported into cells and phosphorylated to [^{18}F]-FDG-6- phosphate at a rate proportional to the rate of glucose utilization within that tissue. [F18]-FDG-6-phosphate presumably is metabolized to 2-deoxy-2-[F18]fluoro-6-phospho-D-mannose([F 18]FDM-6-phosphate).

Fludeoxyglucose F 18 Injection may contain several impurities (e.g., 2-deoxy-2-chloro-D-glucose (ClDG)). Biodistribution and metabolism of ClDG are presumed to be similar to Fludeoxyglucose F 18 and would be expected to result in intracellular formation of 2-deoxy-2-chloro-6-phospho-D-glucose (ClDG-6-phosphate) and 2-deoxy-2-chloro-6-phospho-D-mannose (ClDM-6-phosphate). The phosphorylated deoxyglucose compounds are dephosphorylated and the resulting compounds (FDG, FDM, ClDG, and ClDM) presumably leave cells by passive diffusion. Fludeoxyglucose F 18 and related compounds are cleared from non-cardiac tissues within 3 to 24 hours after administration. Clearance from the cardiac tissue may require more than 96 hours. Fludeoxyglucose F 18 that is not involved in glucose metabolism in any tissue is then excreted in the urine.

Elimination: Fludeoxyglucose F 18 is cleared from most tissues within 24 hours and can be eliminated from the body unchanged in the urine. Three elimination phases have been identified in the reviewed literature. Within 33 minutes, a mean of 3.9% of the administrated radioactive dose was measured in the urine. The amount of radiation exposure of the urinary bladder at two hours post-administration suggests that 20.6% (mean) of the radioactive dose was present in the bladder.

Special Populations:

The pharmacokinetics of Fludeoxyglucose F 18 Injection have not been studied in renally-impaired, hepatically impaired or pediatric patients. Fludeoxyglucose F 18 is eliminated through the renal system. Avoid excessive radiation exposure to this organ system and adjacent tissues.

The effects of fasting, varying blood sugar levels, conditions of glucose intolerance, and diabetes mellitus on Fludeoxyglucose F 18 distribution in humans have not been ascertained [see Warnings and Precautions (5.2)].

13 NONCLINICAL TOXICOLOGY

13.1 Carcinogenesis, Mutagenesis, Impairment of Fertility

Animal studies have not been performed to evaluate the Fludeoxyglucose F 18 Injection carcinogenic potential, mutagenic potential or effects on fertility.

14 CLINICAL STUDIES

14.1 Oncology

The efficacy of Fludeoxyglucose F 18 Injection in positron emission tomography cancer imaging was demonstrated in 16 independent studies. These studies prospectively evaluated the use of Fludeoxyglucose F 18 in patients with suspected or known malignancies, including non-small cell lung cancer, colo-rectal, pancreatic, breast, thyroid, melanoma, Hodgkin's and non-Hodgkin's lymphoma, and various types of metastatic cancers to lung, liver, bone, and axillary nodes. All these studies had at least 50 patients and used pathology as a standard of truth. The Fludeoxyglucose F 18 Injection doses in the studies ranged from 200 MBq to 740 MBq with a median and mean dose of 370 MBq.

In the studies, the diagnostic performance of Fludeoxyglucose F 18 Injection varied with the type of cancer, size of cancer, and other clinical conditions. False negative and false positive scans were observed. Negative Fludeoxyglucose F 18 Injection PET scans do not exclude the diagnosis of cancer. Positive Fludeoxyglucose F 18 Injection PET scans can not replace pathology to establish a diagnosis of cancer. Non-malignant conditions such as fungal infections, inflammatory processes and benign tumors have patterns of increased glucose metabolism that may give rise to false-positive scans. The efficacy of Fludeoxyglucose F 18 Injection PET imaging in cancer screening was not studied.

14.2 Cardiology

The efficacy of Fludeoxyglucose F 18 Injection for cardiac use was demonstrated in ten independent, prospective studies of patients with coronary artery disease and chronic left ventricular systolic dysfunction who were scheduled to undergo coronary revascularization. Before revascularization, patients underwent PET imaging with Fludeoxyglucose F 18 Injection (74 to 370 MBq, 2 to 10 mCi) and perfusion imaging with other diagnostic radiopharmaceuticals. Doses of Fludeoxyglucose F 18 Injection ranged from 74 to 370 MBq (2 to 10 mCi). Segmental, left ventricular, wall-motion assessments of asynergic areas made before revascularization were compared in a blinded manner to assessments made after successful revascularization to identify myocardial segments with functional recovery.

Left ventricular myocardial segments were predicted to have reversible loss of systolic function if they showed Fludeoxyglucose F 18 accumulation and reduced perfusion (i.e., flow-metabolism mismatch). Conversely, myocardial segments were predicted to have irreversible loss of systolic function if they showed reductions in both Fludeoxyglucose F 18 accumulation and perfusion (i.e., matched defects).

Findings of flow-metabolism mismatch in a myocardial segment may suggest that successful revascularization will restore myocardial function in that segment. However, false-positive tests occur regularly, and the decision to have a patient undergo revascularization should not be based on PET findings alone. Similarly, findings of a matched defect in a myocardial segment may suggest that myocardial function will not recover in that segment, even if it is successfully revascularized. However, false-negative tests occur regularly, and the decision to recommend against coronary revascularization, or to recommend a cardiac transplant, should not be based on PET findings alone. The reversibility of segmental dysfunction as predicted with Fludeoxyglucose F 18 PET imaging

depends on successful coronary revascularization. Therefore, in patients with a low likelihood of successful revascularization, the diagnostic usefulness of PET imaging with Fludeoxyglucose F 18 Injection is more limited.

14.3 Neurology

In a prospective, open label trial, Fludeoxyglucose F 18 Injection was evaluated in 86 patients with epilepsy. Each patient received a dose of Fludeoxyglucose F 18 Injection in the range of 185 to 370 MBq (5 to 10 mCi). The mean age was 16.4 years (range: 4 months to 58 years; of these, 42 patients were less than 12 years and 16 patients were less than 2 years old). Patients had a known diagnosis of complex partial epilepsy and were under evaluation for surgical treatment of their seizure disorder. Seizure foci had been previously identified on ictal EEGs and sphenoidal EEGs. Fludeoxyglucose F 18 Injection PET imaging confirmed previous diagnostic findings in 16% (14/87) of the patients; in 34% (30/87) of the patients, Fludeoxyglucose F 18 Injection PET images provided new findings. In 32% (27/87), imaging with Fludeoxyglucose F 18 Injection was inconclusive. The impact of these imaging findings on clinical outcomes is not known.

Several other studies comparing imaging with Fludeoxyglucose F 18 Injection results to subsphenoidal EEG, MRI and/or surgical findings supported the concept that the degree of hypometabolism corresponds to areas of confirmed epileptogenic foci. The safety and effectiveness of Fludeoxyglucose F 18 Injection to distinguish idiopathic epileptogenic foci from tumors or other brain lesions that may cause seizures have not been established.

15 REFERENCES

1. Gallagher B.M., Ansari A., Atkins H., Casella V., Christman D.R., Fowler J.S., Ido T., MacGregor R.R., Som P., Wan C.N., Wolf A.P., Kuhl D.E., and Reivich M. "Radiopharmaceuticals XXVII. 18F-labeled 2-deoxy-2-fluoro-d-glucose as a radiopharmaceutical for measuring regional myocardial glucose metabolism in vivo: tissue distribution and imaging studies in animals," J Nucl Med, 1977; 18, 990-6.
2. Jones S.C., Alavi, A., Christman D., Montanez, I., Wolf, A.P., and Reivich M. "The radiation dosimetry of 2 [F-18] fluoro-2-deoxy-D-glucose in man," J Nucl Med, 1982; 23, 613-617.
3. Kocher, D.C. "Radioactive Decay Tables: A handbook of decay data for application to radiation dosimetry and radiological assessments," 1981, DOE/TIC-I 1026, 89.
4. ICRP Publication 53, Volume 18, No. I-4,1987, pages 75-76.

16 HOW SUPPLIED/STORAGE AND DRUG HANDLING

Fludeoxyglucose F 18 Injection is supplied in a multi-dose, capped 30 mL and 50 mL glass vial containing between 0.740 to 7.40 GBq/mL (20 to 200 mCi/mL), of no carrier added 2-deoxy-2-[F 18] fluoro-D-glucose, at end of synthesis, in approximately 15 to 50 mL. The contents of each vial are sterile, pyrogen-free and preservative-free.

NDC 40028-511-30; 40028-511-50

Receipt, transfer, handling, possession, or use of this product is subject to the radioactive material regulations and licensing requirements of the U.S. Nuclear Regulatory Commission, Agreement States or Licensing States as appropriate.

Store the Fludeoxyglucose F 18 Injection vial upright in a lead shielded container at 25°C (77°F); excursions permitted to 15-30°C (59-86°F).

Store and dispose of Fludeoxyglucose F 18 Injection in accordance with the regulations and a general license, or its equivalent, of an Agreement State or a Licensing State.

The expiration date and time are provided on the container label. Use Fludeoxyglucose F 18 Injection within 12 hours from the EOS time.

17 PATIENT COUNSELING INFORMATION

Instruct patients in procedures that increase renal clearance of radioactivity.

Encourage patients to:

- drink water or other fluids (as tolerated) in the 4 hours before their PET study.
- void as soon as the imaging study is completed and as often as possible thereafter for at least one hour.

Manufactured by: PETNET Solutions Inc.
810 Innovation Drive
Knoxville, TN 37932

Distributed by: PETNET Solutions Inc.
810 Innovation Drive
Knoxville, TN 37932

PETNET Solutions

PN0002262 Rev. A

March 1, 2011

Indications

Fludeoxyglucose F^{18} Injection is indicated for positron emission tomography (PET) imaging in the following settings:

- **Oncology:** For assessment of abnormal glucose metabolism to assist in the evaluation of malignancy in patients with known or suspected abnormalities found by other testing modalities, or in patients with an existing diagnosis of cancer.
- **Cardiology:** For the identification of left ventricular myocardium with residual glucose metabolism and reversible loss of systolic function in patients with coronary artery disease and left ventricular dysfunction, when used together with myocardial perfusion imaging.
- **Neurology:** For the identification of regions of abnormal glucose metabolism associated with foci of epileptic seizures.

Important Safety Information

- **Radiation Risks:** Radiationemitting products, including Fludeoxyglucose F^{18} Injection, may increase the risk for cancer, especially in pediatric patients. Use the smallest dose necessary for imaging and ensure safe handling to protect the patient and healthcare worker.
- **Blood Glucose Abnormalities:** In the oncology and neurology setting, suboptimal imaging may occur in patients with inadequately regulated blood glucose levels. In these patients, consider medical therapy and laboratory testing to assure at least two days of normoglycemia prior to Fludeoxyglucose F^{18} Injection administration.
- **Adverse Reactions:** Hypersensitivity reactions with pruritus, edema and rash have been reported; have emergency resuscitation equipment and personnel immediately available.

Siemens Healthcare Publications

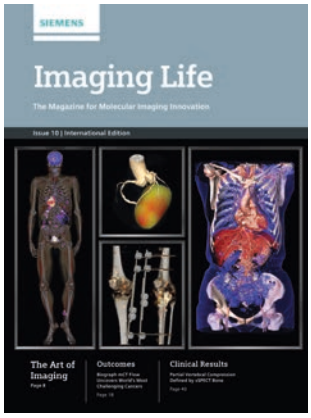
Our publications offer the latest information and background for every healthcare field. From the hospital director to the radiological assistant – here, you can quickly find information relevant to your needs.



MAGNETOM Flash
Everything from the world of magnetic resonance imaging.



SOMATOM Sessions
Everything from the world of computed tomography.



Imaging Life
Everything from the world of molecular imaging innovations.



AXIOM Innovations
Everything from the world of interventional radiology, cardiology, and surgery.



Heartbeat
Everything from the world of sustainable cardiovascular care.



Medical Solutions Online
The online version includes additional video features and greater depth to the articles in the printed healthcare leadership magazine. Read online at:
www.siemens.com/medical-solutions

For current and past issues and to order the magazines, please visit
www.siemens.com/healthcare-magazine

The entire editorial staff at Siemens Healthcare extends their appreciation to all the radiologists, technologists, physicists, experts and scholars who donate their time and energy – without payment – in order to share their expertise with the readers of MAGNETOM Flash.

MAGNETOM Flash – Imprint

© 2015 by Siemens Healthcare GmbH, All Rights Reserved

Publisher:
Siemens Healthcare GmbH
Magnetic Resonance,
Karl-Schall-Straße 6, D-91052 Erlangen, Germany

Editor-in-chief:
Antje Hellwich
(antje.hellwich@siemens.com)

Editorial Board:
Reto Merges; Wellesley Were;
Sunil Kumar S.L., Ph.D.;
Gary R. McNeal, MS (BME);
Peter Kreisler, Ph.D.

Review Board:
Lisa Chuah, Ph.D.; Lars Drüppel, Ph.D.; Berthold Kiefer, Ph.D; Matthias Lichy, M.D., M.Sc.; Heiko Meyer, Ph.D.; Edgar Müller; Gregor Thörmer, Ph.D.; Heike Weh

Production:
Norbert Moser,
Siemens Healthcare GmbH

Layout:
Agentur Baumgärtner,
Friedrichstraße 4, D-90762 Fürth, Germany

Printer:
L/M/B Druck GmbH Mandelkow,
Röntgenstraße 15
D-91074 Herzogenaurach, Germany

Note in accordance with § 33 Para.1 of the German Federal Data Protection Law: Despatch is made using an address file which is maintained with the aid of an automated data processing system.

MAGNETOM Flash is sent free of charge to Siemens MR customers, qualified physicians, technologists, physicists and radiology departments throughout the world. It includes reports in the English language on magnetic resonance: diagnostic and therapeutic methods and their application as well as results and experience gained with corresponding systems and solutions. It introduces from case to case new principles and procedures and discusses their clinical potential. The statements and views of the authors in the individual contributions do not necessarily reflect the opinion of the publisher.

The information presented in these articles and case reports is for illustration only and is not intended to be relied upon by the reader for instruction as to the practice of medicine. Any health care practitioner reading this information is reminded that they must use their own learning, training and expertise in dealing with their individual patients. This material does not substitute for that duty and is not intended by Siemens Healthcare to be used for any purpose in that regard. The drugs and doses mentioned herein are consistent with the approval labeling for uses and/or indications of the drug. The treating physician bears the sole responsibility for the diagnosis and treatment of patients, including drugs and doses prescribed in connection with such use. The Operating Instructions must always be strictly followed when operating the MR system. The sources for the technical data are the corresponding data sheets. Results may vary.

Partial reproduction in printed form of individual contributions is permitted, provided the customary bibliographical data such as author's name and title of the contribution as well as year, issue number and pages of MAGNETOM Flash are named, but the editors request that two copies be sent to them. The written consent of the authors and publisher is required for the complete reprinting of an article.

We welcome your questions and comments about the editorial content of MAGNETOM Flash. Please contact us at magnetomworld.med@siemens.com.

Manuscripts as well as suggestions, proposals and information are always welcome; they are carefully examined and submitted to the editorial board for attention. MAGNETOM Flash is not responsible for loss, damage, or any other injury to unsolicited manuscripts or other materials. We reserve the right to edit for clarity, accuracy, and space. Include your name, address, and phone number and send to the editors, address above.

MAGNETOM Flash is also available online:

www.siemens.com/magnetom-world

On account of certain regional limitations of sales rights and service availability, we cannot guarantee that all products included in this brochure are available through the Siemens sales organization worldwide. Availability and packaging may vary by country and is subject to change without prior notice. Some/All of the features and products described herein may not be available in the United States.

The information in this document contains general technical descriptions of specifications and options as well as standard and optional features which do not always have to be present in individual cases, and which may not be commercially available in all countries. Due to regulatory reasons their future availability cannot be guaranteed. Please contact your local Siemens organization for further details.

Siemens reserves the right to modify the design, packaging, specifications, and options described herein without prior notice. Please contact your local Siemens sales representative for the most current information.

Note: Any technical data contained in this document may vary within defined tolerances. Original images always lose a certain amount of detail when reproduced.

Not for distribution in the US

Siemens Healthcare Headquarters
Siemens Healthcare GmbH
Henkestraße 127
91052 Erlangen
Germany
Phone: +49 9131 84-0
siemens.com/healthcare

Order No. A91MR-1000-116M-7600 | Printed in Germany | CC MR 3113 11150.2. | © Siemens Healthcare GmbH, 2015

siemens.com/magnetom-world